Technische Universität München
TUM School of Engineering and Design

Investigation and Prediction of the Mixture Quality in Multi-Injector Burner Systems

Fabian Ignacio Marquez Macias

Vollständiger Abdruck der von der TUM School of Engineering and Design der Technischen Universitat München zur Erlangung des akademischen Grades eines

DOKTORS DER INGENIEURWISSENSCHAFTEN (DR.-ING.)

genehmigten Dissertation.

Vorsitz:
    Prof. Phaedon-Stelios Koutsourelakis, Ph.D.
Prüfer*innen der Dissertation:
    Prof. Dr.-Ing. Thomas Sattelmayer
    Prof. Jim McGuirk, Ph.D.

Die Dissertation wurde am 13.04.2023 bei der Technischen Universität München eingereicht und durch die TUM School of Engineering and Design am 06.07.2023 angenommen.

Ningún mar en calma hizo experto a un marinero.

Danksagung

Diese Arbeit entstand in den Jahren 2019 bis 2022 am Lehrstuhl für Thermodynamik der Technischen Universität München während meiner Tätigkeit als wissenschaftlicher Mitarbeiter im Rahmen des drittmittelfinanzierten Forschungsvorhabens LaBreVer 1.2 (Last- und brennstoffflexible Verbrennung) in Kooperation mit Siemens Energy. Das Projekt wurde durch den Industriepartner, sowie das Bundesministerium für Wirtschaft und Klimaschutz gefördert.

Mein besonderer Dank gilt meinem Doktorvater Prof. Dr.-Ing. Thomas Sattelmayer für das in mich investierte Vertrauen zur Bearbeitung dieses Forschungsprojekts sowie für die Möglichkeit, den Weg zur Erreichung der Projektziele selbstständig zu erarbeiten. Ihr zielgerichtetes und kritisches Hinterfragen bei sämtlichen Projekttreffen hat erheblich zum Fortschritt dieser Arbeit beigetragen.

Ich möchte mich bei Herrn Dr.-Ing. Christoph Hirsch für die unermüdliche fachliche Betreuung während der Bearbeitungszeit des Projekts ebenfalls sehr herzlich bedanken. Du hast immer an den erfolgreichen Projektabschluss geglaubt - auch in Zeiten mit großen Schwierigkeiten mit dem experimentellen Aufbau; und Du hast mich immer ermutigt weiter zu machen.

Ein besonderer Dank gilt ebenfalls den Siemens-Kollegen Herrn Dr.-Ing. Michael Huth und Herrn Dr.-Ing. Jürgen Meisl für das rege Interesse an dem Projekt, die fachlichen Diskussionen in dem monatlichen Status-Treffen, sowie die erfolgreiche Zusammenarbeit.

Nicht zuletzt möchte ich mich bei allen Mitarbeitern der mechanischen und der elektrischen Werkstatt für ihren Einsatz beim experimentellen Aufbau bedanken. Ein besonderer Dank gilt an dieser Stelle Herrn Jens Hümmer für sein Durchhaltevermögen beim Aufbau des Brennermodells und Herrn Thomas Schleußner für seine Hilfe bei der Entwicklung der CTA-Messtechnik.

An meine Kollegen am Lehrstuhl geht auch ein ganz herzlicher Dank für die tolle Zeit am Lehrstuhl sowie die angenehme Arbeitsatmosphäre. Mit vielen produktiven Diskussionen, Fußball spielen und Unternehmungen am Abend habt ihr mir die Zeit am Lehrstuhl unvergesslich gemacht.

Meinen Studenten Niklas Hain, Johannes Resch, Kevin Schulz, Miguel Domingo, Georg Mederl, Felix Pfündl und Laurenz Schimper danke ich ganz besonders für Eure tolle Arbeitsleistung. Ohne die wäre ich sicher nicht so weit mit dieser Arbeit gekommen.

A mis padres Nancy y Jose Fabián y a mis hermanos Katherine y Erick les agradezco por todo su apoyo desde la distancia, la cual es solo una barrera en número de horas de vuelo, pero no en el corazón, ya que siempre permanecemos uno para todos y todos para uno.

Liebe Kathy, du hast mein Leben schöner und mich glücklicher gemacht. Das hat ebenfalls maßgeblich zu dem Erfolg dieser Arbeit beigetragen. Auch an dich geht deshalb ein ganz herzlicher Dank.

München, den 04.09.2023 Fabian Marquez Macias

Parts of this work were already published by the author in conference proceedings and journal publications [1–5]. All of them are registered according to the currently valid doctoral degree regulations and are thus not explicitly cited.

Teile dieser Arbeit wurden vom Autor bereits vorab als Konferenzbeiträge und Zeitschriftpublikationen veröffentlicht [1–5]. Alle Publikationen sind entsprechend der gültigen Promotionsordnung ordnungsgemäß gemeldet. Sie sind deshalb nicht zwangsläufig im Detail einzeln zitiert. Vielmehr wurde bei der Referenzierung eigener Veröffentlichungen Wert auf Vollständigkeit der Inhalte gelegt.

Abstract

Multi-injector burners offer a high NO_x emissions reduction potential due to the achievable mixture homogeneity and short residence time in the combustion chamber. This potential is reduced by the loss of mixture quality caused by the flow instabilities in the head section originating from the 180° flow turn upstream of the injectors. A deep understanding of this phenomenon helps optimize the flow path in the head section within the spatial and pressure loss constraints of gas turbine combustors to obtain minimal NO_x emissions. In this work, a new model approach was developed to calculate the mixing quality of single injector elements with jet-in-crossflow fuel injection into the turbulent air flow based on experimental data and using the output-based Proper Orthogonal Decomposition (O-POD) approach. The model input is the so-called observable vector, which describes the fluid mechanical effects influencing the mixture quality. The target quantity is the probability mass function (PMF) of the equivalence ratio at the injector outlet. This approach allows a fast estimation of the mixing PMF during the optimization process of the flow path in the head section, which is otherwise only accessible with complex experimental or numerical approaches. The performance of the model was demonstrated with 21 reference datasets, for which a good match between the measurement results and the model output was obtained.

Keywords: Multi-injector burners, NO_x emissions, mixture quality

Zusammenfassung

Multi-Injektor Brenner bieten ein hohes Potential zur Reduzierung der NO_x-Emissionen aufgrund der hohen erreichbaren Mischqualität und kurzen Aufenthaltszeit in der Brennkammer. Dieses Potential wird durch die Erhöhung der Ungemischtheit aufgrund der Strömungsinstabilitäten im Brennerkopf vermindert, die durch die 180° Umlenkung der Strömung stromauf der Injektoren verursacht werden. Ein tieferes Verständnis dieses Phänomens hilft bei der Optimierung der Brennergeometrie im Hinblick auf geringe NO_x Emissionen unter Berücksichtigung der Designanforderungen von Gasturbinenbrennern in Bezug auf den verfügbaren Platz sowie den Gesamtdruckverlust. In dieser Arbeit wurde ein Modell zur Berechnung der Mischqualität in einzelnen Injektoren mit Jet-In-Crossflow Brennstoffeindüsung anhand experimenteller Daten und der O-POD Methode (engl. output-based Proper Orthogonal Decomposition) entwickelt. Die Eingangsgröße ist der sogenannte "observable" Vektor, welcher die strömungsmechanischen Effekte beschreibt, die zu einer Erhöhung der Ungemischtheit führen. Die Wahrscheinlichkeitsdichtefunktion des Äquivalenzverhältnisses am Injektoraustritt wird als Zielgröße betrachtet. Das Modell ermöglicht eine schnelle und einfache Einschätzung der Mischungsstatistik am Injektoraustritt, welche sich ansonsten nur mittels komplexer experimenteller oder numerischer Ansätze bestimmen lässt. Die Anwendbarkeit des Modells wurde mit 21 Referenzdatensätze demonstriert, für welche eine gute Übereinstimmung zwischen der gemessenen und der mit dem Modell berechneten Wahrscheinlichkeitsdichtefunktion erreicht wurde.

Schlüsselwörter: Multi-Injektor Brenner, NO_x Emissionen, Mischqualität

Contents

List of Figures

List of Tables

Nomenclature

Latin Letters

a	Weighting coefficients of modal sum elements $[-]$
A	Cross sectional area $[m^2]$
A_j	Parameter power law jet trajectory $[-]$
A_K	Cable cross sectional area $[m^2]$
b_{bin}	Bin width mixing PMF $[-]$
c	Mass fraction $[-]$
$\overline{c_p}$	Specific heat capacity $[\frac{J}{kgK}]$
d	Diameter $[m]$
d_B	Burner diameter $[m]$
d_H	Hole diameter $[m]$
d_j	Jet diameter $[m]$
d_p	Particle diameter $[m]$
d_{PI}	Particle image diameter $[px]$
D	Molecular diffusion coefficient $[\frac{m^2}{s}]$
D_t	Scalar turbulent diffusivity $[\frac{m^2}{s}]$
E	Energy spectrum $[\frac{J \cdot m}{kg}]$
E_c	Scalar mixing energy spectrum $[\frac{J \cdot m}{kg}]$
f_c	Imaging frequency of the camera $[Hz]$
f_{PIV}	Frequency of image pairs $[Hz]$
F	Number of equivalence ratio values into a determined range $[-]$
H	Height of the burner head $[m]$
H_d	Height of the deflection vane $[m]$
I	Light intensity $[\frac{W}{m^2}]$
j	Momentum flux density ratio $[-]$
j_N	Nominal momentum flux density ratio $[-]$

J	Momentum $[N \cdot s]$
k	Turbulent kinetic energy $[\frac{m^2}{s^2}]$
Kn	Knudsen number $[-]$
l_b	Batchelor length scale $[m]$
l_0	Length scale of largest eddies $[m]$
l_{DI}	Limit between dissipation and inertial subrange $[m]$
l_{EI}	Limit between energy and inertial subrange $[m]$
l_k	Kolmogorov length scale $[m]$
l_m	Micro-mixing length scale $[m]$
L_K	Cable length $[m]$
$\dot{m}$	Mass flow $[\frac{kg}{s}]$
m_j	Exponent power law jet trajectory $[-]$
M	Molar mass $[\frac{g}{mol}]$
Ma	Mach number $[-]$
n	Number of input datasets $[-]$
n_j	Exponent power law jet trajectory $[-]$
n_s	Number of samples of ϕ to obtain the mixing PMF $[-]$
N	Dimension of augmented datasets $[-]$
N_i	Number of injectors $[-]$
N_r	Number of relevant eigenmodes $[-]$
N_R	Number of rows of rectifier plate in radial direction $[-]$
N_U	Number of rows of rectifier plate in tangential direction $[-]$
N_t	Number of snapshots of a time-varying mixture field $[-]$
N_x	Dimension of mixing PMF datasets $[-]$
N_y	Dimension of observable datasets $[-]$
N_ϕ	Number of equivalence ratio values in a mixture snapshot $[-]$
p	Static pressure $[Pa]$
P	Ratio between the static and dynamic pressure $[-]$
P_k	Production rate of kinetic energy $[\frac{m^2}{s^3}]$
Q	Ratio between the perpendicular and the z-velocity $[-]$
r	Radius $[m]$
R	Ratio between the radial and the perpendicular velocity $[-]$
R_K	Cable resistance $[\Omega]$
R_P	Power resistance $[\Omega]$

R_S	Sensor resistance $[\Omega]$
Re	Reynolds number $[-]$
Re_t	Turbulent Reynolds number $[-]$
$\underline{\underline{R}}$	Autocorrelation tensor $[-]$
$\overline{s}$	Displacement of Interrogation Areas (IAs) $[m]$
s_{ij}	Rate of strain $[\frac{1}{s}]$
S	Shear time scale $[s]$
Sc	Schmidt number $[-]$
Sc_t	Turbulent Schmidt number $[-]$
t	Time $[s]$
t_0	Start time for PIV experiments $[s]$
t_{res}	Residence time of the reactants in the combustion chamber $[s]$
$t_{V,C}$	Time delay camera $[s]$
$t_{V,L}$	Time delay between trigger input and output of laser pulse $[s]$
$t_{V,TL}$	Time delay trigger laser $[s]$
T_{ad}	Adiabatic flame temperature $[K]$
T_w	Water temperature $[K]$
u	Flow velocity $[\frac{m}{s}]$
u_{mag}	Velocity magnitude $[\frac{m}{s}]$
u_q	Perpendicular velocity to the main flow direction $[\frac{m}{s}]$
u_r	Radial velocity $[\frac{m}{s}]$
u_θ	Tangential velocity $[\frac{m}{s}]$
U_B	Bridge voltage $[V]$
U_C	Control voltage $[V]$
U_{GND}	Ground voltage $[V]$
U_{Ref}	Reference voltage $[V]$
U_S	Sensor voltage $[V]$
$U_{T,B}$	Transistor basis voltage $[V]$
$U_{T,C}$	Transistor collector voltage $[V]$
$U_{T,E}$	Transistor emitter voltage $[V]$
$\dot{V}$	Volume flow $[\frac{m^3}{h}]$
$\dot{V}_{CTA}$	Measured volume flow with CTA sensor $[\frac{m^3}{h}]$
$\dot{V}_{Ref}$	Measured volume flow with pulse counter $[\frac{m^3}{h}]$
X	Mole fraction $[-]$

x, y, z	Distance in cartesian coordinate system $[m]$
Z_G	Global cell size in the burner head $[-]$

Greek Letters

α	Angular position $[°]$
Δt	Integration time to obtain RANS-equations $[s]$
Δt_{PIV}	Time between two laser pulses during a PIV experiment $[s]$
ΔU_{Offset}	Bridge offset $[V]$
ΔU_T	Transistor offset $[V]$
Δx_p	Camera cut-off $[V]$
ΔX_{NO_X}	Percentage increase of NO_x formation $[-]$
δ_{ij}	Dirac delta $[-]$
ϵ	Turbulent dissipation rate $[\frac{m^2}{s^3}]$
$\underline{\theta}$	Eigenmodes PMF datasets $[-]$
$\underline{\theta^\star}$	Eigenmodes observable velocity datasets $[-]$
$\underline{\theta^\Phi}$	Eigenmodes augmented datasets $[-]$
Θ	Output signal of the camera $[-]$
Θ_{BR}	Background image $[-]$
$\Theta_{C,BR}$	Image output after background correction $[-]$
$\Theta_{C,CAM}$	Image output after correction of the imaging behavior $[-]$
$\Theta_{C,LS}$	Image output after correction of the laser light sheet $[-]$
Θ_{LS}	Picture of the laser light sheet $[-]$
Θ_R	Raw image data $[-]$
κ	Wave number of turbulent eddies $[\frac{1}{m}]$
κ_m	Wave number of micro-mixing scales $[\frac{1}{m}]$
κ_0	Wave number of largest eddies $[\frac{1}{m}]$
λ	Eigenvalue $[-]$
λ_F	Wave length fluorescence light $[m]$
λ_h	Heat conductivity $[\frac{W}{m \cdot K}]$
λ_L	Laser wave length $[m]$
λ_m	Molecule mean free path $[m]$
μ	Dynamic viscosity $[\frac{kg}{m \cdot s}]$
ν	Kinematic viscosity $[\frac{m^2}{s}]$

ν_t	Turbulent viscosity $[\frac{m^2}{s}]$
ρ	Density $[\frac{kg}{m^3}]$
ρ_p	Particle density $[\frac{kg}{m^3}]$
σ_s	Spatial standard deviation $[-]$
σ_{st}	Spatio-temporal standard deviation $[-]$
$\sigma_{u_{mag}}$	Standard deviation of the velocity magnitude $[\frac{m}{s}]$
ρ_p	Particle density $[\frac{kg}{m^3}]$
τ	Turbulent length scale $[s]$
τ_{ij}	Shear stress $[Pa]$
φ	Relative frequency of occurrence mixing PMF $[-]$
φ_{max}	Maximal relative frequency of occurrence mixing PMF $[-]$
$\underline{\varphi}$	Mixing PMF dataset $[-]$
$\varphi^\star$	Observable scalar value $[-]$
$\underline{\varphi^\star}$	Observable velocity data set $[-]$
$\underline{\Phi}$	Augmented data set $[-]$
ϕ	Equivalence ratio $[-]$

Superscripts and subscripts

a	Air
d	Dye
f	Fuel
i	Segment cross sectional area of air flow
k, m	Summation index
M	Mixing tube
L	Laser
p	Particle
q	Perpendicular component to the main flow direction
r	Radial component
θ	Tangential component
N	Nominal value
Ref	Reference
st	Stochiometric

tot	Total
T	Transposed vector
$\dot{(\ )}$	Time derivative
$\overline{(\ )}$	Mean value
$\widetilde{(\ )}$	Absolute value
$(\ )'$	Turbulent fluctuation
$\underline{(\ )}$	Vector quantity
$\underline{\underline{(\ )}}$	Tensor quantity

Abbreviations

BF	Ball Filling
CCD	Charge-Coupled Device
CFD	Computational Fluid Dynamics
CTA	Constant Temperature Anemometry
CO	Carbon monoxide
HC	Honey Comb
LES	Large Eddy Simulation
LIF	Laser Induced Fluorescence
MIB	Multi-Injector Burner
NO_x	Nitric oxide / Nitrogen dioxide
PIV	Particle Image Velocimetry
PMF	Probability Mass Function
$O-POD$	Output based Proper Orthogonal Decomposition
$RANS$	Reynolds Averaged Navier Stokes
RIC	Relative Information Content

1 Introduction

1.1 Motivation

Gas turbines are a key technology to stabilize the electrical power supply in grids with increasing contribution from renewable energy power plants with fluctuating energy output. The efficient utilization of fuels created from renewable energy sources (e.g., natural gas from power-to-gas plants) combined with minimal NO_x and CO emissions is essential for the energy transition. In order to increase the efficiency of lean premixed gas turbine systems, the firing temperature must be increased, and the residence time of the reactants in the combustion chamber must be reduced to suppress the associated increase of NO_x emissions. High mixture homogeneity is also essential for avoiding the occurrence of temperature peaks [6]. In this context, multi-injector burners are a promising alternative to state-of-the-art swirl burners.

Multi-injector burners were already widely investigated in the literature. Matt et al. [7] presented a surface burner concept with which low emission values could be achieved. This concept was not competitive due to the high manufacturing costs and susceptibility to thermo-acoustic instabilities. Tacina et al. [8] proposed a cost-optimized improvement of this concept consisting of 36 single injectors arranged symmetrically in a 15° surface section, as shown in fig. 1.1. The fuel is evenly distributed into the injectors with a distributor welded inside the surface plate. This concept could not enter the gas turbine market despite the achieved low NO_x emissions values as the problems with combustion instabilities remained.

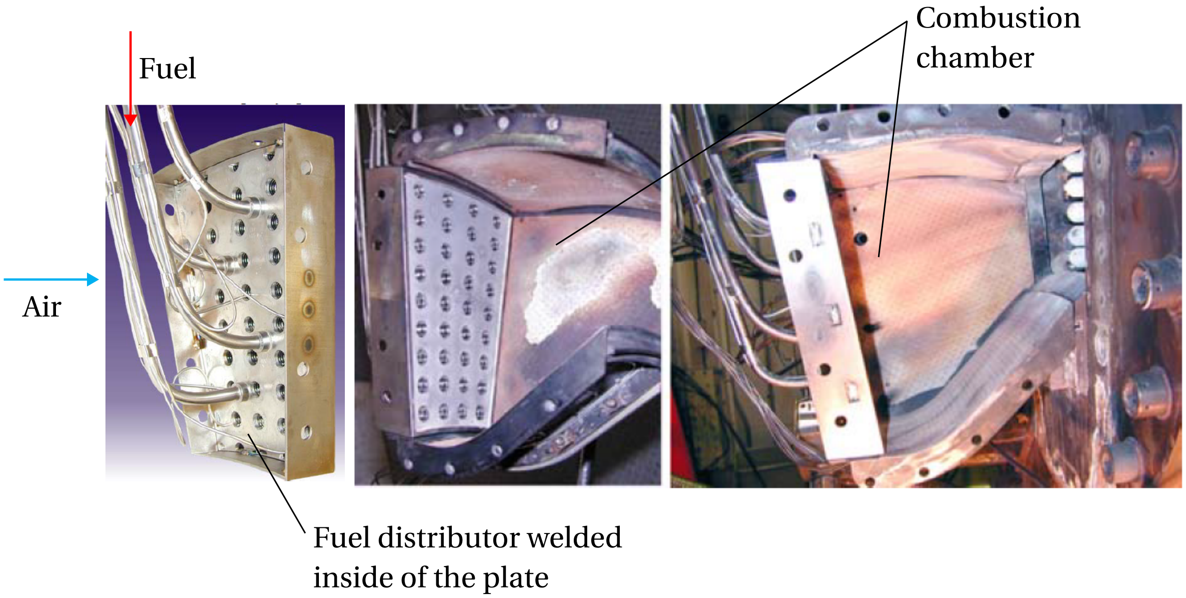

Figure 1.1: Surface burner concept proposed by Tacina et al. [8].

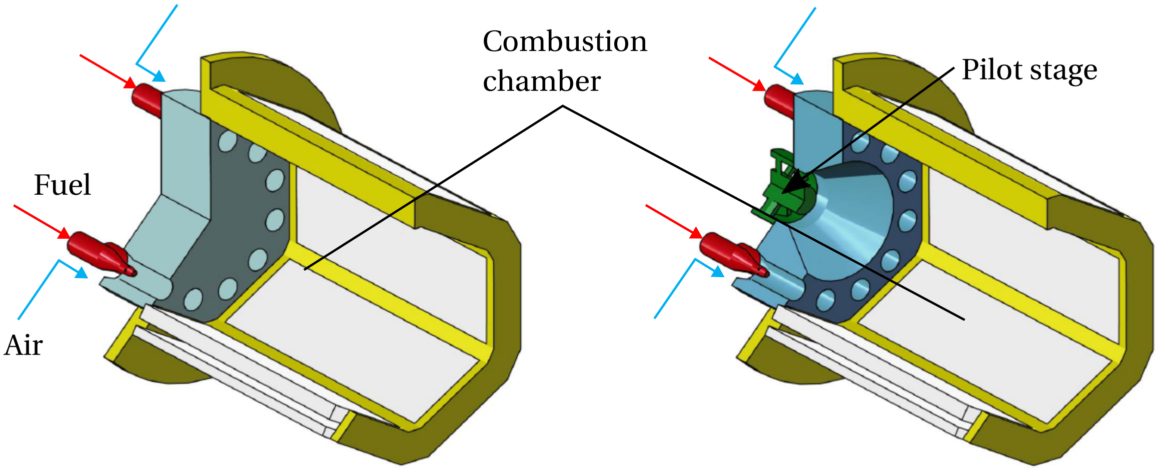

(a) Single stage burner configuration

(b) Piloted system

Figure 1.2: Schematic representation of the can combustor investigated by Lückerath, Schütz and Rödiger et al. [9–11]: (a) single stage, (b) piloted system.

Lückerath et al. [9] investigated the flame position and the emission values of a multi-jet can combustor consisting of 12 single injectors arranged symmetrically around the combustor middle axis, as shown in fig. 1.2(a).

The combustor was operated with natural gas and hydrogen, which were injected in jet-in co-flow through a fuel lance centered in the injector. They obtained the lowest NO_x emissions by increasing the jet exit velocity and thus enhancing the mixture quality at the same mean global equivalence ratio. Schütz et al. [10] made this combustor concept more suitable for gas turbine applications by increasing the power density, also obtaining relatively low emission values. Rödiger et al. [11] increased the operational range of this combustor at lower jet-momentum with satisfactory emission values by changing the air-fuel premixer to a jet-in-crossflow injector and introducing an additional swirl-stabilized pilot stage in the combustor middle axis, as depicted in fig. 1.2(b).

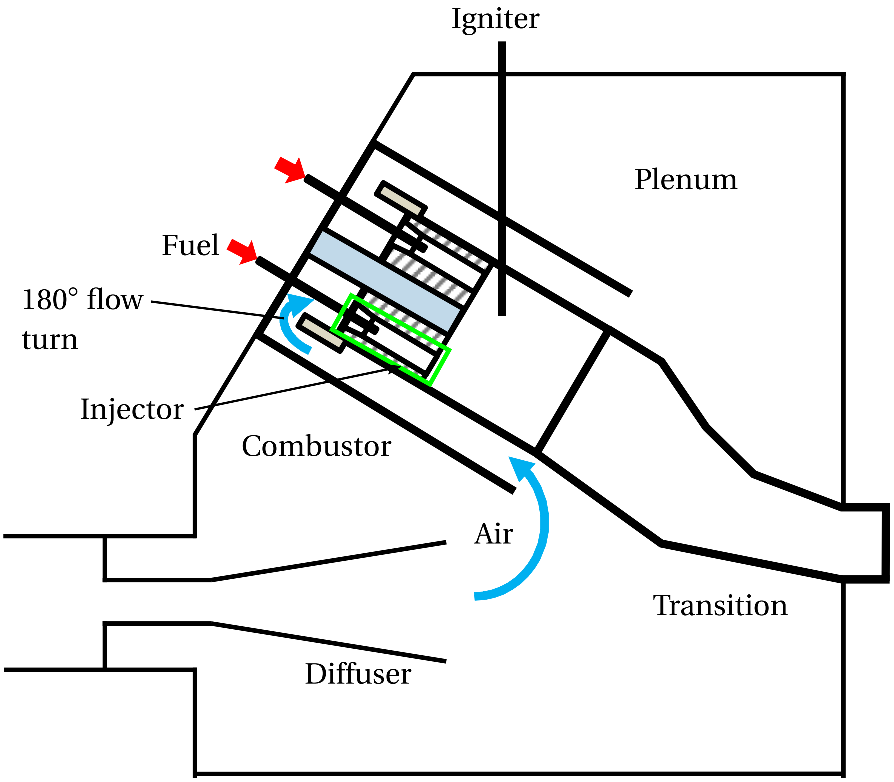

Figure 1.3: Air flow path upstream of the injectors [12].

The combustor in gas turbines is not placed between the compressor and the turbine, as in aircraft engines. Instead, it is mounted diagonally with respect to the middle axis of the compressor in order to keep the rotor length as short as possible. In addition, the combustor must be retractable without dismounting the engine casing for maintenance purposes. The combustion air is also used to cool the combustor walls. Consequently, the combustion air follows a complex flow path downstream of the compressor, which includes a 180° flow turn upstream of the inlet section of the injectors, as shown in fig. 1.3. This sketch shows a meridional cross-section in a typical industrial and power gas turbine where the air flow from the compressor stage is distributed to some can combustors arranged around the circumference of the engine.

This flow path might lead to uneven air distribution through the injectors and high asymmetries of the injector inlet velocity, affecting the mixture quality downstream of the injectors compared with that under symmetric inflow conditions. The correlation between the air flow field at the injector inlet and the mixing quality has not been investigated in the literature and remains uncertain in the development of future gas turbine combustors. The results of this work aim to fill this gap.

1.2 Research Target

The turbulent flow distribution in such complex geometries as the studied combustor can be calculated efficiently and accurately using Reynolds-averaged Navier Stokes (RANS) – Computational Fluid Dynamics (CFD). In contrast, the mixture quality at the injector outlet requires much more complex approaches like Large Eddy Simulations (LES) with a significantly higher computational cost. Alternatively, time-resolved measurement techniques can be used, but the data must be linked to the corresponding turbulent flow distribution in the head section for optimization purposes. This limitation restricts the use of such complex approaches to optimize the flow path in the burner head to obtain optimal NO_x emissions. The complexity of the problem can be reduced by considering the mixing process in an individual injector for a limited number of inflow situations occurring in generic engine configurations. Since the mixing statistic at the injector outlet under arbitrary inflow conditions is needed for optimization, a methodology is required to retrieve the mixing data from the obtained datasets.

This work presents a new model approach to correlate the inflow conditions with the mixture quality based on a limited number of datasets for an injector element. For this purpose, the output-based proper orthogonal decomposition approach (O-POD) is applied. Here the injector inflow conditions are given as the model input with the so-called observable vector. The mixing quality is quantified with the probability mass function (PMF) describing the frequency of occurrence of equivalence ratio values (ϕ) at the injector outlet around the mean $\overline{\phi}$. This function, referred to as the mixing PMF, is the target quantity of the model.

The model is derived from experimental and numerical data for a generic multi-injector burner with the injectors arranged symmetrically around the middle axis in two rows. Jet-in-crossflow injectors with turbulence generators are used as air-fuel premixers. The observable vectors describing the injector inflow conditions are calculated by post-processing RANS-CFD simulation data on the flow path upstream of the injectors. This simulation approach is validated with experimental data on the integral mass flow distribution through the injectors. The mixing PMF is determined experimentally using LIF (Laser-induced Fluorescence) of Uranin in water [13–15] and high-speed imaging in a water channel test rig.

1.3 Thesis Outline

In chapter 2, the fundamentals of turbulent mixing and the similarity rules of the water channel and the reacting flow are presented, followed by a description of the used injection strategy. The O-POD model approach and the reaction mechanisms for NO_x formation are explained afterwards. The experimental methods to quantify the inflow distribution and the mixing PMF are outlined in chapter 3. The RANS-CFD approach to determine the observable vectors is explained in chapter 4. The observable and mixing PMF datasets used to generate the O-POD model are presented in chapter 5. Here the results regarding the dependency of the mixing PMF on the Reynolds number, the momentum flux density ratio, and the inflow distortion in the burner head are discussed in detail. Then, the potentially resulting NO_x formation in the studied multi-injector burner is estimated with the obtained mixing data in chapter 6. The application of the O-POD model approach to predict the mixing PMF for arbitrary inflow conditions is presented in chapter 7. Finally, the conclusions and an outlook with potential future research work are provided in chapter 8.

2 Theory

In this chapter, the theoretical basis for the present work is provided. First, the main concepts and governing equations of turbulent flows are introduced, followed by a discussion of the similarity rules for the water channel test rig and the reacting flow. The injection strategy and the numerical description of the fluid mechanical effects associated with the inflow distortion in the burner head are presented afterwards. Then the developed O-POD model to correlate the inflow conditions with the mixing statistic is presented. Finally, the reaction mechanisms for NO_x formation are discussed.

2.1 Turbulent Flows

Turbulent flows are present in nature and many engineering applications, like the water currents below the surface of oceans and the boundary layer growing on aircraft wings, as instability of laminar flows at increasing Reynolds number. These are characterized by their *randomness* and *diffusivity*, which cause rapid mixing and increased momentum, heat, and mass transfer rates. It makes statistical approaches necessary to solve engineering problems involving turbulence. Furthermore, the dissipated turbulent kinetic energy must be continuously supplied to maintain the turbulent flow regime [16].

2.1.1 Governing Transport Equations

The motion of an incompressible fluid in a turbulent flow regime is characterized by the velocity and pressure field (u_i, p), which are determined by solving the so-called *Navier-Stokes* equations [16]:

$$\frac{\partial \widetilde{u}_i}{\partial t}+\frac{\partial}{\partial x_j}(\widetilde{u_j}\widetilde{u}_i)=\frac{1}{\rho}\frac{\partial}{\partial x_j}(-\widetilde{p}\delta_{ij}+2\mu\widetilde{s_{ij}}), \tag{2.1}$$

$$\frac{\partial \widetilde{u}_i}{\partial x_i}=0, \tag{2.2}$$

with

$$\widetilde{s_{ij}}=\frac{1}{2}\left(\frac{\partial \widetilde{u}_i}{\partial x_j}+\frac{\partial \widetilde{u_j}}{\partial x_i}\right). \tag{2.3}$$

Furthermore, the mixing of a component, whose concentration c does not affect the properties of the main flow, is governed by the passive scalar conservation equation, which includes the convective and diffusive scalar mass transport [17, 18]:

$$\frac{\partial \widetilde{c}}{\partial t}+\frac{\partial}{\partial x_i}(\widetilde{u}_i\widetilde{c})=\frac{\partial}{\partial x_i}\left(D\frac{\partial \widetilde{c}}{\partial x_i}\right). \tag{2.4}$$

A numerical solution to these equations requires an extremely high spatial and temporal resolution to resolve all small-scale turbulence structures. The most widely accepted method to reduce the computational cost consists of decomposing the flow variables as the sum of their mean value and the turbulent fluctuation: $\widetilde{u}_i = U_i + u'_i$; $\widetilde{p} = P + p'$; $\widetilde{c} = C + c'$. By applying this decomposition to eq. 2.1-2.4 and calculating the time average of each term, one obtains the Reynolds-averaged Navier Stokes equations (RANS):

$$\frac{\partial U_i}{\partial t}+\frac{\partial}{\partial x_j}(U_jU_i)=\frac{1}{\rho}\frac{\partial}{\partial x_j}(-P\delta_{ij}+2\mu S_{ij}-\rho\overline{u'_iu'_j}), \tag{2.5}$$

$$\frac{\partial U_i}{\partial x_i}=0, \tag{2.6}$$

$$\frac{\partial C}{\partial t}+\frac{\partial}{\partial x_i}(U_iC)=\frac{\partial}{\partial x_i}\left(D\frac{\partial C}{\partial x_i}-\overline{u'_ic'}\right), \tag{2.7}$$

with:

$$\overline{u'_i u'_j} = \frac{1}{\Delta t} \int_{t_0}^{t_0+\Delta t} u'_i u'_j, \tag{2.8}$$

$$\overline{u'_i c'} = \frac{1}{\Delta t} \int_{t_0}^{t_0+\Delta t} u'_i c'. \tag{2.9}$$

The term in the bracket on the right side of eq. 2.5 represents the sum of three stresses: the isotropic stress of the mean pressure field, the viscous and the apparent stress $\rho \overline{u'_i u'_j}$ arising from the fluctuating velocity field, which is conventionally referred to as the Reynolds stress. The additional vector term in eq. 2.7 appearing through the mean value decomposition $\overline{u'_i c'}$ is referred to as the turbulent scalar flux. It represents the scalar flow rate per unit area due to the fluctuating velocity field [19].

The Reynolds stresses are determined with a turbulence model, either directly with additional Reynolds-stress transport equations or via the isotropic turbulent viscosity hypothesis, which determines the stress components from the mean velocity field as follows:

$$\overline{u'_i u'_j} - \frac{2}{3} k \delta_{ij} = -\nu_t \left(\frac{\partial U_i}{\partial x_j} + \frac{\partial U_j}{\partial x_i} \right). \tag{2.10}$$

The proportionality constant ν_t is the so-called turbulent viscosity, which is calculated as a function of the turbulent kinetic energy k and the turbulent dissipation rate ϵ:

$$\nu_t = c_\mu \frac{k^2}{\epsilon} \approx C u'_i l_t. \tag{2.11}$$

The proportionality to the turbulent velocity fluctuation u'_i and the turbulent length scale l_t becomes clear through the definition of k and ϵ:

$$k = \frac{3}{2} u'^2_i, \tag{2.12}$$

$$\epsilon = \frac{k^{3/2}}{l_t}. \tag{2.13}$$

This hypothesis is directly analogous to the equation for the viscous stress τ_{ij} in a Newtonian fluid:

$$\frac{\tau_{ij} + P\delta_{ij}}{\rho} = \nu \left(\frac{\partial U_i}{\partial x_j} + \frac{\partial U_j}{\partial x_i} \right), \tag{2.14}$$

which was postulated by comparing turbulent flows with the molecule motion in ideal gases. Here, a physical significance to u_i' and l_t was given with an analogy to the molecular speed $\overline{c}$ and the mean free path λ_m as follows:

$$\nu_t \approx C u_i' l_t \rightarrow \nu \approx \frac{1}{2} \overline{c} \lambda_m. \tag{2.15}$$

However, the following examination of the involved time scales shows this analogy has no general validity. In simple laminar shear flows, the ratio between the molecular timescale $\frac{\lambda_m}{\overline{c}}$ and the shear timescale $S^{-1} = \left(\frac{\partial U_i}{\partial x_j} \right)^{-1}$ is:

$$\frac{\lambda_m}{\overline{c}} S \sim Kn \cdot Ma, \tag{2.16}$$

which has an order of magnitude of 10^{-10}. It means that the statistical state of the molecular motion adjusts rapidly to the imposed strain. It is not the case for turbulent shear flows as the ratio between the turbulence timescale $\tau = k/\epsilon$ and the mean shear time scale S^{-1} is many orders of magnitude higher [19].

Nevertheless, for simple shear flows in which the mean velocity gradients and turbulence characteristics develop slowly towards the mean flow direction, the hypothesis was shown to be reasonable. The turbulent kinetic energy production P_k and dissipation ϵ are approximately in balance in such flows. There are several types of flows in which the hypothesis of eq. 2.10 is known to fail significantly. Examples are flows with strong swirling [20], flows with significant streamline curvature [21], and fully developed flows in ducts with no circular cross section [22]. For these types of flows, some special corrections for conventional turbulence modeling have been introduced to improve the approximation with the solution of the RANS equations [23–25]. So it is nowadays possible to model the turbulent flow distribution of complex geometries like the studied multi-injector burner by solving eq. 2.5-2.6 with very good accuracy. As shown in section 4.3, the integral volume flow distribution through the injectors could be reproduced accurately using the $k-\omega$ SST turbulence model [26–28].

The system, including the passive scalar transport equation, is finally closed with the gradient diffusion hypothesis. Here is assumed that the scalar flux vector $\overline{u_i'c'}$ has the same direction of the gradient of the mean scalar concentration $\frac{\partial C}{\partial x_i}$, and both vectors are correlated with a positive scalar turbulent diffusivity D_t:

$$\overline{u_i'c'} = -D_t \frac{\partial C}{\partial x_i}. \tag{2.17}$$

Even though it is widely used for industrial applications, the approximation with this approach is poor for many flows [19]. The gradient-diffusion hypothesis implies that the scalar flux vector is aligned with the mean scalar gradient vector. Even in simple turbulent flows, it was shown that this is not the case. For example, in an experiment on homogeneous turbulent shear flow by Tavoularis and Corrsin [29, 30], the angle between $\frac{\partial C}{\partial x_i}$ and $\overline{u_i'c'}$ was measured to be 65°. Arunajatesan and Bruner [31] also showed that the capability of this approach to predict the mixing behavior in jet-in-crossflow applications is marginal at best.

Consequently, a more complex model is required to accurately predict the mixing statistics, which are essential to estimate the NO_x formation in the combustion chamber. Large Eddy Simulation (LES) is the most accepted approach. However, its implementation for flow simulations in multi-injector burner systems leads to huge computational costs due to the high number of cells necessary to solve the turbulent length scales up to the sub-grid level [32–35]. For this reason, the presented O-POD model approach in this work appears as an attractive alternative to facilitate the optimization of the flow path in the burner head to obtain minimal NO_x emissions.

2.1.2 Turbulent Energy Cascade

Turbulent flows comprise stochastic, vortical structures called *eddies* with different sizes. The largest eddies with the characteristic length l_0 and fluctuating velocity u'_0 are anisotropic, and the mean flow and the boundary conditions determine their geometry. These eddies are unstable and break up, transferring their energy to smaller eddies, according to fig. 2.1. This *energy cascade*, in which the energy is transferred continuously to smaller eddies, continues until the Reynolds number of the eddies is sufficiently small, and the molecular viscosity effectively dissipates the kinetic energy. The length scale of the smallest eddies is called the Kolmogorov scale l_k [19]. The Kolmogorov scale, as well as its characteristic velocity u'_k, are correlated with that of the largest eddies with the turbulent Reynolds number Re_t as follows:

$$\frac{l_k}{l_0} = Re_t^{-3/4}, \tag{2.18}$$

$$\frac{u'_k}{u'_0} = Re_t^{-1/4}. \tag{2.19}$$

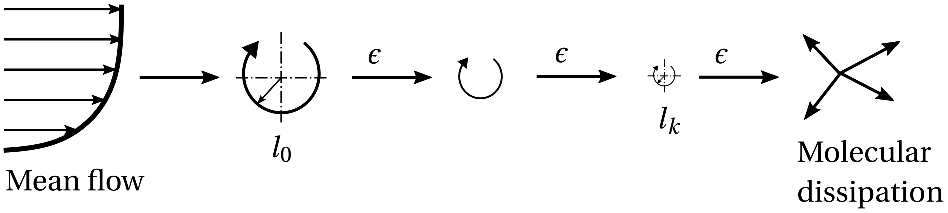

Figure 2.1: Energy transfer from the largest to the smallest eddies.

Fig. 2.2 shows schematically the kinetic energy density $E(\kappa)$ over the wave number $\kappa = \frac{2\pi}{l}$, which is inversely proportional to the size of the turbulent eddies. The integral of $E(\kappa)$ over a given wave number range corresponds to the associated turbulent kinetic energy k, proportional to the mean square of the turbulent velocity fluctuation $\overline{u'^2}$. Interpreting $\overline{u'^2}$ as the "unmixedness" of specific momentum, one can draw an analogy with the scalar concentration variance $\overline{c'^2}$ and set up an analogous scalar spectrum [16]:

$$E_c(\kappa) \sim \frac{\overline{c'^2}}{\overline{u'^2}} E(\kappa)\cdot \tag{2.20}$$

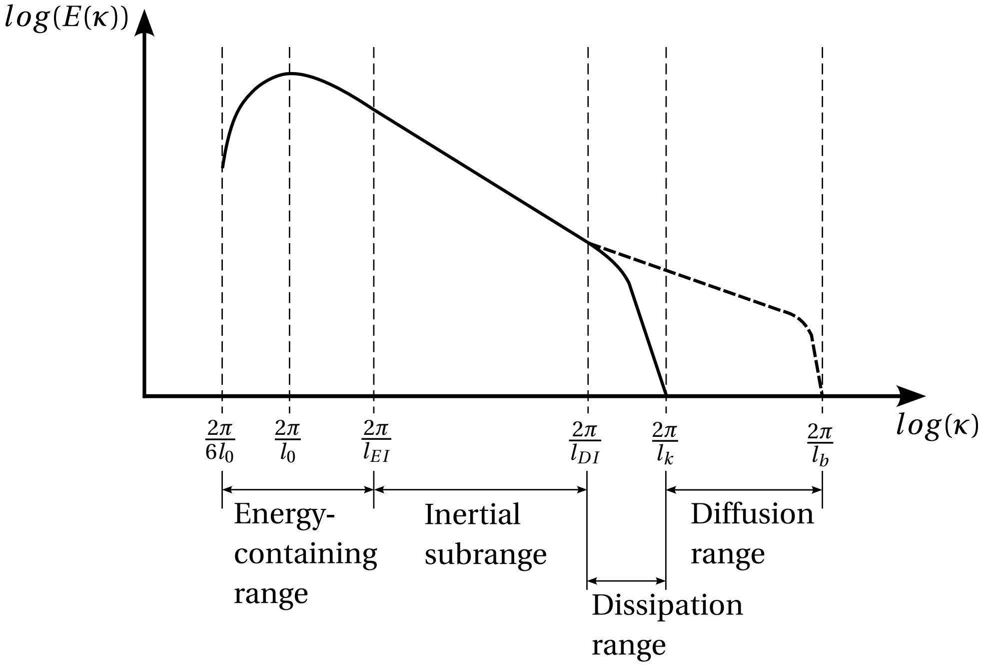

Figure 2.2: Turbulent kinetic energy spectrum [16, 36].

It implies that both processes are completely aligned. This analogy is useful to estimate the accuracy of the concentration measurement as done in section 2.2.1.

The bulk of the energy is contained in the larger eddies within the range $l_{EI} = \frac{1}{6}l_0 < l < 6l_0$, referred to as the *energy-containing range*. In this range, the turbulent motion mainly distributes the specific kinetic energy in space. As these eddies become unstable, they transfer their kinetic energy to smaller eddies at a rate of ϵ. For wave numbers longer than $\frac{2\pi}{l_{EI}}$, the *universal equilibrium range* follows. Here the small eddies can adapt quickly to maintain the dynamic equilibrium with the energy transfer imposed by the large eddies. The statistics of this small-scale motion have a universal form determined only by the viscosity ν and the turbulent dissipation rate ϵ. The universal equilibrium range is further divided into two ranges: the *inertial-subrange* ($l_{EI} > l > l_{DI} \approx 60l_k$) and the *dissipation range* ($l < l_{DI}$).

According to eq. 2.21, the energy spectrum function in the inertial subrange can be approximated with a 5/3 power law:

$$E(\kappa) = C\kappa^{-5/3}. \tag{2.21}$$

Inertial effects determine the motion in the inertial subrange, and the viscous effects are negligible. In the dissipation range, viscosity effects become relevant, and the turbulent kinetic energy is completely dissipated. In the case of scalar mixing, the smallest scale at which molecular diffusion takes place is referred to as the Batchelor scale l_b. It is correlated with the Kolmogorov scale with the Schmidt number as follows [36]:

$$l_b = \frac{l_k}{Sc^{0.5}}. \tag{2.22}$$

At increasing Schmidt number, the scalar energy spectrum extends towards the *diffusion range* ($l_k > l > l_b$, see the dashed line on fig. 2.2) and the smallest mixing length scales are dissipated through molecular diffusion similar to the role of viscosity in the turbulent kinetic energy dissipation.

2.2 Similarity of Water Channel and Reacting Flow

The flow and mixing characteristics of the multi-injector burner were investigated in a water channel test rig due to its high optical accessibility and the possibility of reaching high Reynolds numbers with lower fluid velocities due to the lower kinematic viscosity of water compared to air. According to Leuckel et al. [37], the ratio between the cross-sectional area of the air and the fuel flow, as well as the density and the velocity ratio, must be kept equal in the original and scaled experimental model:

$$\left(\frac{A_f}{A_a}\right)_{scal} = \left(\frac{A_f}{A_a}\right)_{orig}, \tag{2.23}$$

$$\left(\frac{\rho_f}{\rho_a}\right)_{scal} = \left(\frac{\rho_f}{\rho_a}\right)_{orig}, \tag{2.24}$$

$$\left(\frac{u_f}{u_a}\right)_{scal} = \left(\frac{u_f}{u_a}\right)_{orig}. \tag{2.25}$$

It implies that the mass and the momentum flux density ratios are also similar:

$$\left(\frac{\rho_f u_f}{\rho_a u_a}\right)_{scal} = \left(\frac{\rho_f u_f}{\rho_a u_a}\right)_{orig}, \tag{2.26}$$

$$\left(\frac{\rho_f u_f^2}{\rho_a u_a^2}\right)_{scal} = \left(\frac{\rho_f u_f^2}{\rho_a u_a^2}\right)_{orig}. \tag{2.27}$$

By accomplishing these similarity rules, it can be stated that the flow and mixing characteristics of the air and the water flow are proportional. In the water channel experiments, the condition of eq. 2.24 cannot be fulfilled as the air and the fuel flow are simulated with water. This discrepancy is corrected by setting the same momentum flux density ratio j and adjusting the mass flow ratio as follows [13–15, 38, 39]:

$$u = \frac{\dot{m}}{\rho A}. \tag{2.28}$$

By replacing eq. 2.28 in 2.27 and reordering, one obtains the scaling rule for the mass flow ratio of air and fuel in the experiments:

$$j = \left(\frac{\dot{m}_f}{\dot{m}_a}\right)^2 \left(\frac{\rho_a}{\rho_f}\right) \left(\cancel{\frac{A_a}{A_f}}\right)^2_{orig} = \left(\frac{\dot{m}_f}{\dot{m}_a}\right)^2 \overset{=1}{\left(\cancel{\frac{\rho_a}{\rho_f}}\right)} \left(\cancel{\frac{A_a}{A_f}}\right)^2_{exp}, \tag{2.29}$$

$$\left(\frac{\dot{m}_f}{\dot{m}_a}\right)_{exp} = \left(\frac{\dot{m}_f}{\dot{m}_a}\right)_{orig} \left(\sqrt{\frac{\rho_a}{\rho_f}}\right)_{orig}. \tag{2.30}$$

Here the mass flow ratio of the reacting system is calculated with the momentum flux density ratio of the desired operating point as input. The clear water volume flow acting as air in the experiment is kept constant at $\dot{V}_{a,exp} = 20\frac{m^3}{h}$ due to the available pump capacity in the water channel. Hence, the dyed water volume flow acting as fuel for the experiments is calculated with the following equation:

$$\dot{V}_{f,exp} = \dot{V}_{a,exp} \left(\frac{\dot{m}_f}{\dot{m}_a}\right)_{orig} \left(\sqrt{\frac{\rho_a}{\rho_f}}\right)_{orig} \cdot \tag{2.31}$$

The operating parameters for the studied multi-injector burner were designed for natural gas combustion with pre-heating temperatures $T_{a,in} = 778.6K$ and $T_{f,in} = 435.5K$. With the molar mass of air and natural gas ($M_a = 28.97\frac{g}{mol}$ and $M_f = 16.04\frac{g}{mol}$), one obtains the density ratio for the engine operation as follows:

$$\left(\frac{\rho_f}{\rho_a}\right)_{orig} = \frac{\frac{\cancel{p}}{\cancel{R_u}}\frac{M_f}{T_{f,in}}}{\frac{\cancel{p}}{\cancel{R_u}}\frac{M_a}{T_{a,in}}} = 0.9899 \approx 1 \cdot \tag{2.32}$$

Consequently, the correction of eq. 2.31 can be neglected for this study. The turbulent macro- and micro-mixing scales can be considered identical if the injector Reynolds number for the experiments is kept equal to the machine operation:

$$Re = \frac{4\dot{m}_a\left(1 - \%_{Pilot}\right)}{N_i \rho_a \nu_a \pi d_M} \cdot \tag{2.33}$$

With the used clear water volume flow, the injector Reynolds number for the experiments is $Re_{exp} = 13900$, one order of magnitude lower than that for the engine ($Re_{orig} = 363000$). However, as the mixing process takes place in a turbulent flow regime at a sufficiently high Reynolds number ($Re > 6000$), the time-averaged flow fields, the turbulent flow, and the mixing macro-scales are similar for the experiment and the engine operation [13]. The remaining dependency of the mixing statistic on the Reynolds number for the studied injector element in the relevant variation range for the experiments is characterized in section 5.2.2.

The mixing process at the micro-scales is characterized by the Schmidt number as it is dominated by molecular species transport. Due to the high Schmidt number of water ($Sc_w \approx 1000$), some turbulent mixing structures remain after reaching the Kolmogorov length scale l_k in the diffusion range (see fig. 2.2), which are otherwise not present in the reacting flow due to the low Schmidt number of air ($Sc_a \approx 1$). However, these small-scale structures are not captured during the experiments due to the limited spatial resolution of the camera. So the remaining unmixedness in the water flow does not affect the measurement results. The fraction of the energy spectrum of fig. 2.2, which is captured with the experiments, is estimated in the following section.

2.2.1 Accuracy of the Concentration Measurement

The variance of the scalar concentration can be estimated as the integral of the energy spectrum from the macro-scales l_0 to the micro-mixing scales l_m. Approximating the whole spectrum roughly with the equation 2.21 for the inertial subrange, one obtains after reordering:

$$\overline{c'^2} = \int_{\kappa_0}^{\kappa_m} C\kappa^{-5/3} d\kappa = \frac{2}{3} C\kappa_0^{-2/3} \left[1 - \left(\frac{l_0}{l_m} \right)^{-2/3} \right] \cdot \tag{2.34}$$

Replacing l_m with the camera cutoff through the spatial resolution Δx_p and the Kolmogorov scale l_k, one obtains the ratio between the measured and the relevant scalar fluctuations for the reacting flow as follows:

$$\frac{\overline{c'^2}_{meas}}{\overline{c'^2}_{exp}} \approx \frac{1 - \left(\frac{l_0}{\Delta x_p} \right)^{-2/3}}{1 - \left(\frac{l_0}{l_k} \right)^{-2/3}} \approx \frac{1 - \left(\frac{l_0}{\Delta x_p} \right)^{-2/3}}{1 - Re_t^{-1/2}} \approx 0.92 \cdot \tag{2.35}$$

The measured variance of the equivalence ratio is 8% smaller than in reality. For this calculation, the largest mixing scale l_0 was estimated as $l_0 \approx 0.5 \cdot (d_M - d_{Inj}) = 0.00575 m$ according to observations in the mixture snapshots for an experiment with an individual injector for a cross-sectional area at $z/L = 0.5$. The camera cutoff through the spatial resolution was $\Delta x_p = 0.000269m$, and the relevant turbulent Reynolds number for the energy cascade was calculated as $Re_t \approx 0.1 \cdot Re_{exp}$.

As a final remark, it has to be mentioned that the measured flow and mixture fields of the isotherm water channel experiment can be compared with the engine operation only upstream of the reaction zone in the combustion chamber, where the flow begins to be accelerated due to the heat release. As this work is aimed at estimating the influence of the inflow distortion in the burner head on the mixing statistics in the cross-sectional area at the outlet of the injectors, and hence to the potentially resulting NO_x formation, this effect is not further considered relevant.

2.3 Jet-In-Crossflow Injection Strategy

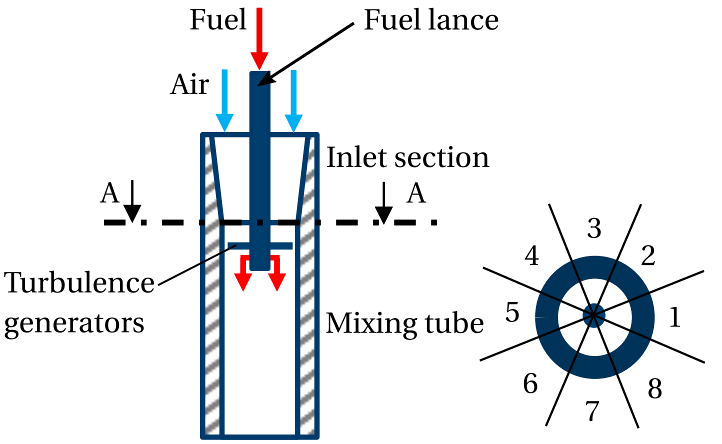

(a) Injector element (b) Sectional view A-A

Figure 2.3: Representation of the injector element.

The injector used as the air-fuel premixer in the studied burner geometry is sketched in fig. 2.3. It consists of a converging inlet section followed by a straight mixing tube. The fuel lance is located on the symmetry axis of the injector, and the fuel is injected in jet-in-crossflow through 8 injection holes distributed evenly around the circumference. For the analysis described below, the cross-sectional area at the end of the inlet section (A-A) is divided into eight segments of 45° (1-8) located directly upstream of the injection holes, as shown in fig. 2.3(b). The mixing process is further stimulated with turbulence generators placed directly upstream of the injection holes.

In the literature, multiple research works were conducted to determine the jet trajectory and the mixing field of jet-in-crossflow configurations [40–53]. Most of them characterized the jet trajectory as a function of the jet diameter d_j and the momentum flux density ratio j with the following power law:

$$\frac{z}{d_j} = A_j \cdot j^{n_j} \left(\frac{x}{d_j}\right)^{m_j}. \tag{2.36}$$

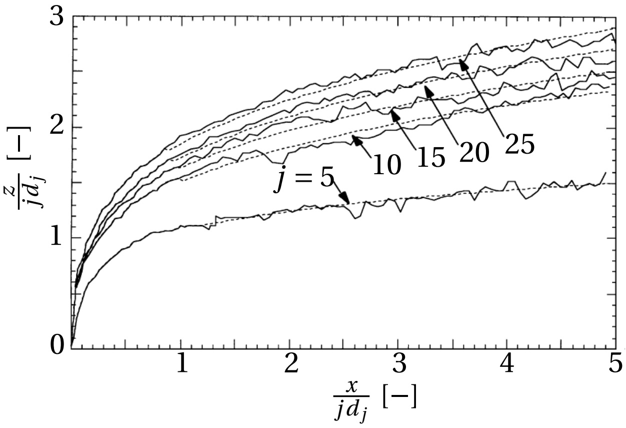

Figure 2.4: Dependency of the jet trajectory on jd_j [54].

According to this equation, a higher penetration depth of the jets in the main flow is obtained by increasing the momentum flux density ratio, as shown in fig. 2.4. Fig. 2.5 illustrates the time-average scalar mixing field and an instantaneous mixture snapshot in the center plane of a mixing process with jet-in-crossflow at $j = 5$ with a constant pressure and inlet velocity as a representative example for the operating range in the studied multi-injector burner. The concentration has its maximum value at the jet-inlet section. It decays rapidly downstream due to the macro- and micro-mixing process associated with the turbulent kinetic energy transfer from the largest to the smallest eddies discussed in section 2.1.2.

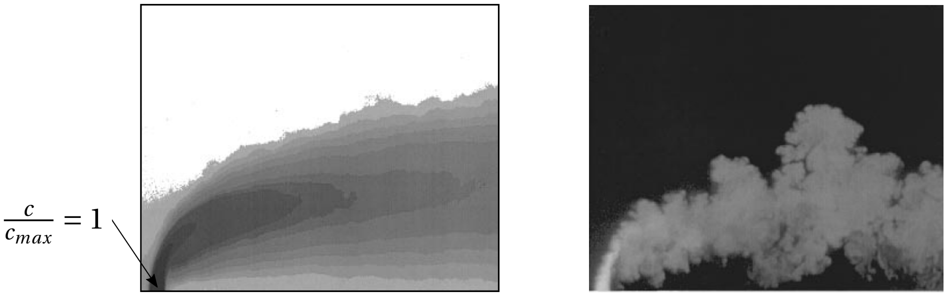

(a) Time-average mixture field (b) Mixture snapshot

Figure 2.5: (a) Time-average mixture field and (b) individual mixture snapshot for $j = 5$ and $Re_j = 16600$. Both images cover an area of $5jd_j$ by $4jd_j$ [54].

2.3.1 Description of the Inflow Distortion

The inflow distortion caused by the 180° flow turn in the burner head leads to an uneven momentum flux distribution at the injector inlet, which is reflected in high velocity and pressure gradients (see section 4.4 CFD results). The velocity has a significant component perpendicular to the main flow direction (z-direction), which can be decomposed into a radial and a tangential component for a system of coordinates related to the middle axis of the injectors.

These effects are quantified with the surface average velocity and pressure values for each segment of the cross-sectional area (A-A) in fig. 2.3(b). The local momentum flux density ratio in each injection hole is calculated with the mean-squared z-velocity value ($\overline{u_z^2}$) obtained from the integration of the total momentum through each segment as follows [50]:

$$j = \frac{u_f^2}{\overline{u_z^2}}, \tag{2.37}$$

$$\dot{J} = \int \rho u_z^2 dA = \rho \overline{u_z^2} \int dA, \tag{2.38}$$

$$\overline{u_z^2} = \frac{\int u_z^2 dA}{\int dA}. \tag{2.39}$$

Furthermore, it is assumed that the radial velocity component $\overline{u_r}$ affects the penetration depth of the jets, and the tangential component $\overline{u_\theta}$ disturbs the jet flow direction. In order to capture both effects, the ratio between the total perpendicular velocity $\overline{u_q}$ and the main z-velocity $\overline{u_z}$ (Q) as well as the ratio between $\overline{u_r}$ and $\overline{u_q}$ (R) are introduced:

$$\overline{u_q} = \sqrt{\overline{u_r}^2 + \overline{u_\theta}^2}, \tag{2.40}$$

$$Q = \frac{\overline{u_q}}{\overline{u_\infty}} = \frac{\overline{u_q}}{\overline{u_z}}, \tag{2.41}$$

$$R = \frac{\overline{u_r}}{\overline{u_q}}. \tag{2.42}$$

R acts as an identifier for ideal inflow conditions, as here $R = -1$ due to the tangential velocity near zero and the negative radial velocity originating from the flow acceleration in the inlet section. Finally, the influence of static pressure gradients between the segments is considered with the normalized value with the mean dynamic pressure:

$$P = \frac{\Delta p}{\rho \overline{u_z^2}} = \frac{\overline{p} - p_{min}}{\rho \overline{u_z^2}}. \tag{2.43}$$

p_{min} corresponds to the lowest calculated static pressure, considered the reference level. The input observable vector for applying the O-POD model approach is generated with the parameters Q, R, and P, and the momentum flux density ratio for each segment, as described in the following section.

2.4 Output-Based Proper Orthogonal Decomposition (O-POD)

The output-based Proper Orthogonal Decomposition approach (O-POD) is used to create a low-order model to describe the sensitivity of the mixing quality to the inflow distortion. Everson and Sirovich developed the method [55] to reconstruct incomplete images of faces. Astrid et al. [56, 57] extended the model approach by calculating the coefficients of high dimensional flow fields. Christ [58–60] used this model approach to determine the enthalpy flux distribution in a heating, ventilation, and air conditioning (HAVC) unit.

The O-POD aims to create a link between variables easily accessible describing a system, denoted as the observable ($\underline{\varphi^\star}$), with variables which are more complex to determine, considered as the target quantity ($\underline{\varphi}$). Both the observable and the target quantity are structured as column vectors, which are put together to generate a snapshot vector describing the system state $\underline{\Phi} = [\underline{\varphi};\underline{\varphi^\star}]$. The snapshot vectors, also referred to as augmented datasets, can be expressed as the series expansion of linearly independent vectors, the so-called eigenmodes ($\underline{\theta^\Phi}$), using Proper Orthogonal Decomposition [55]:

$$\Phi = \sum_{k=1}^{N} a_k \underline{\theta_k^\Phi}, \tag{2.44}$$

$$\left[\begin{array}{c} \underline{\varphi} \\ \hline \underline{\varphi^\star} \end{array}\right] = \sum_{k=1}^{N} a_k \left[\begin{array}{c} \underline{\theta_k} \\ \hline \underline{\theta_k^\star} \end{array}\right]. \tag{2.45}$$

Knowing the eigenmodes, which represent the fundamental behavior of the system, the observable can be correlated with the target quantity as follows: The input $\underline{\varphi^\star}$ vector is approximated as the sum of the corresponding part of the eigenmodes $\underline{\theta^\star}$ multiplied by their weighting coefficients a_k using the least squares method [61–63]:

$$\underline{\varphi^\star} \approx \sum_{k=1}^{N} a_k \underline{\theta_k^\star}, \tag{2.46}$$

$$\min_{a_k} \left\| \sum_{k=1}^{N} a_k \underline{\theta_k^\star} - \underline{\varphi^\star} \right\| = \min_{a_k} \sum_{m=1}^{N_y} \left(\sum_{k=1}^{N} a_k \theta_{k,m}^\star - \varphi_m^\star \right)^2 . \tag{2.47}$$

The obtained coefficients a_k are then used to determine the target quantity $\underline{\varphi}$ as the weighted sum of the corresponding part of the eigenmodes $\underline{\theta}$ as follows:

$$\underline{\varphi} \approx \sum_{k=1}^{N} a_k \underline{\theta_k}. \tag{2.48}$$

In the present application, the inflow characteristics described in chapter 2.3.1 make up the observable vector $\underline{\varphi^\star}$, which is considered as the model input. The probability mass function (PMF) describing the frequency of occurrence of equivalence ratio ϕ around the mean $\overline{\phi}$, referred to as the mixing PMF, is considered as the target quantity $\underline{\varphi}$.

The observable vector is calculated by post-processing a RANS-CFD simulation of the flow path through the injectors (see chapter 4). The mixing PMF is obtained by evaluating LIF experimental data (see section 3.2.2) on the time-varying mixing field in the outlet section of the considered injector element. The observable and the mixing PMF will be introduced in the following two sections of this chapter. The detailed procedure of model application is finally explained in the last section.

2.4.1 Input Observable Vector

The $\underline{\varphi^\star}$ observable vector consists of four parts with eight elements (see eq. 2.49). These elements are the surface averaged values evaluated at the end of the inlet section in each of the eight segments shown in fig. 2.3(b). They describe the fluid mechanical boundary conditions of the injector for a particular mixing PMF.

$$\underline{\varphi^{\star}} = \begin{bmatrix} \frac{j_1}{j_N} \\ \vdots \\ \frac{j_8}{j_N} \\ Q_1 \\ \vdots \\ Q_8 \\ R_1 \\ \vdots \\ R_8 \\ P_1 \\ \vdots \\ P_8 \end{bmatrix} = \begin{bmatrix} \varphi_1^{\star} \\ \vdots \\ \varphi_{32}^{\star} \end{bmatrix}. \tag{2.49}$$

The proportionality of the penetration depth of the jets to the momentum flux density ratio is taken into account with the first part of the vector ($\frac{j_1}{j_N}, ..., \frac{j_8}{j_N}$, see eq. 2.37). Here the values are normalized with the nominal momentum flux density ratio j_N, which is calculated by considering the nominal mass flow and density values for the machine operation as well as the ratio between the cross-sectional areas at the injection point as follows:

$$j_N = \left(\frac{\dot{m}_{N,f}}{\dot{m}_{N,a}}\right)^2 \left(\frac{\rho_{N,a}}{\rho_{N,f}}\right) \left(\frac{A_a}{A_f}\right)^2. \tag{2.50}$$

The influence of the velocity components perpendicular to the main flow direction is considered in the second and third parts of the vector. The second part reflects the ratio between the total perpendicular velocity component $\overline{u_q}$ to the velocity in main flow direction $\overline{u_z}$ ($Q_1, ..., Q_8$, see eq. 2.41). The third part comprises the ratio between the radial velocity $\overline{u_r}$ and the perpendicular velocity component $\overline{u_q}$ ($R_1, ..., R_8$, see eq. 2.42). The last part considers the effect of the static pressure gradients ($P_1, ..., P_8$, see eq. 2.43).

2.4.2 Mixing PMF

The mixing PMF $\underline{\varphi}$ describes the histogram of the equivalence ratio during the experiments. It is obtained by dividing the whole variation range of the equivalence ratio ($0 < \phi < 1$) into multiple intervals with a constant bin width of $b_{bin} = 0.005$, which was calculated with eq. 2.51 as proposed by Feedman and Diaconis [64].

$$b_{bin} = \frac{\phi_{max} - \phi_{min}}{\sqrt[3]{n_s}} = \frac{\phi_{max} - \phi_{min}}{\sqrt[3]{N_\phi \cdot N_t}} = 0.0045 \approx 0.005 \tag{2.51}$$

The number of samples of the equivalence ratio n_s was obtained from the number of mixture snapshots per experiment ($N_t = 10918$, see section 3.2.2) and the number of pixels covering the area of interest at the injector outlet ($N_\phi \approx 1000$). The relative frequency of occurrence for each interval, which is characterized by its central value x, is calculated by counting the number F of values of ϕ falling between $x - \frac{b_{bin}}{2} < \phi - \overline{\phi} \leq x + \frac{b_{bin}}{2}$ and dividing this by the sum of F for all intervals according to eq. 2.52.

$$\varphi_{(x)} = \frac{F(x - \frac{b_{bin}}{2} < \phi - \overline{\phi} \leq x + \frac{b_{bin}}{2})}{\sum F(x - \frac{b_{bin}}{2} < \phi - \overline{\phi} \leq x + \frac{b_{bin}}{2})} \tag{2.52}$$

With the chosen bin width, a mixing PMF with $N_x = 81$ relative frequency values covering the most relevant variation range for the experiments ($-0.2 < \phi - \overline{\phi} < 0.2$, see section 5.2) is obtained:

$$\underline{\varphi} = \begin{bmatrix} \varphi_{(-0.2)} \\ \varphi_{(-0.195)} \\ \vdots \\ \varphi_{(0.195)} \\ \varphi_{(0.2)} \end{bmatrix} = \begin{bmatrix} \varphi_1 \\ \vdots \\ \varphi_{81} \end{bmatrix}. \tag{2.53}$$

The width of the mixing PMF is quantified with the spatio-temporal standard deviation σ_{st}, which is calculated with the PMF data as follows:

$$\sigma_{st} = \sqrt{\frac{\sum_{m=1}^{N_x} \varphi_m \left(\phi_m - \overline{\phi}\right)^2}{\sum_{m=1}^{N_x} \varphi_m}}. \tag{2.54}$$

The mixing PMF for the whole combustion chamber $\underline{\varphi_{CC}}$ for a determined operating point is calculated from the contribution of all injector elements with the following equation:

$$\underline{\varphi_{CC}} = \frac{\sum_{k=1}^{N_i} \varphi_{k,m}}{\sum_{m=1}^{N_x} \sum_{k=1}^{N_i} \varphi_{k,m}}. \tag{2.55}$$

N_i and N_x correspond to the total number of injectors in the mixing section and the dimension of the mixing PMF datasets, respectively.

2.4.3 Model Application

The O-POD model application consists of two fundamental steps, which are explained in the following: the model generation consisting of the calculation of the eigenmodes describing the fundamental characteristics of the system from the input datasets, and the use of these eigenmodes to predict the mixing PMF for different reference datasets.

2.4.3.1 Calculation of the Eigenmodes

For this step, multiple input datasets for different inflow situations are considered. Here the mixing PMF for each dataset is merged with the corresponding observable vector to obtain the augmented dataset with a length $N = 113$ ($N_x = 81$ from $\underline{\varphi}$ and $N_y = 32$ from $\underline{\varphi^{\star}}$):

$$\underline{\Phi} = \left[\underline{\varphi}; \underline{\varphi^{\star}}\right] = \begin{bmatrix} \varphi_1 \\ \vdots \\ \varphi_{81} \\ \varphi_1^{\star} \\ \vdots \\ \varphi_{32}^{\star} \end{bmatrix} \cdot \tag{2.56}$$

All n input augmented datasets for the considered inflow conditions are then joined to form the auto-correlation tensor $\underline{\underline{R}}$ of size NxN:

$$\underline{\underline{R}} = \frac{1}{n} \sum_{i=1}^{n} \underline{\Phi_i} \left[\underline{\Phi_i}\right]^T, \tag{2.57}$$

$$\underline{\underline{R}} = \frac{1}{n} \sum_{i=1}^{n} \begin{bmatrix} \varphi_{1,i} \\ \vdots \\ \varphi_{81,i} \\ \varphi_{1,i}^{\star} \\ \vdots \\ \varphi_{32,i}^{\star} \end{bmatrix} \cdot \left[\varphi_{1,i} \dots \varphi_{81,i}\, \varphi_{1,i}^{\star} \dots \varphi_{32,i}^{\star}\right] \cdot \tag{2.58}$$

The eigenmodes are calculated by solving the following eigenvalue problem for $\underline{\underline{R}}$:

$$\underline{\underline{R}} \cdot \underline{\theta_i^{\Phi}} = \lambda_i \cdot \underline{\theta_i^{\Phi}} \cdot \tag{2.59}$$

The number of obtained eigenmodes is given by the dimension of the input datasets N, but only a few contain the most relevant information about the studied phenomena. The number of relevant modes N_r is defined so that the so-called relative information content (RIC) is bigger than 99% ($N_r << N$):

$$RIC = \frac{\sum_{i=1}^{N_r} \lambda_i}{\sum_{i=1}^{N} \lambda_i} \cdot 100\% > 99\% \cdot \tag{2.60}$$

Finally, the eigenmodes are decomposed into the parts corresponding to the mixing and the observable datasets $\underline{\theta^{\Phi}} = \left[\underline{\theta};\underline{\theta^{\star}}\right]$. Here the individual components of $\underline{\theta}$ and $\underline{\theta^{\star}}$ are associated with their original values of the mixing PMF $\underline{\varphi}$ and the input observable $\underline{\varphi^{\star}}$ vector as follows:

$$\underline{\theta^{\Phi}} = \left[\underline{\theta};\underline{\theta^{\star}}\right] = \begin{bmatrix} \theta_1 \\ \vdots \\ \theta_{81} \\ \theta^{\star}_1 \\ \vdots \\ \theta^{\star}_{32} \end{bmatrix}, \tag{2.61}$$

$$\underline{\theta} = \begin{bmatrix} \theta_1 \\ \vdots \\ \theta_{81} \end{bmatrix} = \begin{bmatrix} \theta_1 \rightarrow \varphi_{(-0.2)} \\ \theta_2 \rightarrow \varphi_{(-0.195)} \\ \vdots \\ \theta_{80} \rightarrow \varphi_{(0.195)} \\ \theta_{81} \rightarrow \varphi_{(0.2)} \end{bmatrix}, \tag{2.62}$$

$$\underline{\theta^{\star}} = \begin{bmatrix} \theta^{\star}_1 \\ \vdots \\ \theta^{\star}_{32} \end{bmatrix} = \begin{bmatrix} \theta^{\star}_1 \rightarrow j_1/j_N \\ \vdots \\ \theta^{\star}_8 \rightarrow j_8/j_N \\ \theta^{\star}_9 \rightarrow Q_1 \\ \vdots \\ \theta^{\star}_{16} \rightarrow Q_8 \\ \theta^{\star}_{17} \rightarrow R_1 \\ \vdots \\ \theta^{\star}_{24} \rightarrow R_8 \\ \theta^{\star}_{25} \rightarrow P_1 \\ \vdots \\ \theta^{\star}_{32} \rightarrow P_8 \end{bmatrix}. \tag{2.63}$$

2.4.3.2 Prediction of the Mixing PMF

In order to predict the mixing PMF for a given inflow situation, the corresponding observable vector $\underline{\varphi^\star}$ is approximated as the weighted sum of the corresponding part of the most relevant N_r eigenmodes ($\underline{\theta^\star}$) using the weighting coefficients a_k:

$$\underline{\varphi^\star} \approx \sum_{k=1}^{N_r} a_k \underline{\theta_k^\star} \approx \sum_{k=1}^{N_r} a_k \begin{bmatrix} \theta_1^\star \\ \vdots \\ \theta_{32}^\star \end{bmatrix} . \tag{2.64}$$

The weighting coefficients a_k are determined by solving the following optimization problem:

$$\min_{a_k} \left\| \sum_{k=1}^{N_r} a_k \begin{bmatrix} \theta_1^\star \\ \vdots \\ \theta_{32}^\star \end{bmatrix} - \begin{bmatrix} \varphi_1^\star \\ \vdots \\ \varphi_{32}^\star \end{bmatrix} \right\| = \min_{a_k} \sum_{j=1}^{32} \left(\sum_{k=1}^{N_r} a_k \theta_{k,j}^\star - \varphi_j^\star \right)^2 . \tag{2.65}$$

Having determined the a_k values, the mixing PMF $\underline{\varphi}$ is finally calculated as the series expansion of the corresponding part of the most relevant N_r eigenmodes ($\underline{\theta}$):

$$\underline{\varphi} = \sum_{k=1}^{N_r} a_k \underline{\theta_k} = \sum_{k=1}^{N_r} a_k \begin{bmatrix} \theta_1 \\ \vdots \\ \theta_{81} \end{bmatrix} . \tag{2.66}$$

2.5 Nitrogen Oxide Formation

There are multiple known routes for NO_x formation in gas turbines using clean fuels without nitrogen compounds, which can be divided as follows: N_2O-, NNH-, Zeldovich- and prompt NO mechanism [65]. The relevance of each route as a function of the equivalence ratio and the combustion temperature is represented in fig. 2.6.

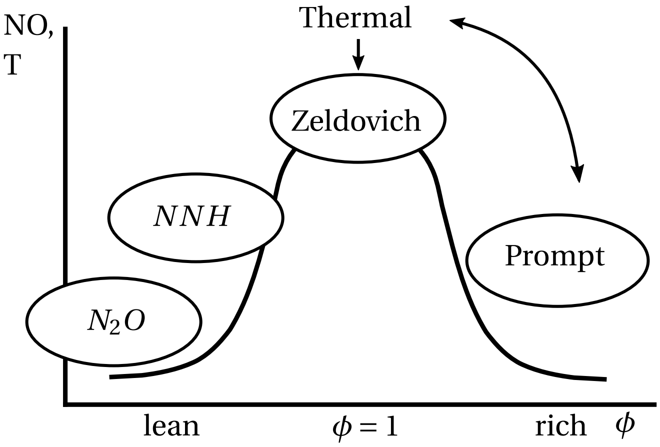

Figure 2.6: NO_x formation routes [66].

The N_2O mechanism is related to the reaction of N_2 and O molecules with an additional third body at lean conditions leading to the formation of N_2O, which further reacts with an O radical to form NO [67]. The NNH mechanism becomes relevant at increasing temperatures in the flame front due to the present high NNH and O radical concentrations, which can also react to form NO [68]. The Zeldovich mechanism, also denoted as thermal NO, is referred to as the oxidation of N_2 according to the following reaction scheme:

$$\mathrm{N_2 + O \rightleftharpoons NO + N}, \tag{2.67}$$

$$\mathrm{N + O_2 \rightleftharpoons NO + O}, \tag{2.68}$$

$$\mathrm{N + OH \rightleftharpoons NO + H\cdot} \tag{2.69}$$

This reaction occurs at sufficiently high temperatures ($T > 1800K$) due to the high activation energy necessary to separate the triple bond of the N_2 molecules [69]. The NO formation through the Fenimore mechanism [70], also known as prompt NO, results from the reaction of CH radicals with N_2 molecules to the formation of HCN and N. HCN reacts through multiple chain reactions to a further N molecule. NO is finally formed from both N radicals with reactions 2.68 and 2.69 [71, 72]. NO_2 results mainly from areas with low combustion temperatures due to the interaction of NO molecules with HO_2 radicals. The resulting NO and NO_2 together are referred to as NO_x.

In order to assess the increase of NO_x formation caused by the remaining unmixedness in the multi-injector burner, the method proposed by Sangl et al. [73] is used. Here the NO_x formation as a function of the equivalence ratio ϕ at an assumed residence time t_{res} is calculated from numerical simulations of a *freely propagating adiabatic one-dimensional flame* conducted in Cantera [74] with the optimized *GRI-Mech 3.0* mechanism for natural gas [75] considering a fluid domain with L = 200 mm.

The nominal inlet temperature and pressure for the engine operation were given as boundary conditions for the simulations ($T_{in,N} = 778\ K$, $p_N = 22.8\ bar$). The gas composition was varied in dependency on the input equivalence ratio. The start of the reaction zone in the fluid domain p_0 is identified through the steep increase of fluid velocity due to the heat release. The end of the reaction zone p_{end} is determined by summing up the space between two neighbor points divided by the mean velocity until reaching the input residence time t_{res} as follows:

$$t_{res} = \int_{x_0}^{x_{end}} \frac{dx}{u(x)} \approx \sum_{k=p_0}^{p_{end}} \frac{2\,(x_{k+1} - x_k)}{u_{k+1} + u_k}. \tag{2.70}$$

The NO and NO_2 mole fractions are extracted at p_{end} to obtain the total NO_x mole fraction. The associated NO_x formation to the mixing PMFs is finally calculated with eq. 2.71:

$$X_{NO_x,\varphi} = \frac{\sum_{m=1}^{N_x} \varphi_m \cdot X_{NO_x @ \phi = \phi_m}}{\sum_{m=1}^{N_x} \varphi_m}. \tag{2.71}$$

The mean equivalence ratio $\overline{\phi}$ for all mixing PMFs is calculated from the volume flows of fuel and air during the experiments as follows:

$$\overline{\phi} = \frac{\frac{\dot{V}_f}{\dot{V}_a}}{\left(\frac{m_f}{m_a}\right)_{st}}. \tag{2.72}$$

The mass and volume flow ratios are equal as the fuel and the air are simulated with water during the experiments. The percentage deviation of the NO_x formation (ΔX_{NO_x}) compared with the perfectly premixed case is calculated with the resulting $X_{NO_x,\varphi}$ for each mixing PMF and the NO_x mole fraction at the same $\overline{\phi}$ ($X_{NO_x@\phi=\overline{\phi}}$) with the following equation:

$$\Delta X_{NO_x} = \frac{X_{NO_x,\varphi} - X_{NO_x@\phi=\overline{\phi}}}{X_{NO_x@\phi=\overline{\phi}}}. \tag{2.73}$$

The simulation results for the adiabatic flame temperature, the NO_x mole fraction, and the increase of the NO_x mole fraction with the equivalence ratio are shown in fig. 2.7 with the plots at the top, in the middle, and at the bottom, respectively. The adiabatic flame temperature increases exponentially towards stoichiometric conditions due to the higher heat release, which is seen as a linear proportionality in the graph due to the logarithmic scale. The maximum value is reached at slightly fuel-rich conditions ($\phi = 1.04$).

The NO_x mole fraction also exhibits a similar monotonic exponential increase until $\frac{dX_{NO_x}}{d\phi}$ becomes maximum and the inflection point of the X_{NO_x} curve is reached (see dashed lines in fig. 2.7). At low mean equivalence ratios ($\overline{\phi}$), ΔX_{NO_x} scales with the residence time due to the higher $\frac{dX_{NO_x}}{d\phi}$, as the whole ϕ variation range covered by the mixing PMF falls below this inflection point. At higher mean equivalence ratios ($\overline{\phi}$), the inflection point falls into the ϕ variation range covered by the mixing PMF and the contribution of the range $\phi > \overline{\phi}$ to the NO_x formation decreases. Consequently, ΔX_{NO_x} drops with the residence time, as shown in section 6.1. Note that the data points with $\frac{dX_{NO_x}}{d\phi} < 0$ are not shown in the lower plot of fig. 2.7 due to the logarithmic scale.

The lean blowout limit of the studied multi-injector burner is reached at $\overline{\phi} \approx 0.4$. In order to calculate the NO_x formation for this extreme value with eq. 2.71, the behavior down to $\phi = 0.2$ must be considered with the one-dimensional flame simulations, as the mixing PMFs cover the variation range between $-0.2 < \phi - \overline{\phi} < 0.2$ (see fig. 5.2). The simulation results for the range $0.2 < \phi < 0.4$, in which no stable deflagrating flames exist in reality, are shown in appendix A.2.

As a final remark, it can be stated that the calculated NO_x mole fraction based on the PMF data with eq. 2.71 is roughly proportional to the spatio-temporal standard deviation (see eq. 2.54) for the same mean equivalence ratio $\overline{\phi}$. The reason therefore is that σ_{st} and $X_{NO_x,\varphi}$ are calculated as the weighted average of $(\phi - \overline{\phi})^2$ and X_{NO_x}, respectively. This fact is essential to understand the results regarding the NO_x formation shown in chapter 6.

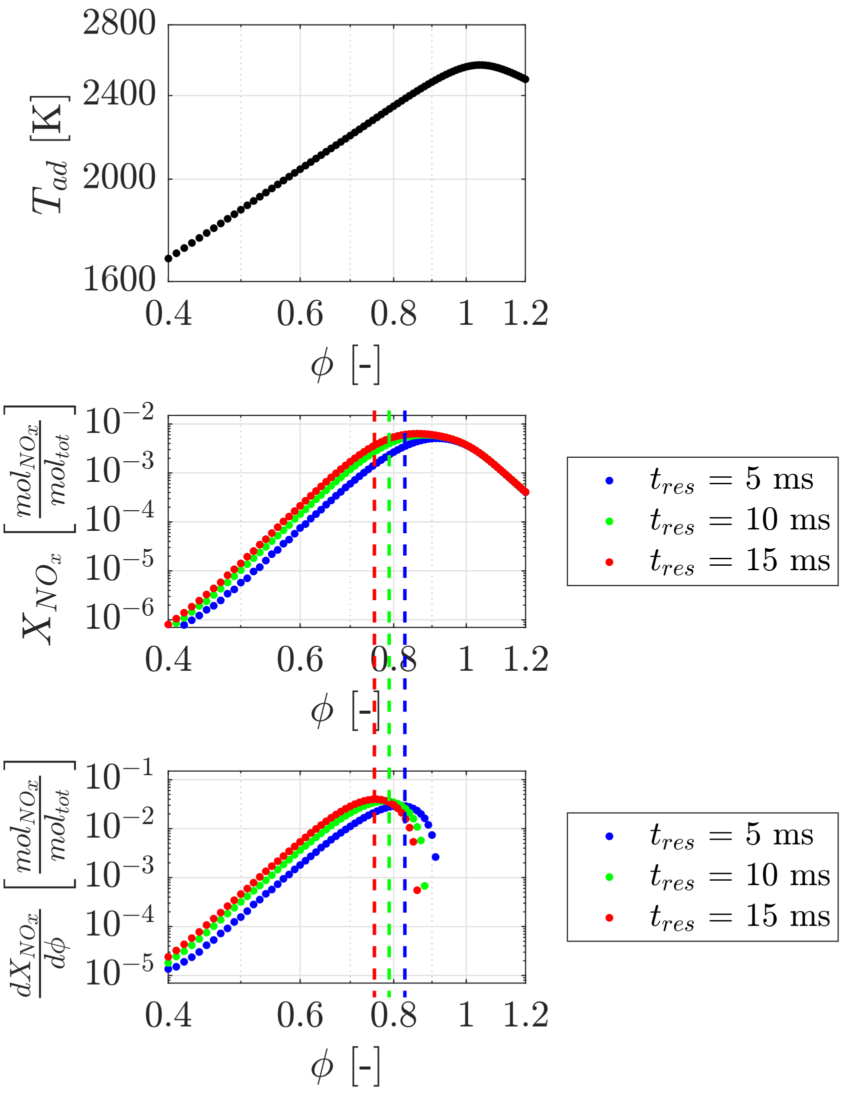

Figure 2.7: T_{ad}, X_{NO_x} and $\frac{dX_{NO_x}}{d\phi}$ as functions of the equivalence ratio and the residence time for a freely-propagating one-dimensional flame in logarithmic scale.

3 Experiments

The experiments to determine the sensitivity of the mixture quality to the inflow distortion are presented in this chapter. First, the water channel and the measurement techniques are described. The experimental setups are explained afterwards, including the single injector under ideal inflow conditions and a generic multi-injector burner representative of an engine configuration. Finally, the experimental matrix for this study is provided.

3.1 Water Channel Test Rig

The experiments are conducted in the water channel test rig shown in fig. 3.1. It consists of an inlet, an outlet section, a measurement section, and a water supply system. It was developed by Sangl et al. [13] and adapted for the investigations in this work. The measurement area is optically accessible from four sides: front, left, right, and top. The windows are made from perspex on the sides and the top and from glass in the front to allow high-power density laser light beams.

The air and the fuel flow are simulated with clear and dyed water. The clear water flow is provided with pump 1 from tanks 1 and 2. The dyed water is supplied from tank 3 with pump 2. The test rig is designed for both flow and mixture investigations. During the flow investigations, the clear water is pumped back into the tanks after flowing through the measuring section. During the mixture investigations, the mixed water during the mixture investigations has to be dumped in order to avoid a continuous increase in the background signal of the measured dye concentration.

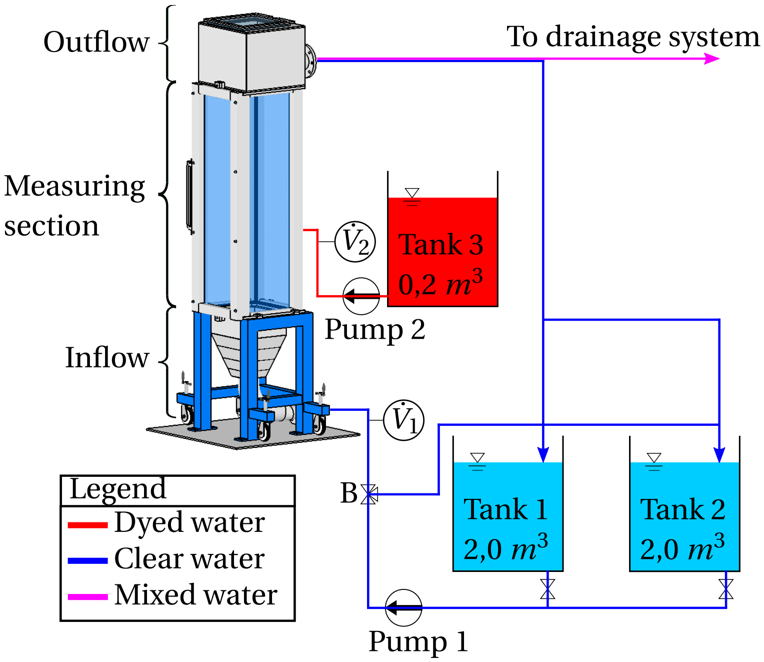

Figure 3.1: Water channel test bench.

3.2 Measurement Techniques

In this section, the measurement techniques used for this investigation are outlined. The necessary components to obtain the desired inflow conditions in the multi-injector burner were selected based on PIV experiments. The mixture quality at the injector outlet was investigated using LIF and high-speed imaging. The volume flow through the injectors was determined with hot-film flow sensors, which work according to the CTA measurement principle.

3.2.1 Particle Image Velocimetry

The measurement principle of Particle Image Velocimetry (PIV) is illustrated in fig. 3.2. The clear water is mixed with seeding particles and illuminated with a laser light sheet in the area of interest. The incoming light is reflected on the particles in all directions without energy exchange according to the theory of Mie scattering [77,78]. Consequently, the reflected light has the same wavelength as the laser light beam. The reflected light perpendicular to the measurement area is then captured with a high-speed camera.

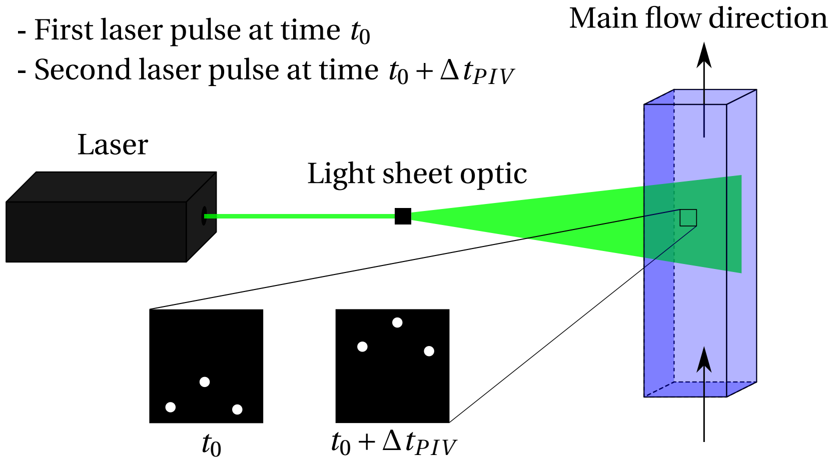

Figure 3.2: PIV measurement principle [78].

The images are pre-processed before the measurement data evaluation with background subtraction and the exclusion of the non-relevant areas belonging to the wall areas of the experimental model. The velocity fields are obtained based on the particle displacement from two consecutive snapshots, also called an image pair. The displacement vector $\underline{\Delta s}$ is divided by the time interval between the snapshots Δt_{PIV} to obtain the velocity vector $\underline{u}$ as follows [79]:

$$\underline{u} = \frac{\underline{\Delta s}}{\Delta t_{PIV}}. \tag{3.1}$$

For this, the images are divided into smaller interrogation areas (IAs), and their displacement is obtained through cross-correlation. The calculated flow field at this step is finally post-processed with the identification and elimination of vectors that do not follow the main flow path or do not have a physically meaningful value, as well as the re-calculation of the eliminated vectors through interpolation based on the obtained values for the surrounding vectors. This measurement data evaluation process is done with the Matlab-Toolbox PIVLab [80].

The experiments are conducted with polyamide seeding particles ($d_p = 57\mu m$, $\rho_p = 1016\frac{kg}{m^3}$, $c_p = 20-40\frac{g}{m^3}$). A similar density to the water flow is necessary to ensure that the particles follow the main flow without slipping. Furthermore, the particle diameter d_p was selected to capture a single particle with approximately 2 pixels ($d_{PI} = 2px$). It is important to increase the exactitude of the calculated displacement of the IAs with cross-correlation [81]. The particles are illuminated with a double pulse laser (New Wave GEMINI PIV, $\lambda_L = 532nm$, $f_{PIV} = 15Hz$, $\Delta t_{PIV} = 1.5ms$). The sending of the pulses and the image capture are synchronized with the following procedure:

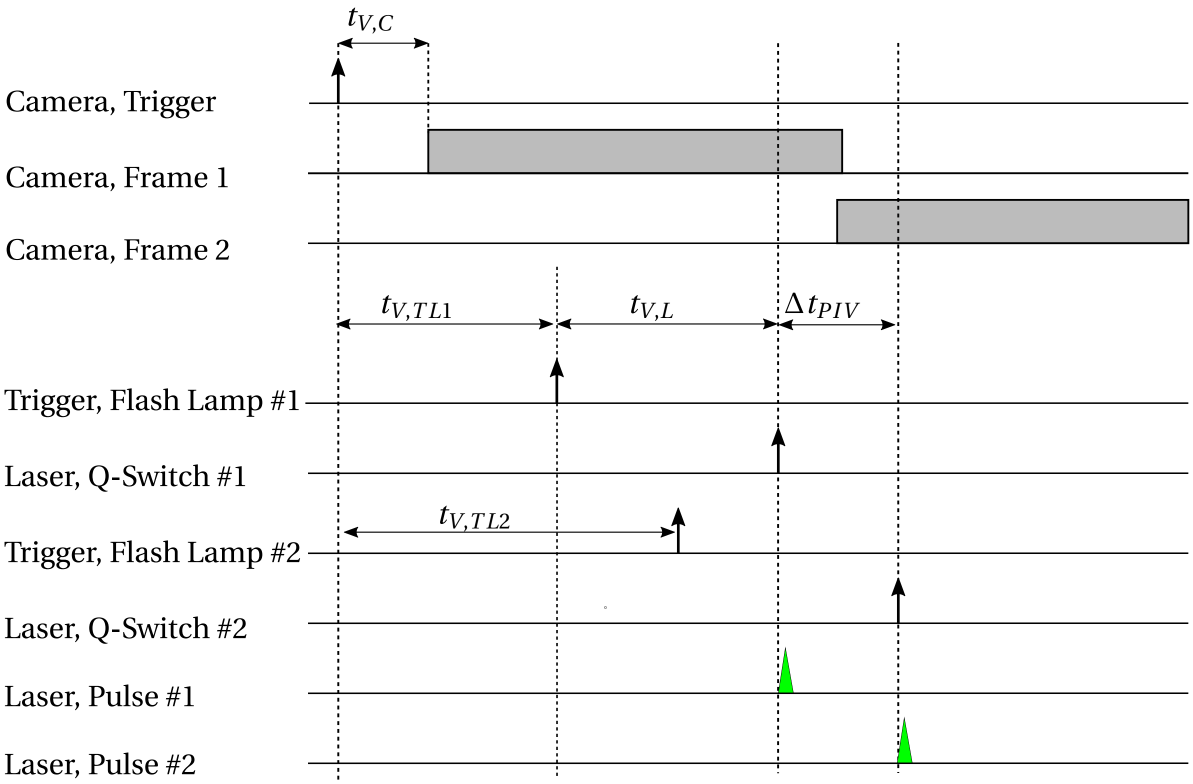

Figure 3.3: Synchronization of laser and camera.

The trigger signals are sent to the laser cavities and the camera with a measuring card of type *NI 9472* according to the scheme shown in fig. 3.3. The recording of an image pair begins after sending a trigger signal to the camera system, which is configured to take two images per trigger input, one for each laser pulse. For this, the first and the second laser pulse are sent exactly $\frac{\Delta t_{PIV}}{2}$ seconds before finishing the first frame and beginning the second frame, respectively. For this purpose, the time delay between the camera and the laser must be considered. The manufacturer specified a time delay between the trigger input and the beginning of the first frame in the camera of $t_{V,C} = 2.3\mu s$ [82]. The time delay between the trigger input of the laser (Trigger, Flash lamp) and the output of the light pulse (Laser, Q-Switch) was quantified with an oscilloscope to be $t_{V,L} = 200\mu s$. Considering both time delay values, the time between sending the trigger signal to the camera and both laser cavities is calculated as follows:

$$t_{V,TL1} = t_{V,C} + \frac{1}{f_c} - (0.5 \cdot \Delta t_{PIV} + t_{V,L}), \tag{3.2}$$

$$t_{V,TL2} = t_{V,TL1} + \Delta t_{PIV}. \tag{3.3}$$

3.2.2 Laser-Induced Fluorescence

Laser-induced Fluorescence (LIF) is used to investigate the mixing quality at the outlet section of the injector elements. The fuel is simulated with a Uranin dyed water solution (Basacid Yellow 226, $c_{d,max} = 2\frac{mg}{l}$). A horizontal laser light sheet (Coherent Genesis CX 488-4000 SLM, $\lambda_L = 488nm$, 1.5 W) continuously illuminates the outflow area downstream of the injectors, as shown later in fig. 3.12 and 3.13(e). The incoming laser light continuously stimulates the dye molecules to a higher rotational and vibration energy level. The absorbed photon energy is then emitted after a few milliseconds through the following mechanisms, illustrated in fig. 3.4 [83, 84].

- Energy release through collision with other molecules (Quenching).
- Energy exchange in each rotational and vibrational level.
- Emission of photon energy (Fluorescence).

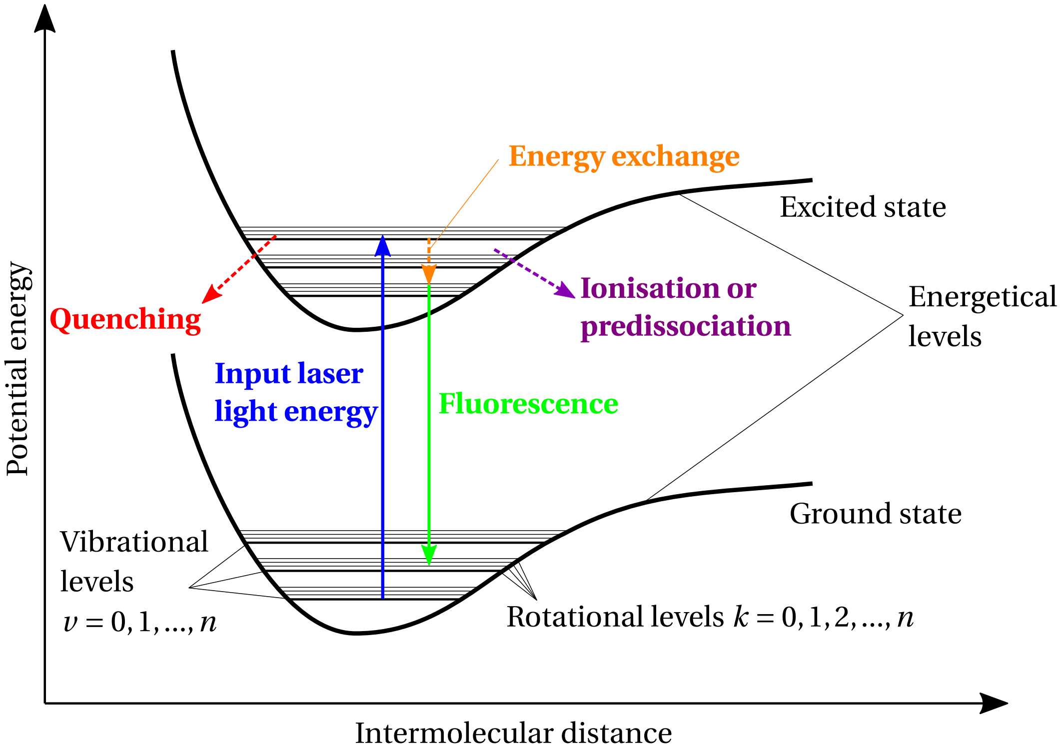

Figure 3.4: LIF measurement principle [83].

The light energy supply might also remove individual electrons (Ionisation) or even separate chemical compounds (Predissociation). With the dye molecules used for this investigation and laser wavelength, fluorescence becomes the decisive mechanism for this process [15, 85]. It takes place frequency-shifted due to the occurring energy exchange. The emitted light has a wavelength between $530nm < \lambda_F < 590nm$ and is proportional to the incoming light intensity and the dye concentration, with an intensity maximum at $\lambda_F = 537nm$ [14, 15, 85].

The fluorescence light is recorded with a high-speed camera (Photron Fastcam SA5). An optical bandpass filter is used in front of the CCD sensor of the camera to filter out the reflected laser light from the measured images, as it allows the light transmission at $\lambda_F > 539nm$. The images are recorded with a frequency of $f_c = 250Hz$, and the measurement time is 43.67 s, obtaining 10918 mixture snapshots per experiment. The area of interest is the outlet section of a single injector element. For this reason, the laser light sheet must be centered with the middle axis to achieve a nearly uniform light intensity distribution. It is necessary to capture the small concentration gradients in the outlet area of the injector accurately.

The mixture snapshots are obtained by post-processing the raw image data with the following steps: Background subtraction (eq. 3.4); correction of the non-linear behavior of the camera (eq. 3.5); and correction of the laser light intensity profile in the outlet area (eq. 3.6) [84, 86]:

$$\Theta_{C,BR}(i,j) = \Theta_R(i,j) - \Theta_{BR}(i,j), \tag{3.4}$$

$$\Theta_{C,CAM}(i,j) = \Theta_{C,BR}(i,j)\frac{I}{I_{max}}(i,j), \tag{3.5}$$

$$\Theta_{C,LS}(i,j) = \Theta_{C,CAM}(i,j)\frac{\overline{\Theta_{LS}}}{\Theta_{LS}(i,j)}. \tag{3.6}$$

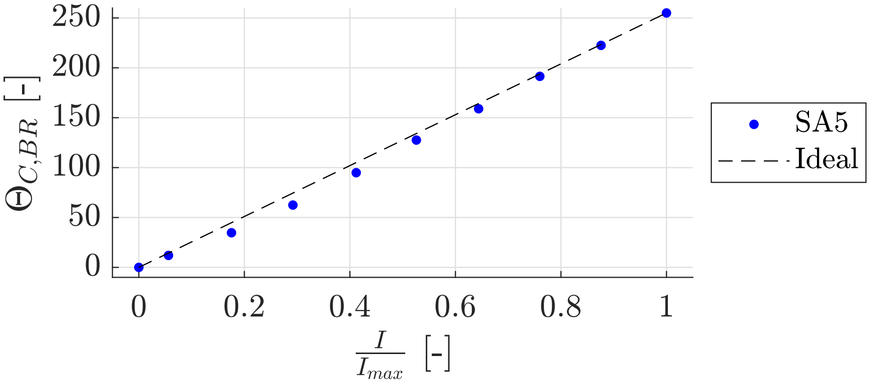

Figure 3.5: Imaging behavior of the Photron Fastcam SA5 at $f_c = 250Hz$.

The background image (Θ_{BR}) is taken with the channel filled with clear water. The imaging behavior of the camera is shown in fig 3.5. Here the output of the camera Θ_R is measured as a function of the relative light intensity $\frac{I}{I_{max}}$ with a LED light placed in the measurement plane for the experiments. The light intensity is assumed to be proportional to the input current [87]. The intensity distribution of the laser light sheet (Θ_{LS}) is captured with the channel filled with dyed water solution at $c_d = 0.02\frac{mg}{l}$ ($\frac{c_d}{c_{d,max}} = 0.01$). With this concentration range, the light absorption along the entire measurement section of the water channel can be considered negligible [15], and a high enough signal-to-noise ratio can be obtained.

The concentration of dyed water for each pixel is calculated as follows:

$$c_d = \Theta_{C,LS} \frac{c_{d,Ref}}{\Theta_{Ref}}, \tag{3.7}$$

$$c = \frac{c_d}{c_{d,max}}. \tag{3.8}$$

$c_{d,Ref}$ and Θ_{Ref} are calculated from the mean values of the camera output and the actual fuel concentration obtained from the air and fuel volume flow values through the injector. The equivalence ratio distribution ϕ for the reacting flow is finally obtained from the dyed water concentration with the following procedure (see section 2.2):

$$\left(\frac{m_f}{m_a}\right)_{orig} \approx \left(\frac{m_f}{m_a}\right)_{exp} = \frac{c}{1-c}, \tag{3.9}$$

$$\phi = \frac{\left(\frac{m_f}{m_a}\right)_{orig}}{\left(\frac{m_f}{m_a}\right)_{st}}. \tag{3.10}$$

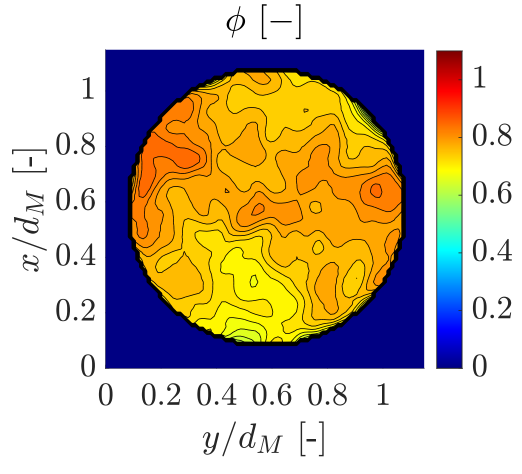

Figure 3.6: Individual snapshot of the mixing process.

The obtained mixture snapshots, from which the mixing PMF is calculated according to the procedure explained in section 2.4.2, are illustrated in fig. 3.6 as example.

3.2.3 Injector Flow Rate Sensor

In order to measure the flow rate through the injector elements without disturbing the mixing process, a hot film sensor based on the CTA principle (Constant Temperature Anemometry) [88, 89] was developed. Four 20Ω compensation resistance pads normally used in strain measurement are symmetrically glued to the inner wall of the perspex sensor body, as shown in fig. 3.7, obtaining a sensor resistance of $R_S = 5\Omega$ with a temperature coefficient of $0.0269\frac{\Omega}{K}$. Mounting this sensor behind a 90° bend in a test loop revealed that the parallel connection of the pads makes the sensor insensitive to flow asymmetries in the velocity profile at the sensor location.

During the experiments, the flow sensors are connected to a Wheatstone bridge, which consists of three power resistors $R_{P,1}$, $R_{P,2}$ and $R_{P,Ref}$ with the resistance values $R_{P,1} = R_{P,2} = 25\Omega$ and $R_{P,Ref} = 5.6\Omega$. It allows keeping a constant sensor resistance close to the reference resistance by keeping the bridge offset ($\Delta U_{Offset} = U_S - U_{Ref}$) constant at a small temperature-dependent value (see fig. 3.8). By doing so, a volume flow depending voltage (U_B) is applied to the bridge to keep a constant resistor pad temperature. This behavior is due to the proportionality of the heat transfer coefficient with the mean flow velocity. The Wheatstone bridge is regulated with a PI controller (PI-C) shown in the lower part of figure 3.7.

The bridge offset is used as the input to the PI-C, which is implemented into a LabVIEW control program. Here, a control voltage U_C is generated as the manipulated variable, used as input to the control circuit [90]. This signal is then inverted and amplified to a (0 - 30)V signal ($U_{T,B}$) with an operational amplifier. This voltage is fed into the basis of a PNP-transistor, which gives out the bridge voltage U_B from the emitter of the transistor with the necessary electrical power output for the bridge. It has the same value as the basis voltage minus the transistor offset ΔU_T, an individual parameter for each transistor type [90,91]. In addition, the operational amplifier and the collector of the transistor must be connected to a power supply with $(U_{T,C}, V) > U_{T,B}$ to avoid these components reaching the saturation state.

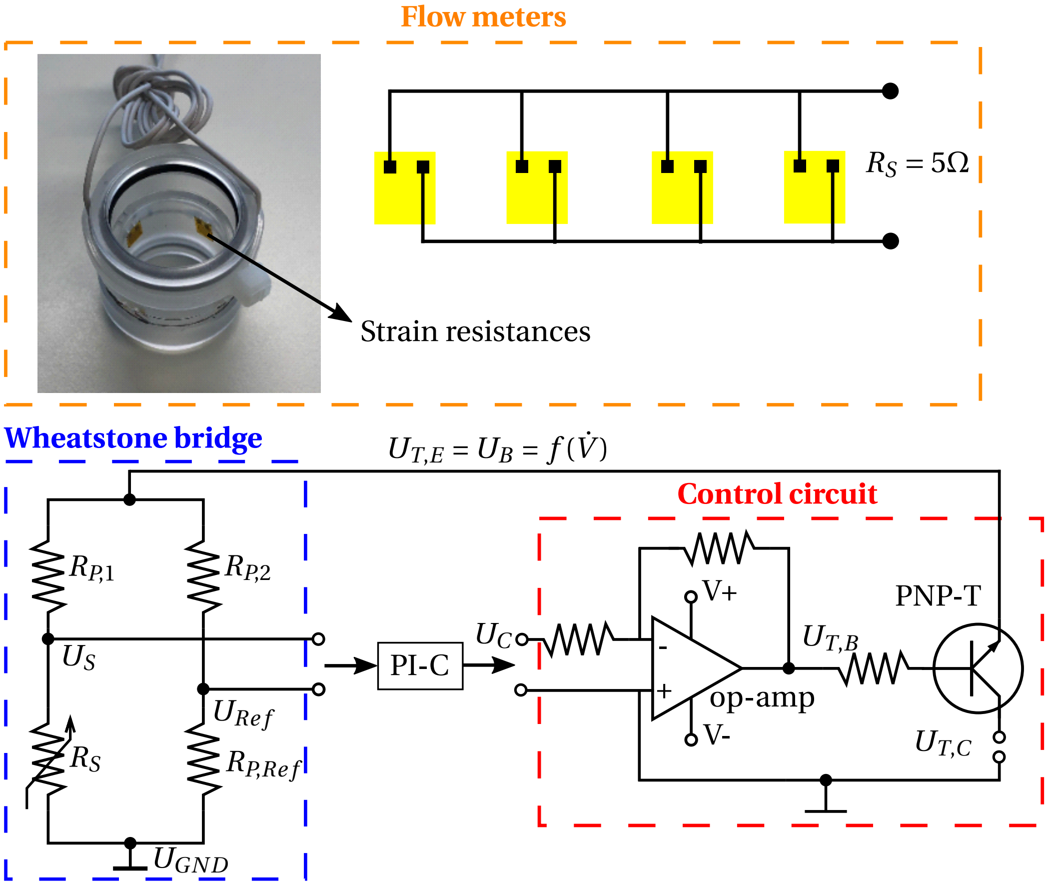

Figure 3.7: Volume flow meters.

The measurement system allows the implementation of a temperature compensation strategy to make the behavior of the bridge voltage independent of the water temperature. For this, the target value of the bridge offset is set as a function of the water temperature ($\Delta U_{Offset} = f(T_W)$, see fig. 3.8), obtaining the behavior of the bridge voltage shown in fig. 3.9. This measurement strategy is mainly useful to avoid changes in the measurement signal through variations of the water temperature due to the heat release of the pumps of the water supply system in the water channel.

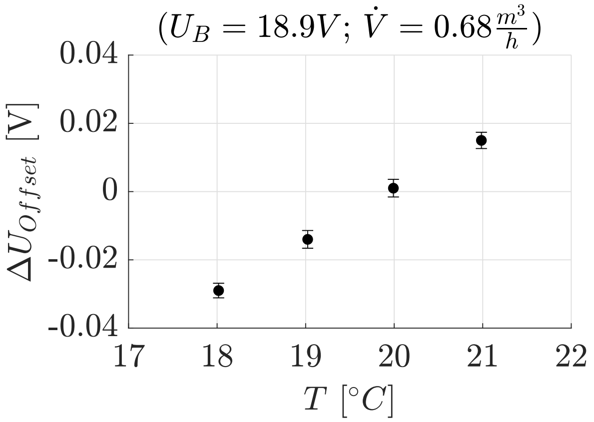

Figure 3.8: Bridge offset as a function of the temperature.

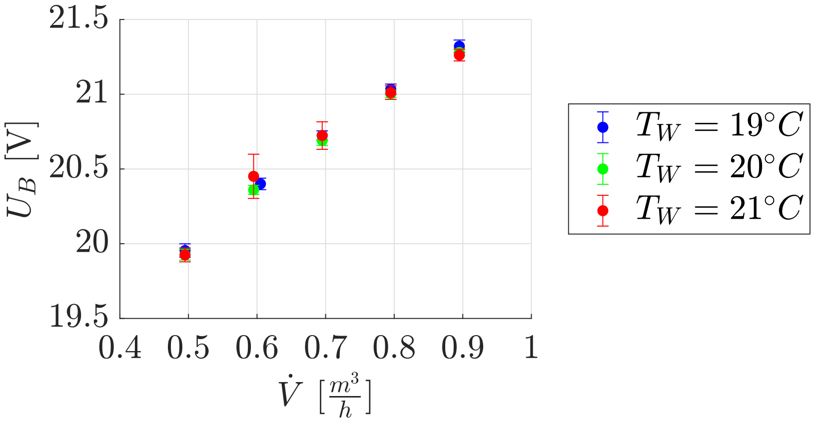

Figure 3.9: Bridge voltage as a function of the volume flow.

3.2.3.1 Calibration Test Rig

The flow sensors were calibrated with the test bench shown in fig. 3.10. The desired volume flow during the calibration is set with a centrifugal pump and a frequency inverter, which operates with a rotation velocity proportional to an input analog signal between (0-10)V. The rectifier plates, which are perforated plates with a high pressure-loss coefficient, are used to minimize the remaining volume flow fluctuations from the pump at a constant rotational speed. The water temperature (T1) upstream of the sensor is measured with a PT1000 platinum resistor. The volume flow through the sensor ($\dot{V}_1$) is quantified with a pulse counter with an output of 80 pulse/l.

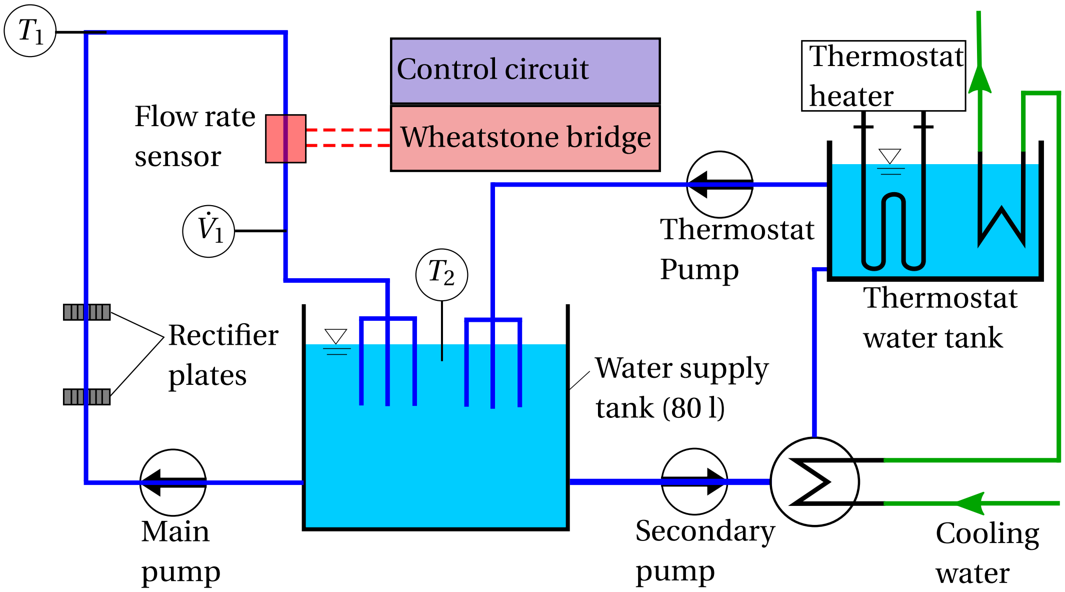

Figure 3.10: Calibration test bench.

The water temperature during the calibration is regulated with a thermostat and tap water. The secondary pump keeps the water level in the thermostat tank in the desired range during operation. With a volume in the water supply tank of 80 l, achieving temperature stability of $\pm 0.1K$ with a two-point controlling strategy was possible. The water outflow from the thermostat and the sensors are mixed in the main tanks with turbulent free jets for a uniform water temperature distribution.

3.2.3.2 Accuracy of the Sensors

In order to reach the desired accuracy of the experimental data, the thermal drift of the power resistors ($R_{P,1}$, $R_{P,2}$ and $R_{P,Ref}$) must be taken into account due to the high electrical power necessary for measurements in a turbulent water flow. The thermal drift can be reduced by using ventilators with sufficient cooling power. The contact resistances in the circuit must also be reduced by increasing the thickness of the connecting cables and the conductor tracks of the bridge circuit board. For the experiments, a cable with $L_K = 3.5m$ and $A_K = 1mm^2$ was used to connect the sensor pads with the Wheatstone bridge circuit ($R_K \approx 0.08\Omega$). With this cable length, no thermal drift during the operation of the sensors was observed.

The ground level of the bridge must be measured against an absolute ground provided by the earth. The bridge, sensor, and reference voltage (U_B, U_S, and U_{Ref}) must be measured against the bridge ground voltage (U_{GND}). The reason is that the voltage drop through the cables and the terminal clamps of the power supply can affect the voltage signals if measured against the absolute ground.

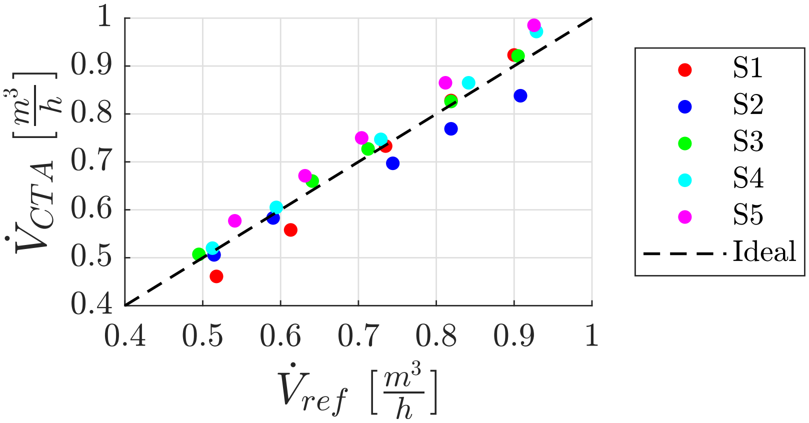

Figure 3.11: Accuracy of the sensors tested in situ.

The accuracy of the sensors was assessed in an in-situ test with five sensor probes. For this, the burner model was mounted in the measuring section of the water channel in the same position as for LIF experiments (see fig. 3.13(c)), and the outflow of the injector with the tested sensor was connected to a pipe and led out to the drainage system. The volume flow was then measured in the pipe outlet with a pulse counter similar to the calibration test bench. The output of the flow rate sensor ($\dot{V}_{CTA}$) was compared with the pulse counter ($\dot{V}_{Ref}$), leading to the results shown in fig. 3.11. In general, a good agreement between the measured volume flows was achieved. 19 of the 25 obtained data points have a discrepancy $\leq 5\%$ so that the accuracy of the measuring system is considered adequate for the experiments.

3.3 Measuring Objects

3.3.1 Single Injector Under Ideal Inflow

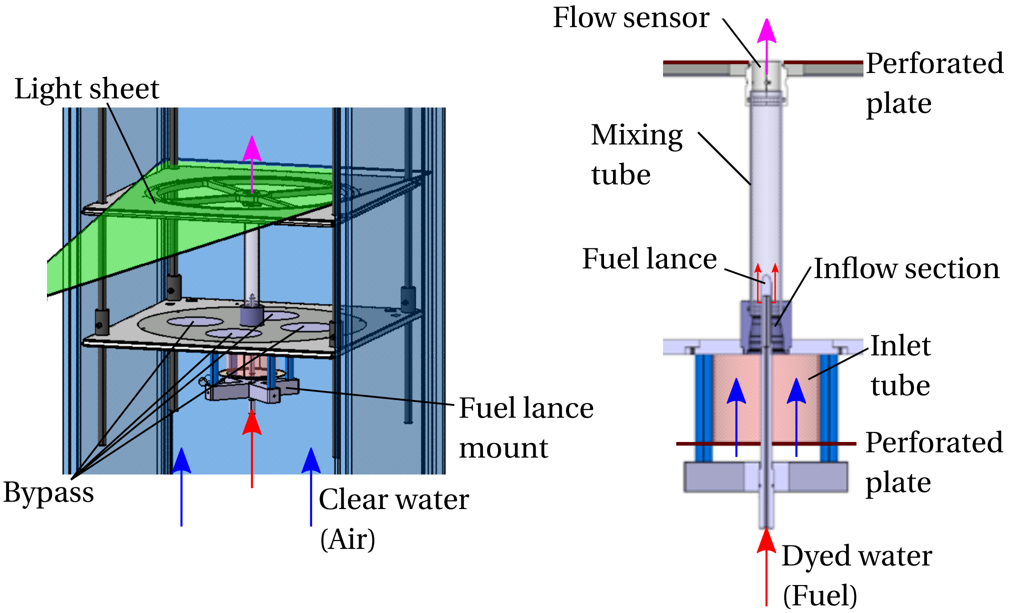

Figure 3.12: Single injector under perfectly symmetric inflow conditions.

Fig. 3.12 shows the experimental setup for investigating the mixing behavior of a single injector under ideal inflow conditions. It has an inlet tube with a bigger diameter than the injector element, preceded by a perforated plate to suppress velocity gradients from the water channel inflow. The fuel lance is placed in the middle axis of the injector with a corresponding mount. Downstream of the fuel injection, a straight mixing tube follows. In the outlet section, a hot-film flow sensor is mounted flush with the inner surface of the tube to determine the total flow rate through the injector. The mixing PMF is measured using LIF with a light sheet perpendicular to the main flow direction in the cross-sectional area directly downstream of the injector. In particular, the influence of the injector Reynolds number and the momentum flux density ratio j are considered.

3.3.2 Multi-Injector Burner

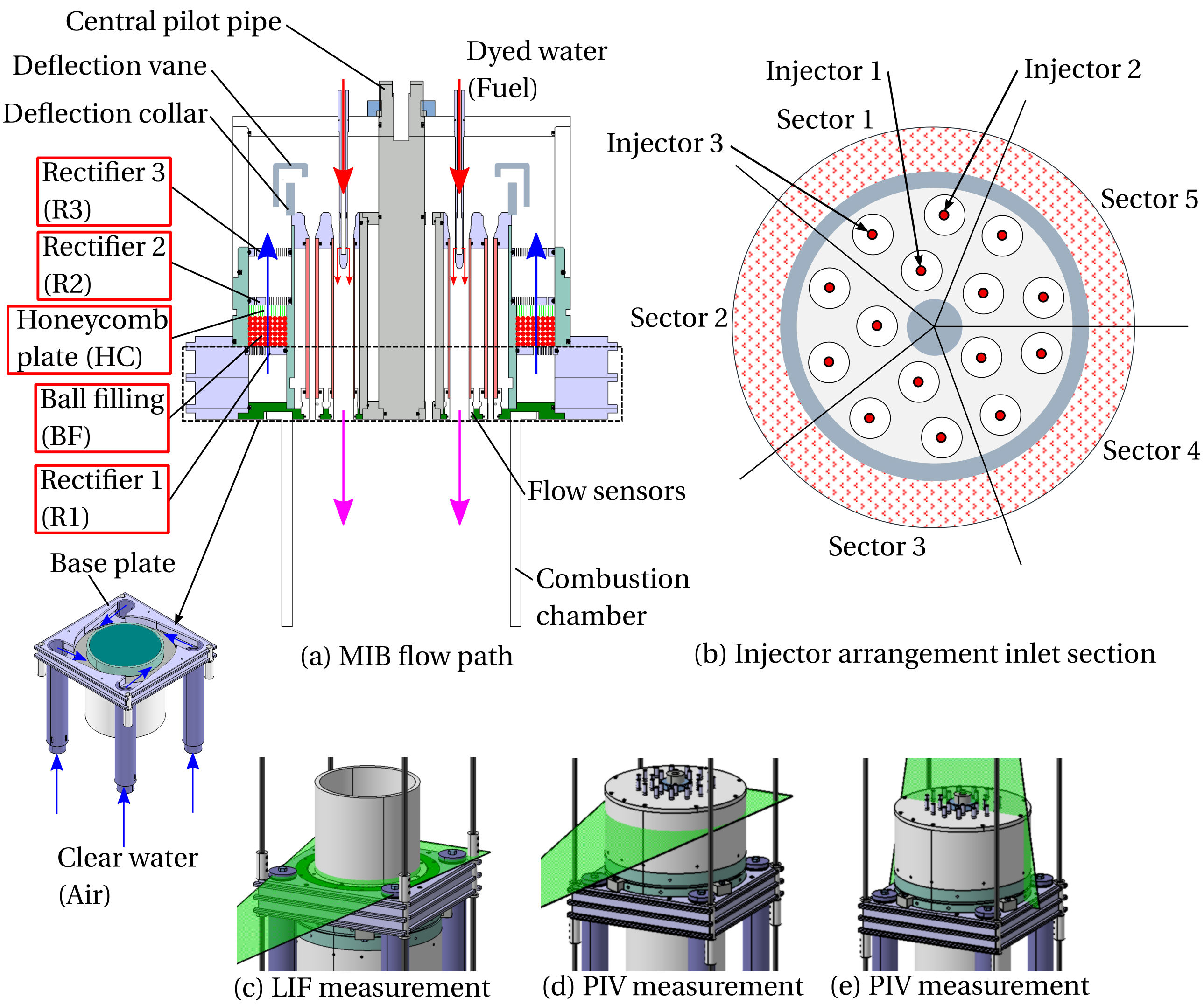

(a) MIB flow path

(b) Injector arrangement inlet section

(c) LIF measurement mixture quality

(d) PIV measurement inflow distribution

(e) PIV measurement radial velocity profile

Figure 3.13: Multi-injector burner close to an engine configuration.

The loss of mixing quality due to the inflow distortion in the burner head is investigated with the experimental model of the multi-injector burner shown in fig. 3.13. The burner head and the combustion chamber are built from perspex to provide optimum optical access. The flow path is shown in fig. 3.13(a). The clear water is equally split into four symmetrically arranged pipes. These are connected with the base plate, where water flows tangentially into the annular gap. The 180° flow turn is accomplished in the subsequent head section of the combustor model, and the water flow is distributed among the mixing tubes. A flow reversal section comprising a deflection vane and a deflection collar is used to tune the flow field at the inlet of the injectors.

The injectors are symmetrically arranged around a pilot injector dummy in 5 sectors of 72° into two concentric rows, as depicted in fig. 3.13(b). Similar to the single injector test configuration, a hot-film sensor is mounted at the end section of the injectors to quantify the integral mass flow distribution. The mixing PMF is measured by LIF with a horizontal light sheet, as depicted in fig. 3.13(c). The radial and tangential velocity distribution in the head section of the combustor was measured with PIV, as shown in fig. 3.13(d). In this setup, the fuel lances and the central pilot pipe are left out to increase the optical accessibility of the burner head. The radial velocity profiles upstream of the flow reversal section are measured with the setup illustrated in fig. 3.13(e).

Figure 3.14: Tornado-like structure with R1.

The velocity gradients from the inlet tubes and the base plate are suppressed with the components marked with red borders in fig. 3.13, referred to as the flow conditioning unit. It consists of three evenly spaced perforated plates, rectifiers 1-3 (R1-R3), and a ball packing above R1 followed by a short honeycomb section. Initially, rectifier 1 with a high pressure-loss coefficient was expected to suppress the velocity gradients completely, but PIV experiments with the setup of fig. 3.13(c) showed that this is not the case. The remaining asymmetries in the inflow distribution formed a rotating tornado-like structure, which originates from the superposition of the asymmetrical tangential and radial momentum distribution over the whole annular cross-section upstream of the 180° turning. This structure was seen during the venting process of the head section of the burner prior to the image recording as a rotating vortex along the middle axis, as shown in fig. 3.14.

Multiple tests were conducted during the development phase of the experiment to find the origin of this effect. The following changes in the experimental setup were made without achieving the desired effect of suppressing the formation of the tornado-like structure:

- Increasing the pressure loss coefficient of rectifier 1 by reducing the hole diameter and the number of holes.
- Increasing the pressure of the sealing elements and covering the interface between the rectifier plate and the base plate with epoxy resin.
- Hydraulic balancing of the inlet pipes.

The origin of the problem could be understood with a simulation of the flow path with rectifier 1, which is explained in appendix A.3. The results revealed that the asymmetric radial and tangential momentum distribution originates from an uneven total pressure distribution in the holes of the rectifier plate. The jets with higher pressure entrain the weaker jets and thus create spots with higher momentum over the whole sectional area of the annular gap.

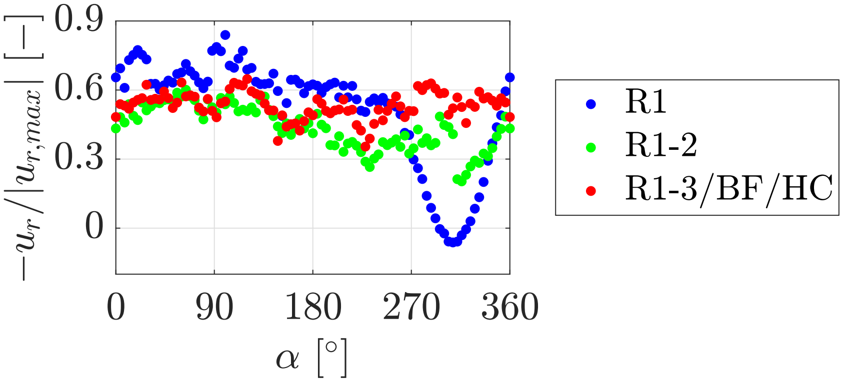

Figure 3.15: Comparison u_r at $r/d_B = 0.39$.

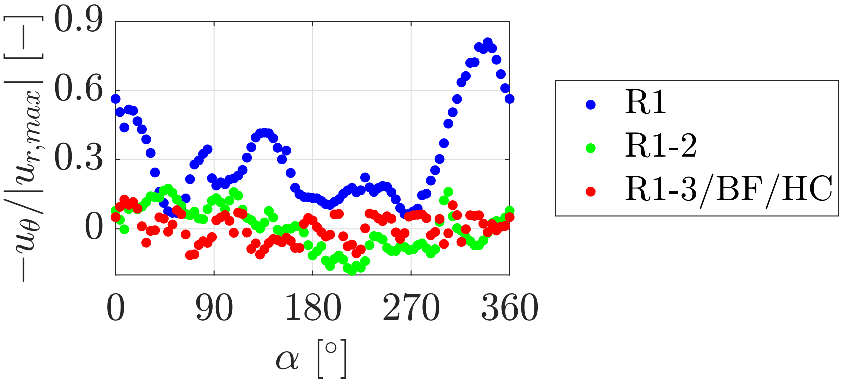

Figure 3.16: Comparison u_θ at $r/d_B = 0.39$.

In order to re-distribute the total pressure in radial and tangential direction over the annular gap, the ball filling (BF) above rectifier 1 was introduced ($d_B = 6mm$). The honeycomb plate holds the balls in place such that they can not block the holes of rectifier 2. Finally, rectifier 3 adjusts the desired inflow conditions upstream of the flow reversal section, obtaining the final arrangement (R1-3/BF/HC). The measured radial and tangential velocity distribution with the experimental setup of fig. 3.13(d) for the different stages of the flow conditioning unit are shown in fig. 3.15 and 3.16. The velocities at $r/d_B = 0.39$ were extracted from the whole velocity field for these plots.

The lowest radial velocity values with rectifier 1 only (blue dots) are observed close to 280°, originating from the asymmetric inflow distribution during the experiments. In addition, the flow had a strong tangential component in a clockwise direction, counter-rotating with respect to the inlet swirl in the base plate. This effect could be reduced in configuration R1-2 (green dots). However, the flow field upstream of the flow reversal section was not repeatable due to the stochastic formation of the small tornado-like flow structures mentioned above, which resulted from a superposition of the remaining asymmetrical tangential and radial momentum distribution originating from the inflow. With the final arrangement $R1-3/BF/HC$ (red dots), the most uniform radial and tangential velocity distribution was achieved with low angular deviations from the mean $\overline{u_r}$ and $u_\theta = 0$.

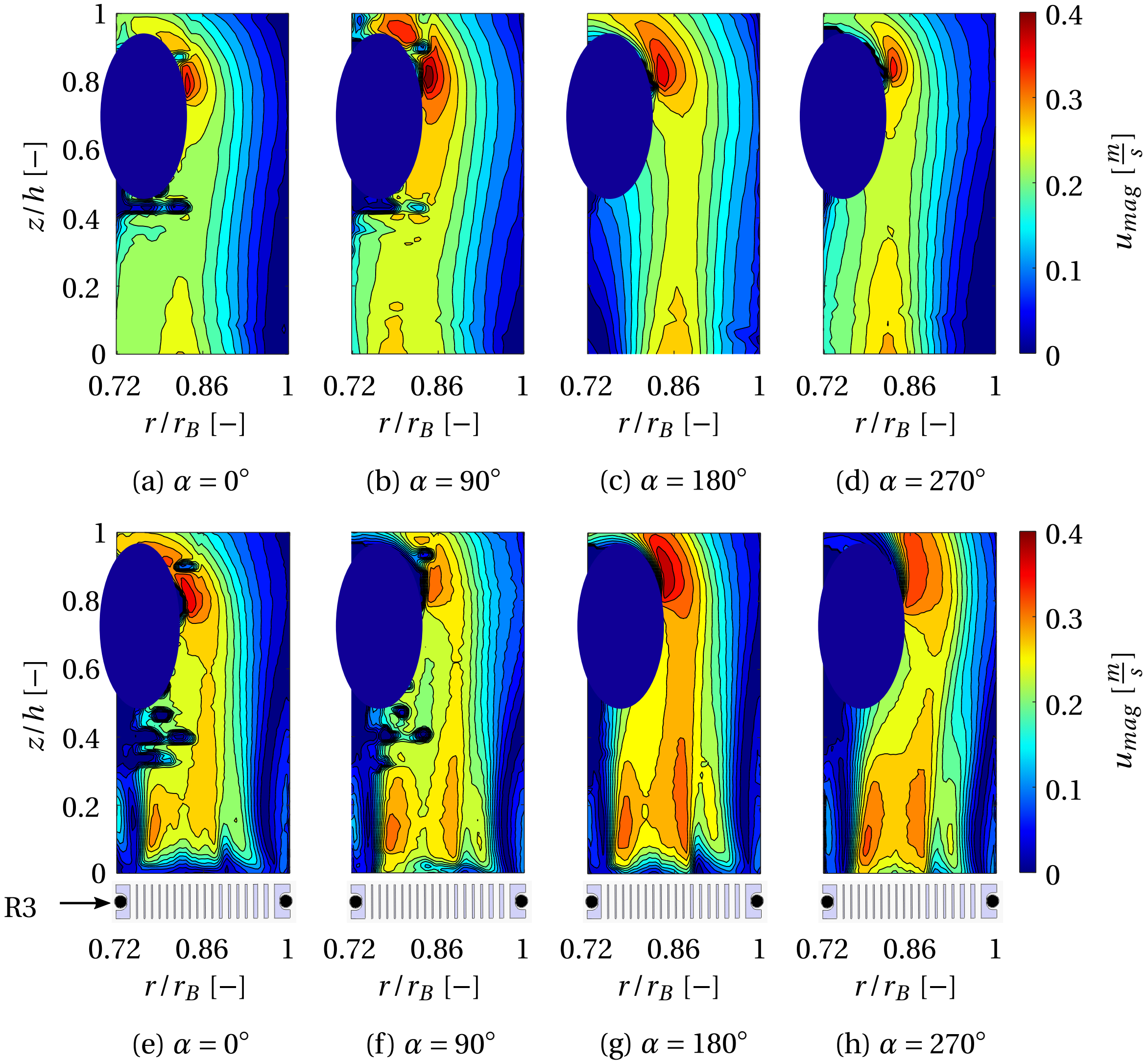

(a) $\alpha = 0°$ (b) $\alpha = 90°$ (c) $\alpha = 180°$ (d) $\alpha = 270°$

(e) $\alpha = 0°$ (f) $\alpha = 90°$ (g) $\alpha = 180°$ (h) $\alpha = 270°$

Figure 3.17: Comparison vertical velocity field: (a)-(d) R1-2; (e)-(h) R1-3/BF/HC.

The velocity profile upstream of the flow reversal section is shown in fig. 3.17. Here the results for the arrangements R1-2 (first four contour plots) and R1-3/BF/HC (last four contour plots) at the angular positions $\alpha = (0, 90, 180, 270)°$ are compared with each other (see also fig. 3.13(e)). The non-uniformity with arrangement R1-2 was also seen in the measured velocity profiles. In particular, the velocity field at $\alpha = 180°$ has different flow structures than the remaining angular positions for this arrangement.

In contrast, the final arrangement R1-3/BF/HC generates very similar flow structures upstream of the flow reversal section at all measured angular positions, thus providing the desired uniformity of the inflow conditions for the mixture investigation in the multi-injector burner. The measured velocity profile is used as the inlet boundary condition for the CFD simulations of the air flow path upstream of the injectors, as reported in chapter 4.

A further important aspect is the standard deviation of the velocity magnitude ($\sigma_{u_{mag}}$), which provides information regarding the turbulent kinetic energy. Based on the obtained data, it has a maximum value of $\sigma_{u_{mag}} \approx 0.3 u_{mag}$ slightly above the deflection vane. The high turbulent kinetic energy in this area is convected into the inlet sections of the injectors, and thus leads to enhanced mixing in the multi-injector burner compared with a single injector under ideal inflow, as shown in section 5.2.3.

3.4 Experimental Matrix

Experiment	Re/Re_{exp}	$u_f/u_{f,N}$
1	1	0.74; 0.92; 1; 1.07; 1.21; 1.32; 1.44
2	1; 1.25; 1.5; 1.75; 2	1; 1.25; 1.5; 1.75; 2

Table 3.1: Experimental matrix for LIF experiments in the single injector under ideal inflow.

The mixing behavior of a single injector under ideal inflow is characterized by the experiments summarized in table 3.1. The influence of the fuel inlet velocity is quantified by keeping the injector Reynolds number constant at $Re = Re_{exp} = 13900$. For this, the normalized fuel velocity with its nominal value is varied between $0.74 < u_f/u_{f,N} < 1.44$. For this particular setup, one obtains a constant momentum flux density ratio in all injection holes due to the even momentum distribution at the injector inlet (see also figs. 4.7 and 5.1). The influence of the Reynolds number is investigated by increasing the air and the fuel velocity simultaneously by the same factor starting from their nominal values, thus keeping the momentum flux density ratio in all injection holes constant at $j = j_N$. In these experiments, the injector Reynolds number is increased to $Re/Re_{exp} = 2$.

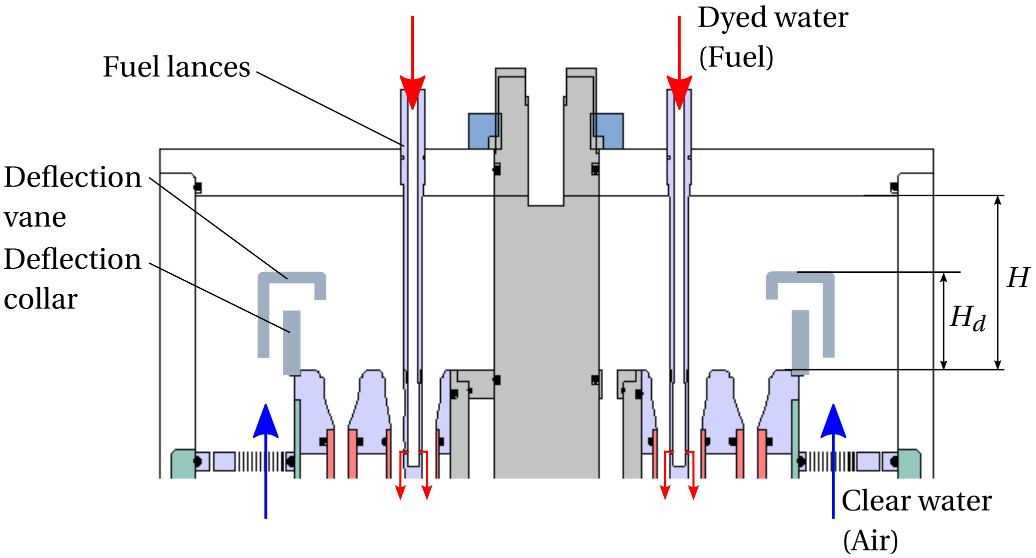

Figure 3.18: Components flow reversal section.

$u_f/u_{f,N} = (0.74;0.92;1;1.07;1.21;1.32;1.44)$				
Config.	Def. collar	Def. vane	H_d/H	Nr. of datasets
0	Symmetric inflow conditions			7
1	x	x	0.48	21
2	x	x	0.52	21
3	x	x	0.56	21
4	x	x	0.60	21
5	x		n/a	21

Table 3.2: Experimental matrix for LIF experiments in the multi-injector burner.

The influence of the inflow distortion in the burner head is investigated with the multi-injector burner model shown in fig. 3.13. The mixing PMFs are measured individually in the outlet section of injectors 1, 2, and 3. The inflow conditions are varied by changing the position of the deflection vane (see fig. 3.18 and table 3.2). Four configurations (config. 2-4) are considered by varying the height of the deflection vane ($H_d/H = (0.48;0.52;0.56;0.6)$). A last configuration (config. 5) is considered by completely removing the deflection vane to create the highest velocity gradients. The experiments are conducted with the same fuel velocities as those with a single injector under ideal inflow at constant $Re = Re_{exp}$. Hence, 21 datasets for each configuration are obtained, 7 for each injector. The datasets for the multi-injector burner, together with the obtained for a single injector under ideal inflow describing the dependency of the mixing PMF on $u_f / u_{f,N}$, are used as input to generate the O-POD model. The experimental matrix is summarized in table 3.2. The seven datasets for the single injector are referred to as config. 0.

The validation data for the RANS-CFD simulation are generated by measuring the volume flows through injectors 1 and 2 in all sectors of the multi-injector burner model with the hot-film flow sensors mounted at the end of the mixing tubes (see fig. 3.13(a)-(b)). Note that the sketch of fig. 3.13 is only a schematic representation of the multi-injector burner model and does not correspond to the original geometry. In reality, the velocity profile in injectors 2 and 3 differed due to the actual arrangement of the mixing tubes in the MIB. However, the CFD simulations and an additional experiment for an entire sector of the multi-injector revealed that the volume flow through injector 3 is very similar to injector 2. The experiments are conducted with config. 1 and 5 (see table 3.2) without fuel injection. Additional data are also obtained by removing the fuel lances for an overall evaluation of the CFD model (config. 1* and 5*).

4 RANS-CFD Approach for Calculating the Observable Vectors

The RANS-CFD approach to calculate the $\underline{\varphi^\star}$ observable vectors is presented in this chapter. First, the simulation setup and the fluid domains for the single injector and the multi-injector burner are described. Then the mesh dependency of the volume flows and the validation approach are presented. Finally, the resulting flow fields for config. 3 (see table 3.2) are shown, as these datasets are considered as the reference to demonstrate the performance of the O-POD model.

4.1 Simulation Setup

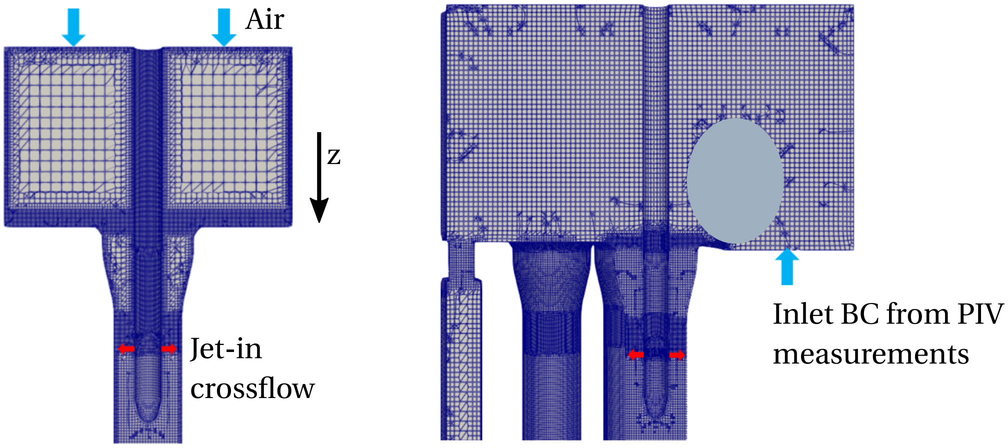

(a) Single injector (b) Multi-injector burner

Figure 4.1: CFD simulation domains.

The CFD simulations of the air flow path upstream of the injectors are conducted with the open-source CFD code OpenFOAM [92]. A sectional view of the numerical domains is shown in fig. 4.1. These are modeled with a structured mesh generated with the utility *cartesianMesh* of the software *cfMesh* [93]. The single injector (left) is modeled with an inlet tube with a bigger diameter followed by the injector element as in the experimental setup of fig. 3.12. The multi-injector burner (right) is simulated with a sector geometry of 72° according to the symmetry shown in fig. 3.13.

The velocity and pressure fields are obtained by solving the RANS equations (see eq. 2.1-2.3). For this, the *simpleFoam* solver for incompressible flows is used, and the turbulence is calculated with the $k-\omega$ SST model [26–28]. The fuel concentration is modeled with the passive scalar transport equation (see eq. 2.4-2.7). A constant air inlet velocity is set as the boundary condition for the single injector. For the sector geometry, the measured inflow velocity profile directly upstream of the flow reversal section (see fig. 3.17) is set as the inlet boundary condition for the air flow with the OpenFOAM utility *timeVaryingMappedFixedValue* [92, 94]. The normalized fuel inlet velocity in the injection holes $u_f/u_{f,N}$ is set equal to the values shown in tables 3.1 and 3.2 as *surfaceNormalFixedValue*.

The divergence terms are discretized with the *limitedLinear* scheme, which switches over to upwind discretization in regions of rapidly changing gradient and thus gives the simulation adequate numerical stability [95]. For this, a high mesh quality is also of particular importance [96], which is evaluated with the max. non-orthogonality[1] and skewness[2] of the cells. A large max. non-orthogonality of the cells (>65°) or a high skewness of the cells (>3) leads to convergence problems in the simulation. The velocity and pressure fields at the end of the injector inlet section (see cross-sectional area A-A in fig. 2.3) are used to calculate the observable vectors, which are shown in section 5.1. The fuel concentration field at the injector outlet is used to assess the measured mixing behavior of the multi-injector burner in section 5.2.3.

---

[1] The non-orthogonality is defined as the angle between the line made by two adjacent cell centers and the common face normal vector

[2] The cell skewness is the deviation of the line connecting two adjacent cell centers to the middle point of the common face

4.2 Mesh Dependency of the Volume Flows

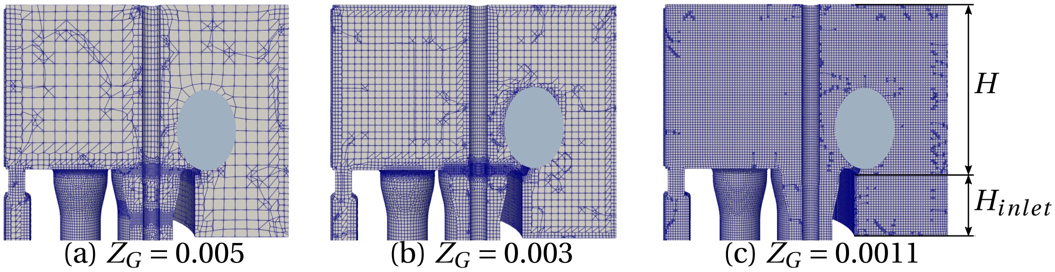

(a) $Z_G = 0.005$ (b) $Z_G = 0.003$ (c) $Z_G = 0.0011$

Figure 4.2: Global cell size in the burner head.

The global cell size in the burner head Z_G was chosen to make the volume flows through the injectors mesh independent. Here a compromise must be made between cells small enough to accurately represent the momentum distribution in the burner head and adequate numerical stability. It was found that the smallest possible global cell size in the burner head is $Z_G = 0.002$ (see fig. 4.2). A further reduction of Z_G makes obtaining an adequate mesh quality with the used meshing utility difficult and leads to an oscillatory behavior of the flow variables.

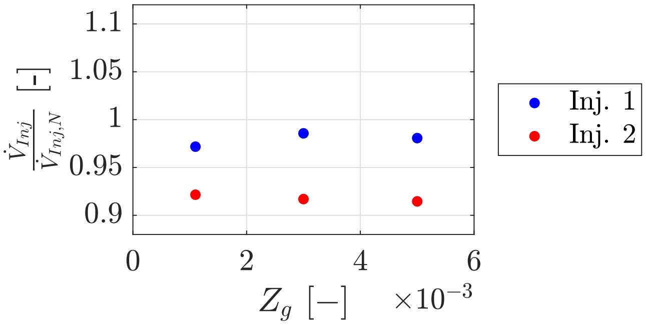

Figure 4.3: Sensitivity of the volume flows to the global mesh size and the divergence discretization scheme.

Fig. 4.3 shows the resulting average volume flow in injectors 1 and 2 (see fig. 3.13(b)) as a function of the global cell size in the burner head for config. 1. As mentioned in section 3.4, the volume flow through injector 3 was very similar to injector 2 with the CFD simulations and an additional experiment for an entire sector. The values are normalized with the nominal flow rate of the injectors $V_{Inj,N}$ defined as the mean value for the nominal operating point for the actual machine scaled to the experimental model. It can be observed that the resulting volume flow distribution is nearly independent of the global cell size for the chosen variation range. It should be noted that this study was conducted with a simulation setup that was still not validated with the measured inflow distribution, so the results of fig. 4.3 differs from the measured values for config. 1.

4.3 Validation

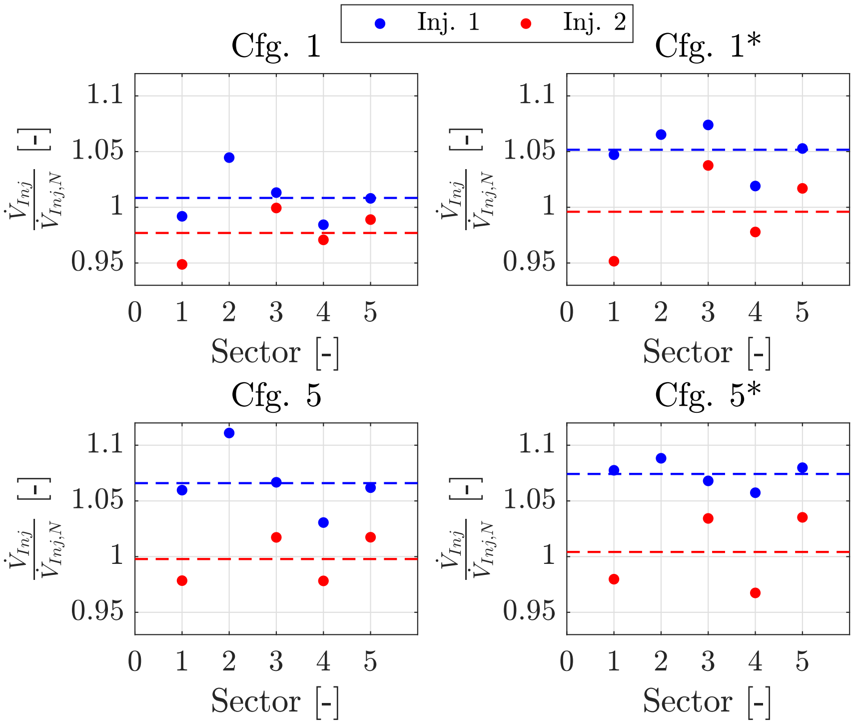

Figure 4.4: Measured volume flows for all considered configurations.

For validation purposes, the volume flows through injectors 1 and 2 in all sectors of the multi-injector burner model (see fig. 3.13) were measured with the hot-film flow sensors mounted at the end of the injectors for config. 1 and 5 (see table 3.2) as well as the corresponding setups without fuel lances (config. 1* and 5*). The measured volume flow distributions are shown in fig. 4.4. The air inflow distribution in config. 1 was very symmetric with a volume flow gradient between injectors 1 and 2 of around 2.5 %. Removing the fuel lances (config. 1*) causes an increase in the volume flow of injectors 1 and 2, and the volume flow gradient increases to 5 %. Removing the deflection vane (config. 5 and 5*) further increases the volume flows and the relative gradients (6.6 % for config. 5 and 7.5 % for config. 5*). The deviation of the measured values from the mean (denoted with a dashed line) can be explained by the limited accuracy of the sensors (approx. ±5%, see section 3.2.3.2) as well as the remaining slight deviations of the velocity profile upstream of the deflection geometry shown in fig. 3.17.

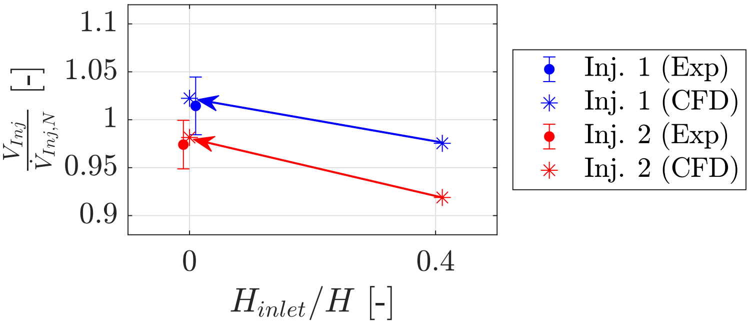

Figure 4.5: Fine-tuning location inlet boundary.

The simulation approach was validated with the volume flows in each configuration as reference data. Fig. 4.5 shows the dependency of the flow rate through the injectors 1 and 2 on the distance of the inlet boundary at the beginning of the flow reversal section (denoted with H_{inlet}/H) for config. 1. The CFD simulation results are marked with asterisks, and the measured volume flows are summarized with the mean value and the error bars representing the variation range during the experiments. For each data point, the velocity values at the inlet boundary are extracted from the flow field shown in fig. 3.17 accordingly with the actual location of the inlet plane. It can be observed that the best match between the measurement and the simulation was obtained by placing the inlet boundary directly at the beginning of the flow reversal section at $\frac{H_{inlet}}{H} = 0$.

Finally, the volume flow distribution was calculated for the remaining configurations and compared with the measurements. These results are shown in fig. 4.6. A good match between the CFD and the experimental results was obtained, especially for configs. 1 and 1*. The deviations for the remaining configurations were considered acceptable, and the CFD model approach was further used for the calculation of the $\underline{\varphi}^\star$ observable vectors for each dataset listed in table 3.2.

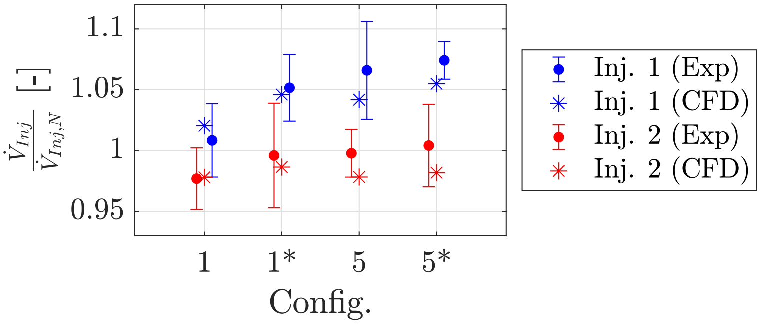

Figure 4.6: CFD validation results.

4.4 CFD Results Inflow Conditions of the Injectors

The sectional view of the calculated flow fields at the end of the inlet section is presented in this section. For this, the results for config. 0 and config. 3 $u_f/u_{f,N} = 1.44$ (see table 3.2) are shown in figs. 4.7-4.10. These datasets were chosen as they are used as a reference to represent the $\underline{\varphi}^\star$ observable vectors in section 5.1 and to compare the model output with the measured mixing PMF in section 7.2. As the simulation data is evaluated upstream of the fuel injection, the influence of the fuel velocity on the flow fields was fairly low. The velocity in the main flow direction (u_z) and the radial velocity (u_r) are shown in the top left and right figures, respectively. The tangential velocity (u_θ), which is considered as positive counterclockwise in the direction out of the page, and the relative static pressure field ($\Delta p = p - p_{min}$) are represented by the lower left and right graphs. All velocity components and the static pressure are normalized with the mean z-velocity ($\overline{u_z}$) and dynamic pressure ($\rho \overline{u_z^2}$). The dashed line shows the location of the middle axis of the multi-injector burner and will be referred to as the MIB center line.

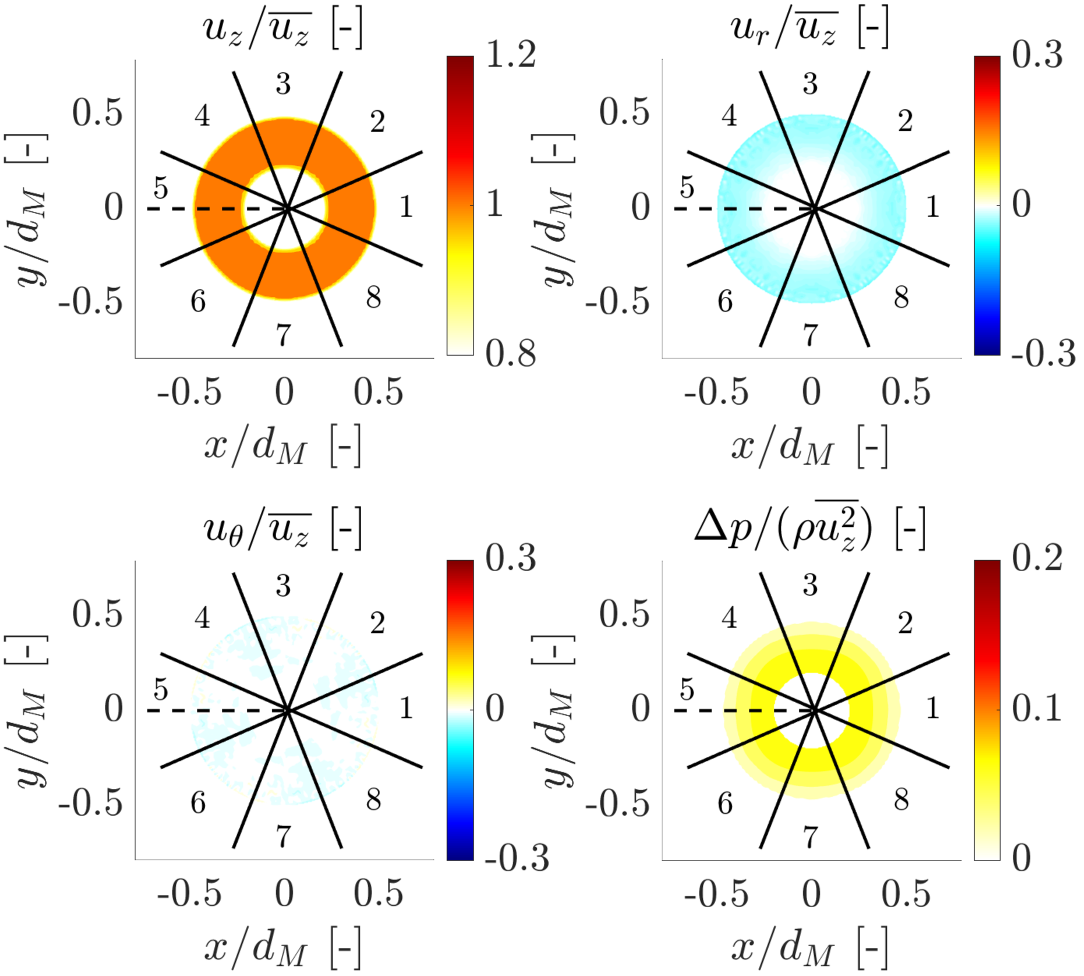

Figure 4.7: Flow field for config. 0 ($u_f/u_{f,N} = 1.44$).

The flow field for config. 0 exhibits a nearly constant z-velocity (see fig. 4.7). The additional radial velocity component caused by the flow acceleration in the inlet section is minimal compared to the z-velocity. The tangential velocity is close to zero over the whole sectional area. Furthermore, the pressure distribution has a symmetric pattern, which results from the blockage of the turbulence generators upstream of the injection holes.

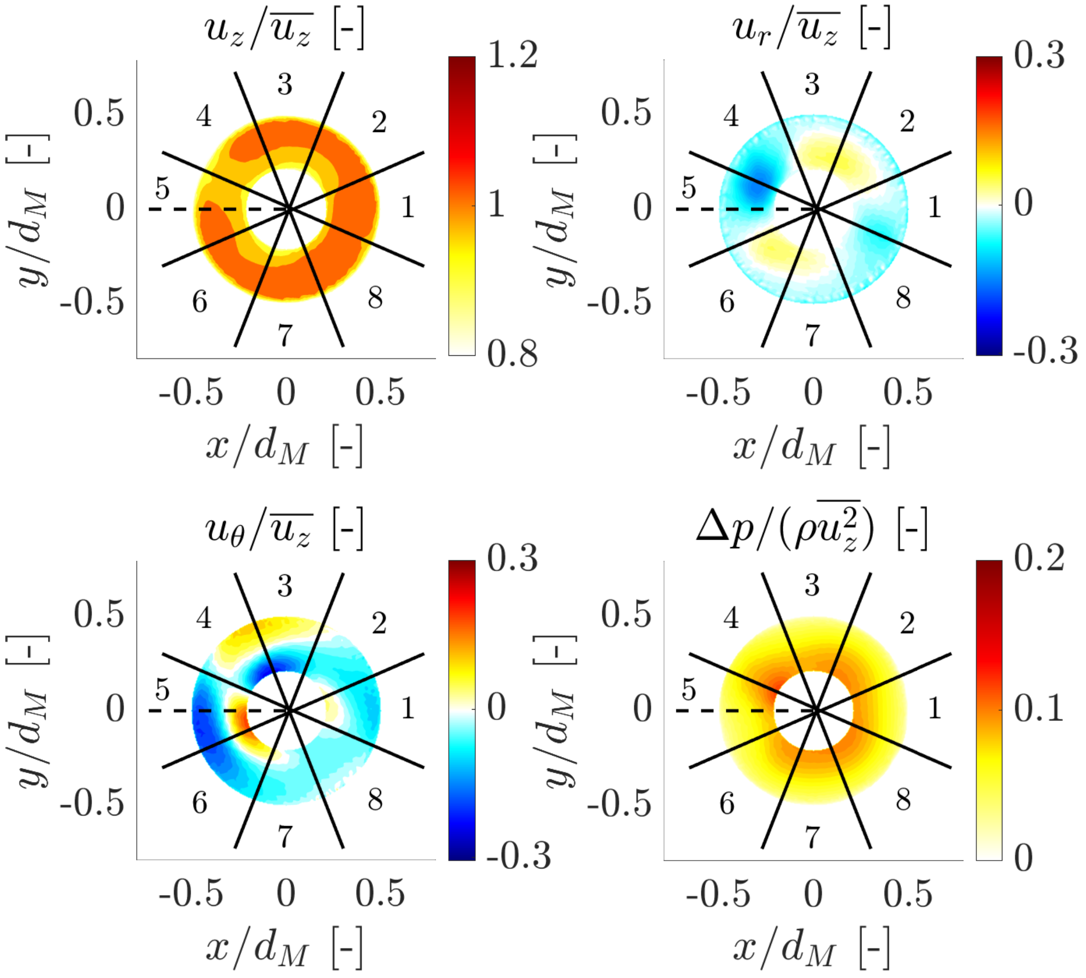

Figure 4.8: Flow field for config. 3, injector 1 ($u_f/u_{f,N} = 1.44$).

The flow field for injector 1 in config. 3 also has a uniform z-velocity distribution except in a small area with a lower velocity between segments 4 and 5 (see fig. 4.8). The highest negative radial velocity values and the biggest tangential velocity gradients are observed in this area. The static pressure also has a slight overshoot in the area with the z-velocity deficit.

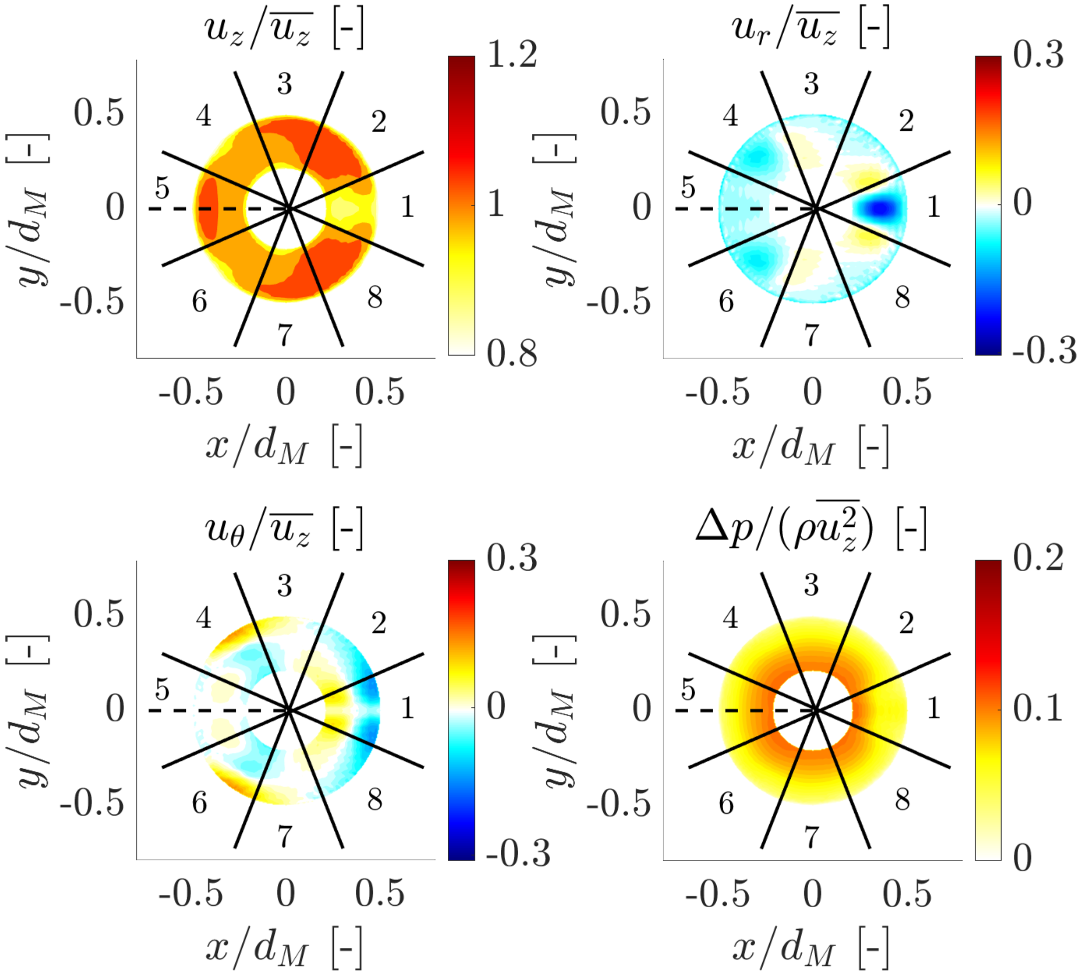

Figure 4.9: Flow field for config. 3, injector 2 ($u_f/u_{f,N} = 1.44$).

The z-velocity distribution for injector 2 in config. 3 shows three areas with higher velocity symmetric to the MIB center line (see fig. 4.9). The radial and tangential velocity, as well as the static pressure, also have the same symmetry line. The highest negative radial and tangential velocity and the lowest static pressure are observed in segment 1.

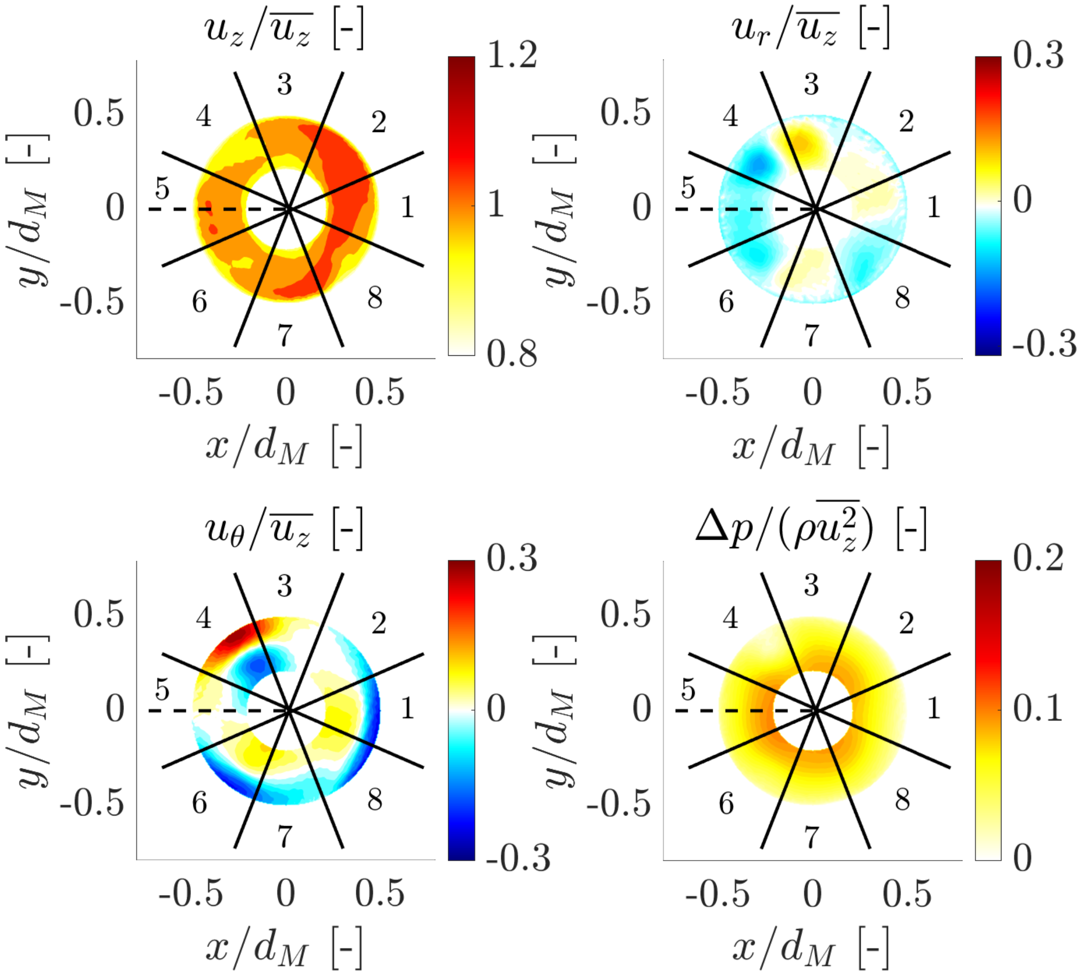

Figure 4.10: Flow field for config. 3, injector 3 ($u_f/u_{f,N} = 1.44$).

The z-velocity field of injector 3 in config. 3 shows the highest gradients (see fig. 4.10). It has a large zone with higher velocity values covering segments 1, 2, 7, and 8. In addition, the tangential velocity and the static pressure differ from the ideal inflow behavior over the whole sectional area more than in injectors 1 and 2. The highest values can be observed in segments 4 and 5, respectively.

The flow fields for the remaining configurations are shown in appendix A.4. In general, a similar flow behavior to the one presented here in terms of velocity and pressure gradients was obtained for all configurations. Even though the velocity and pressure fields are evaluated upstream of the flow injection, the influence of the fuel momentum must be considered in the CFD calculation as it had a small but not negligible influence on the results.

5 Observable and Mixing PMF Datasets

In the following, the considered datasets to apply the O-POD model approach are shown and discussed. First, the observable ($\underline{\varphi^\star}$) vectors describing the inflow conditions of the injectors are discussed. Then the mixing PMFs at the outlet section of the injectors ($\underline{\varphi}$) obtained for the configurations given in table 3.1 and 3.2 are presented. Finally, these datasets are used to quantify the mixing PMFs for the whole combustion chamber ($\underline{\varphi_{CC}}$), which includes the contribution of all injector elements.

5.1 $\underline{\varphi^\star}$ Observable Vectors

The components of the $\underline{\varphi^\star}$ observable vector for config. 0. (denoted with solid black lines) and config. 3 (represented with color dots) at $u_f/u_{f,N} = 1.44$ are shown in fig. 5.1. This velocity was chosen to illustrate the datasets with the most asymmetric momentum flux density ratio. As mentioned above, the $\underline{\varphi^\star}$ observable vectors for config. 3 are used as input to predict the mixing PMF with the created O-POD model and compare the output with the measurement results in section 7.2. The momentum flux density ratio ($\frac{j_1}{j_N}, ..., \frac{j_8}{j_N}$) and the ratio between the perpendicular and the z-velocity ($Q_1, ..., Q_8$) are shown in the upper left and right plots. The ratio between the radial and the perpendicular velocity component ($-R_1, ..., -R_8$) and the static pressure distribution ($P_1, ..., P_8$) are illustrated with the lower left and right plots.

For config. 0, the post-processing of the flow field provides nearly constant velocity and pressure values, denoted with the horizontal lines. The values $Q_1 = 0.0193$ and $-R_1 = 1$ indicate that the perpendicular velocity component corresponds to 1.93% of the u_z value and consists exclusively of a radial component showing to the injector middle axis. A constant $P = 0$ means that the surface averaged static pressure value was constant for all segments.

The momentum flux density ratio for injector 1 in config. 3 has a small variation range between $\frac{j}{j_N} = 1.64 - 1.76$. The perpendicular velocity component increases to $Q = 0.08$ in segment 5 and has a high oscillatory behavior. It is also the case for $-R$, reflecting the direction changes of the radial velocity shown in fig. 4.8. The static pressure has a maximum value of $P = 0.0133$.

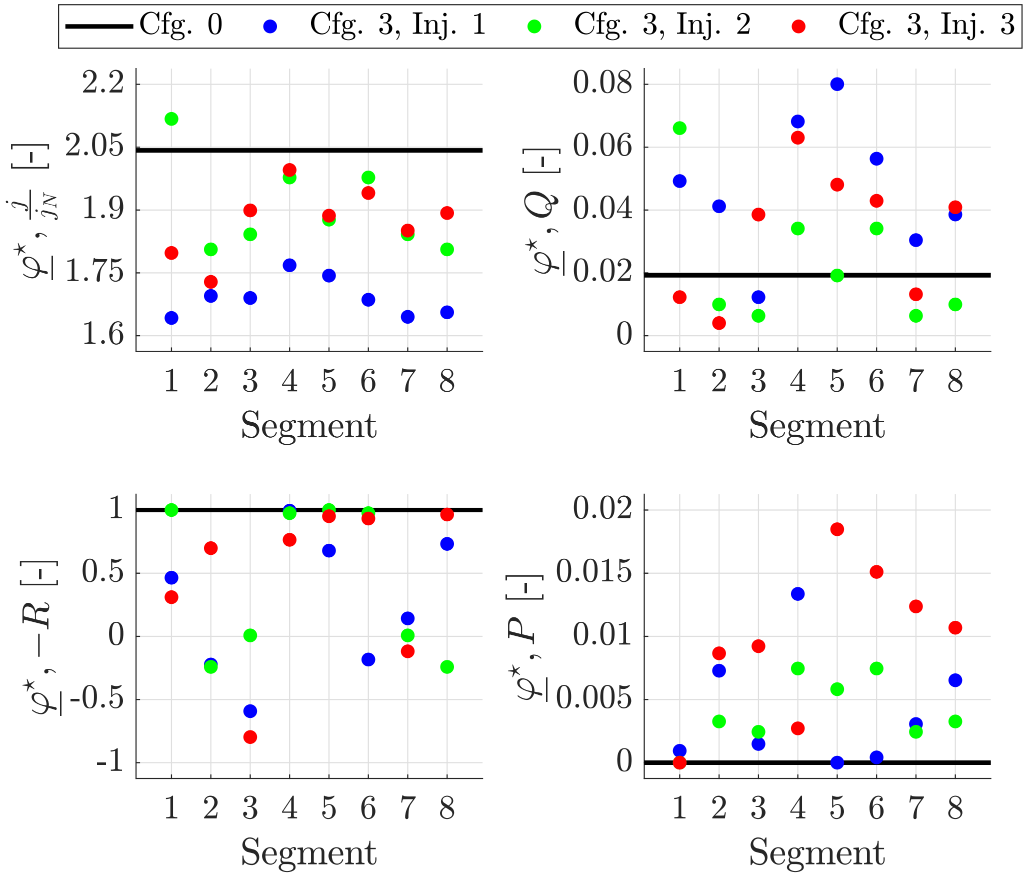

Figure 5.1: Components of the $\underline{\varphi}^{\star}$ vectors for config. 0 and 3 ($u_f / u_{f,N} = 1.44$).

Due to the symmetry of the flow field to the MIB center line, the velocity and pressure values of segments 2-8, 3-7, and 4-6 of injector 2 are the same. Segment 1 has the highest momentum flux density ratio and radial velocity pointing towards the injector middle axis ($\frac{j_1}{j_N} = 2.11$, $Q_1 = 0.066$,

$-R_1 = 1$). Similar behavior can be observed for segments 4-6 with high momentum flux density ratio and radial velocity.

The z-velocity gradients for injector 3 (see fig. 4.10) lead to the most asymmetric momentum flux density ratio. The variation range is very similar to the dataset for injector 2 but without the symmetries resulting from the flow field. The behavior of Q and $-R$ in injector 3 is similar to the results for injector 1. The static pressure was higher than the results with injectors 1 and 2 for segments 2-3 and 5-8.

The obtained $\underline{\varphi^\star}$ observable vectors for the remaining configurations are shown in appendix A.5. In general, qualitatively similar behavior of the $\underline{\varphi^\star}$ vector was obtained for all configurations. The resulting velocity and pressure values depend on the flow field at the inlet section of the injectors, which was altered by changing the position of the deflection vane (see table 3.2).

5.2 Mixing PMF at Injector Outlet

This section presents the mixing PMF based on the experimental data for the parameter range of interest. The width of the statistic distribution is quantified with the spatio-temporal standard deviation σ_{st} (see eq. 2.54). First, the results under ideal inflow conditions are presented. The obtained datasets for the single injector elements of the multi-injector burner are shown afterwards. Finally, the mixing PMFs for the whole outlet section of the multi-injector burner are presented.

5.2.1 Influence of the Fuel Inlet Velocity Under Ideal Inflow

The dependency of the mixing PMF on the fuel inlet velocity under ideal inflow was investigated by keeping the injector Reynolds number constant at $Re = Re_{exp} = 13900$ and gradually increasing the fuel inlet velocity between $0.74 < u_f / u_{f,N} < 1.44$. The results are shown in fig. 5.2. The shape of the PMF is close to a Gaussian, but it can be seen that depending on $u_f / u_{f,N}$, there is a small asymmetry from the mean $\overline{\phi}$. The narrowest distributions can be observed for the extreme values $u_f/u_{f,N} = 0.74$ and $u_f/u_{f,N} = 1.44$.

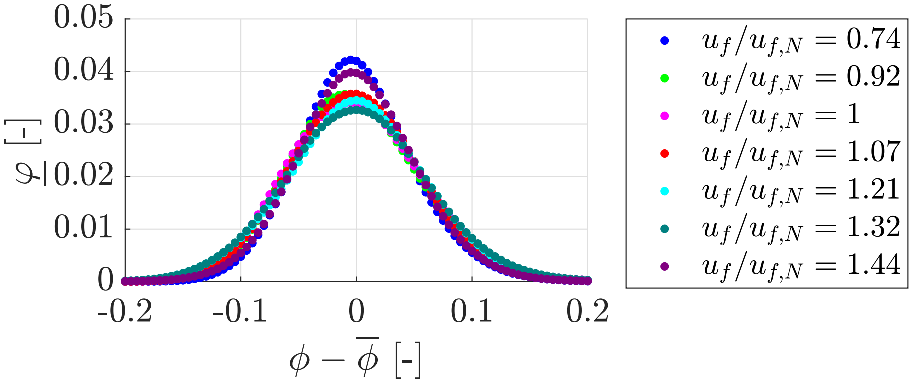

Figure 5.2: Mixing PMFs as a function of the fuel inlet velocity under ideal inflow.

Fig. 5.3 shows the associated spatio-temporal standard deviation under ideal inflow ($\sigma_{st,ref}$). The values are normalized with the mean $\overline{\sigma_{st,ref}}$, chosen as the reference value for all the results in this chapter. It can be seen that the narrower distributions at $u_f/u_{f,N} = 0.74$ and $u_f/u_{f,N} = 1.44$ are reflected in a lower standard deviation of approx. 90% of the mean $\overline{\sigma_{st,ref}}$. Based on these results, the dependency of mixing PMF on the fuel inlet velocity $u_f/u_{f,N}$ is relatively low. This behavior is due to the use of turbulence generators, which make the mixing behavior mainly dependent on the turbulent air inflow distribution.

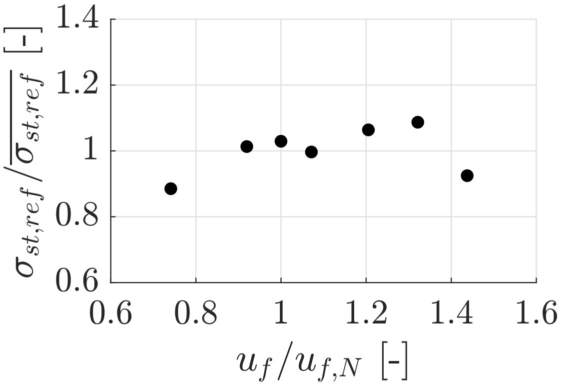

Figure 5.3: Spatio-temporal standard deviation as a function of the fuel inlet velocity under ideal inflow.

5.2.2 Influence of the Injector Reynolds Number Under Ideal Inflow

The dependency of the mixing PMF on the Reynolds number was investigated under ideal inflow by increasing Re above the nominal operating point of the injector. For this, the air and fuel flow rates were increased by the same factor to keep the momentum flux density ratio in all injection holes constant at $j = j_N$. The PMFs obtained at the injector outlet are presented in fig. 5.4. The shape of the PMF is rather symmetric around the mean value $\overline{\phi}$ and close to a Gaussian. The mixing PMF becomes narrower for $Re/Re_{exp} > 1.5$, reflecting the decrease of the spatio-temporal variance due to the enhancement of fine scalar mixing. Nevertheless, the mixing PMFs for $Re/Re_{exp} < 1.25$ remains almost unchanged.

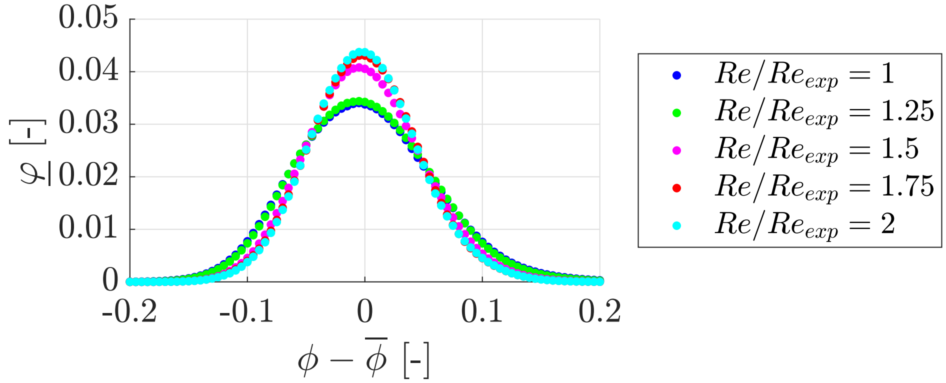

Figure 5.4: Mixing PMFs as a function of the Reynolds number under ideal inflow.

Fig. 5.5 shows the associated spatio-temporal standard deviation σ_{st} normalized with $\overline{\sigma_{st,ref}}$ similar to the results of fig. 5.3. The narrower distribution at $Re/Re_{exp} > 1.5$ is seen as an asymptotic decrease of the standard deviation up to $\sigma_{st} \approx 0.8 \cdot \overline{\sigma_{st,ref}}$. Here, it can also be observed that the dependency of the mixing behavior on the Reynolds number up to $Re/Re_{exp} = 1.25$ is marginal.

Based on these results, the variations of the mixing PMF in the multi-injector burner presented in the following section can not be associated with local variations of the Reynolds number in the injector elements. The reason is that the highest measured gradient of the flow rate through the injectors was only

7.5% for config. 5* (see fig. 4.4).

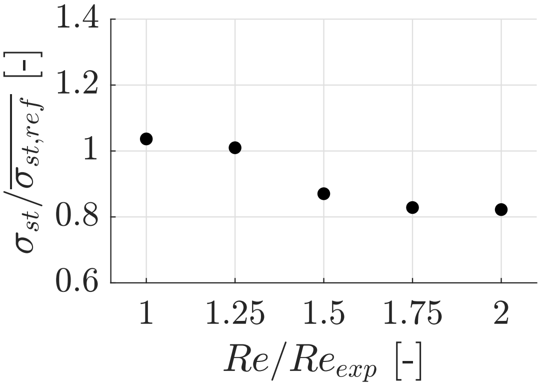

Figure 5.5: Spatio-temporal standard deviation as a function of the Reynolds number under ideal inflow.

5.2.3 Influence of the Inflow Distortion in the Burner Head

The influence of the inflow distortion on the mixing PMF was investigated with the multi-injector burner by keeping a constant air volume flow through the combustor and gradually increasing the fuel inlet velocity between $0.74 < u_f/u_{f,N} < 1.44$ similar to the investigations for a single injector under ideal inflow. The results are shown in fig. 5.6 (Injector 1), fig. 5.7 (Injector 2) and fig. 5.8 (Injector 3) for all configurations listed in table 3.2. Each plot shows the results obtained at a specific normalized fuel inlet velocity. The PMFs for config. 0 and config. 1-5 are plotted with black asterisks and color dots, respectively.

For injector 1, small asymmetries from the mean $\overline{\phi}$ with a maximum frequency of occurrence sensitive to a change of the inflow condition ($\varphi_{max} = 0.042 - 0.048$) at $u_f/u_{f,N} = 0.74$ can be observed (see fig. 5.6). Increasing the fuel velocity reduces these asymmetries, and the width of the PMFs is slightly increased. For $u_f/u_{f,N} = (0.92, 1.07, 1.32)$, the differences between the measured PMFs are very low. This variation is higher for $u_f/u_{f,N} = (1, 1.21, 1.44)$. It can be roughly observed that the measured mixing PMF in injector 1 is slightly narrower than that for a single injector under ideal inflow except for the extreme value at $u_f/u_{f,N} = 1.44$. However, the deviation from the ideal inflow behavior for this injector was very low. This behavior can be explained by the variations of the momentum flux density ratio in all injection holes (see fig. 5.1 and appendix A.5), which are not high enough to affect the mixture behavior significantly.

For injector 2, the asymmetries at $u_f/u_{f,N} = 0.74$ are higher (see fig. 5.7) with an increased variation range of the maximal frequency of occurrence ($0.04 < \varphi_{max} < 0.052$). This behavior remains similar at $u_f/u_{f,N} = 0.92$. For $1 \le u_f/u_{f,N} \le 1.44$, a more symmetrical distribution can be observed, and the with of the mixing PMF increases with the fuel velocity. In general, the results for injector 2 are more sensitive to the inflow condition. However, the PMF for all datasets is nearly symmetric and slightly narrower than under ideal inflow and for injector 1. This behavior might be unexpected regarding the asymmetries of the momentum flux density ratio shown in fig. 5.1, but it can be explained with the symmetry of the flow field to the MIB center line. The higher penetration depth of the jets in segments 1, 4, and 6 is compensated by a high radial velocity towards the middle axis of the injector, thus leading to the observed symmetric mixture behavior, which is reproducible for the whole investigated operational range.

For injector 3, the behavior at $u_f/u_{f,N} \le 1.07$ is similar to the observed for injectors 1 and 2. At $u_f/u_{f,N} = 1.21$, a significantly wider distribution for config. 5 can be observed. A further increase of the fuel velocity to $u_f/u_{f,N} = 1.32$ leads to negative skewness for config. 1, 3, and 5. For $u_f/u_{f,N} = 1.44$, the resulting PMF for config. 4 exhibits a weak negative skewness with a high φ_{max}. This behavior results from the asymmetric momentum flux density ratio shown in fig. 5.1, which is not compensated with a counteracting radial velocity component. These asymmetries lead to an uneven penetration depth of the jets around the middle axis of the injector and, consequently, to the asymmetric PMF at higher fuel velocities. This behavior is also reproducible for the whole investigated operational range.

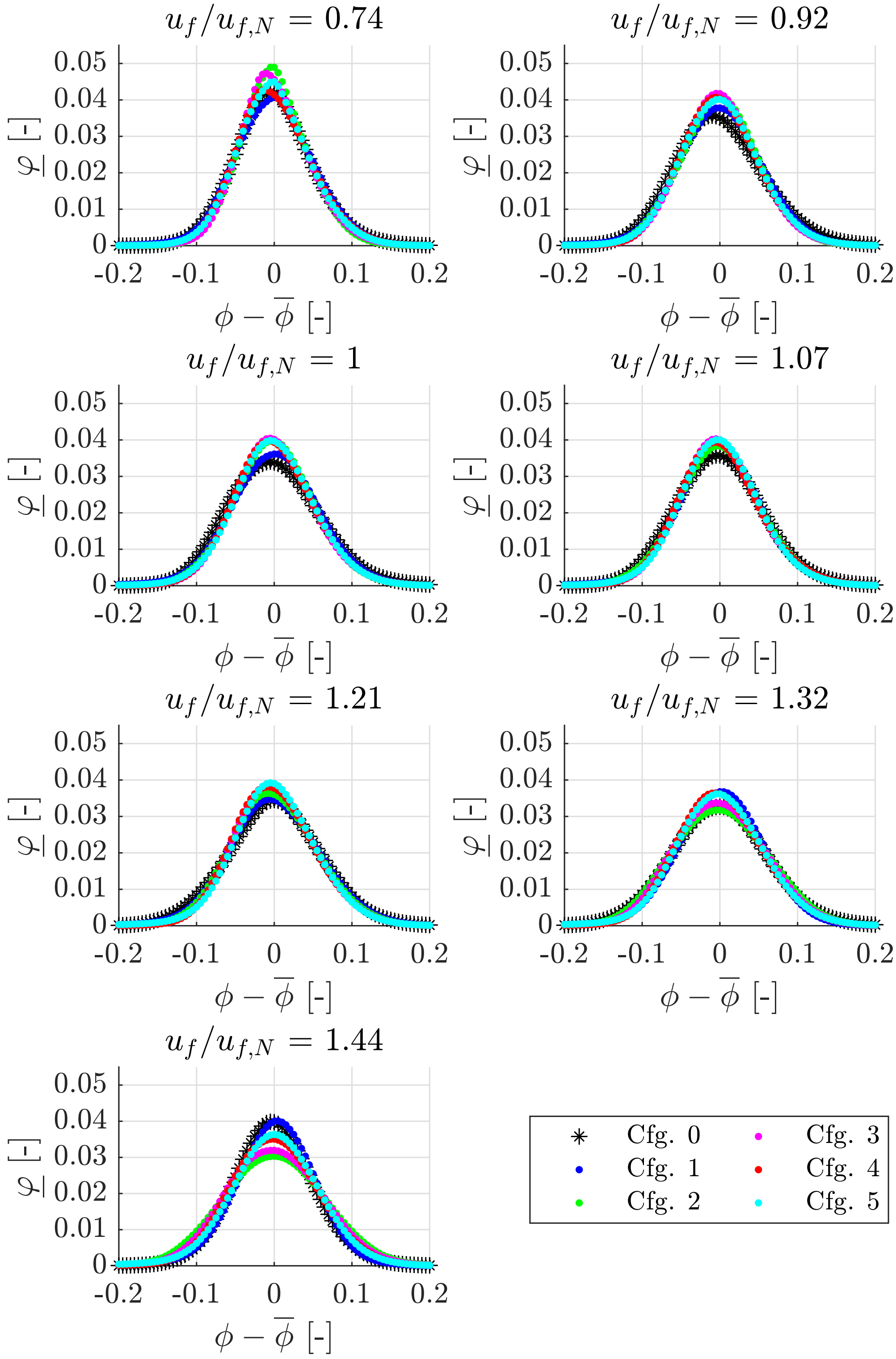

Figure 5.6: Mixing PMFs multi-injector burner (Injector 1).

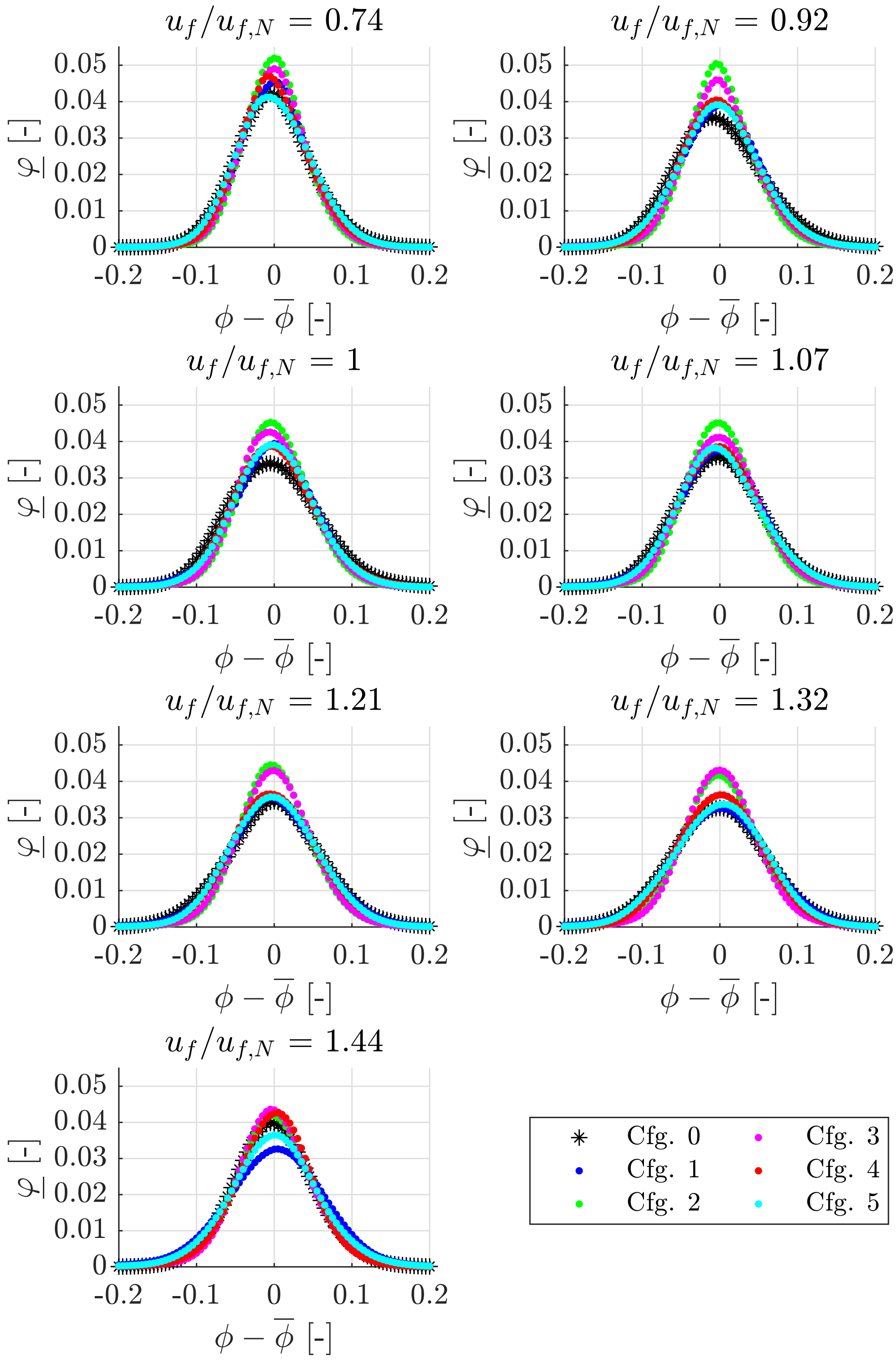

Figure 5.7: Mixing PMFs multi-injector burner (Injector 2).

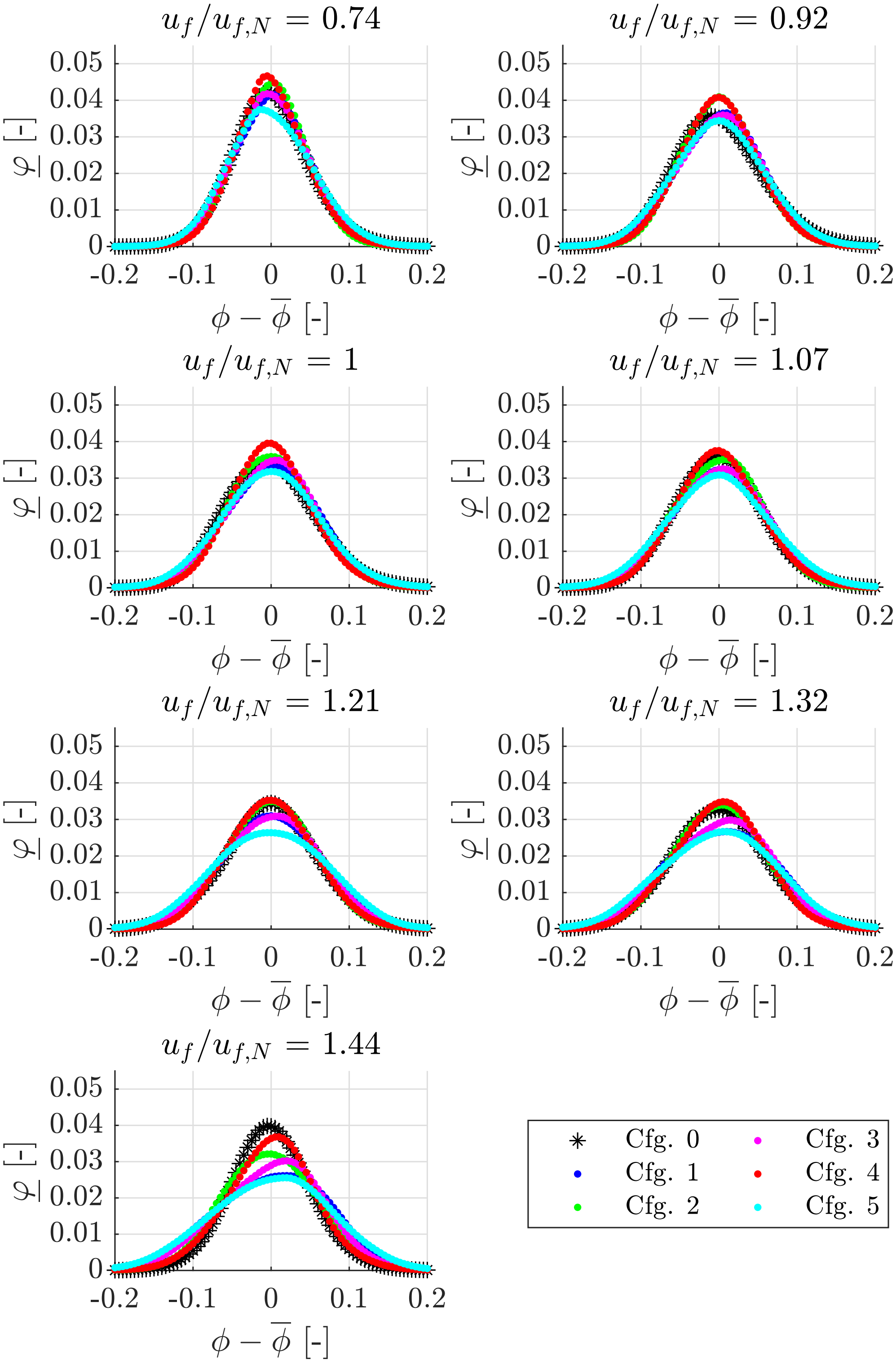

Figure 5.8: Mixing PMFs multi-injector burner (Injector 3).

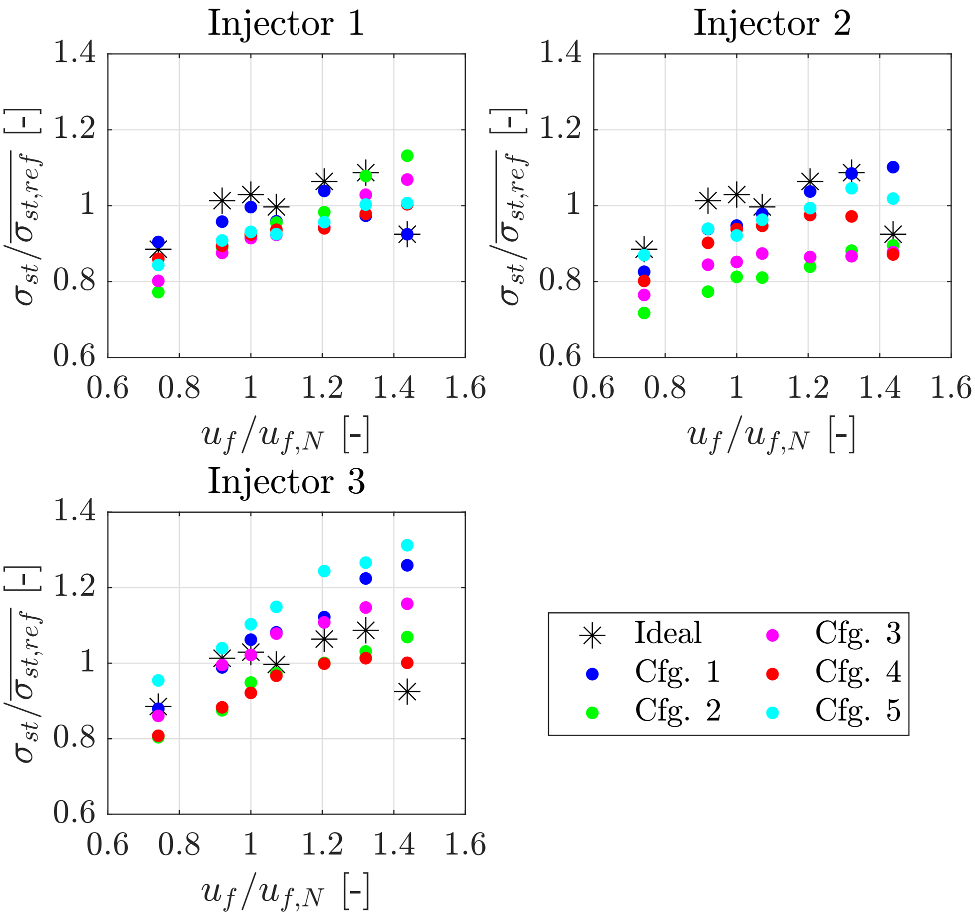

Figure 5.9: Spatio-temporal standard deviation at injector outlet as a function of the fuel inlet velocity in the multi-injector burner.

Fig. 5.9 shows the spatio-temporal standard deviation for all injector elements. The slightly narrower mixing PMFs for injector 1 at $u_f/u_{f,N} < 1.44$ are reflected in a σ_{st} reduction up to 10% from the corresponding value under ideal inflow. The wider PMFs for the extreme value $u_f/u_{f,N} = 1.44$ are seen as an increase of σ_{st} of up to 20%. Injector 2 exhibits similar behavior with a σ_{st} reduction up to 20% for config. 2 and 3. In contrast, the negative skewness in the mixing PMFs of injector 3 causes an increase of σ_{st} up to 40% for config. 5.

The lower σ_{st} in injectors 1 and 2 might seem counter-intuitive. However, it can be associated with the inflow conditions and the high turbulent kinetic energy originating from the flow separation in the deflection vane (see section 3.3.2). Fig. 5.10 shows the influence of the inflow conditions on the mixing field at the injector outlet, determined with RANS-CFD simulations. The mixing field under ideal inflow at $u_f/u_{f,N} = 1$ (left) has a fuel overshoot around the central axis of the injector and four regions with a lower concentration symmetrically distributed over the cross-sectional area of the injector. This symmetry results from the arrangement of the injection holes and the turbulence generators in the studied injector element. The mixing field for injector 2 in config. 1 at $u_f/u_{f,N} = 1$ (right) is symmetric to the MIB center line, similar to the flow field shown in fig. 4.9. Here the fuel from the center axis is convected to the upper and the lower cross-sectional area, leading to a spatial standard deviation σ_s[1] 8% smaller than that under ideal inflow. The further reduction of σ_{st} up to 20% in the experiments is caused by the high turbulent kinetic energy above the deflection vane, which is convected into the inlet sections of the injectors and, consequently, leads to enhanced mixing.

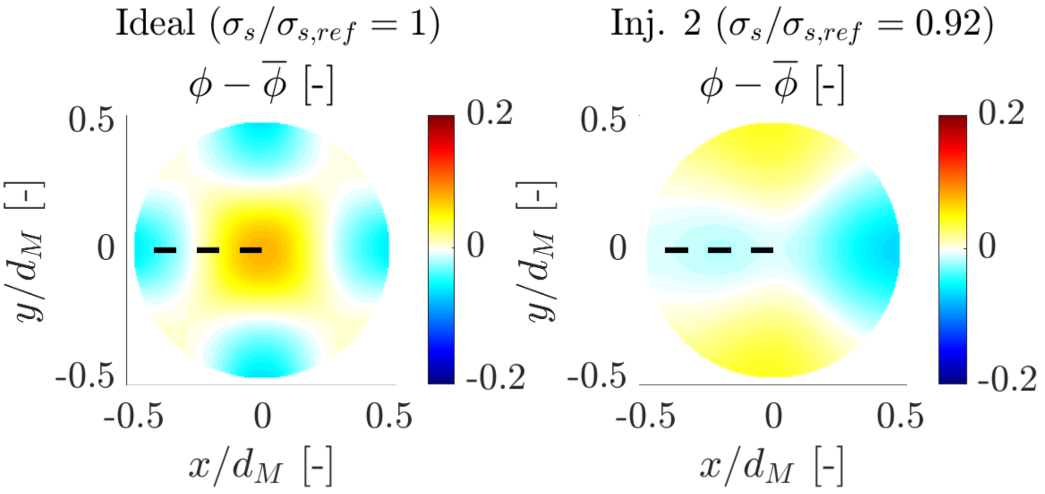

Figure 5.10: Time-average mixing field at injector outlet for config. 0 and for injector 2 in config. 1 from RANS-CFD simulations ($u_f/u_{f,N} = 1$).

Based on these results, the spatio-temporal standard deviation σ_{st} in the multi-injector burner under low velocity gradients is lower than that under ideal inflow. This unexpected behavior can be associated with a better fuel distribution over the cross-sectional area caused by the inflow conditions and

---

[1] The spatial standard deviation σ_s is calculated through post-processing of the CFD data at injector outlet as the surface average standard deviation of the equivalence ratio.

an increased turbulent kinetic energy at the injector inlet in the combustor originating from the flow separation in the deflection vane. In contrast, high inlet velocity and pressure gradients at the injector inlet increase the spatio-temporal standard deviation σ_{st} at high fuel inlet velocities. This effect is caused by the uneven penetration depth of the jets associated with the asymmetric momentum flux density ratio.

5.2.4 Mixing PMF for the Whole Combustion Chamber

The mixing PMF for the whole combustion chamber was calculated with eq. 2.55 by considering the datasets for each injector element presented in the last section. Fig. 5.12 shows the obtained mixing PMFs ($\overline{\varphi_{CC}}$) for the measured configurations in the multi-injector burner (config. 1-5) together with the results under ideal inflow at the same fuel inlet velocity (config. 0). For $0.74 < u_f/u_{f,N} < 1$, the mixing PMFs in the multi-injector burner are still narrower than that under ideal inflow due to the contribution of injector 1 and 2. For $1.07 < u_f/u_{f,N} < 1.32$, all mixing PMFs are very similar. For the extreme value $u_f/u_{f,N} = 1.44$, a slightly negative skewness for config. 3 and 5 can be observed, which results from the contribution of injector 3.

Fig. 5.12 shows the associated spatio-temporal standard deviation to the mixing PMFs for the complete outlet section of the combustor. The narrower distributions for $0.74 < u_f/u_{f,N} < 1$ are reflected in a lower standard deviation for the multi-injector burner in all configurations. For $1.07 < u_f/u_{f,N} < 1.32$, the obtained σ_{st} for the multi-injector burner is very close to the value for the single injector with a deviation of approx. ±7%. The remaining skewness in the mixing PMFs at the extreme value $u_f/u_{f,N} = 1.44$ is reflected in a higher standard deviation for the multi-injector burner in all configurations with a maximum increase of 30% from the value at ideal inflow conditions for config. 5.

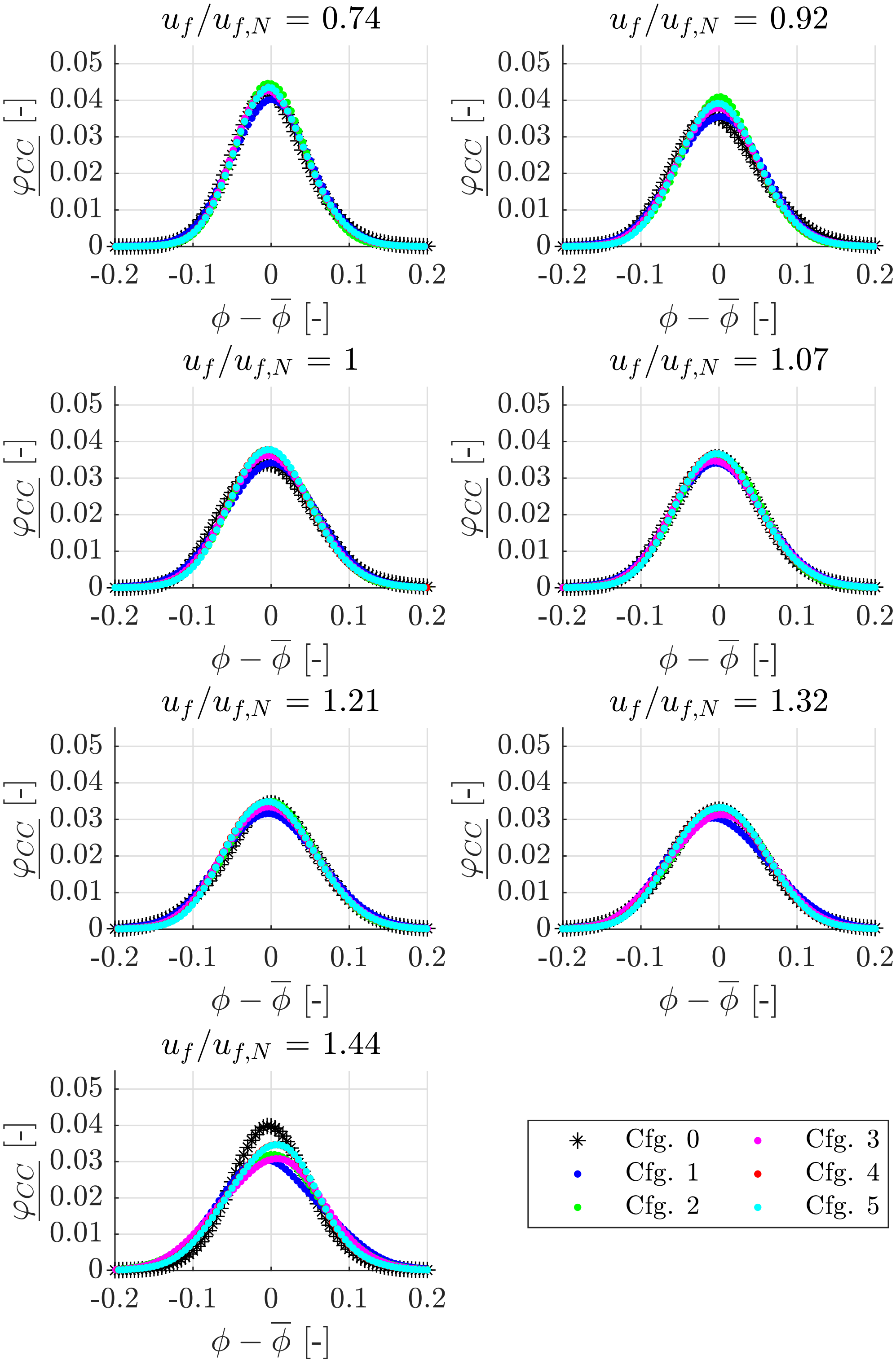

Figure 5.11: Integrated mixing PMFs in the complete outlet section of the combustor.

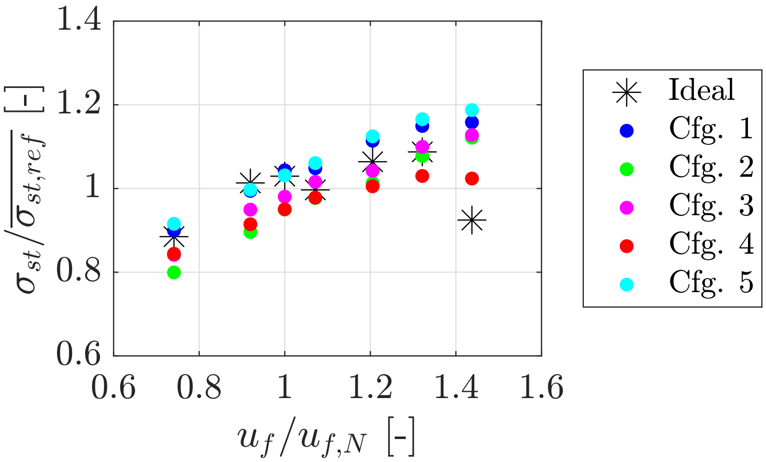

Figure 5.12: Spatio-temporal standard deviation in the complete outlet section of the combustor as a function of the fuel inlet velocity.

6 NO$_x$ Formation Analysis

The increase of NO_x formation caused by the remaining unmixedness in the multi-injector burner is assessed in the following based on the mixing PMF datasets presented in the last chapter. For this, ΔX_{NO_x} is calculated at $t_{res} = 5\ ms$, $t_{res} = 10\ ms$ and $t_{res} = 15\ ms$ with the procedure explained in section 2.5. The analysis is structured as follows: First, the increase of NO_x formation due to the remaining unmixedness under ideal inflow is evaluated. Then the deviations due to the inflow distortion in the burner head are determined.

6.1 Higher NO$_x$ Formation Under Ideal Inflow

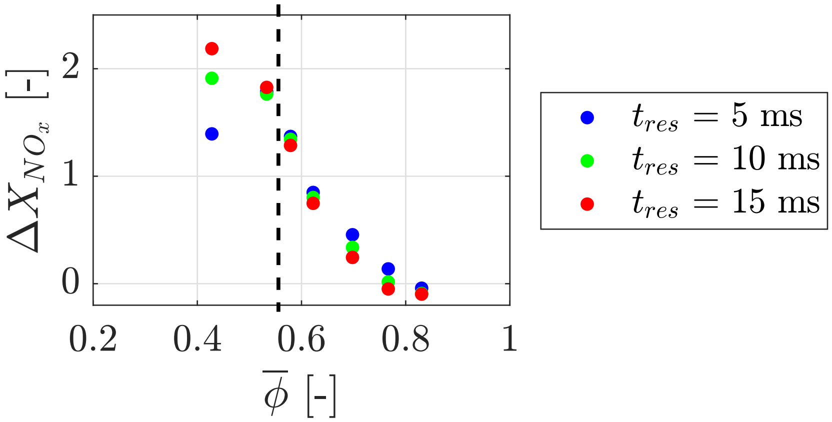

Figure 6.1: Higher NO_x formation at ideal inflow conditions.

Fig. 6.1 shows the increase of NO_x formation caused by the unmixedness under ideal inflow. The seven data points for each t_{res} correspond to the fuel velocity values shown in fig. 5.2. In general, ΔX_{NO_x} decreases at higher mean $\overline{\phi}$ due to the exponential increase of the reference value $X_{NO_x@\phi=\overline{\phi}}$ for the perfectly premixed case. At low mean equivalence ratios ($\overline{\phi} < 0.55$, see black dashed line), ΔX_{NO_x} scales with the residence time due to the larger $\frac{dX_{NO_x}}{d\phi}$ values and because the whole ϕ variation range covered by the mixing PMF falls below the inflection points denoted with the color dashed lines in fig. 2.7. This behavior is inverted at higher mean equivalence ratios ($\overline{\phi} > 0.55$) because the equivalence ratio with the highest $\frac{dX_{NO_x}}{d\phi}$ falls into the ϕ variation range covered by the PMFs and, consequently, the contribution of the range $\phi > \overline{\phi}$ to the NO_x formation decreases. At $\overline{\phi} = 0.76$ and $\overline{\phi} = 0.83$, this contribution drops so far that some ΔX_{NO_x} values become slightly negative. These values indicate that the NO_x formation is slightly lower than that for the perfectly premixed case at the highest $\overline{\phi}$ values.

6.2 Higher NO_x Formation in the Single Injector Elements of the Multi-Injector Burner

Fig. 6.2 shows the increase of NO_x formation in the single injector elements of the multi-injector burner. The results for $t_{res} = 5\ ms$, $t_{res} = 10\ ms$ and $t_{res} = 15\ ms$ are shown in the first, second, and third row of plots, respectively. The corresponding injector is given in the title (1 on the left, 2 in the middle, and 3 on the right). The increase of NO_x formation for injectors 1 and 2 is lower than that under ideal inflow for almost all operating points, which can be explained by the lower spatio-temporal standard deviation shown in fig. 5.9. Note that the increase of NO_x formation is very sensitive to the spatio-temporal standard deviation at low mean equivalence ratios. For example, the 20% lower σ_{st} at $u_f/u_{f,N} = 0.74$ ($\overline{\phi} = 0.4$) for injector 2 in config. 5 compared with the result under ideal inflow is reflected in a reduction of ΔX_{NO_x} of approx. 50%. The higher σ_{st} at the extreme value $u_f/u_{f,N} = 1.44$, which corresponds to the data points at $\overline{\phi} = 0.75$ for injector 1 and $\overline{\phi} = 0.79$ for injector 2, is not reflected in a significant increase of ΔX_{NO_x} due to the huge reference value $X_{NO_x@\phi=\overline{\phi}}$ for the perfectly premixed case (see fig. 2.7).

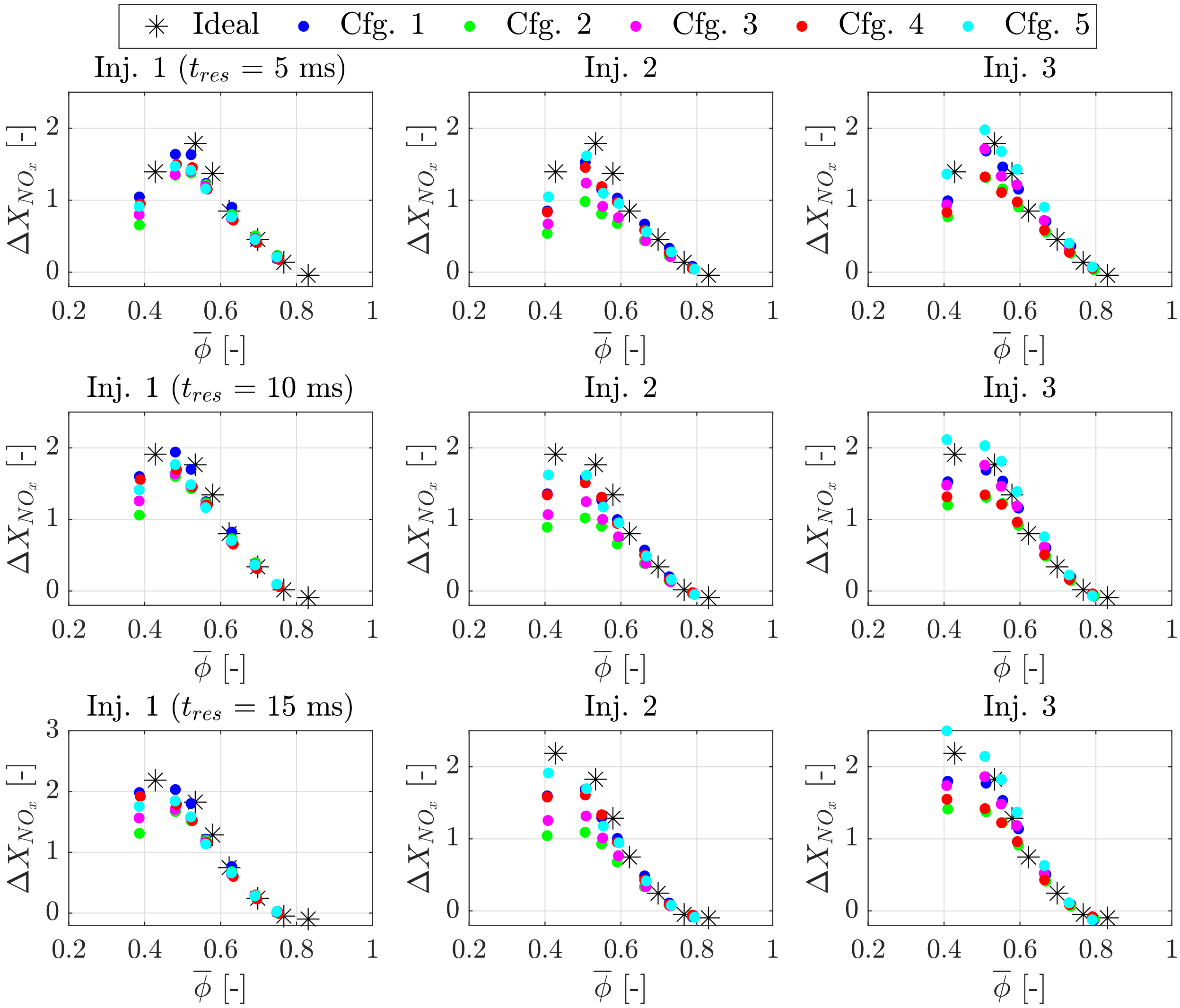

Figure 6.2: Higher NO_x formation in the single injector elements of the multi-injector burner.

The increase of NO_x formation for injector 3 at the lowest three $\overline{\phi}$ values is also smaller than that for a single injector under ideal inflow except for config. 5, which reflects the behavior of the spatio-temporal standard deviation shown in fig. 5.9. The higher σ_{st} in config. 1, 3, and 5 at increasing $\overline{\phi}$ leads to a further increase of NO_x formation, which can be seen in more detail in fig. 6.3 for the datasets at $\phi > 0.6$. The NO_x formation can be up to 30% higher than that for a single injector under ideal inflow for $\overline{\phi} = 0.66$ at $t_{res} = 5\ ms$. ΔX_{NO_x} becomes lower at increasing $\overline{\phi}$ due to the higher reference value $X_{NO_x@\phi=\overline{\phi}}$

for the perfectly premixed case and is close to zero for the mixing PMFs with the highest negative skewness at the extreme value $\overline{\phi} = 0.79$ ($u_f/u_{f,N} = 1.44$) similar to the results under ideal inflow.

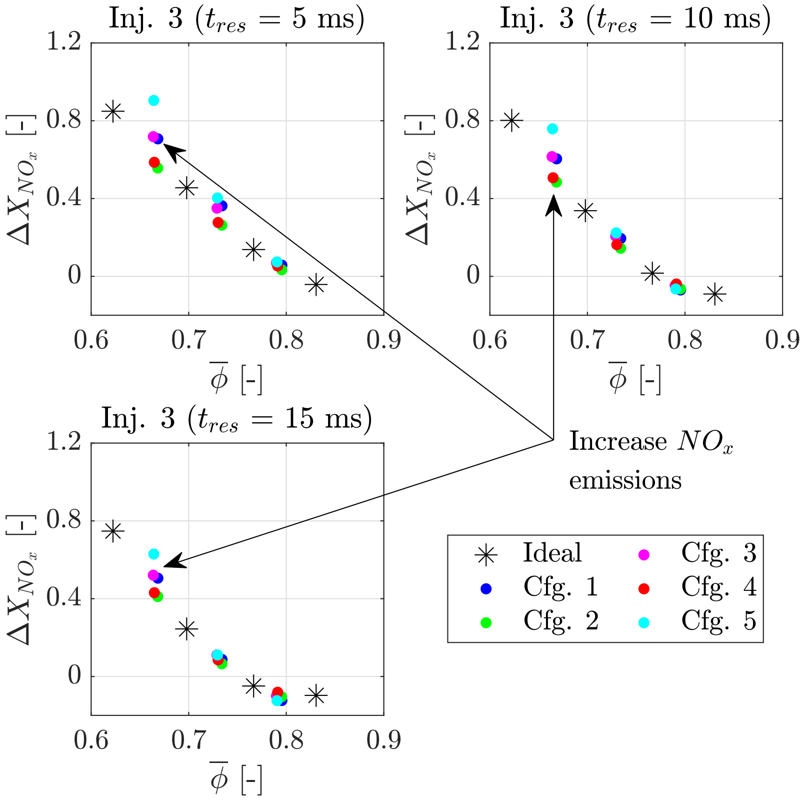

Figure 6.3: Higher NO_x formation in injector 3 due to the negative skewness in the mixing PMF.

6.3 Higher NO$_x$ Formation in the Whole Combustor

Fig. 6.4 shows the increase of NO_x formation for the whole combustion chamber obtained with the mixing PMFs shown in fig. 5.11. For the lowest three $\overline{\phi}$ values, a lower increase of NO_x formation for the multi-injector burner than for a single injector under ideal inflow for config. 2, 3, and 4 can be observed, which reflects the lower σ_{st} values for these configurations shown in fig. 5.12. For $\overline{\phi} = 0.58$, the deviations between the NO_x formation of the single injector and the multi-injector burner are fairly low due to the similarity of the

PMFs and the σ_{st} values shown in fig. 5.11 and 5.12.

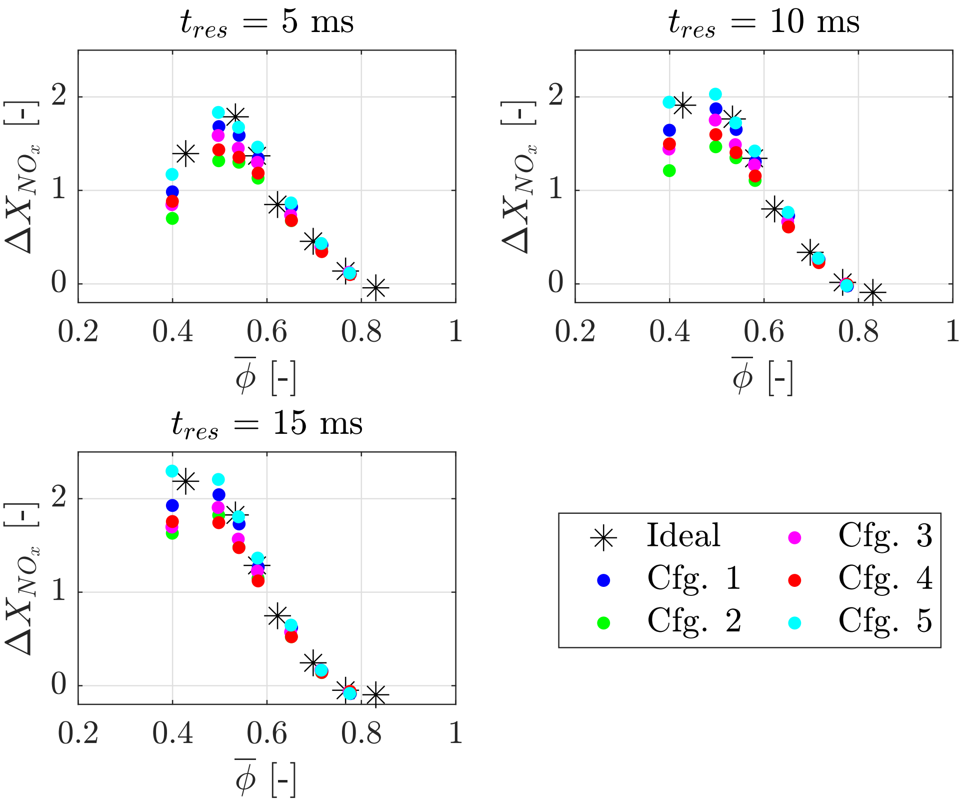

Figure 6.4: Higher NO_x formation in the whole combustor.

The contribution of injector 3 leads to an increased NO_x formation at $\overline{\phi} = 0.67$, as shown in fig. 6.5. Through the contribution of injectors 1 and 2 to the mixing PMFs for the whole combustion chamber, the maximum increase of NO_x formation in config. 5 is reduced from 30% to 20% compared to the results for injector 3 only. The remaining skewness of the mixing PMFs at $u_f/u_{f,N} = 1.44$ has no negative impact on the NO_x formation, as the obtained ΔX_{NO_x} values are also close to zero similar to the results under ideal inflow.

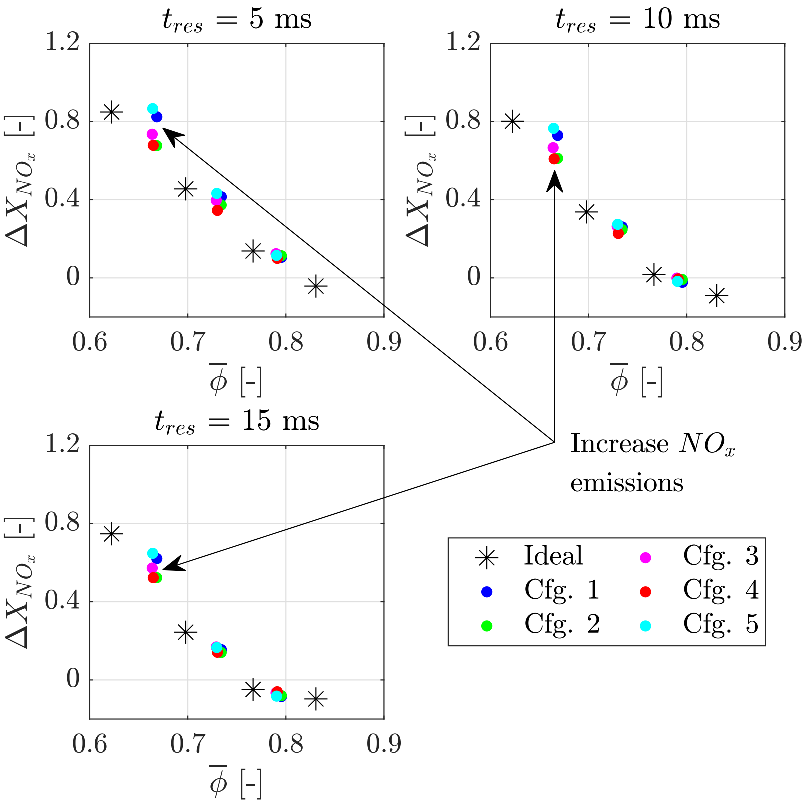

Figure 6.5: Higher NO_x formation in the whole combustor due to the negative skewness in the mixing PMF.

7 Application of the O-POD Model

The application of the O-POD model approach with the datasets shown in chapter 5 is presented in the following. The datasets for configurations 0, 1, 2, 4, and 5 are considered as input to calculate the eigenmodes. The remaining datasets for config. 3 are used as the reference to demonstrate the performance of the model approach by comparing the model output with the corresponding measured mixing PMF.

7.1 Calculation of the Eigenmodes

The eigenmodes are calculated with the procedure explained in section 2.4. The $\underline{\varphi}$ and $\underline{\varphi^{\star}}$ vectors for configuration 0, 1, 2, 4, and 5 are put together to generate the augmented input datasets ($\underline{\Phi} = [\underline{\varphi}, \underline{\varphi^{\star}}]$, see eq. 2.56). In total, $n = 91$ input datasets are obtained, which are used to calculate the auto-correlation tensor ($\underline{\underline{R}}$) with eq. 2.58 and the eigenmodes $\underline{\theta^{\Phi}}$ through the solution of the eigenvalue problem of eq. 2.59. Afterwards, the eigenmodes are decomposed into the two parts corresponding to the mixing PMF ($\underline{\theta}$) and the observable vectors ($\underline{\theta^{\star}}$) ($\underline{\theta^{\Phi}} = \left[\underline{\theta}, \underline{\theta^{\star}}\right]$, see eq. 2.62 and 2.63). In total, $N = 113$ eigenmodes are obtained, which corresponds to the dimension of the input $\underline{\Phi}$ vectors ($N_x = 81$ from $\underline{\varphi}$ and $N_y = 32$ from $\underline{\varphi^{\star}}$). A $RIC = 99,9\%$ results with $N_r = 17$ eigenmodes only.

Fig. 7.1 shows the corresponding part of the eigenmodes 1, 5, and 14 associated with the observable datasets ($\underline{\theta_1^{\star}}$, $\underline{\theta_5^{\star}}$, $\underline{\theta_{14}^{\star}}$) as representative results describing the mixing behavior of the studied injector element. Mode 1 reflects the ideal inflow conditions with a constant momentum flux density ratio, velocity, and static pressure for all segments, as shown in fig. 5.1. Mode 5 represents the velocity and static pressure variations caused by the inflow distortion. Mode 14 contains information related to the observed asymmetries of the momentum flux density ratio for injector 3.

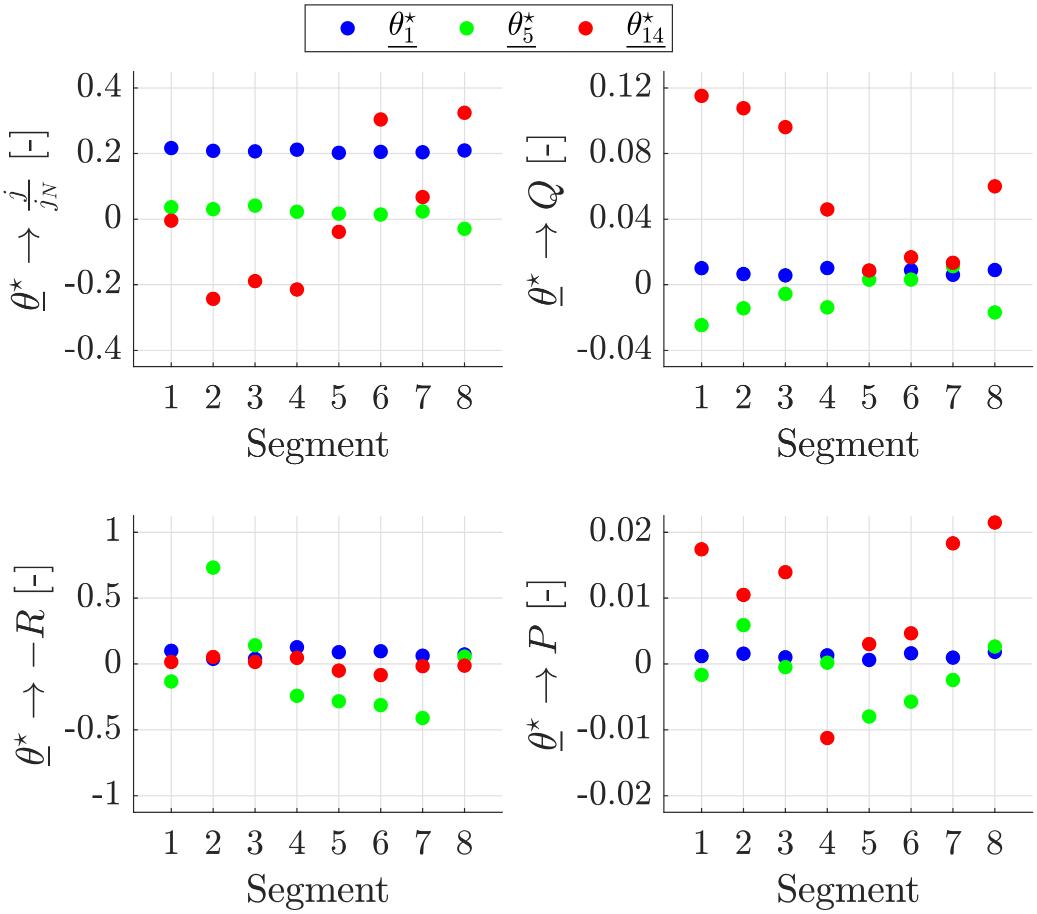

Figure 7.1: Part of the eigenmodes associated with the observable vectors ($\underline{\theta}_1^\star$, $\underline{\theta}_5^\star$, $\underline{\theta}_{14}^\star$).

Fig. 7.2 shows the corresponding part of the eigenmodes 1, 5, and 14 associated with the mixing PMF ($\underline{\theta}_1$, $\underline{\theta}_5$, $\underline{\theta}_{14}$). The eigenmode 1 represents the mixing behavior under ideal inflow shown in fig. 5.2 characterized by a symmetric mixing PMF close to a Gaussian. The eigenmode 5 reflects the results obtained for injector 1. Here the velocity and pressure gradients do not lead to significant deviations from the ideal inflow behavior. The eigenmode 14 describes the negative skewness of the mixing PMF of injector 3 caused by the asymmetries of the momentum flux density ratio.

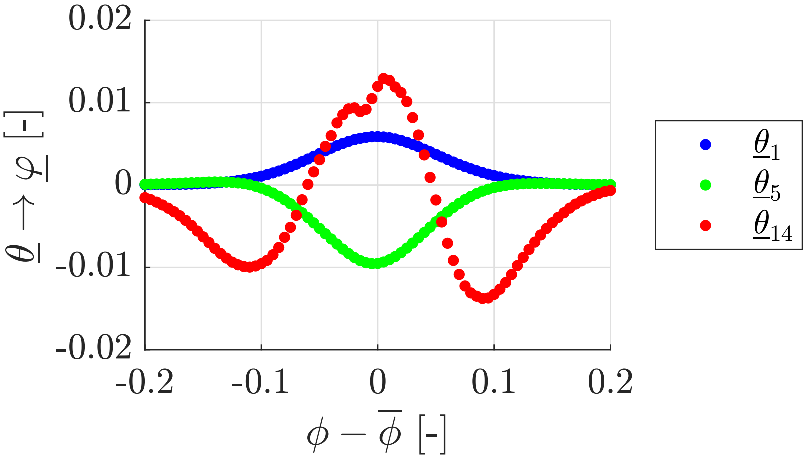

Figure 7.2: Part of the eigenmodes associated with the mixing PMFs ($\underline{\theta}_1$, $\underline{\theta}_5$, $\underline{\theta}_{14}$).

The remaining eigenmodes contain further information on the mixing behavior of the studied injector element, making it possible to predict the mixing PMF under arbitrary inflow conditions with the model, as shown in the following section. For completeness, all calculated eigenmodes are shown in appendix A.6.

7.2 Prediction of the Mixing PMF

The obtained eigenmodes are used to calculate the mixing PMF for the reference datasets in config. 3. The results are then compared with the measurement results. For this, the weighting coefficients (a_k) for all datasets are calculated by approximating the observable ($\underline{\varphi}^\star$) vectors as the sum of their parts of the eigenmodes ($\underline{\varphi}^\star \approx \sum_{k=1}^{N_r} a_k \underline{\theta}_k^\star$, see eq. 2.65) using the least-squares method. The approximation of $\underline{\varphi}^\star$ for injector 3 at $u_f/u_{f,N} = 1.44$ is shown in fig. 7.3 as a representative dataset with the most asymmetric momentum flux density ratio. The approximation is represented similarly to fig. 5.1 with the $\underline{\varphi}^\star$ vectors marked with red dots and the O-POD results with asterisks.

The momentum flux density ratio ($\frac{j}{j_N}$) and the ratio between the radial and total perpendicular velocity component ($-R$) are approximated accurately with the solution of the optimization problem for all segments. In contrast, a slight deviation of the ratio between the perpendicular and the main velocity component (Q) and the relative static pressure (P) remained for some segments. The order of magnitude of the variables can explain this deviation. However, the physical behavior is described qualitatively correctly with the approximation. $\underline{\varphi}^{\star}$ was similarly approximated for the remaining reference datasets.

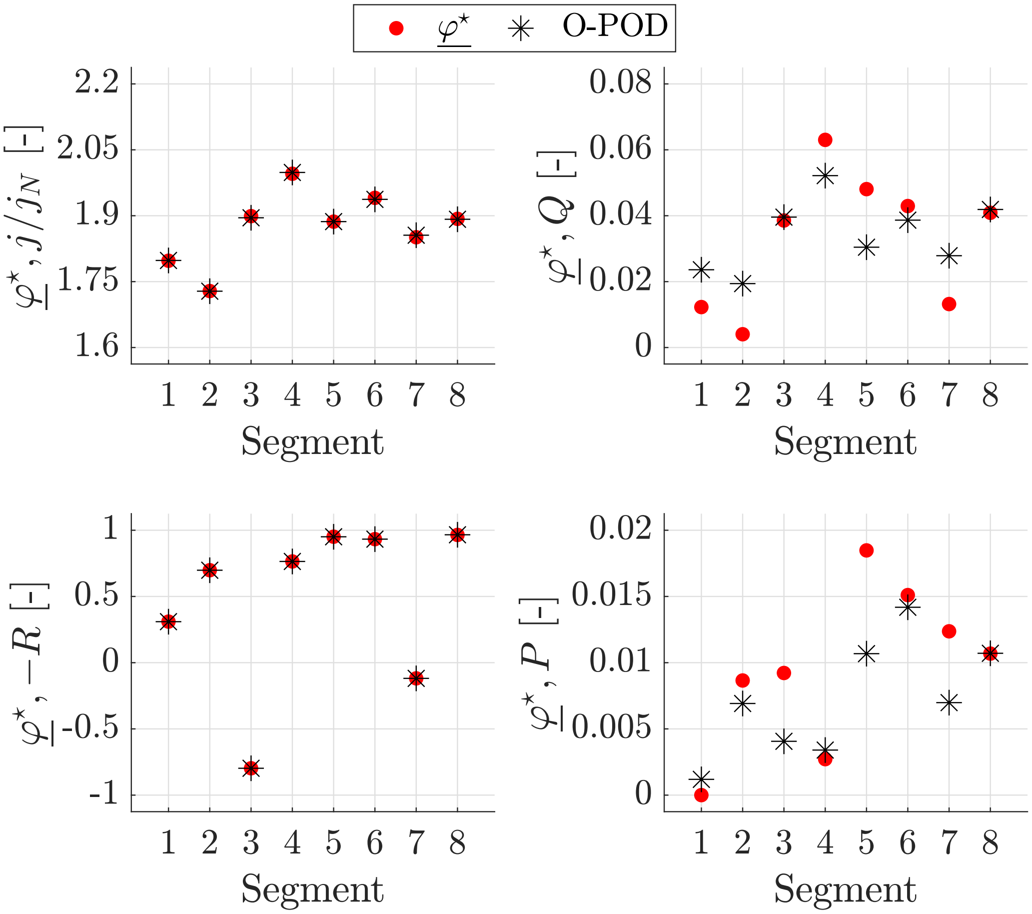

Figure 7.3: Calculation of weighting coefficients by approximating the input $\underline{\varphi}^{\star}$ vector as the modal sum of the eigenmodes $\underline{\theta}^{\star}$ (Inj. 3 - cfg. 3, $\overline{u_f}/u_{f,N} = 1.44$).

Finally, the obtained weighting coefficients for all reference datasets are used to calculate the mixing PMF with eq. 2.66 and to compare the model output with the corresponding measurement results. This comparison is shown in fig. 7.4. The plots in the first two rows correspond to the reference datasets for injector 1 at increasing fuel velocity, whose normalized value ($u_f/u_{f,N}$) is given in the title. The datasets for injectors 2 and 3 are illustrated similarly in the next rows. The experimental results are shown in each plot with red dots and the O-POD model output with black asterisks.

For injectors 1 and 2, the model output and the measured mixing PMF for all considered fuel velocities agree very well with each other, except for the dataset for injector 2 at $u_f/u_{f,N} = 1.44$, for which a small deviation of the maximal frequency of occurrence φ_{max} can be seen. It is also the case for injector 3 between $0.92 \leq u_f/u_{f,N} \leq 1.32$. These deviations may be associated with the imperfect approximation of the $\underline{\varphi^\star}$ vector shown in fig. 7.3.

However, the occurrence of a negative skewness of the PMFs of injector 3 at increasing fuel velocity is represented adequately, as can be observed for the dataset at $u_f/u_{f,N} = 1.44$. This finding primarily supports the applicability of the presented model approach to calculate the mixing PMF under arbitrary inflow conditions, as the generated model can accurately predict the fundamental mixing behavior of the injector element and the deviations due to inflow distortions in the burner head.

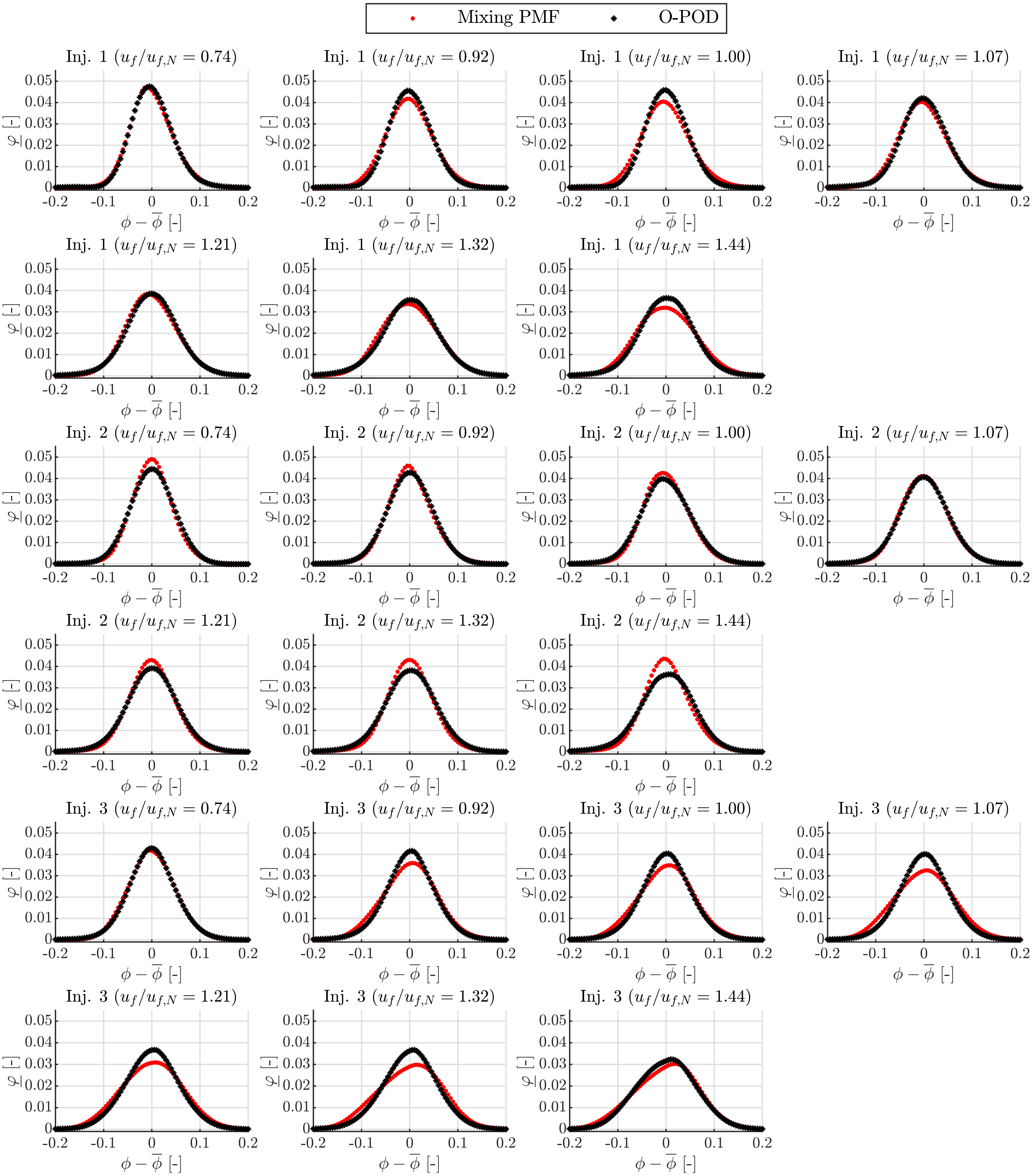

Figure 7.4: Comparison measurement with O-POD model output for all reference datasets.

8 Summary and Outlook

8.1 Summary

The mixing behavior of a generic multi-injector burner system with jet-in-crossflow fuel injection was investigated experimentally in this work. The mixing quality was quantified with the Probability Mass Function of the equivalence ratio at the injector outlet, the mixing PMF. The experimental data were obtained from two different setups: the single injector under ideal inflow and the multi-injector burner model close to an engine configuration. With this approach, the influence of the inflow distortion in the head section on the mixing quality could be determined by directly comparing the obtained data. The experiments were conducted in a water channel test rig. The increase of NO_x formation associated with the remaining unmixedness at the injector outlet compared with the perfectly premixed case was also assessed based on the obtained data.

The mixing PMF of a single injector under ideal inflow was symmetric and close to a Gaussian for the whole parameter range of interest. It remained nearly invariant to the fuel inlet velocity due to the use of turbulence generators, which makes the mixing behavior less dependent on the jet momentum. The enhancement of scalar mixing with increasing Reynolds number was also confirmed with these investigations.

The percentage increase of NO_x formation under ideal inflow drops with the mean equivalence ratio due to the exponentially increasing reference NO_x mole fraction for the perfectly premixed case. At low mean equivalence ratios ($\overline{\phi} < 0.55$), the NO_x formation increase scales with the residence time due to the larger $\frac{dX_{NOx}}{d\phi}$ values over the whole ϕ variation range covered by the mixing PMFs. At higher mean equivalence ratios ($\overline{\phi} > 0.55$), this behavior is inverted as the equivalence ratio with the highest $\frac{dX_{NOx}}{d\phi}$ falls into the ϕ variation range covered by the mixing PMFs and, consequently, the contribution of the range $\phi > \overline{\phi}$ to the NO_x formation decreases.

The mixing PMF in the multi-injector burner under low inlet velocity and pressure gradients was also symmetric and close to a Gaussian, but the spatial-temporal unmixedness was slightly lower than that under ideal inflow. This unexpected behavior resulted from a better fuel distribution over the injector cross-sectional area associated with the inlet boundary conditions and an increase of turbulent kinetic energy caused by the flow separation in the flow reversal section. The enhanced mixing was reflected in a lower NO_x formation increase compared with the results under ideal inflow.

In contrast, high inlet velocity and pressure gradients led to a negative skewness in the mixing PMF at high fuel inlet velocities. This effect was caused by the uneven penetration depth of the jets associated with the asymmetric momentum flux density ratio. However, the associated decrease of mixing quality was not reflected in a significant percentage increase of NO_x formation, as the mean equivalence ratios and, consequently, the reference NO_x mole fraction for the perfectly premixed case were extremely high.

The mixing PMF of the single injector elements was modeled as a function of the inflow conditions with the output-based Proper Orthogonal Decomposition approach (O-POD). The model input was the so-called observable vector, generated with the surface-average velocity and pressure values upstream of each injection hole calculated from RANS-CFD simulations of the flow path in the combustor. The model accurately reproduced the symmetric mixing PMFs close to a Gaussian under ideal inflow and low inlet velocity gradients, as well as the negative skewness associated with an asymmetric penetration depth of the jets.

The added value of the presented O-POD model approach is that the observable vectors can be determined very fast with a RANS-CFD simulation. This result can then be used as input to estimate the mixing PMF, which is otherwise only accessible through a complex LIF experiment or using Large Eddy Simulations (LES) with a high computational cost. Hence, the

O-POD model approach can be used to optimize the flow path upstream of the injectors to obtain minimal NO_x emissions through a fast estimation of changes in the mixing PMF, which can result due to alterations of the inflow conditions in the burner head or design changes of the flow reversal section.

The essential features for the success of the experiments were the development of the rectifier arrangement and the flow rate measurement system, which were indispensable for obtaining the presented results. On the one hand, the total pressure must be evenly distributed to obtain a symmetric momentum distribution, which cannot be accomplished with perforated plates due to the occurrence of spots with higher total pressure. On the other hand, the thermal drift of the CTA measurement system occurring due to the high electrical power input necessary for measurements in a turbulent water flow must be minimized to obtain the desired performance for the experiments.

8.2 Outlook

Many mixing PMF datasets were acquired for the studied multi-injector burner. With these data, an LES simulation to calculate the mixing PMFs could be validated and used to understand the mixing process over the whole length of the injectors. Furthermore, the influence of all velocity components perpendicular to the main flow direction and the static pressure gradients on the mixing behavior could be determined through corresponding test cases. The dependency of the mixing PMF on the turbulent kinetic energy at the injector inlet could also be quantified with the validated LES simulation. With this information, a new formulation of the observable vectors based on the obtained data can be derived, and the performance of the O-POD model could be further improved.

In this context, obtaining further experimental data on the flow behavior in the inlet region of the injectors could also become a relevant part of future research work. This data could also be used for validation purposes and to better understand the influence of the inflow distortion on the resulting mixing behavior. The execution of such measurement campaigns was initially planned for this work. However, technical difficulties due to the limited optical accessibility to the inlet region of the injectors led to the decision to restrict the scope of the PIV measurement campaigns to the development of the flow conditioning unit based on the data presented in chapter 3.3.2.

The possible changes in the mixing PMF due to a rotation of the injectors with a fixed inlet velocity field could also be investigated in future works. A preliminary study with RANS-CFD showed that it is possible to optimize the fuel distribution by finding an angular position in which the uneven penetration depth of the jets is suppressed with counteracting perpendicular velocity components and pressure gradients. A similar study could be conducted experimentally with the available infrastructure, and the obtained data could be used to expand the applicability of the presented model approach.

Bibliography

[1] Marquez Macias, F., Hirsch, C., Sattelmayer, T., Huth, M. and Meisl, J., 2022, "Investigating the Mixture Quality in Multi-Injector Burner Systems, Part I: Experimental Setup," Proceedings of the ASME Turbo Expo 2022: Power for Land, Sea, and Air. Volume 3B: Combustion, Fuels, and Emissions. GT2022-82157. `https://doi.org/10.1115/GT2022-82157`

[2] Marquez Macias, F., Hirsch, C., Sattelmayer, T., Huth, M. and Meisl, J., 2022, "Investigating the Mixture Quality in Multi-Injector Burner Systems—Part I: Experimental Setup," *Journal of Engineering for Gas Turbines and Power,* ***144***(12), pp. 121008. `https://doi.org/10.1115/1.4055491`

[3] Marquez Macias, F., Hirsch, C., Sattelmayer, T., Huth, M. and Meisl, J., 2023, "Investigating the Mixture Quality in Multi-Injector Burner Systems, Part II: Model Application," Proceedings of the ASME Turbo Expo 2023: Power for Land, Sea, and Air. Volume 3A: Combustion, Fuels, and Emissions. GT2023-101439. `https://doi.org/10.1115/GT2023-101439`

[4] Marquez Macias, F., Hirsch, C., Sattelmayer, T., Huth, M. and Meisl, J., 2022, "Investigating the Mixture Quality in Multi-Injector Burner Systems, Part II: Model Application," *Journal of Engineering for Gas Turbines and Power.* `https://doi.org/10.1115/1.4063589`.

[5] Marquez Macias, F., Hirsch, C., Sattelmayer, T., Huth, M. and Meisl, J., 2023, "Untersuchung der Mischungsstatistik in

Multi-Injektor-Brennern," 31. Deutscher Flammentag für Nachhaltige Verbrennung. Paper No. 101.

[6] Dederichs, S., Prade, B., Habisreuther, P., Zarzalis, N., Beck, C. and Krebs, W., 2013, "Assessment of a Gas Turbine NO_x Reduction Potential Based on a Spatio-temporal Unmixedness Parameter," Proceedings of the ASME Turbo Expo 2013: Power for Land, Sea, and Air. Volume 1A: Combustion, Fuels and Emissions. GT2013-94404.

[7] Matt, B., Woringer, T. and Zouzoulas, G., 1984, Ring Combustion Chamber with Ring Burner for Gas Turbines, US Patent 4, pp. 455-840.

[8] Tacina, R. T., Wey, C., Laing, P. and Mansour, A., 2002, "Sector Tests of a low NO_x, Lean-Direct-Injection, Multipoint Integrated Module Combustor Concept," Proceedings of the ASME Turbo Expo 2002: Power for Land, Sea, and Air. Volume 1: Turbo Expo 2002. GT2002-30089.

[9] Lückerath, R., Meier, W. and Aigner, M., 2008, "FLOX® Combustion at High Pressure With Different Fuel Compositions," *Journal of Engineering for Gas Turbines and Power,* ***130***(1), pp. 011505.

[10] Schütz, H., Lammel, O., Schmitz, G., Rödiger, T. and Aigner, M., 2012, "EZEE®: A High Power Density Modulating FLOX® Combustor," Proceedings of the ASME Turbo Expo 2012: Power for Land, Sea, and Air. Volume 2: Combustion, Fuels and Emissions, Parts A and B. GT2012-68997.

[11] Rödiger, T., Lammel, O., Aigner, M., Beck, C. and Krebs, W., 2013, "Part-Load Operation of a Piloted FLOX® Combustion System," *Journal of Engineering for Gas Turbines and Power,* ***135***(3), pp. 031503.

[12] Gruschka, U., Janus, B., Meisl, J., Huth, M. and Wasif, S., 2008, "ULN System for the New SGT5-8000H Gas Turbine: Design and High Pressure Rig Test Results," Proceedings of the ASME Turbo Expo 2008: Power for Land, Sea, and Air. Volume 3: Combustion, Fuels and Emissions, Parts A and B. GT2008-51208.

[13] Sangl, J., 2011, "Erhöhung der Brennstoffflexibilität von Vormischbrennern durch Beeinflussung der Wirbeldynamik,"

Dissertation, Technische Universität München. `https://www.epc.ed.tum.de/fileadmin/w00cgc/td/Forschung/Dissertationen/sangl11.pdf`.

[14] Utschick, M., 2016, "Sicherheitskriterien für die Vorgemischte Verbrennung Wasserstoffhaltiger Brennstoffe in Gasturbinen," Dissertation. Technische Universität München. `https://www.epc.ed.tum.de/fileadmin/w00cgc/td/Forschung/Dissertationen/utschick16.pdf`.

[15] Löw, E.-M., 2016, "Analyse von Verbrennungsvorgängen im Selbstzündungsdominierten Regime Mittels Mischungsstatistik," Dissertation. Technische Universität München. `https://www.epc.ed.tum.de/fileadmin/w00cgc/td/Forschung/Dissertationen/Loew16.pdf`.

[16] Tennekes, H. and Lumley, J., 1972, *A First Course in Turbulence,* The MIT Press Cambridge, Massachusetts, and London, England.

[17] Jischa, M., 1982, *Konvektiver Impuls-, Wärme- und Stoffaustausch,* Springer Fachmedien Wiesbaden GmbH.

[18] Alfonsi, G., 2009, "Reynolds-Averaged Navier-Stokes Equations for Turbulence Modeling," *Journal of Applied Mechanics Reviews, **62***(4), pp. 040802.

[19] Pope, S., 2000, *Turbulent Flows,* Cambridge University Press.

[20] Weber, R., Visser, B. M. and Boysan, F., 1990, "Assessment of Turbulence Modeling for Engineering Prediction of Swirling Vortices in the Near Burner Zone," *International Journal of Heat and Fluid Flow, **11***(3), pp. 225-235.

[21] Patel, V. C. and Sotiropoulos, F., 1997, "Longitudinal Curvature Effects in Turbulent Boundary Layers," *Progress in Aerospace Sciences, **33***(1), pp. 1-70.

[22] Melling, A. and Whitelaw, J. H., 1976, "Turbulent Flow in a Rectangular Duct," *Journal of Fluid Mechanics, **78***(2), pp. 289-315.

[23] Bui, A., 2008, "Simplified Turbulence Models for Confined Swirling Flows," *Engineering Applications of Computational Fluid Mechanics,* ***2***(4), pp. 404-410.

[24] Arolla, S. and Durbin, P., 2014, "A Rotation/Curvature Correction for Turbulence Models for Applied CFD," *Progress in Computational Fluid Dynamics,* ***14***(6), pp. 341-351.

[25] Cokijat, D. P., 1993, "Turbulence Models for Non-Circular Ducts and Channels," Ph.D. Dissertation, California Institute of Technology. `https://openaccess.city.ac.uk/id/eprint/8019/`

[26] Menter, F. R., 1994, "Two-Equation Eddy-Viscosity Turbulence Models for Engineering Applicacions," *AIAA Journal,* ***32***(8), pp. 1598-1605.

[27] Menter, F. and Esch, T., 2001, "Elements of Industrial Heat Transfer Prediction," *Proceedings of COBEM 2001, Invited Lectures,* ***20***, pp. 117-127.

[28] Menter, F., Kuntz, M. and Langtry, R., 2003, "Ten Years of Industrial Experience with the SST Turbulence Model," *Turbulence, Heat and Mass Transfer,* ***4***, pp. 625-632.

[29] Tavoularis, S. and Corrsin, S., 1981, "Experiments in Nearly Homogeneous Turbulent Shear Flow with an Uniform Mean Temperature Gradient. Part 1," *Journal of Fluid Mechanics,* ***104***, pp. 311-347.

[30] Tavoularis, S. and Corrsin, S., 1981, "Experiments in Nearly Homogeneous Turbulent Shear Flow with an Uniform Mean Temperature Gradient. Part 2: The Fine Structure," *Journal of Fluid Mechanics,* ***104***, pp. 349-367.

[31] Arunajatesan, S. and Bruner, C., 2012, "Evaluation of Two-Equations RANS Models for Simulation of Jet-in-Crossflow Problems," 50th AIAA Aerospace Sciences Meeting including the New Horizons Forum and Aerospace Exposition, SAND2011-3448C.

[32] Hassel, E., Jahnke, S., Kornev, N., Tkatchenko, I. and Zhdanov, V., 2006, "Large-Eddy Simulation and Laser Diagnostic Measurements of Mixing in a Coaxial Jet Mixer," *Chemical Engineering Science,* ***61***(9), pp. 2908-2912.

[33] Wiltschko, F., Qu, W. and Xiong, J., 2021, "Validation of RANS Models and Large Eddy Simulation for Predicting Crossflow Induced by Mixing Vanes in Rod Bundle," *Nuclear Engineering and Technology,* ***53***(11), pp. 3625-3634.

[34] Geurts, B. and Holm, D., 2002, *Alpha-Modeling Strategy for LES of Turbulent Mixing,* Springer Netherlands.

[35] Wegner, B., Huai, Y. and Sadiki, A., 2004, "Comparative Study of Turbulent Mixing in Jet in Crossflow Configurations Using LES," *4th International Symposium on Turbulence Heat and Mass Transfer,* ***25***(5), pp. 767-775.

[36] Baldyga, J. and Bourne, J., 1999, *Turbulent Mixing and Chemical Reactions,* John Wiley & Sons.

[37] Leuckel, W., Schmittel, P. and Weber, R., 2002, "Ähnlichkeitsbasierte Skalierung Turbulenter Gasflammen," *Fachbericht aus Gaswärme International,* ***51***(9), pp. 400-403.

[38] Sangl, J., Mayer, C. and Sattelmayer, T., 2014, "Prediction of the NO$_x$ Emissions of a Swirl Burner in Partially and Fully Premixed Mode on the Basis of Water Channel Laser Induced Fluorescence and Particle Image Velocimetry Measurements," *Journal of Engineering for Gas Turbines and Power,* ***136***(6), pp. 061503.

[39] Utschick, M., Eiringhaus, D., Köhler, C. and Sattelmayer, T., 2016, "Predicting Flashback Limits of a Gas Turbine Model Combustor Based on Velocity and Fuel Concentration for H2-Air-Mixtures," *Journal of Engineering for Gas Turbines and Power,* ***139***(4), pp. 041502.

[40] Margason, R. J., 1993, "Fifty Years of Jet in Cross Flow Research," *AGARD-CP,* ***534***, Paper 1.

[41] Besnard, A., Shoji, T., Schein, S., Harris, E. and Karagozian, A., 2019, "Exploration of Asymmetric Forcing on Mixing and Structural Characteristics for Transverse Jets," AIAA Scitech 2019 Forum. AIAA 2019-0321.

[42] Callaghan, E. and Ruggeri, R., 1948, "Investigation of the Penetration of an Air Jet Directed Perpendicularly to an Air Stream," National Advisory Committee for Aeronautics. Tech. Rep. TN 1615.

[43] Pratte, B. and Baines, D., 1967, "Profiles of the Round Turbulent Jet in a Cross Flow," *Journal of Hydraulic Engineering,* ***96***(6), pp. 53-64.

[44] Kamotani, Y. and Greber, I., 1972, "Experiments on a Turbulent Jet in a Cross Flow," *AIAA Journal,* ***10***(11), pp. 1425-1429.

[45] Fearn, R. and Weston, R., 1974, "Vorticity Associated with a Jet in a Cross Flow," *AIAA Journal,* ***12***(12), pp. 1666-1671.

[46] Cortelezzi, L. and Karagozian, A., 2001, "On the Formation of the Counter-Rotating Vortex Pair in Transverse Jets," *Journal of Fluid Mechanics,* ***446***, pp. 347-373.

[47] Krothapalli, A., Lourenco, L. and Buchlin, J. M., 1990, "Separated Flow Upstream of a Jet in a Crossflow," *AIAA Journal,* ***28***(3), pp. 414-420.

[48] Kelso, R. and Smits, A., 1995, "Horseshoe Vortex Systems Resulting From the Interaction Between a Laminar Boundary Layer and a Transverse Jet," *Physics of Fluids,* ***7***(1), pp. 153-158.

[49] Fric, T. and Roshko, A., 1994, "Vortical Structure in the Wake of a Transverse Jet," *Journal of Fluid Mechanics,* ***279***, pp. 1-47.

[50] Kuzo, D., 1996, "An Experimental Study of the Turbulent Transverse Jet," Ph.D. Dissertation. Technische Universiteit Eindhoven, Eindhoven, Holland. `https://thesis.library.caltech.edu/715/`.

[51] Abramovich G. N., 1963, *The Theory of Turbulent Jets,* MIT Press, Cambridge, Massachusetts, U.S.

[52] Broadwell, J. and Breidenthal, R., I., 1984, "Structure and Mixing of a Transverse Jet in Incompressible Flows," *Journal of Fluid Mechanics, **148***, pp. 405-412.

[53] Hasselbrink, E. F. and Mungal, M. G., 2001, "Transverse Jets and Jet Flames. Part 1. Scaling Laws For Strong Transverse Jets," *Journal of Fluid Mechanics, **443***, pp. 1-25.

[54] Smith, S. H. and Mungal, M. G., 1998, "Mixing, Structure and Scaling of the Jet in Crossflow," *Journal of Fluid Mechanics, **357***, pp. 83-122.

[55] Sirovich, L., 1987, Turbulence and the Dynamics of Coherent Structures, *Quarterly of Applied Mathematics, **45***(3), pp. 561-571.

[56] Astrid, P., 2004, "Reduction of Process Simulation Models: A Proper Orthogonal Decomposition Approach," Ph.D. Dissertation. Technische Universiteit Eindhoven, `https://pure.tue.nl/ws/portalfiles/portal/1936139/200413220.pdf`

[57] Astrid, P., Weiland, S., Willcox, K. and Backx, T., 2008, "Missing Point Estimation in Models Described by Proper Orthogonal Decomposition," *IEEE Transactions on Automatic Control, **53***(10), pp. 2237-2251.

[58] Christ, P., and Sattelmayer, T., 2018, "Reduced Order Modelling of Flow and Mixing in an Automobile HVAC System Using Proper Orthogonal Decomposition," *Journal of Applied Thermal Engineering, **133***, pp. 212-223.

[59] Christ, P. and Sattelmayer, T., 2018, "Thermal Modeling of an Automotive HVAC Unit Using a Coupled POD and Flow Resistance Network Approach," World Congress Experience 2018. SAE International. Detroit, USA.

[60] Christ, P., 2019, "Modeling of Automotive HVAC Units Using Proper Orthogonal Decomposition," Ph.D. Dissertation. Technische Universität München, `https://mediatum.ub.tum.de/doc/1464400/document.pdf`

[61] Coleman, T. F. and Yuying, L., 1996, "An Interior Trust Region Approach for Nonlinear Minimization Subject to Bounds," *SIAM Journal on Optimization,* ***6***(2), pp. 418-445.

[62] Coleman, T. F. and Yuying, L., 1992, "On the Convergence of Reflective Newton Methods for Large-Scale Nonlinear Minimization Subject to Bounds," *Mathematical Programming,* ***67****,* pp. 189–224.

[63] Marquardt, D. W., 1963, "An Algorithm for Least-Squares Estimation of Nonlinear Parameters," *Journal of the Society for Industrial and Applied Mathematics,* ***11***(2), pp. 431-441.

[64] Freedman, D. and Diaconis, P., 1981, "On the Histogram as a Density Estimator: L2 Theory," *Probability Theory and Related Fields,* ***57****,* pp. 453-476.

[65] Richards, G. and Weiland, N. and Strakey, P., 2007, *Combustion Strategies for Syngas and High-Hydrogen Fuel,* Gas Turbine Handbook.

[66] Joos, F., 2006, *Technische Verbrennung: Verbrennungstechnik, Verbrennungsmodellierung, Emissionen,* Springer Berlin Heidelberg.

[67] Wolfrum, J., 1972, *Bildung von Stickstoffoxiden bei der Verbrennung,* Chemie-Ingenieur-Technik.

[68] Bozelli, J. W. and Dean, A. M., 1995, "O + NNH: A Possible New Route for NO_x Formation in Flames," *International Journal of Chemical Kinetics,* ***27****,* pp. 1097-1109.

[69] Lechner, C. and Seume, J., 2010, *Stationäre Gasturbinen,* Springer Link.

[70] Fenimore, C. P., 1971, "Formation of Nitric Oxide in Premixed Hydrocarbon Flames," *Symposium International on Combustion,* ***13***(1), pp. 373-380.

[71] Kuo, K., 2006, *Principles of Combustion,* Springer Link.

[72] Miller, J. A. and Bowman, C. T., 1989, "Mechanism and Modeling of Nitrogen Chemistry in Combustion," *Progress in Energy and Combustion Science,* ***15***(4), pp. 287-338.

[73] Sangl, J., Mayer, C. and Sattelmayer, T., 2013, "Prediction of the NO_x-Emissions of a Swirl Burner in Partially and Fully Premixed Mode on the Basis of Water Channel LIF and PIV Measurements," Proceedings of the ASME Turbo Expo 2022: Power for Land, Sea, and Air. Volume 1B: Combustion, Fuels and Emissions. GT2013-95796.

[74] "One-Dimensional Reacting Flows," `https://cantera.org/documentation/dev/sphinx/html/cython/onedim.html#freeflame`. Accessed: 2023-01-05.

[75] "GRI-Mech 3.0," `http://combustion.berkeley.edu/gri-mech/version30/text30.html`. Accessed: 19-12-2022.

[76] Brückner-Kalb, J. R., 2008, "Sub-ppm-NO_x-Verbrennungsverfahren für Gasturbinen," Dissertation, Technische Universität München. `https://www.epc.ed.tum.de/fileadmin/w00cgc/td/Forschung/Dissertationen/brueckner_kalb08.pdf`.

[77] Adrian, R. J. and Westerweel, J., 2011, *Particle Image Velocimetry,* Cambridge Univ. Press.

[78] Raffel, M., Willert, C. E., Scarano, F., Kähler, C. J., Wereley, S. T. and Kompenhans, J., 2018, *Particle Image Velocimetry: A Practical Guide,* Springer International Publishing.

[79] Rapp, C., 2008, "Experimentelle Studie der Turbulenten Strömung über Periodische Hügel," Dissertation, Technische Universität München. `https://mediatum.ub.tum.de/doc/677970/document.pdf`.

[80] Thielicke, W., 2020, "PIVlab - Particle Image Velocimetry (PIV) Tool with GUI," `https://www.mathworks.com/matlabcentral/fileexchange/27659-pivlab-particle-image-velocimetry-piv-tool-with-gui`. Accessed: 2021-04-20.

[81] Sciacchitano, A., 2019, "Uncertainty Quantification in Particle Image Velocimetry," *Measurement Science and Technology,* ***30***(9), pp. 092001.

[82] "FASTCAM SA5: Hardware Manual," Photron Limited, 2009.

[83] Walker, D. A., 1986, "A Fluorescence Technique for Measurement of Concentration in Mixing Liquids," *Journal of Physics E: Scientific Instruments, **20***, pp. 217.

[84] "Product-Manual for DaVis 8.1 (LIF in Liquid Fluids)," LaVision GmbH, 2012.

[85] "Product Information Basacid ® Yellow 226," BASF CORPORATION, 2000.

[86] Pernpeintner, M., Lauer, M., Hirsch, C. and Sattelmayer, T., 2011, "A Method to Obtain Planar Mixture Fraction Statistics in Turbulent Flows Seeded with Tracer Particles," Proceedings of the ASME Turbo Expo 2012: Power for Land, Sea, and Air. Volume 2: Combustion, Fuels and Emissions, Parts A and B. GT2011-46844.

[87] Reisch, M., 2005, *Halbleiter-Bauelemente,* Springer.

[88] Hoffmann, K., 1974, *Applying the Wheatstone Bridge Circuit,* HBM Germany.

[89] Lomas, C. G., 1986, *Fundamentals of Hot Wire Anemometry,* Cambridge University Press.

[90] Tietze, U. and Schenk, C., 2008, *Electronic Circuits,* Springer.

[91] Palma, J. and Labbe, R., 2007, "Rugged Constant Temperature Thermal Anemometer," *Review of Scientific Instruments, **87***, pp. 217.

[92] The OpenFOAM Foundation, 2003, *OpenFOAM User Guide,* OpenFOAM Foundation Ltd, `https://openfoam.org/`.

[93] Juretic, F., 2015, *cfMesh v1.1, User Guide,* Creative Fields, Ltd.

[94] Polifke, W., Bruno, D., Bomberg, S., Cardenas, A., Carneiro, J., Collonval, F., Dems, P., Ettner, F., Holzinger, T., Seidel, V. and Weinzierl, J., 2019, *Hand Out of the Praktikum: Simulation of Thermo-Fluids with Open Source Tools,* Professur für Thermofluiddynamik.

[95] "OpenFOAM V6 User Guide (Numerical Schemes," `https://doc.cfd.direct/openfoam/user-guide-v6/fvschemes`. Accessed: 2022-11-07.

[96] "Mesh Quality," `https://www.openfoam.com/documentation/guides/latest/doc/guide-meshing-snappyhexmesh-meshquality.html`. Accessed: 2022-11-07.

A Appendix

A.1 Supervised Student Theses

During the execution of this research work, several student theses were realized at the Chair of Thermodynamics of the TUM School of Engineering and Design under the supervision of the author. Part of these works may be incorporated in the present dissertation and are not explicitly cited. The author would like to express his great appreciation and gratefulness to all these students for supporting the progress of this thesis with their works at the chair, which are listed in the following table.

Während der Bearbeitung dieser Dissertation sind mehrere Abschlussarbeiten am Lehrstuhl für Thermodynamik der TUM School of Engineering and Design unter der Anleitung des Autors dieser Arbeit entstanden. Teile dieser studentischen Arbeiten sind in diese Dissertation eingeflossen und sind nicht explizit zitiert. Der Autor drückt hiermit seine ganz ehrliche Anerkennung für die Unterstützung während ihrer Tätigkeit am Lehrstuhl aus und bedankt sich bei den jeweiligen Studenten für ihren Beitrag zum Fortschritt dieser Dissertation.

Student	**Thesis type**	**Title**	**Submission date**
Niklas Jakob Hain	Bachelor thesis	Implementation of the CTA Method for Flow Investigation in a Water Channel Test Bench	03.11.2020
Miguel Domingo	Semester thesis	Flow and Mixture Modeling for a Multi-Injector Burner Model for Water Channel Investigation Using CFD and the POD Method	11.11.2020
Kevin Schulz	Bachelor thesis	Modeling of the Flow Distribution in a Multi-Injector Burner by menas of a Flow Resistance Network	25.11.2020
Johannes Resch	Bachelor thesis	Charakterisierung der Brennstoffeindüsungsstrategie eines neuartigen Multi-Injektor-Brenners	13.04.2021
Georg Mederl	Semester thesis	Strömungsuntersuchungen in einem Multi-Injektor-Brenner mittels PIV	05.07.2021
Felix Pfündl	Bachelor thesis	Bestimmung der Massenstromverteilung in einem Multi-Injektor-Brenner mittels CTA	31.01.2022
Laurenz Schimper	Bachelor thesis	Optimierung einer Simulationsmethode zur Mischqualitätberechnung in Multi-Injektor-Brennern mittels RANS-CFD	28.04.2022

Table A.1: Supervised student theses by the author.

A.2 NO$_x$ Formation for $0.2 < \phi < 0.4$

The simulation results for the adiabatic flame temperature, the NO_x mole fraction, and the increase of the NO_x mole fraction with the equivalence ratio for $0.2 < \phi < 0.4$ are shown in fig. A.1 with the plots at the top, in the middle, and at the bottom, respectively.

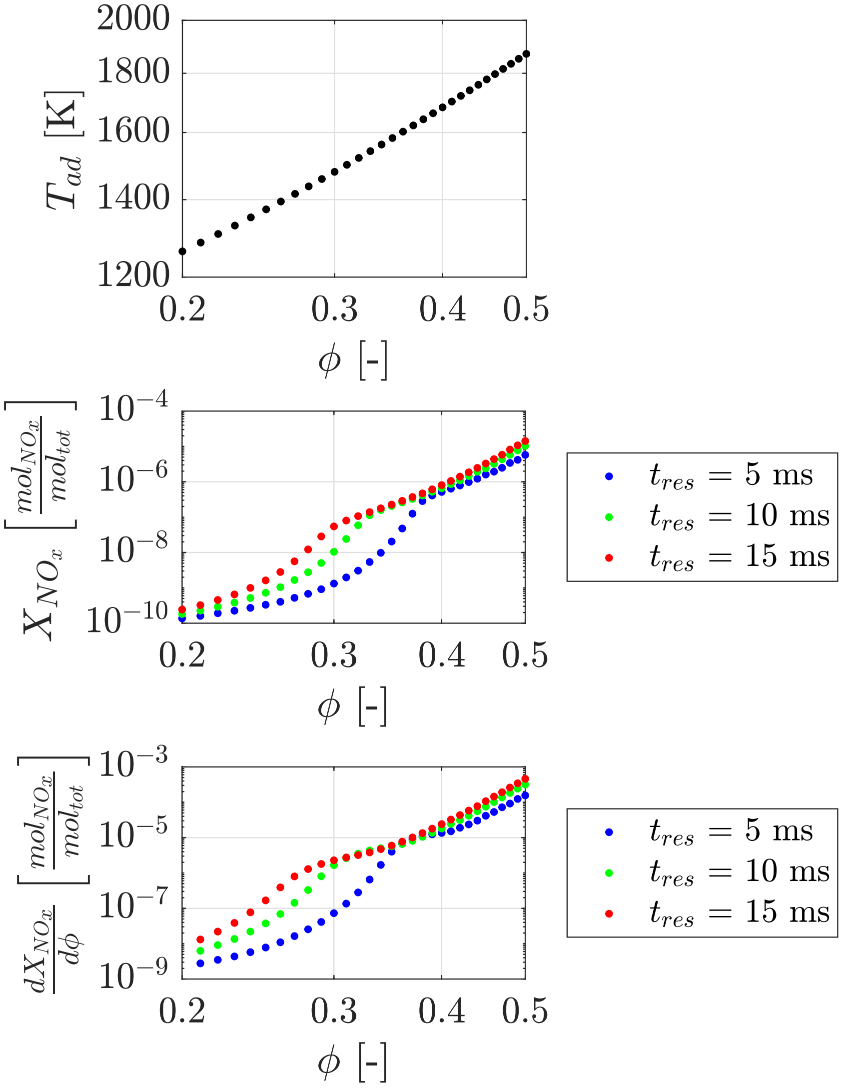

Figure A.1: T_{ad}, X_{NO_x} and $\frac{dX_{NO_x}}{d\phi}$ as functions of the equivalence ratio and the residence time for a freely-propagating one-dimensional flame in logarithmic scale for $0.2 < \phi < 0.4$.

The adiabatic flame temperature increases exponentially with the equivalence ratio similar to the results of fig. 2.7. In contrast, the behavior of X_{NO_x} between $0.2 < \phi < 0.4$ differs from the exponential increase. This behavior can be explained with the detailed simulation results for the limiting case at $\phi = 0.4$ as well as a further case at $\phi = 0.3$, in which X_{NO_x} is far from the exponential behavior for $t_{res} = 5$ ms and $t_{res} = 10$ ms (i.e. from the linear increase in the logarithmic scale). These results are shown in fig. A.2. At $\phi = 0.3$ (see upper plots), the chemical time scale is relatively low, and the first limiting value of $t_{res} = 5$ ms is reached almost immediately after the beginning of the reaction zone. At $\phi = 0.4$ (see lower plots), the reaction becomes faster, and the post-flame zone is reached at $t_{res} < 5$ ms. According to these results, X_{NO_x} increases exponentially with the equivalence ratio as long as the post-flame zone is reached after the given residence time.

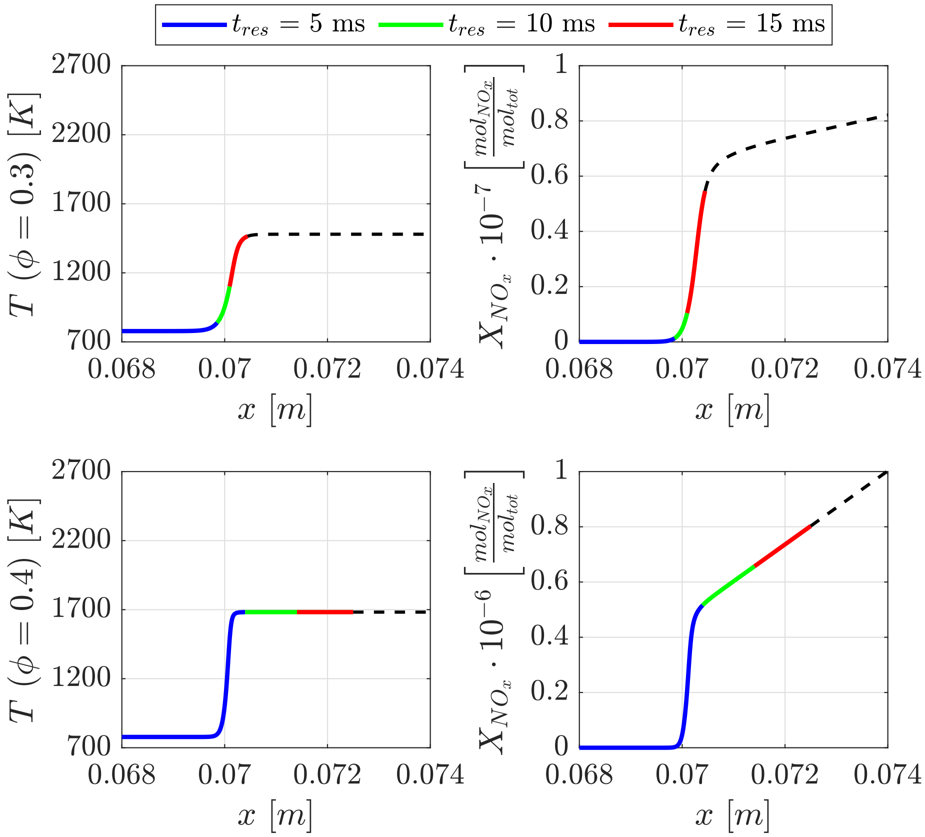

Figure A.2: Flame temperature and NO_x mole fraction in the reaction zone of a freely-propagating one-dimensional flame for $\phi = 0.3$ (top row plots) and $\phi = 0.4$ (bottom row plots).

A.3 CFD Simulation with Rectifier 1

This appendix explains the CFD simulation of the flow path through the multi-injector burner model with rectifier 1. The used fluid domain is shown in fig. A.3. The inlet tubes, the tangential re-direction in the base plate, and the holes of rectifier 1 were resolved with the simulation, as shown in fig. A.3(a). The outlet boundary is placed at the end of the mixing tubes, neglecting the flow path in the combustion chamber to reduce the computational cost. Furthermore, the injector lances and the central pilot pipe are left out, similar to the setup of fig. A.3(b).

The rectifier plate has 948 holes with a diameter of $d_H = 2\ mm$, symmetrically distributed in $N_U = 158$ rows around the circumference and $N_R = 6$ in the radial direction, as shown in fig. A.3(c). The inlet velocity is configured for an inlet volume flow of $20\frac{m^3}{h}$ and the modeling approach was the same as explained in chapter 4. The simulation aimed not to reproduce the occurrence of the tornado-like structure. However, it should instead serve as an explanation for this unexpected behavior during the design phase of the experiment.

The main velocity (u_z) and static pressure upstream of the holes (p) are calculated as surface averaged values through post-processing of the simulation results. For this, the minimum value for the static pressure is taken as a reference level similar to the calculation of P in the observable vectors (see eq. 2.43). The volume flow $\dot{V}$ is calculated through integration over the whole sectional area of the holes, and the total pressure (p_{tot}) is calculated as the sum of the static and dynamic pressure:

$$p_{tot} = p + \frac{\rho u_z^2}{2} \tag{A.1}$$

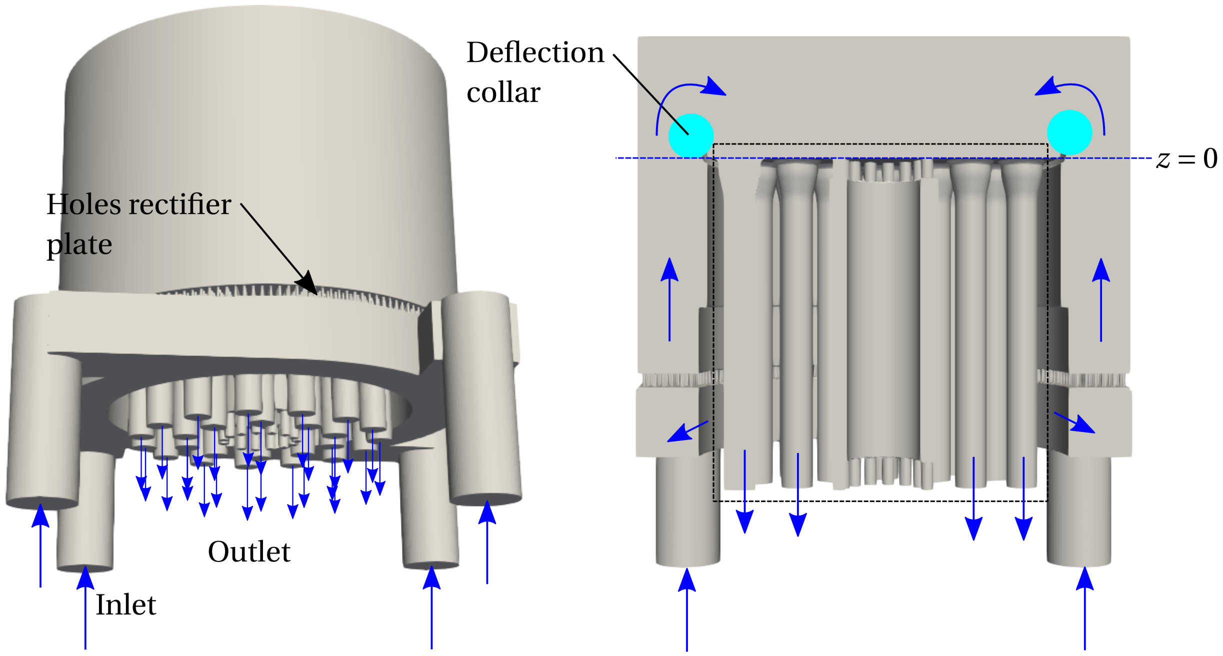

(a) Fluid domain

(b) Sectional view flow path

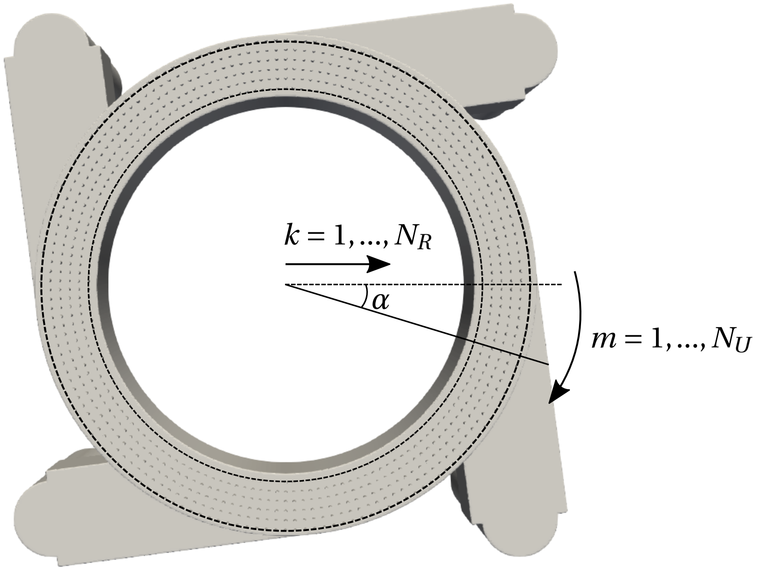

(c) Sectional view rectifier plate

Figure A.3: Fluid domain simulation rectifier 1.

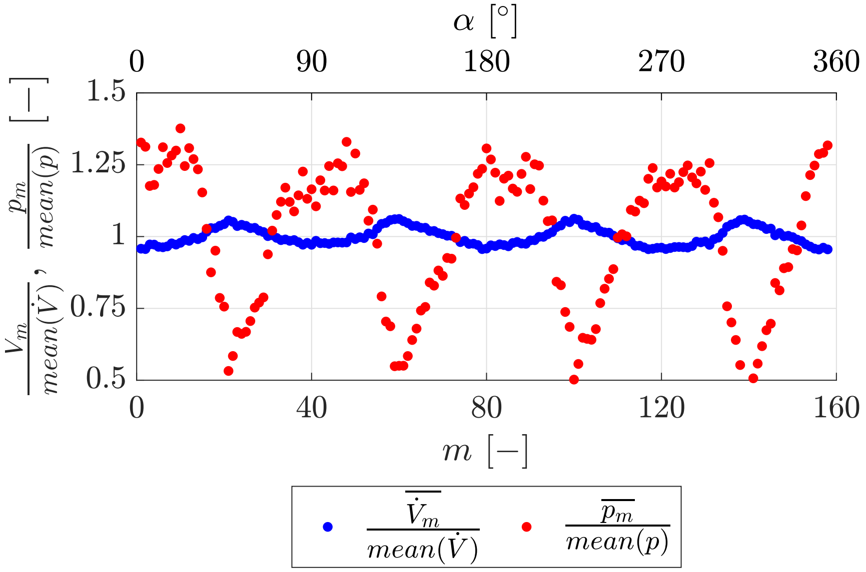

Figure A.4: Volume flow and pressure distribution over the angular position.

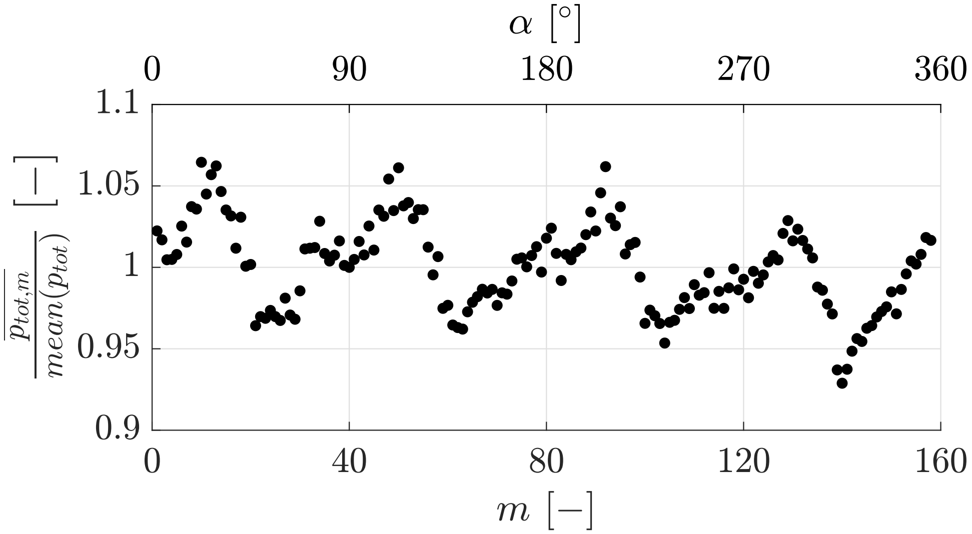

Figure A.5: Total pressure distribution over the angular position.

Fig. A.4 shows the mean value of the volume flow ($\overline{\dot{V}_m}$) and the static pressure ($\overline{p_m}$) of the holes located in each angular position divided by the corresponding mean values for all holes of the rectifier plate ($mean(\dot{V})$, $mean(p)$). In general, the volume flow distribution was nearly constant over the whole annular gap. The maximum value is located at $\alpha = 45°$ and is repeated every 90° according to the symmetry of the inlet tubes. In contrast, the static pressure remains nearly constant between $\alpha \approx 0 - 22.5^\circ$ and then decays to its minimum value at $\alpha \approx 45^\circ$, which also occurs every 90°. This behavior leads to the asymmetric total pressure distribution over the angular position shown in fig. A.5. The minimum static pressure is compensated with the slightly increased dynamic pressure at $\alpha = 45^\circ$ so that the total pressure varies only around 5% from the mean value with a periodically repeated behavior every 90°. These 4 spots with higher total pressure create unstable jet plumes around the circumference, thus acting as the driving mechanism for the formation of the observed tornado-like structures.

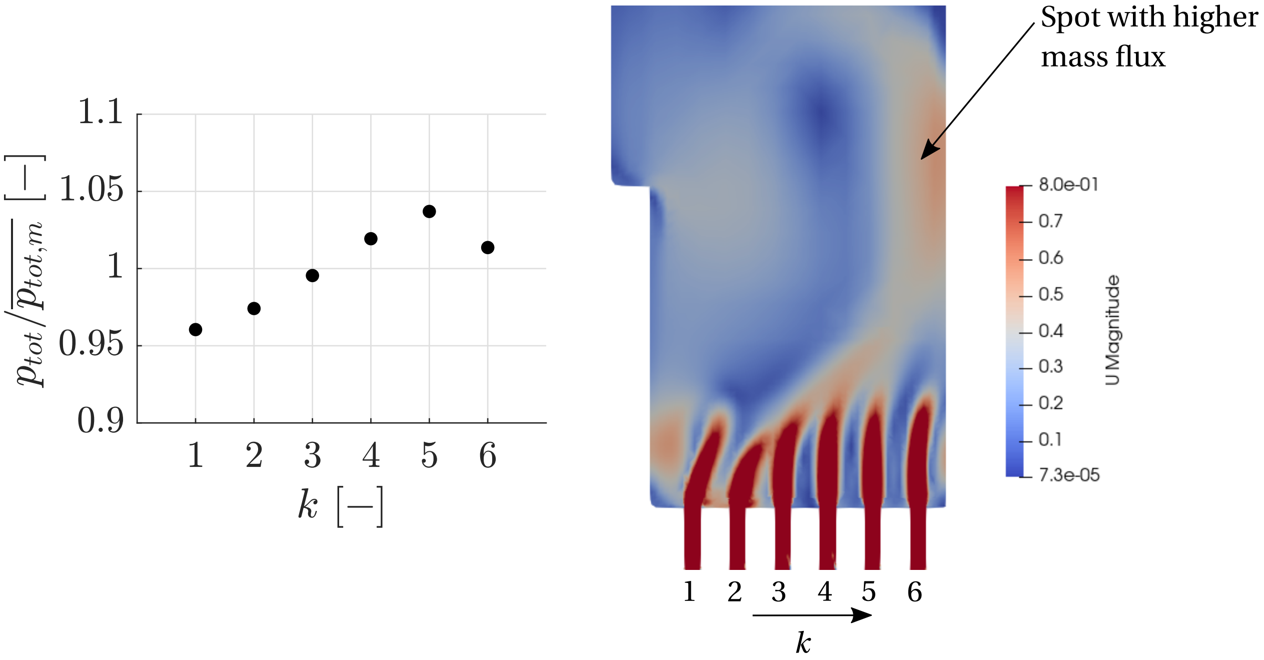

Spot with higher mass flux

Figure A.6: Total pressure distribution (left) and sectional view of the flow field downstream of the injection holes (right) at $\alpha = 0^\circ$ $(m = 1)$.

This statement can be better understood with the total pressure distribution and the sectional view of the flow field at the angular position $\alpha = 0^\circ$ shown in fig. A.6. The total pressure (left) has the highest value in the holes $k = 4 - 5$. In the resulting flow field (right), it can be observed that the jets downstream of holes 4-5 entrain the weaker jets and thus create a spot of higher mass flux. This phenomenon occurs similarly in all areas with total pressure gradients.

A.4 Flow Fields ($u_f/u_{f,N} = 1.44$)

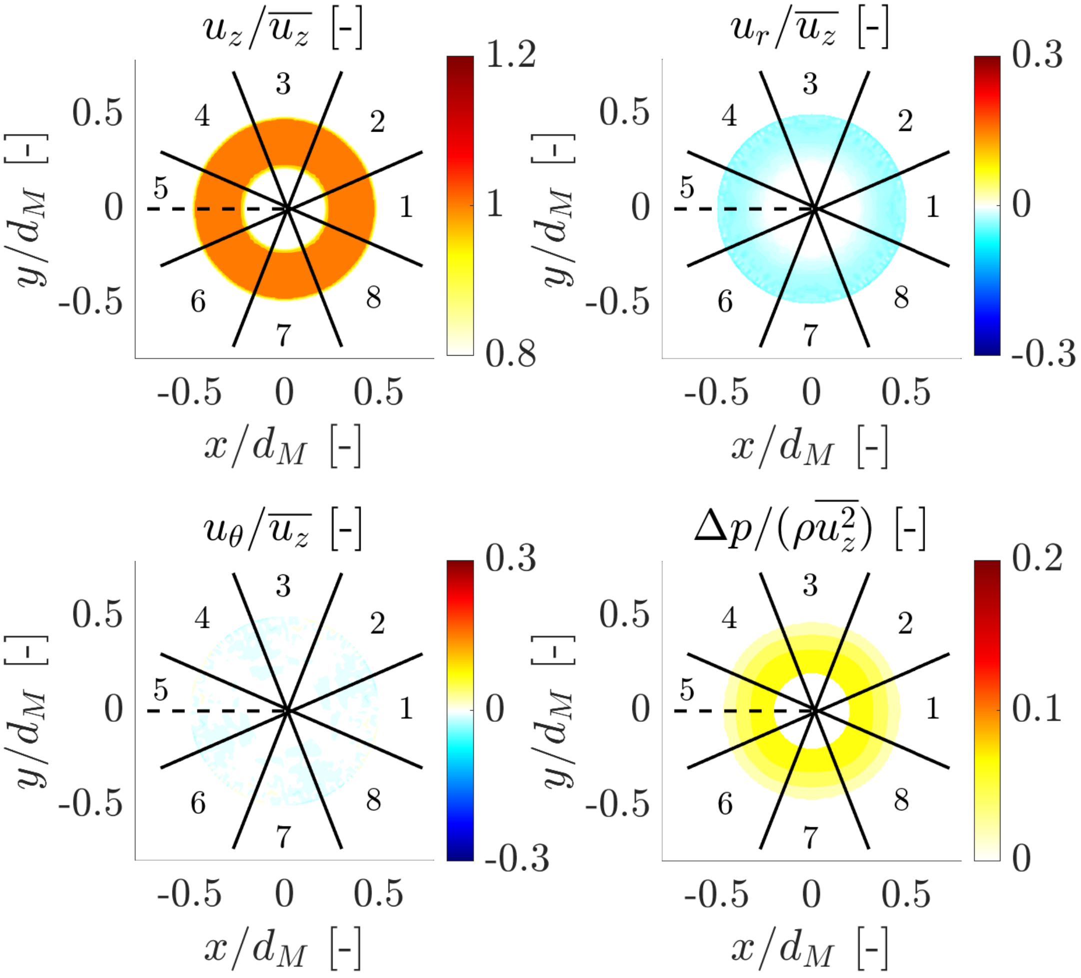

Figure A.7: Flow field for config. 0 ($u_f/u_{f,N} = 1.44$).

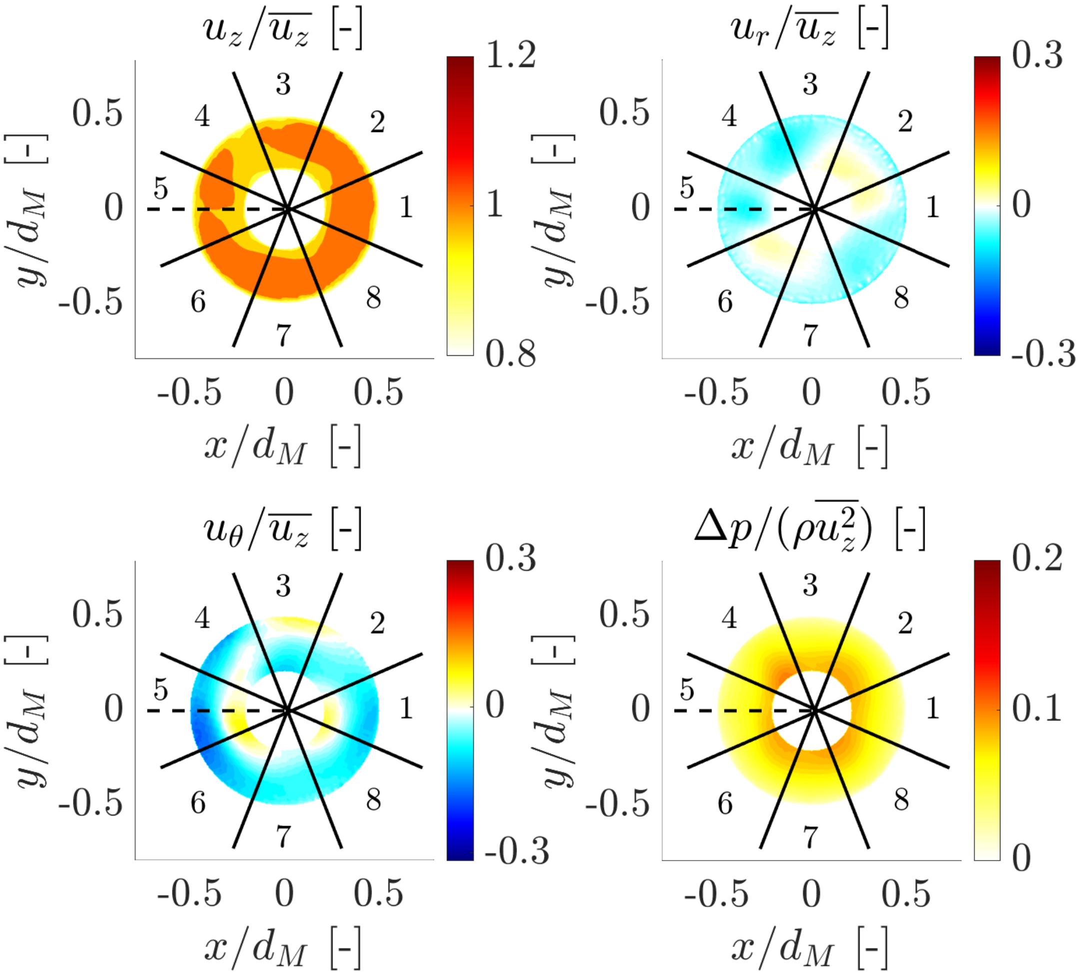

Figure A.8: Flow field for config. 1, injector 1 ($u_f/u_{f,N} = 1.44$).

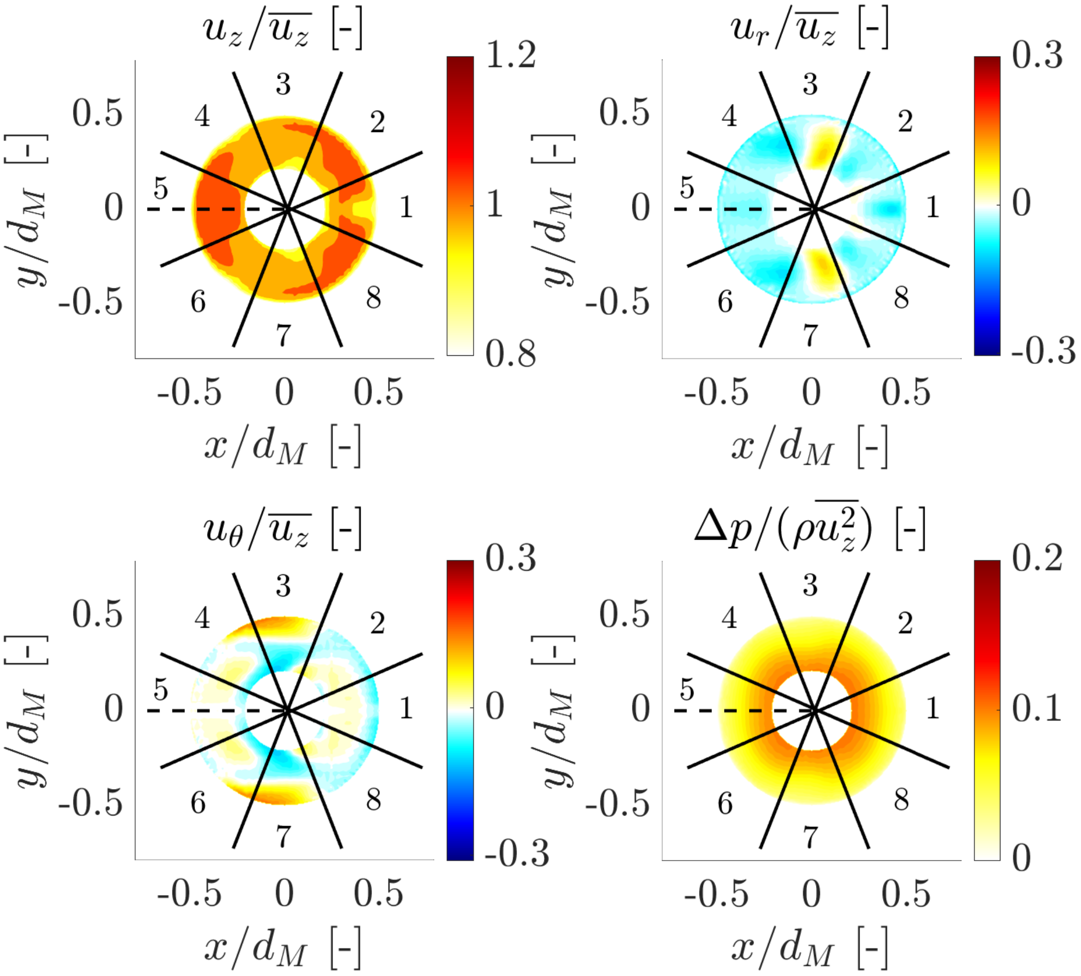

Figure A.9: Flow field for config. 1, injector 2 ($u_f / u_{f,N} = 1.44$).

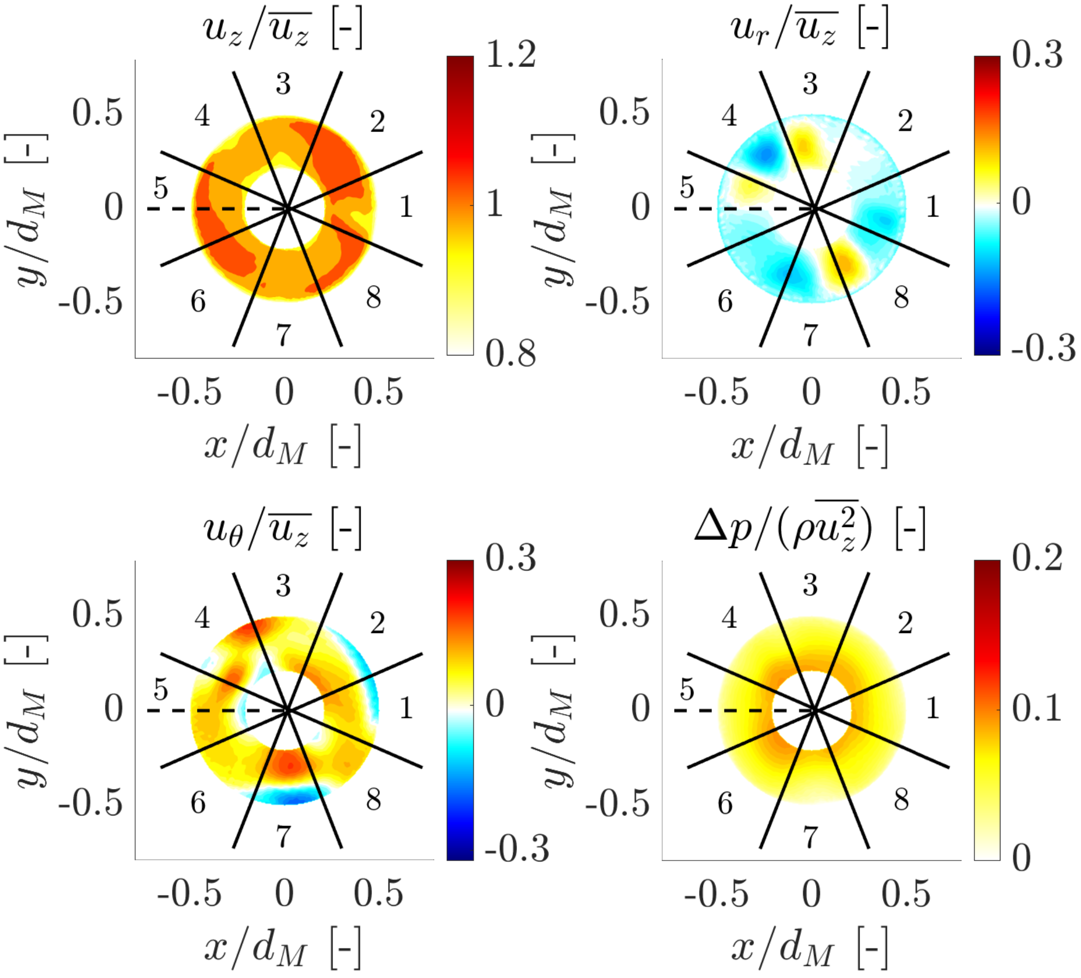

Figure A.10: Flow field for config. 1, injector 3 ($u_f/u_{f,N} = 1.44$).

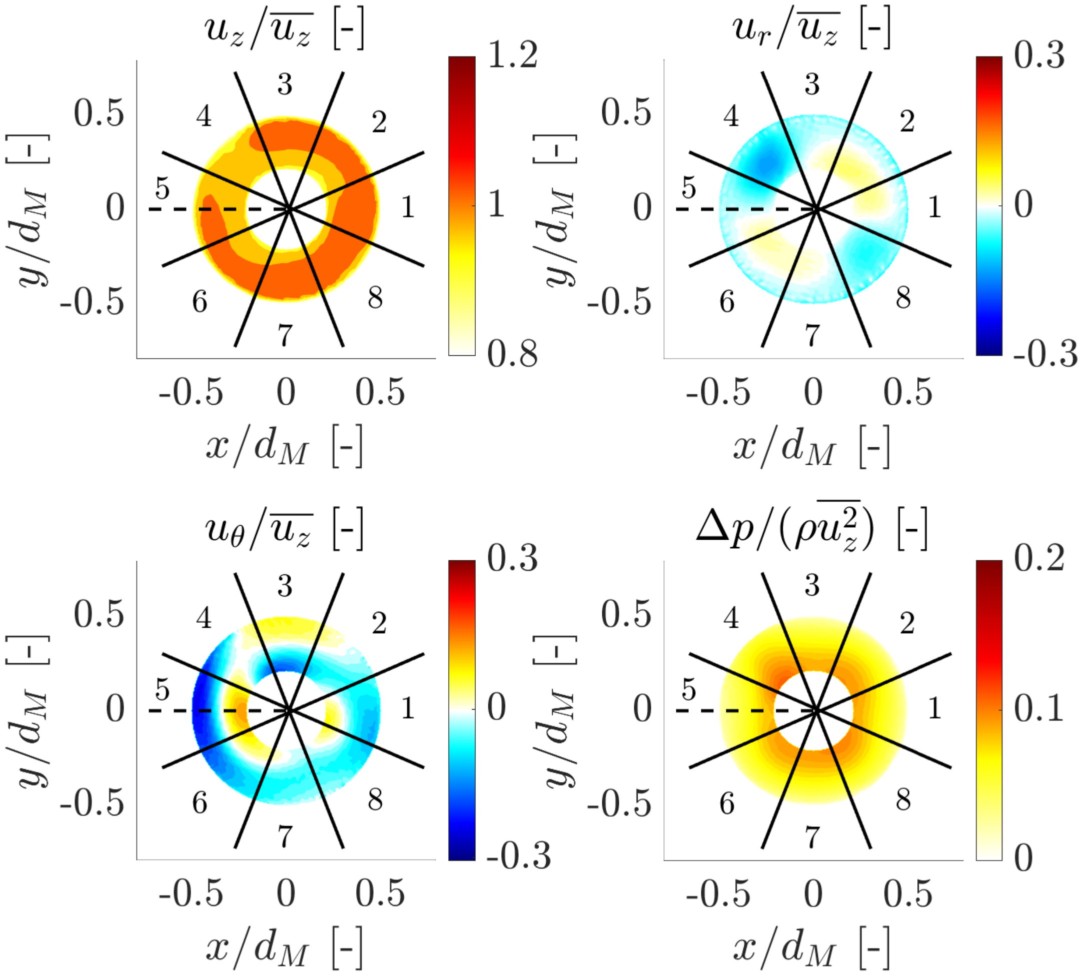

Figure A.11: Flow field for config. 2, injector 1 ($u_f/u_{f,N} = 1.44$).

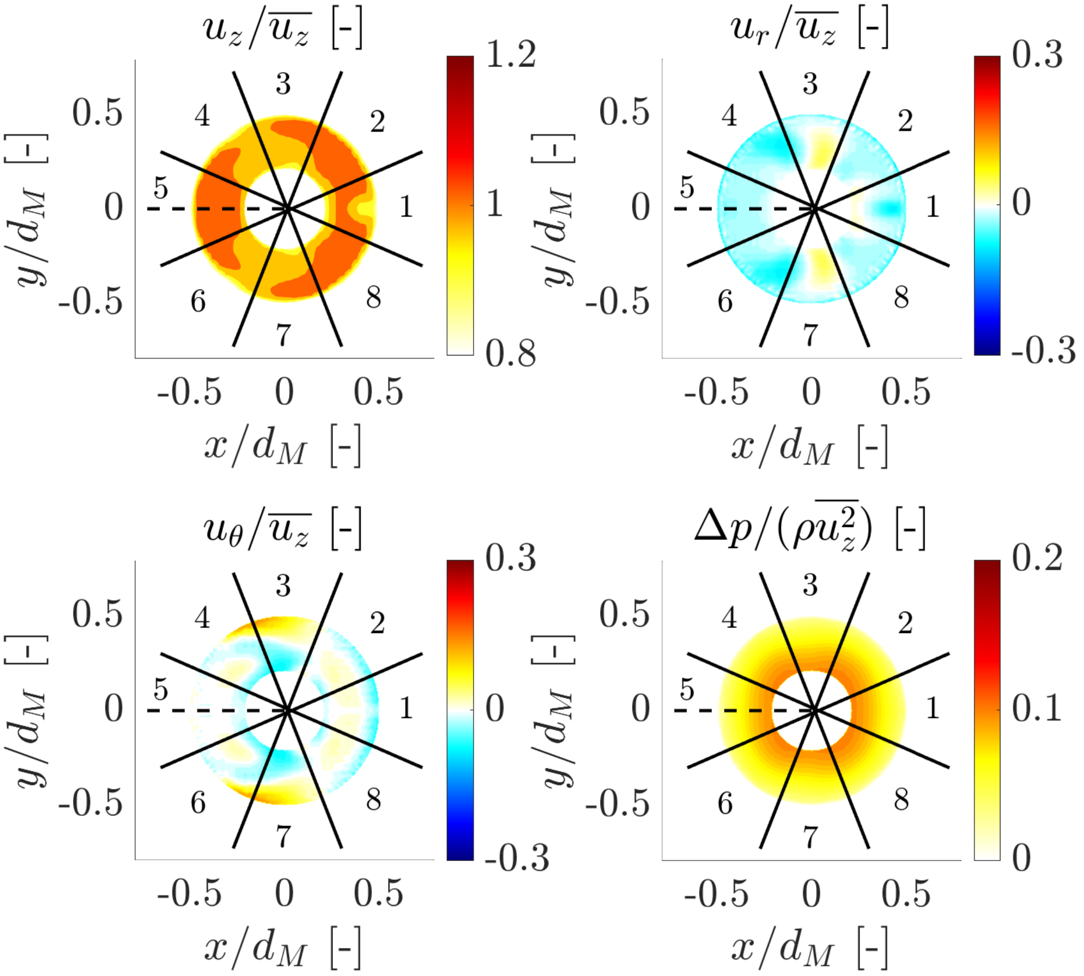

Figure A.12: Flow field for config. 2, injector 2 ($u_f/u_{f,N} = 1.44$).

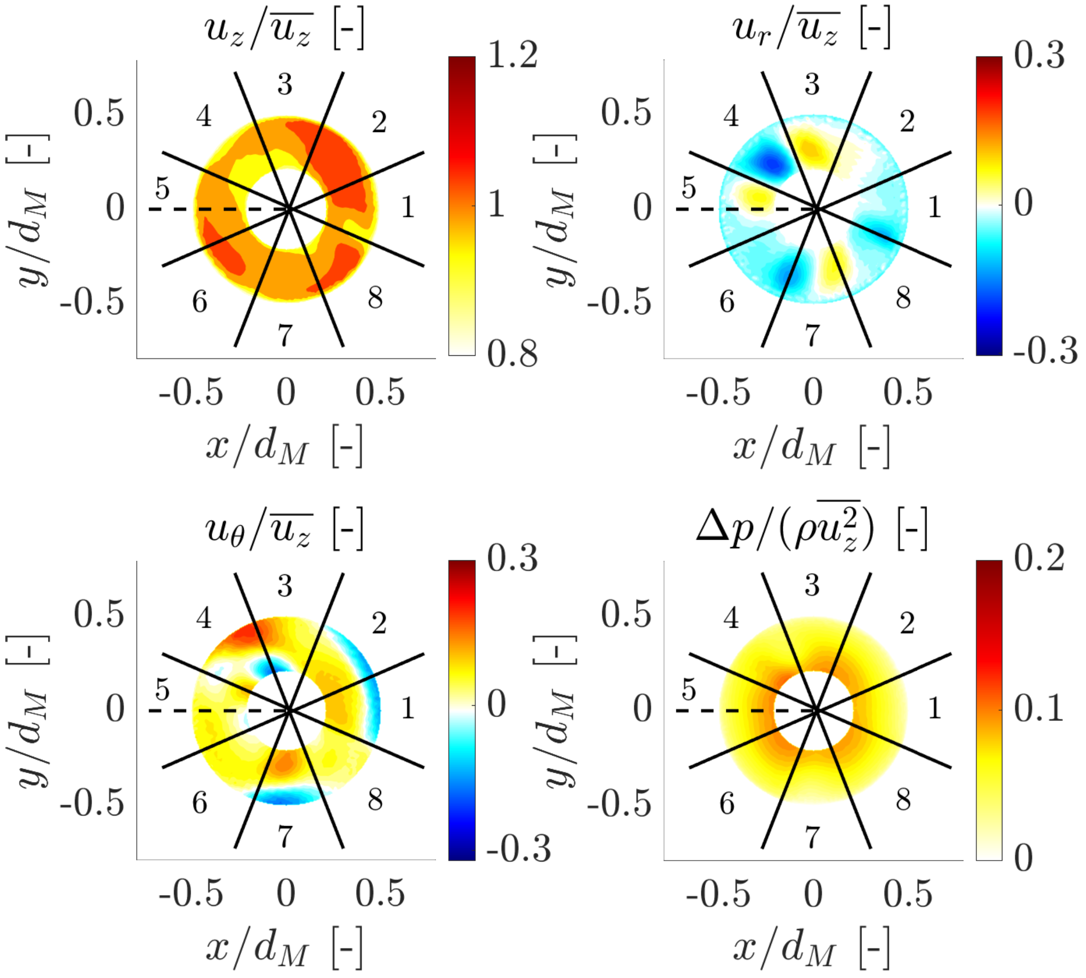

Figure A.13: Flow field for config. 2, injector 3 ($u_f / u_{f,N} = 1.44$).

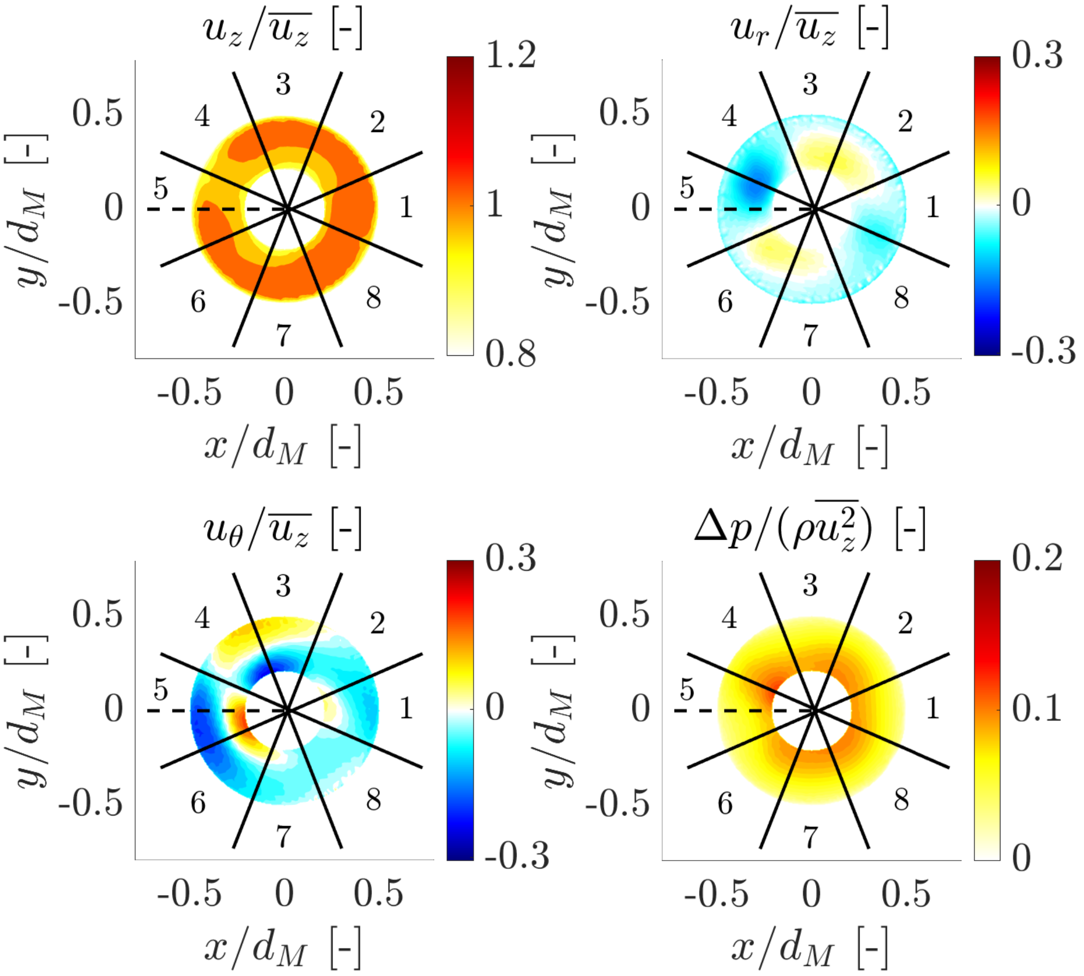

Figure A.14: Flow field for config. 3, injector 1 ($u_f/u_{f,N} = 1.44$).

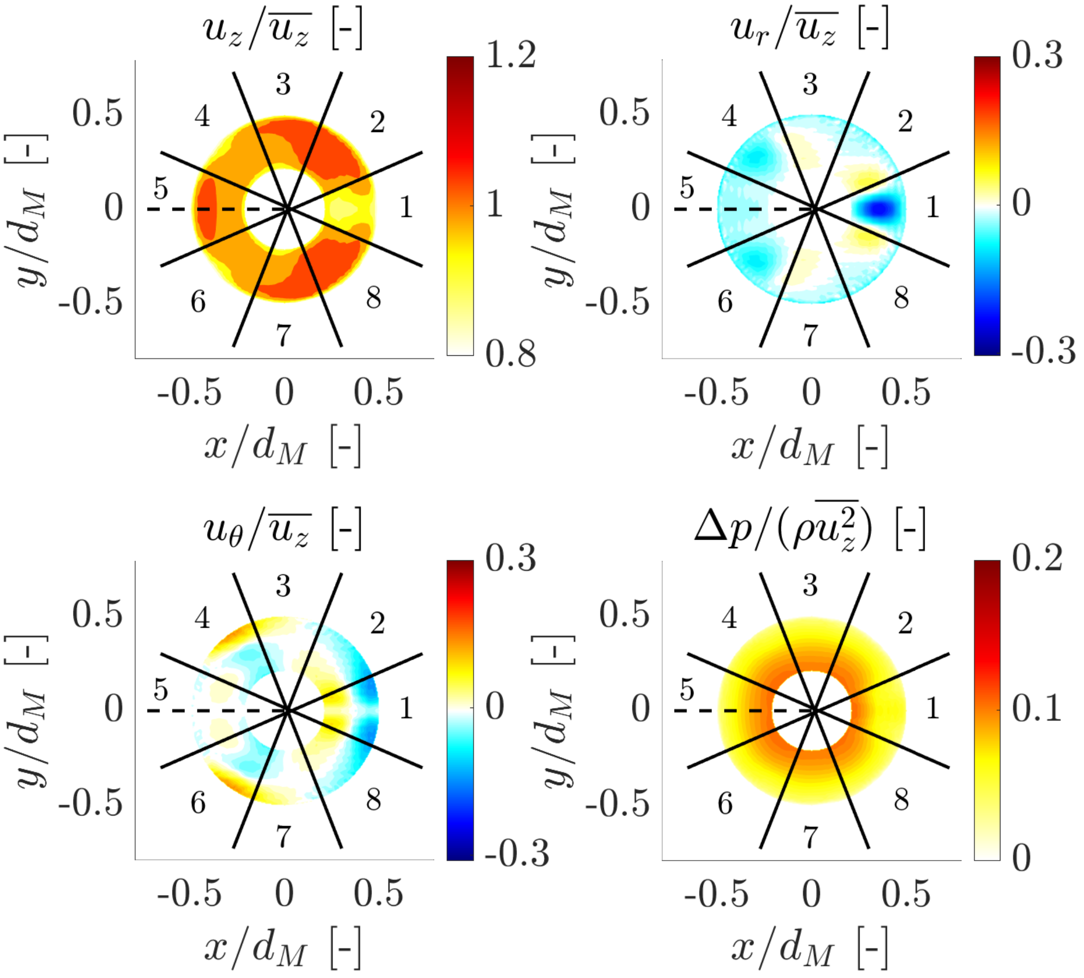

Figure A.15: Flow field for config. 3, injector 2 ($u_f/u_{f,N} = 1.44$).

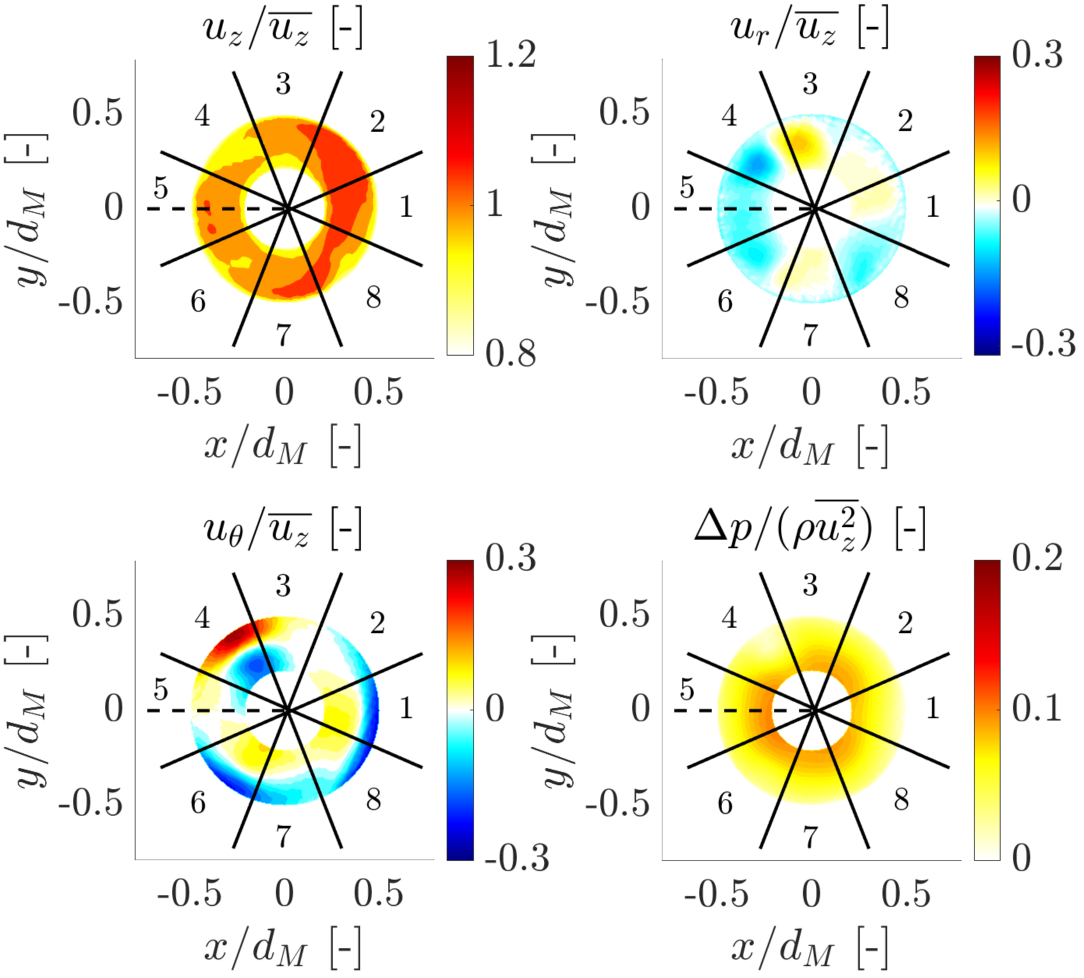

Figure A.16: Flow field for config. 3, injector 3 ($u_f/u_{f,N} = 1.44$).

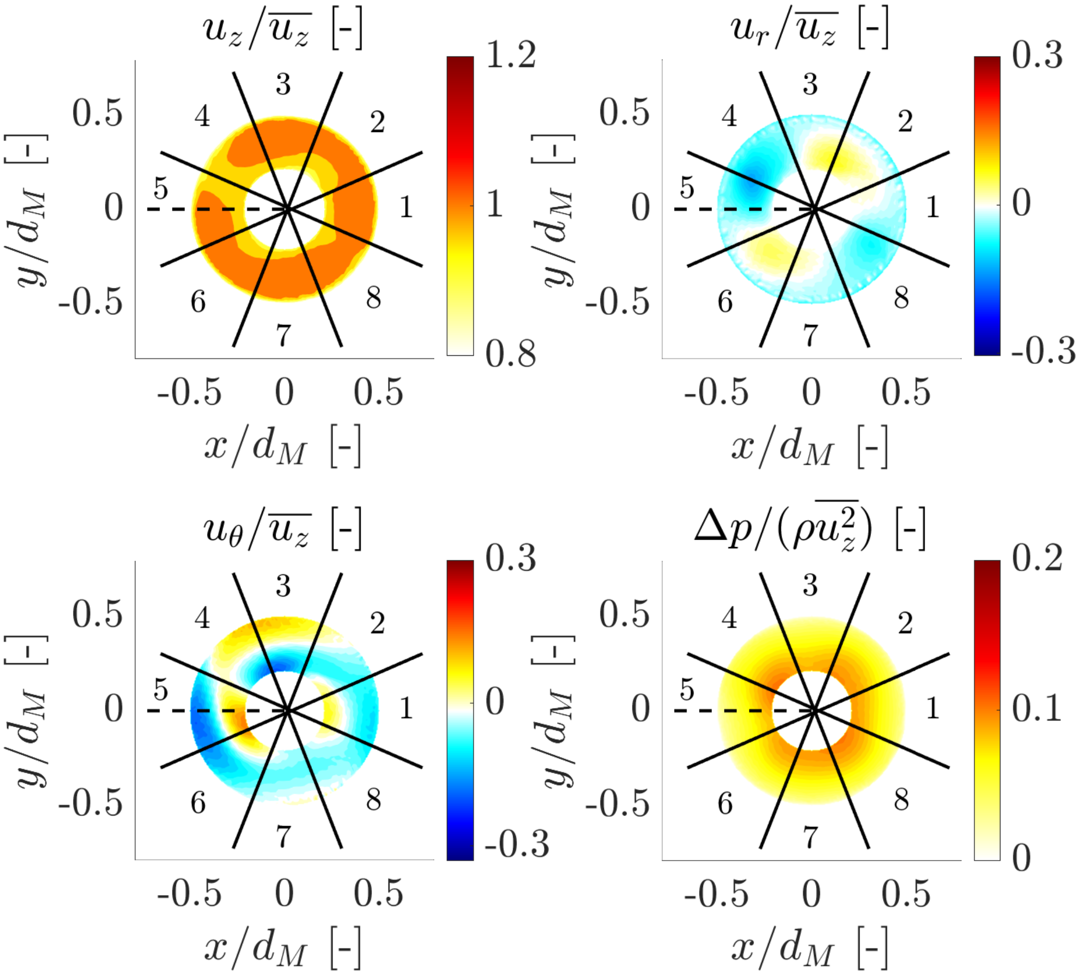

Figure A.17: Flow field for config. 4, injector 1 ($u_f/u_{f,N} = 1.44$).

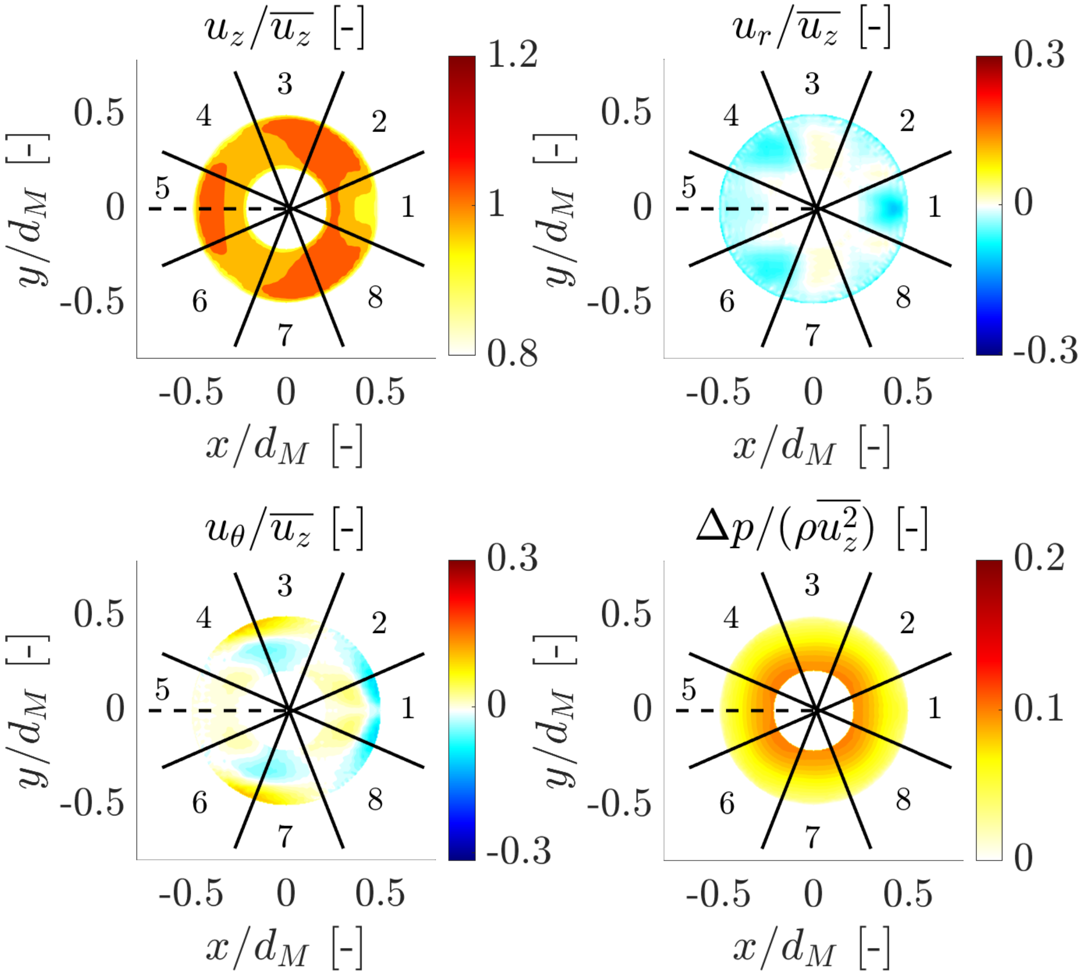

Figure A.18: Flow field for config. 4, injector 2 ($u_f/u_{f,N} = 1.44$).

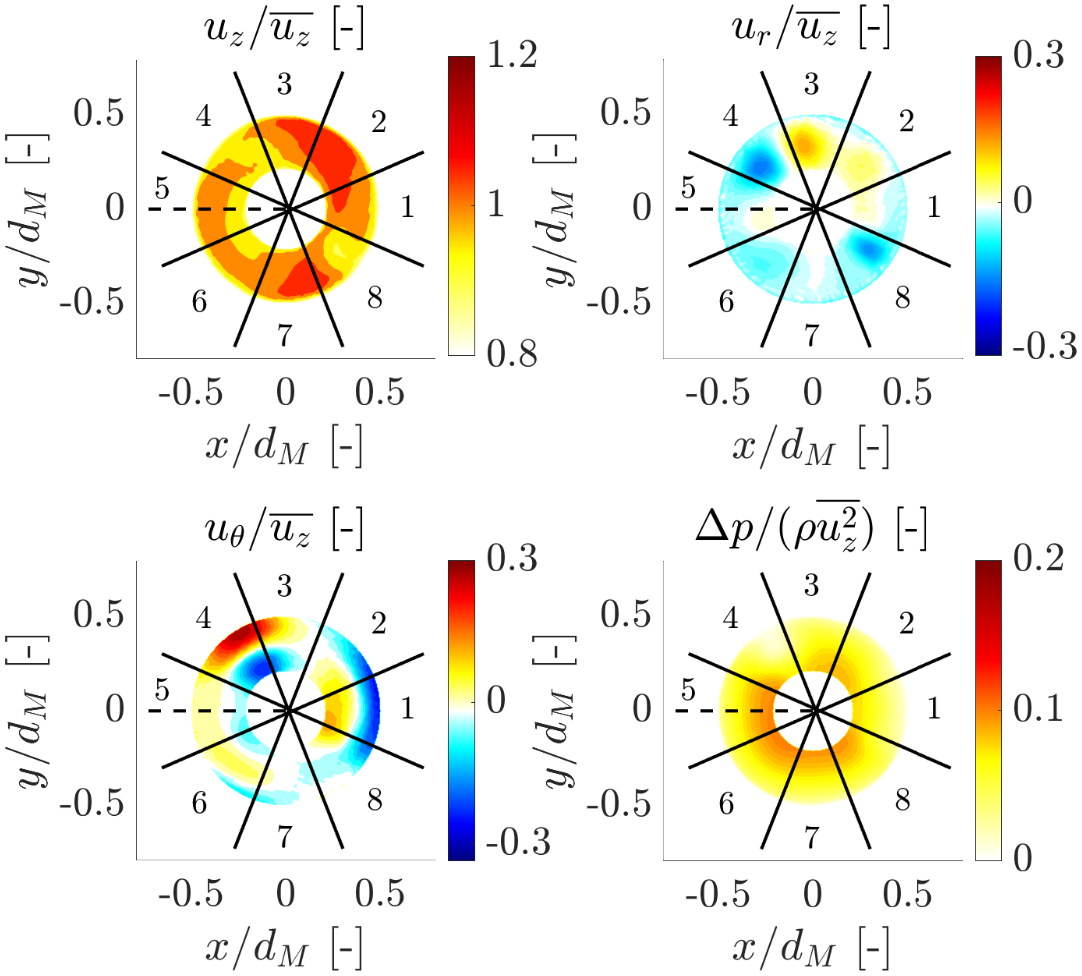

Figure A.19: Flow field for config. 4, injector 3 ($u_f/u_{f,N} = 1.44$).

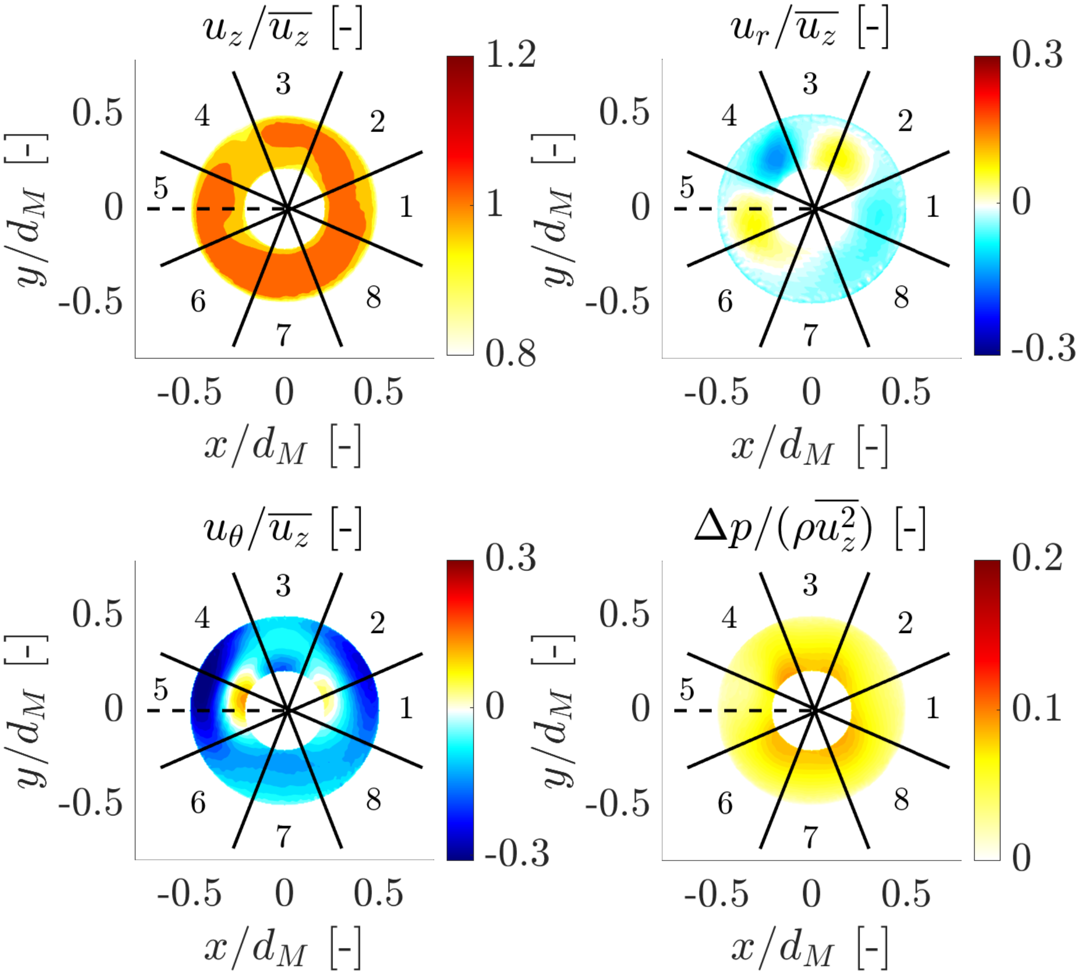

Figure A.20: Flow field for config. 5, injector 1 ($u_f/u_{f,N} = 1.44$).

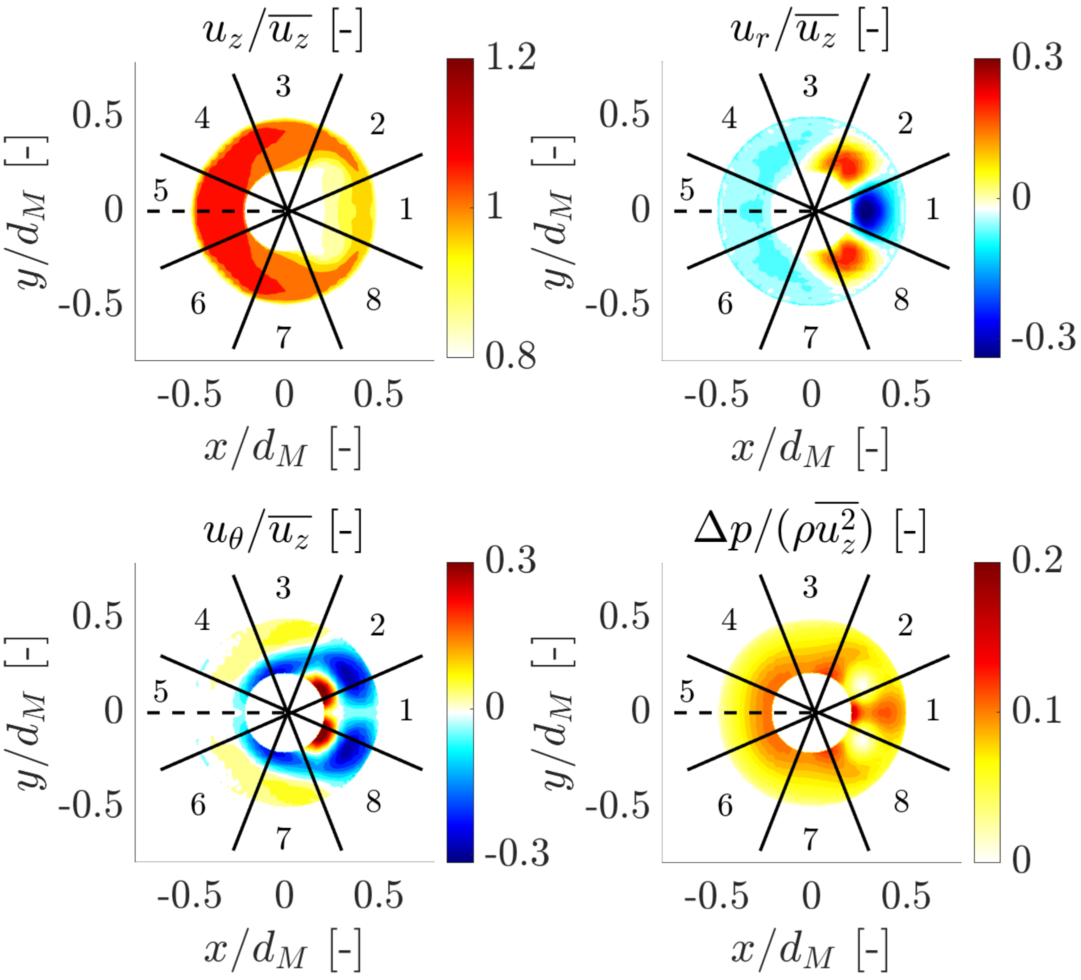

Figure A.21: Flow field for config. 5, injector 2 ($u_f/u_{f,N} = 1.44$).

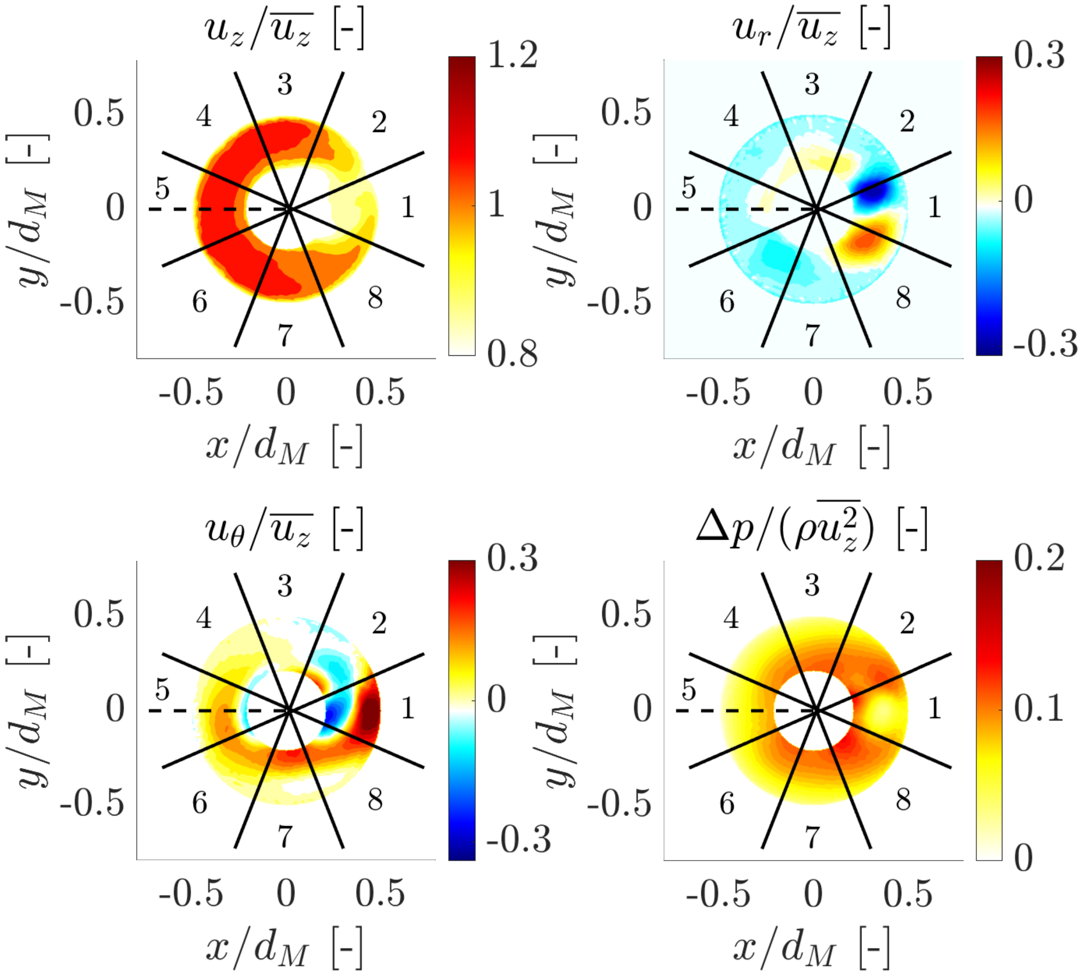

Figure A.22: Flow field for config. 5, injector 3 ($u_f/u_{f,N} = 1.44$).

A.5 Observable Datasets ($u_f / u_{f,N} = 1.44$)

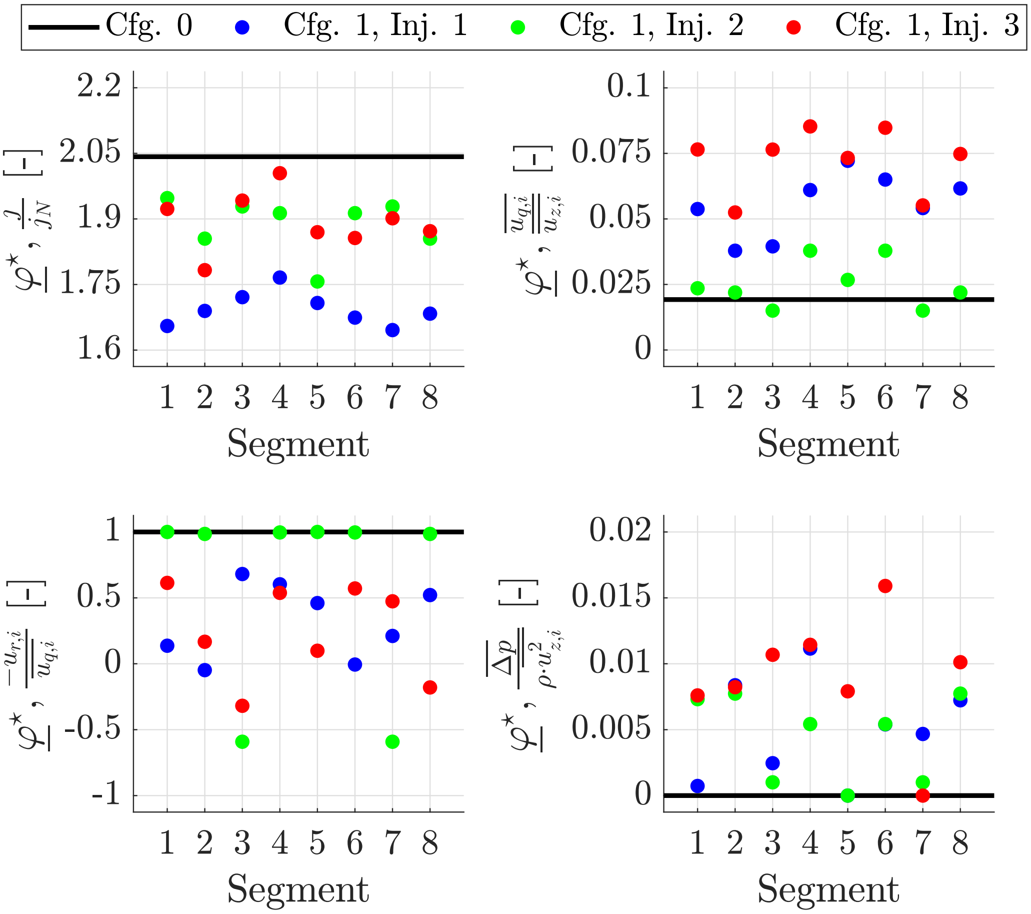

Figure A.23: Components of the $\underline{\varphi}^\star$ vectors for config. 1 ($u_f / u_{f,N} = 1.44$).

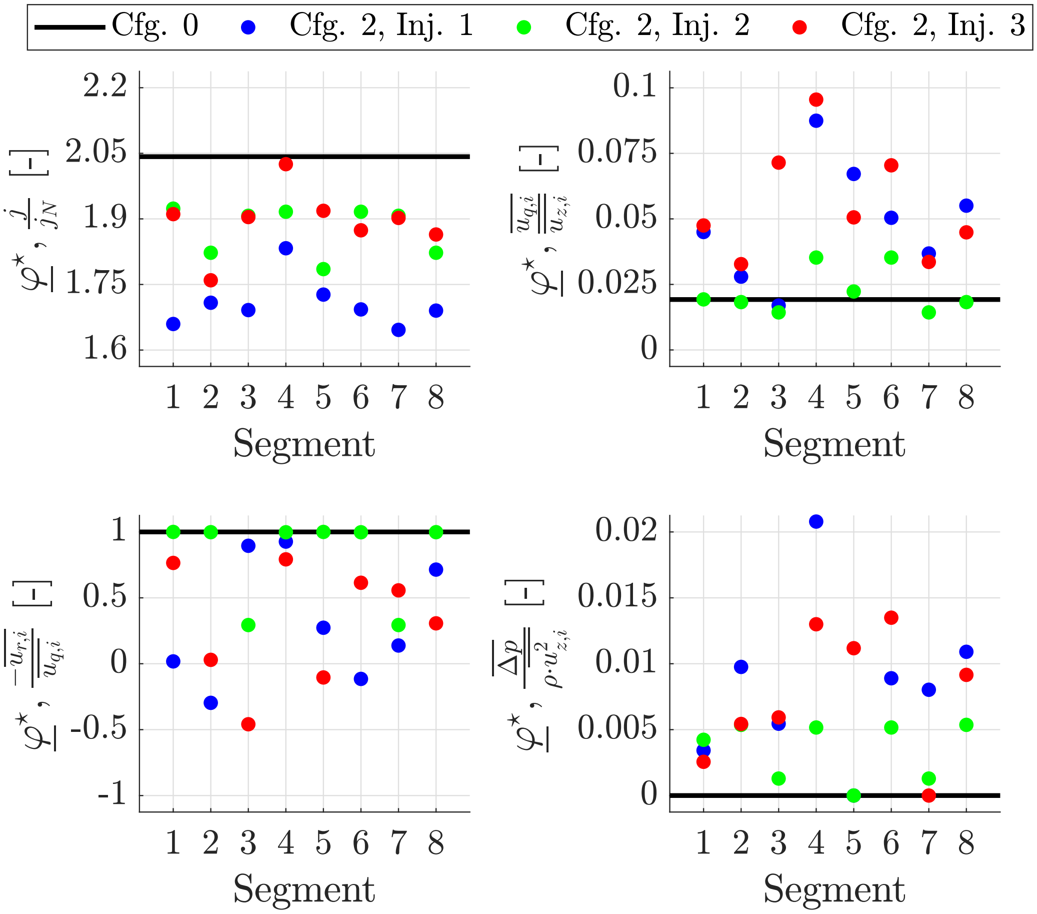

Figure A.24: Components of the $\underline{\varphi}^{\star}$ vectors for config. 2 ($u_f / u_{f,N} = 1.44$).

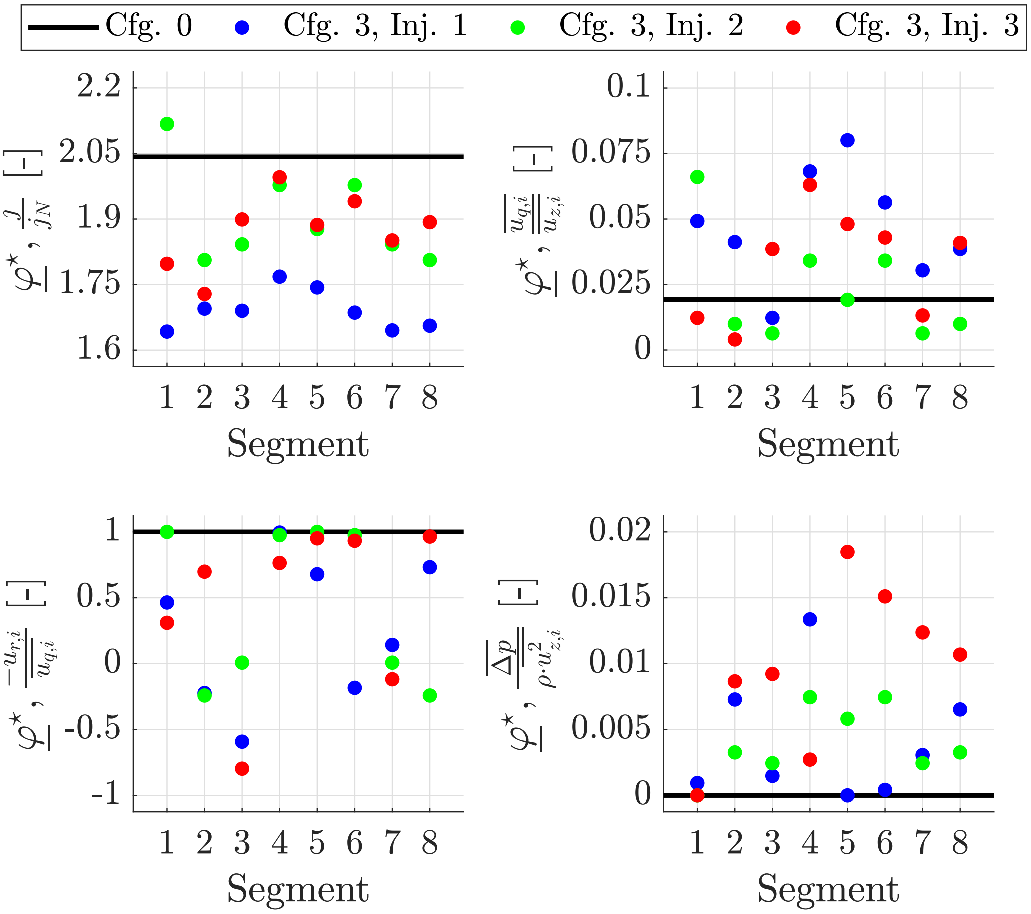

Figure A.25: Components of the $\underline{\varphi}^\star$ vectors for config. 3 ($u_f / u_{f,N} = 1.44$).

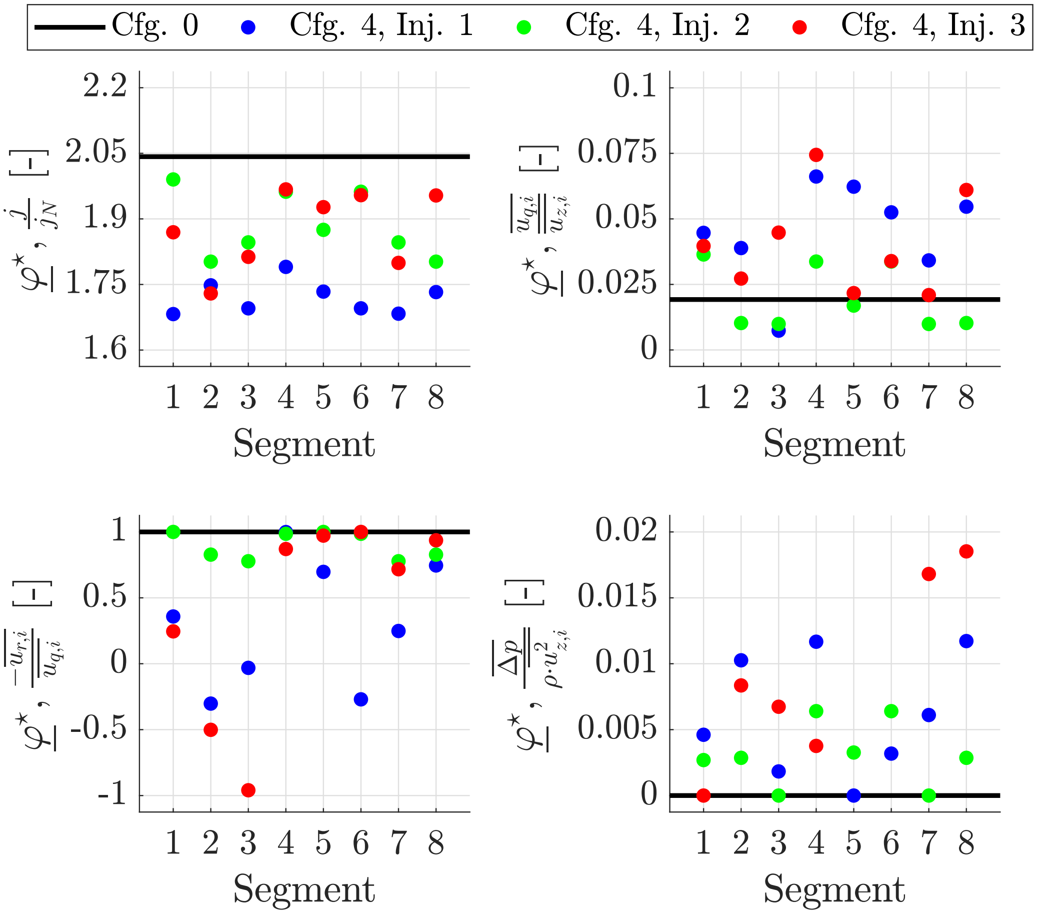

Figure A.26: Components of the $\underline{\varphi}^{\star}$ vectors for config. 4 ($u_f / u_{f,N} = 1.44$).

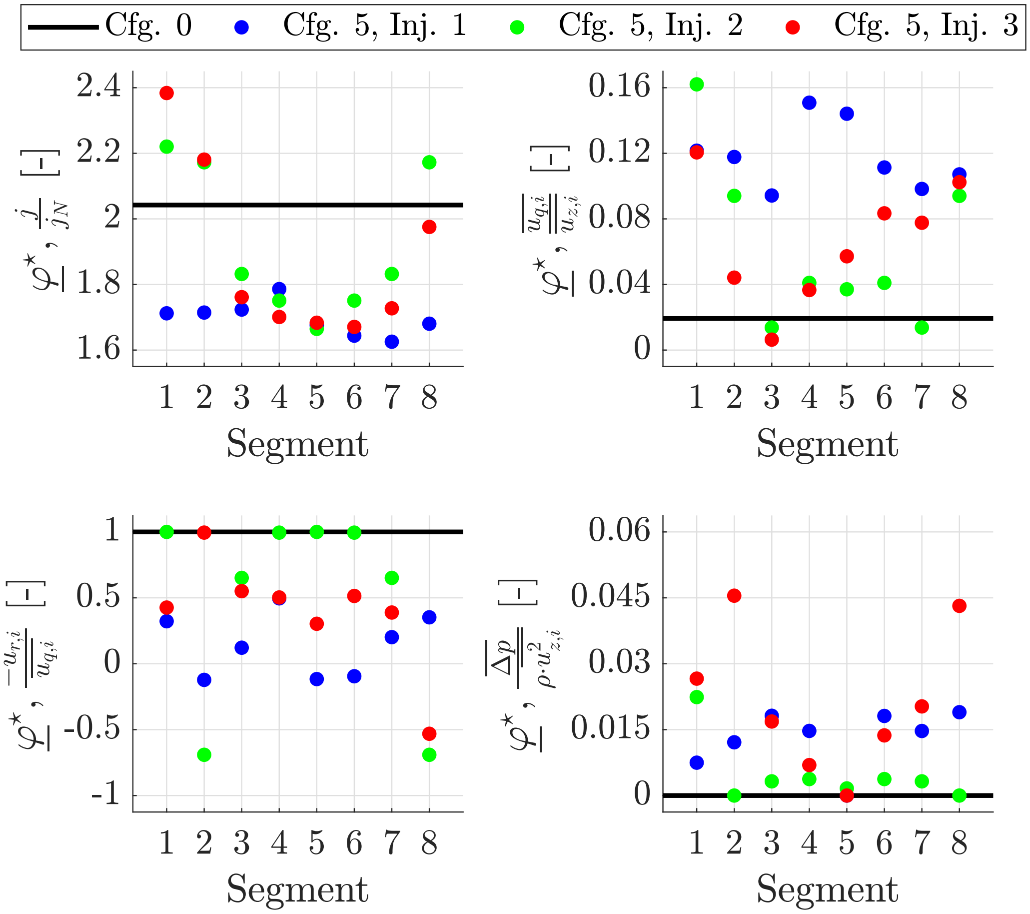

Figure A.27: Components of the $\underline{\varphi}^\star$ vectors for config. 5 ($u_f / u_{f,N} = 1.44$).

A.6 Eigenmodes of Observable and Mixing PMF Datasets

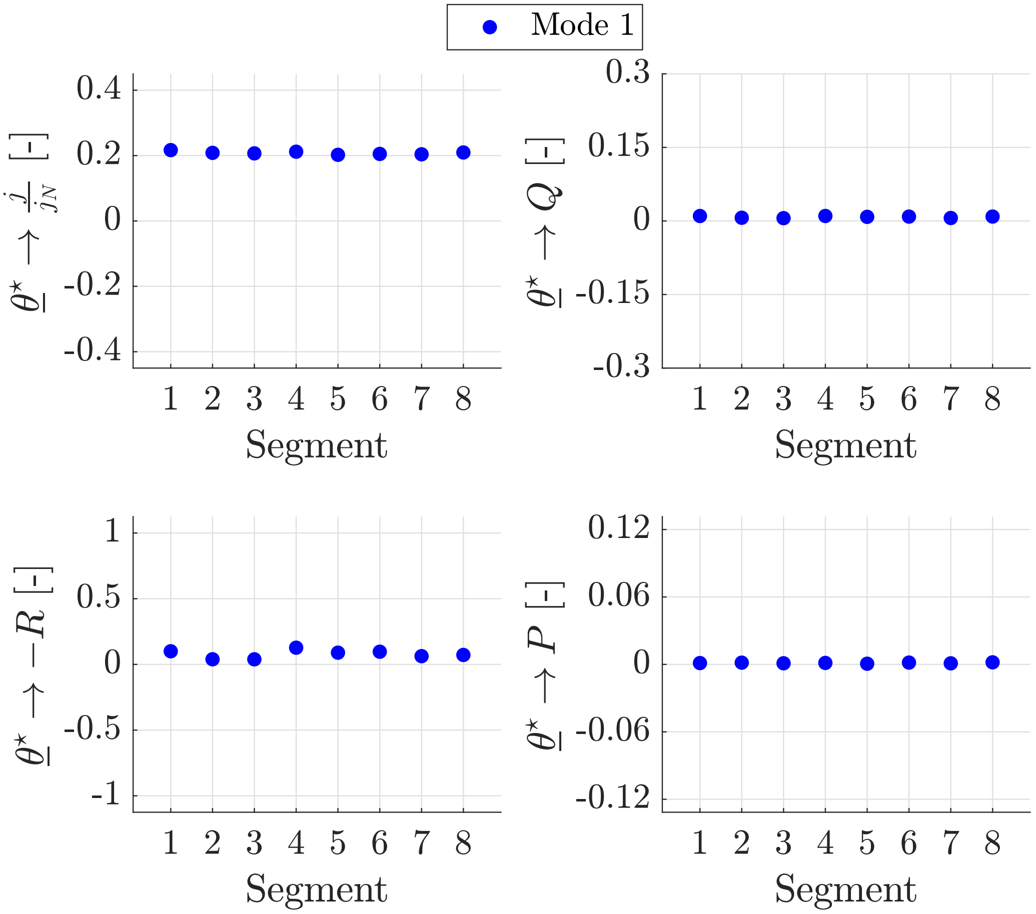

Figure A.28: Eigenmode associated with the observable vectors ($\underline{\theta_1^{\star}}$).

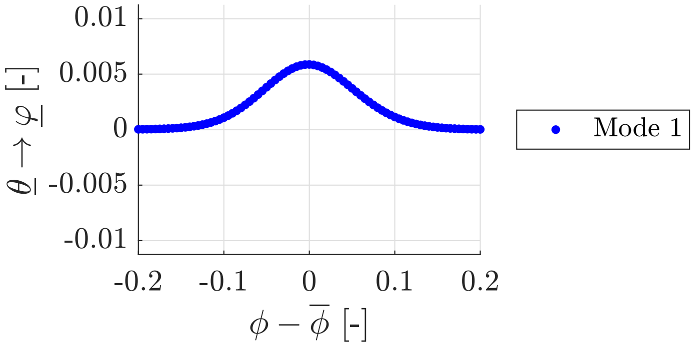

Figure A.29: Eigenmode associated with the mixing PMFs ($\underline{\theta_1}$).

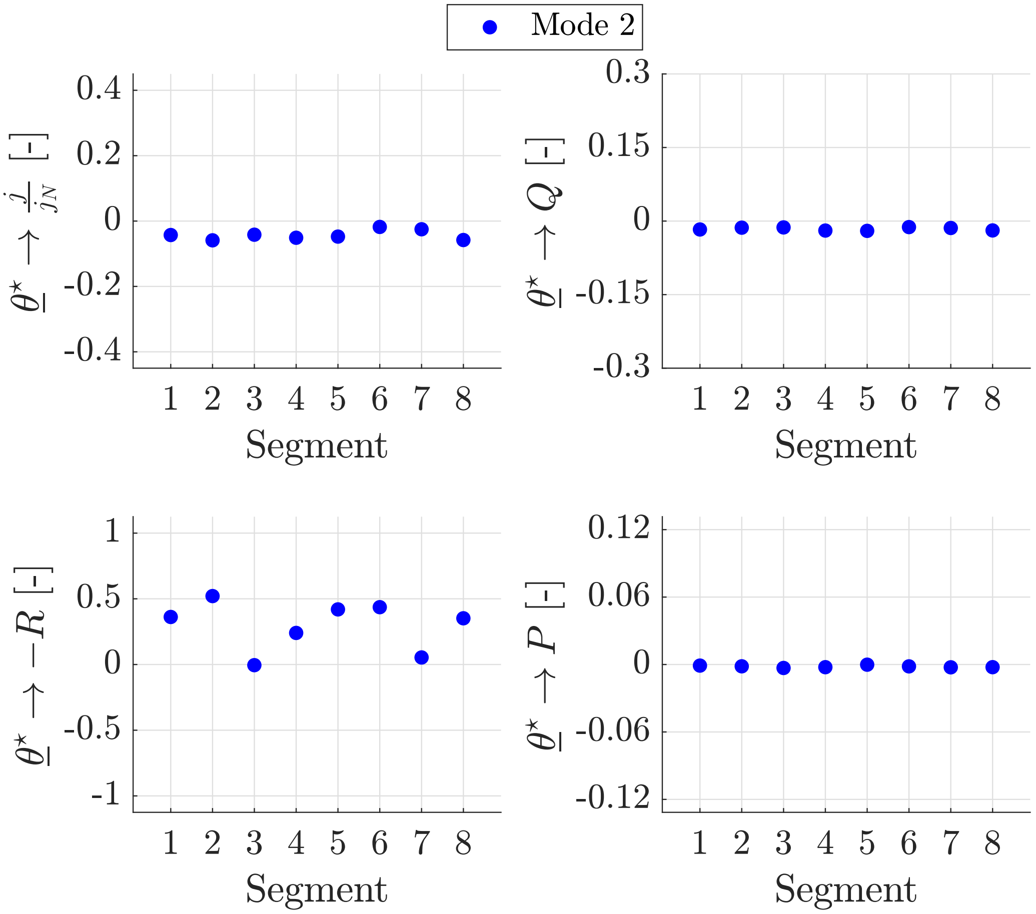

Figure A.30: Eigenmode associated with the observable vectors ($\underline{\theta}_2^{\star}$).

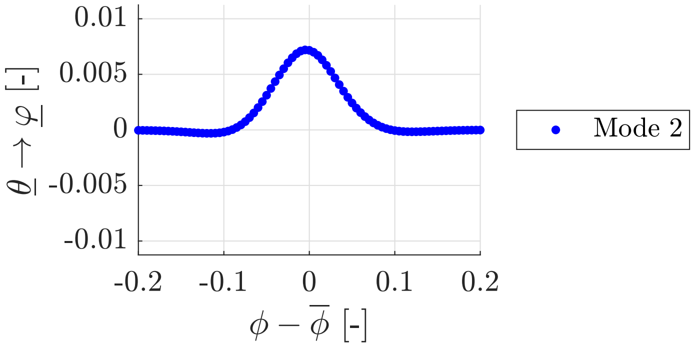

Figure A.31: Eigenmode associated with the mixing PMFs ($\underline{\theta}_2$).

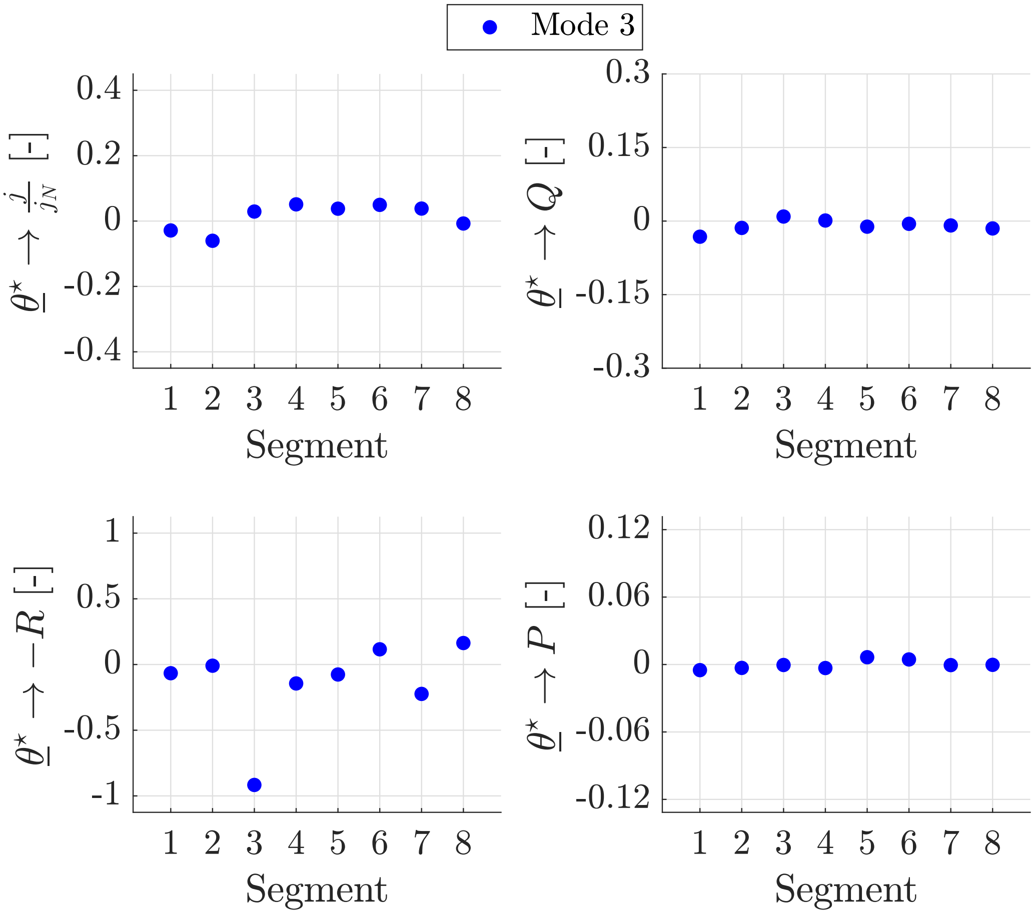

Figure A.32: Eigenmode associated with the observable vectors ($\underline{\theta_3^{\star}}$).

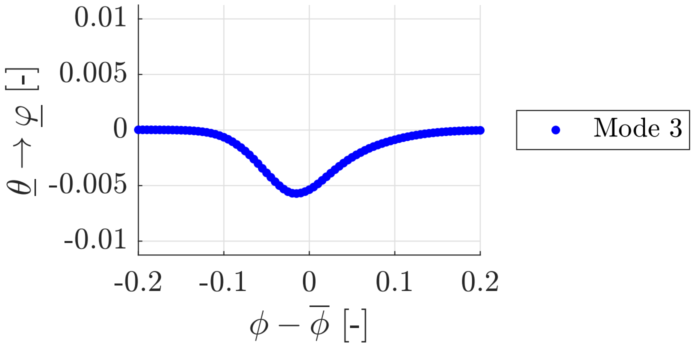

Figure A.33: Eigenmode associated with the mixing PMFs ($\underline{\theta_3}$).

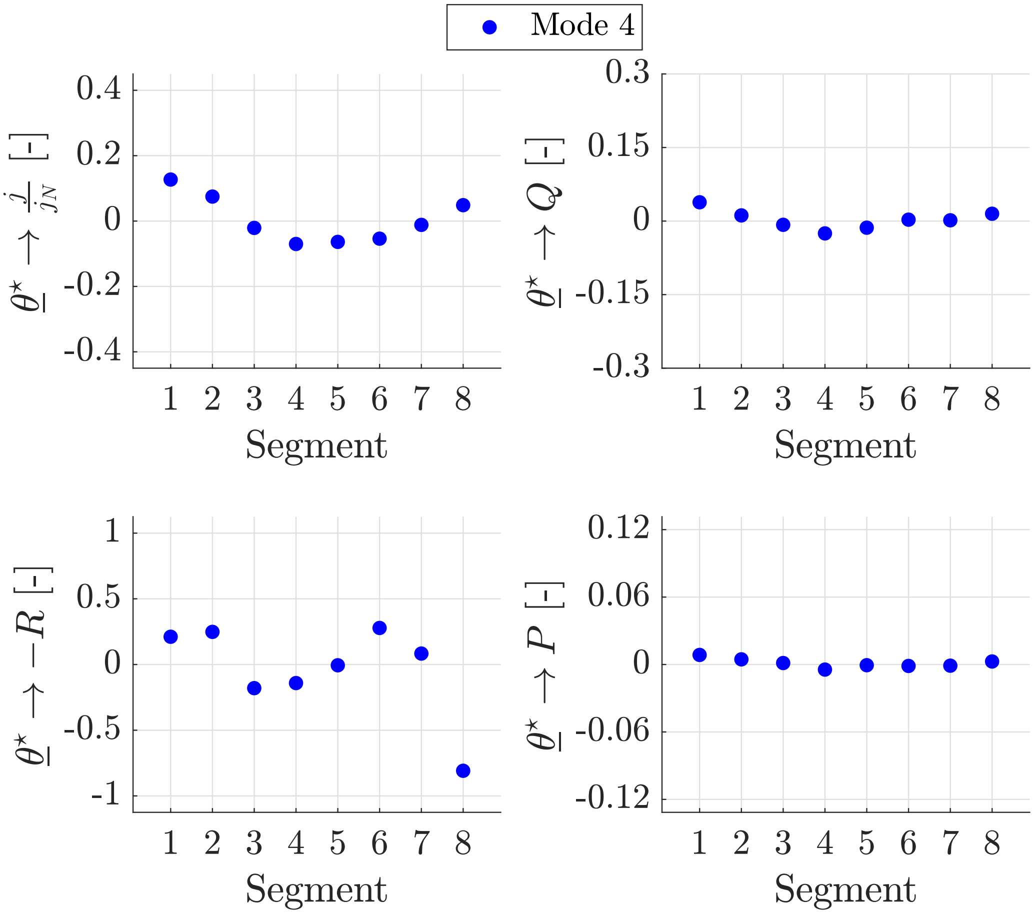

Figure A.34: Eigenmode associated with the observable vectors ($\underline{\theta}_4^\star$).

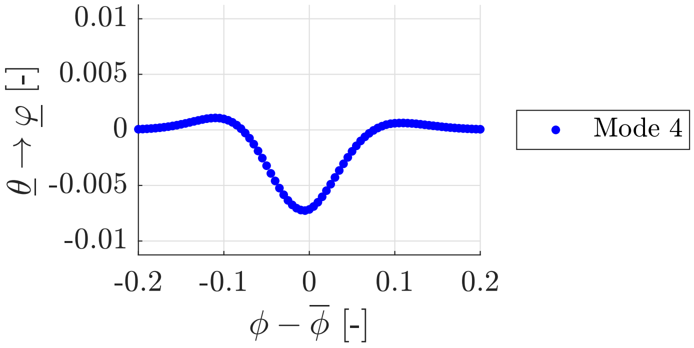

Figure A.35: Eigenmode associated with the mixing PMFs ($\underline{\theta}_4$).

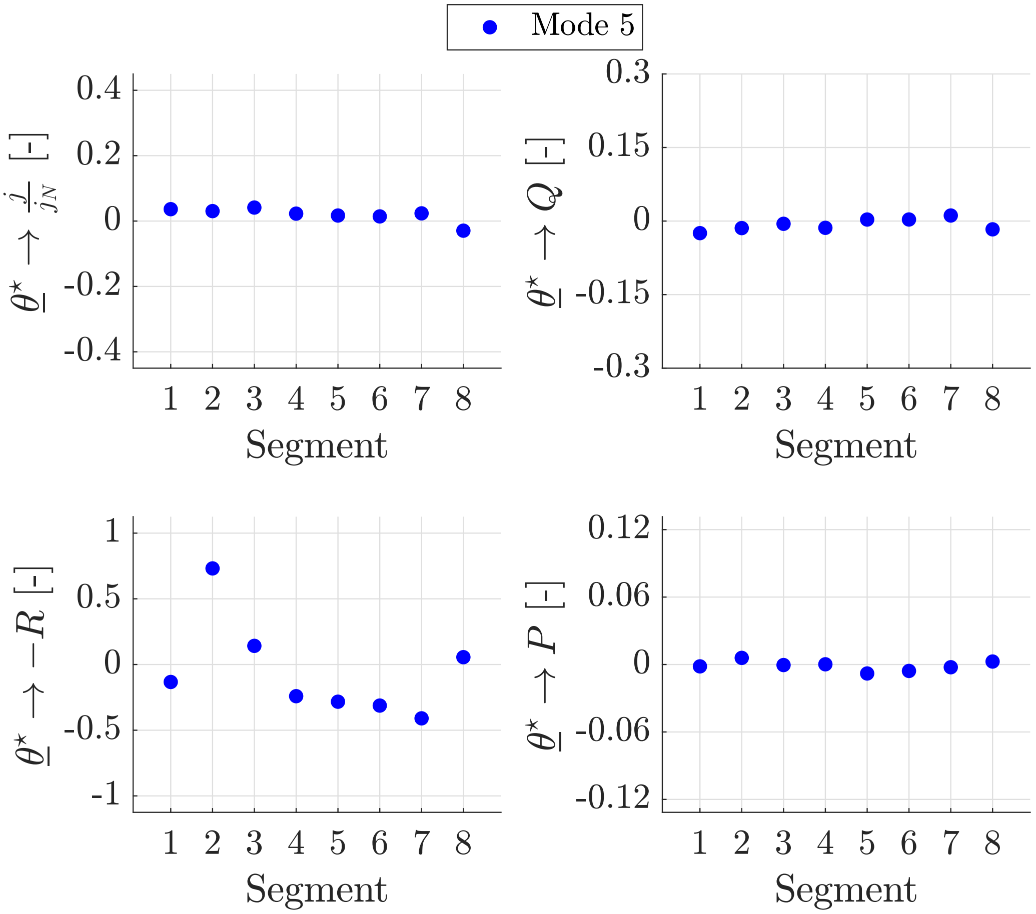

Figure A.36: Eigenmode associated with the observable vectors ($\underline{\theta_5^\star}$).

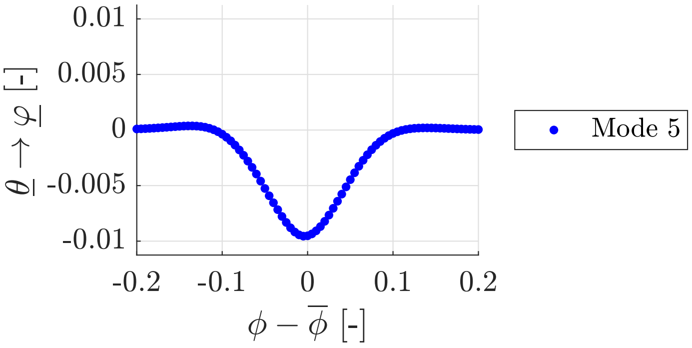

Figure A.37: Eigenmode associated with the mixing PMFs ($\underline{\theta_5}$).

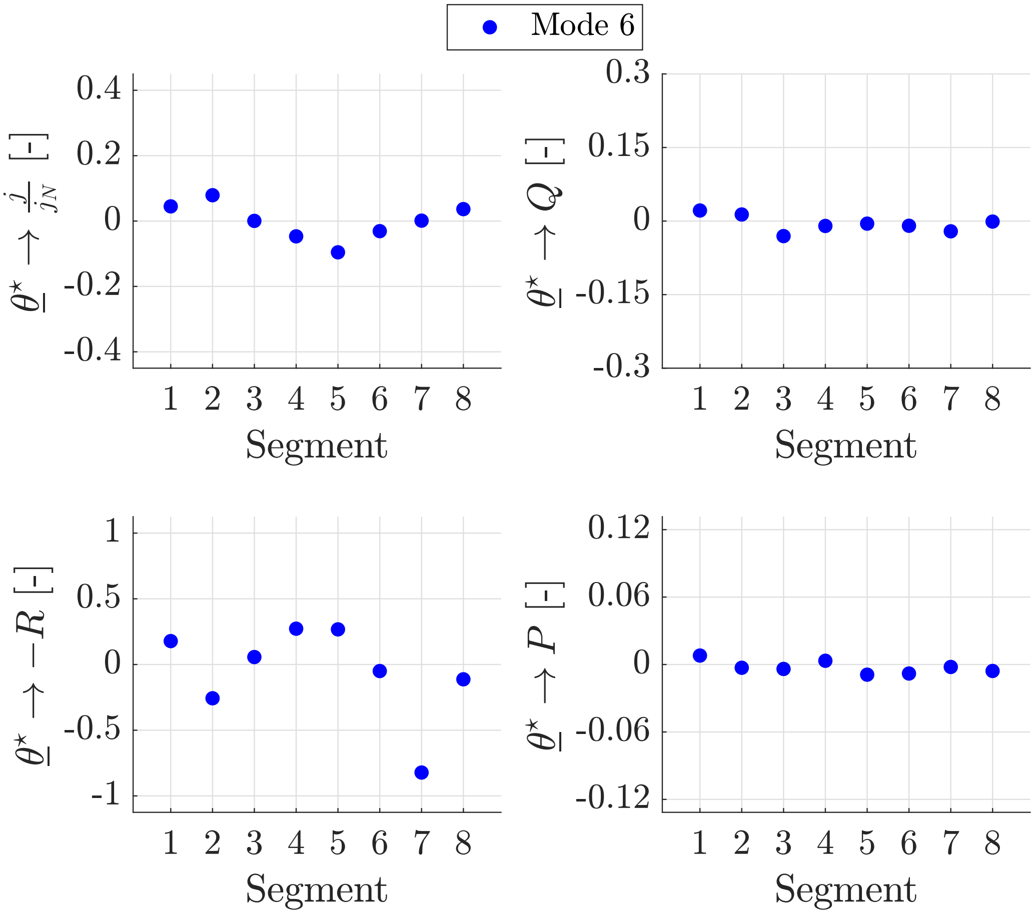

Figure A.38: Eigenmode associated with the observable vectors ($\underline{\theta}_6^\star$).

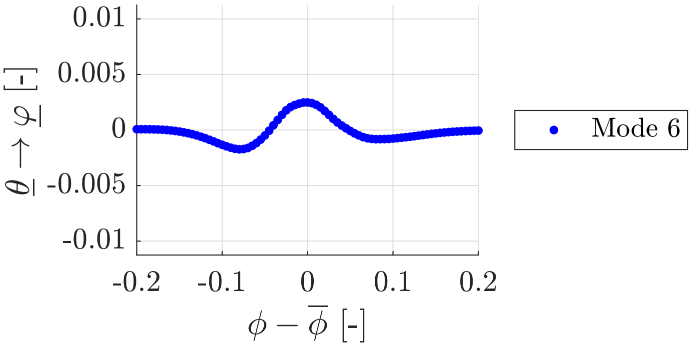

Figure A.39: Eigenmode associated with the mixing PMFs ($\underline{\theta}_6$).

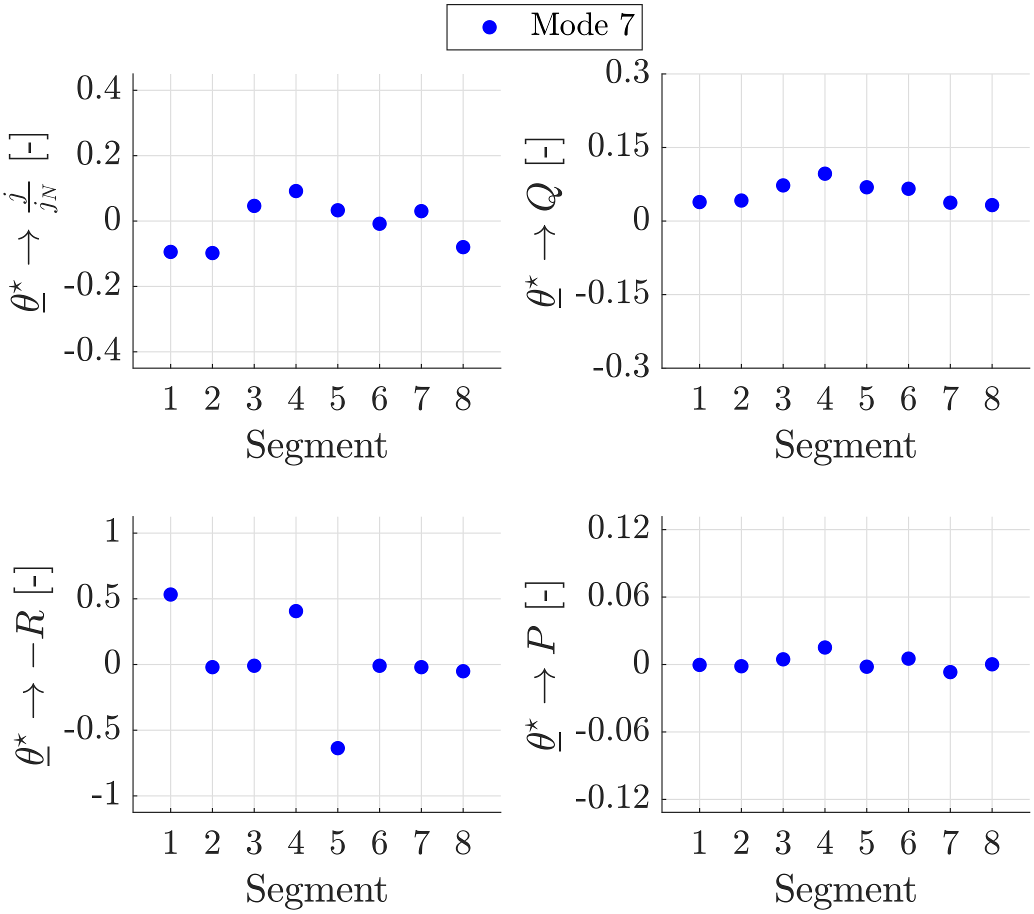

Figure A.40: Eigenmode associated with the observable vectors ($\underline{\theta_7^\star}$).

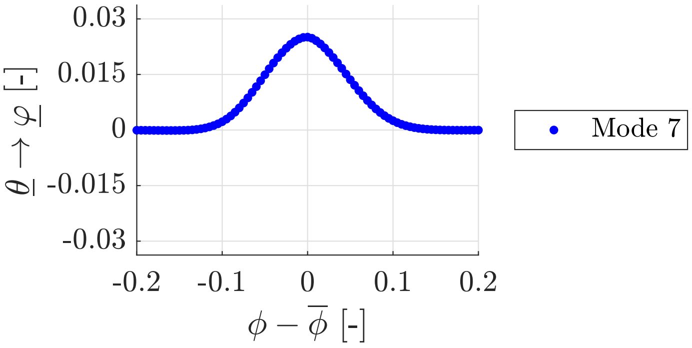

Figure A.41: Eigenmode associated with the mixing PMFs ($\underline{\theta_7}$).

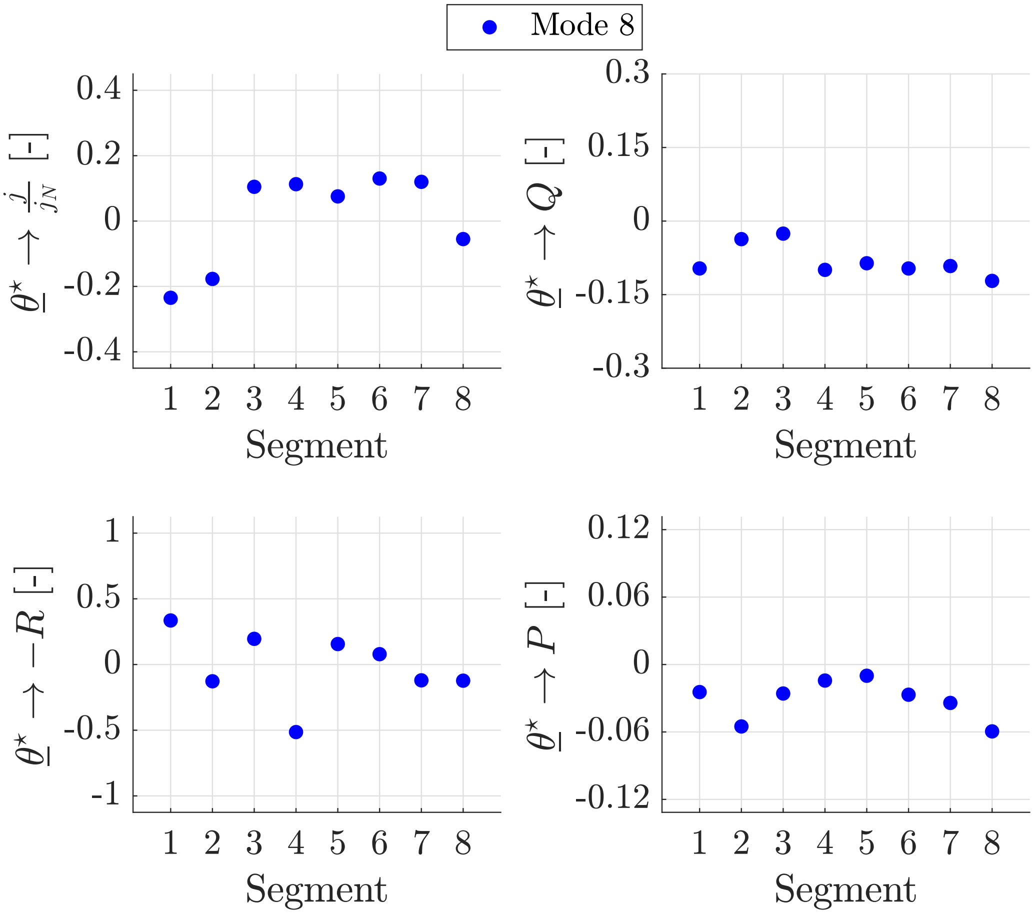

Figure A.42: Eigenmode associated with the observable vectors ($\underline{\theta}_8^{\star}$).

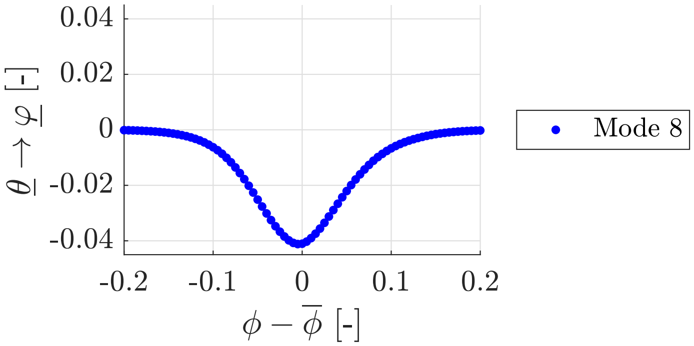

Figure A.43: Eigenmode associated with the mixing PMFs ($\underline{\theta}_8$).

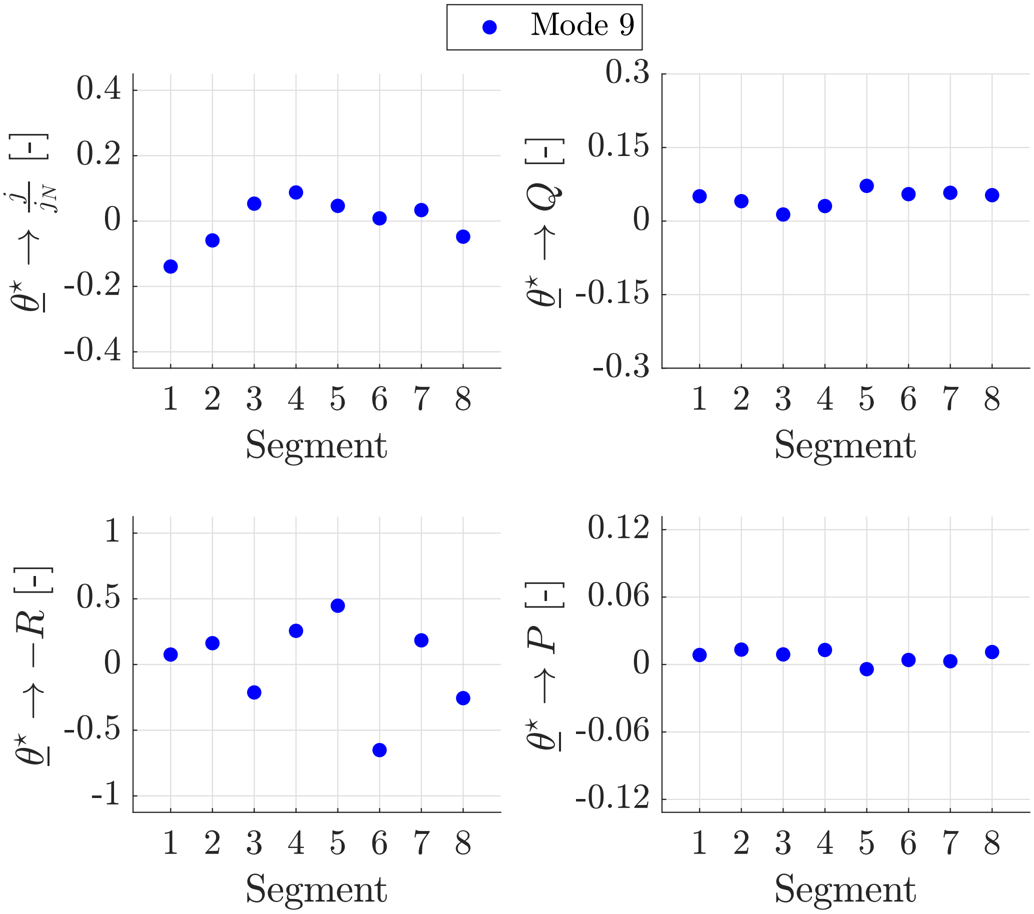

Figure A.44: Eigenmode associated with the observable vectors ($\underline{\theta_9^{\star}}$).

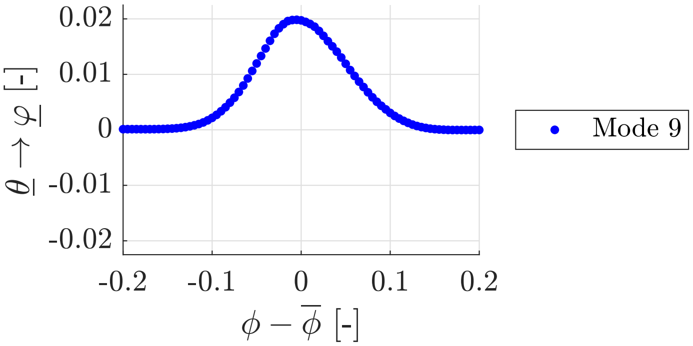

Figure A.45: Eigenmode associated with the mixing PMFs ($\underline{\theta_9}$).

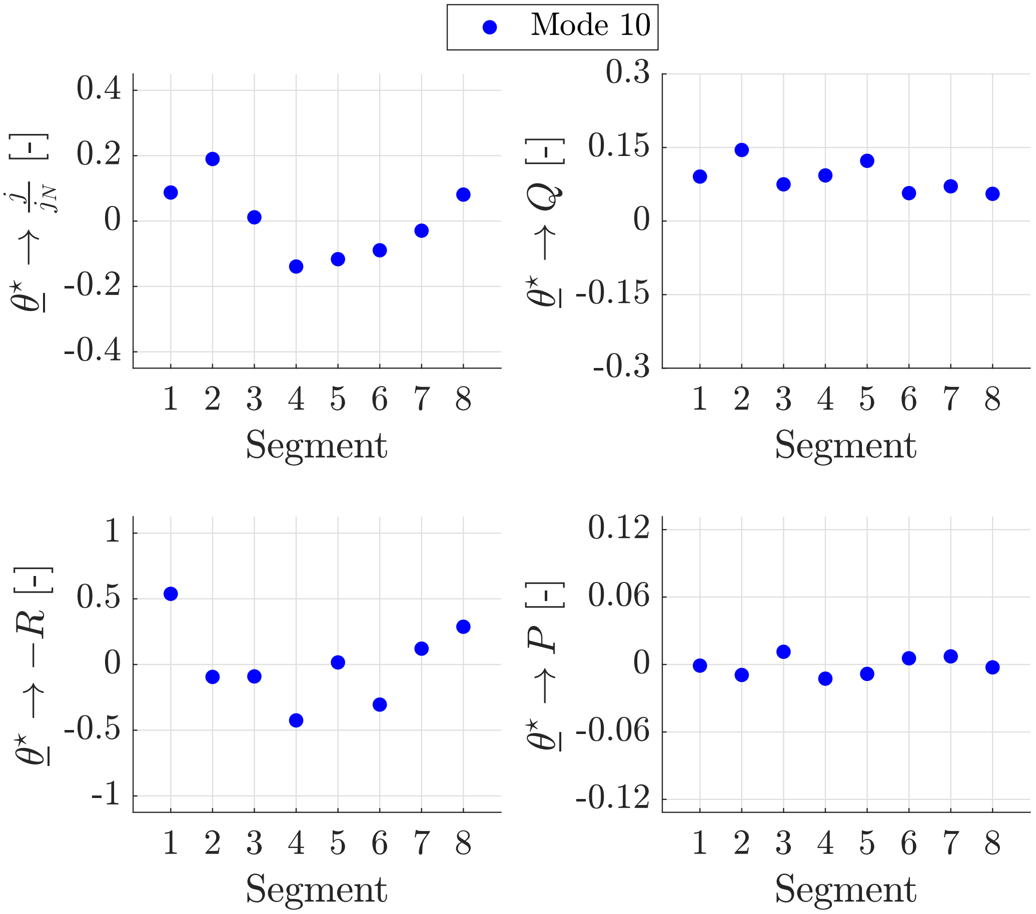

Figure A.46: Eigenmode associated with the observable vectors ($\underline{\theta^\star_{10}}$).

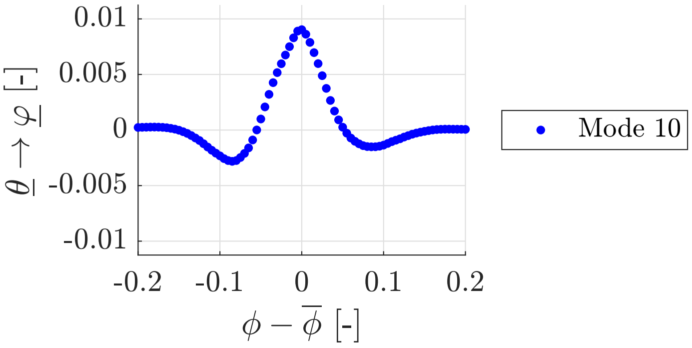

Figure A.47: Eigenmode associated with the mixing PMFs ($\underline{\theta_{10}}$).

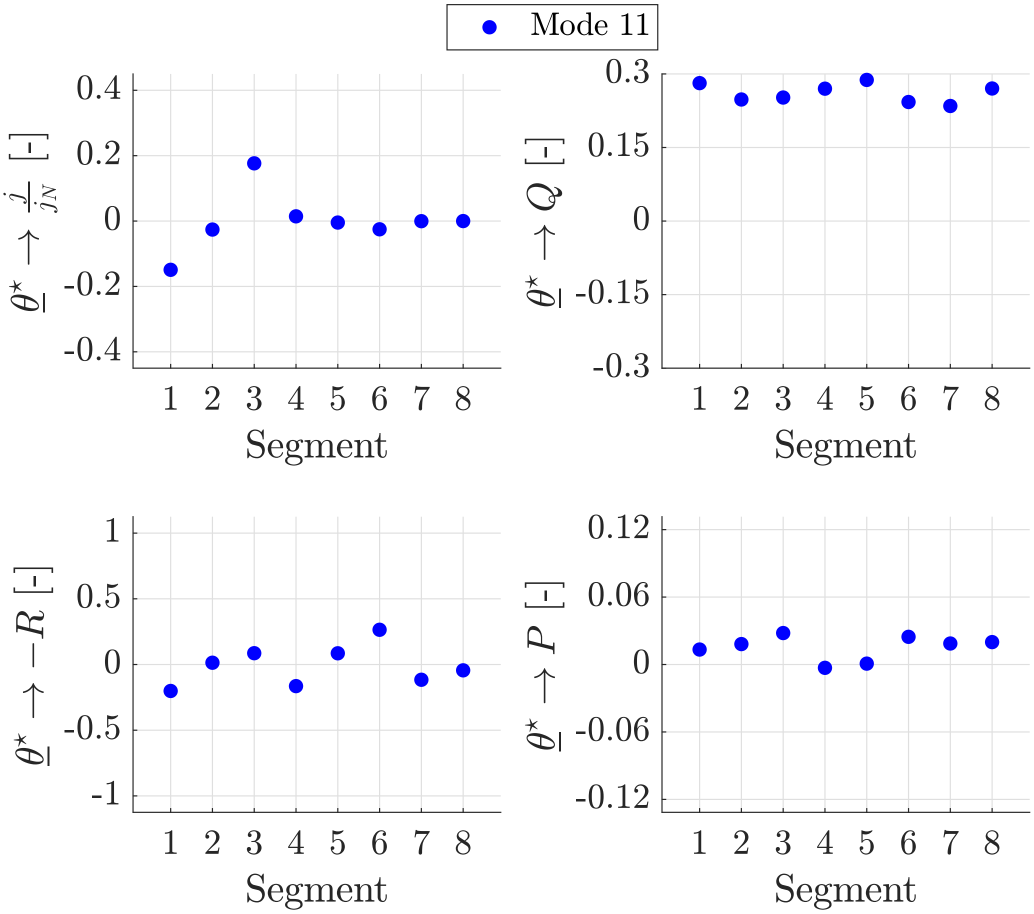

Figure A.48: Eigenmode associated with the observable vectors ($\underline{\theta}^{\star}_{11}$).

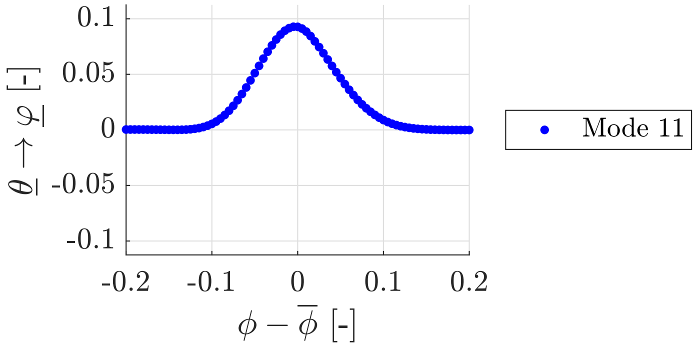

Figure A.49: Eigenmode associated with the mixing PMFs ($\underline{\theta}_{11}$).

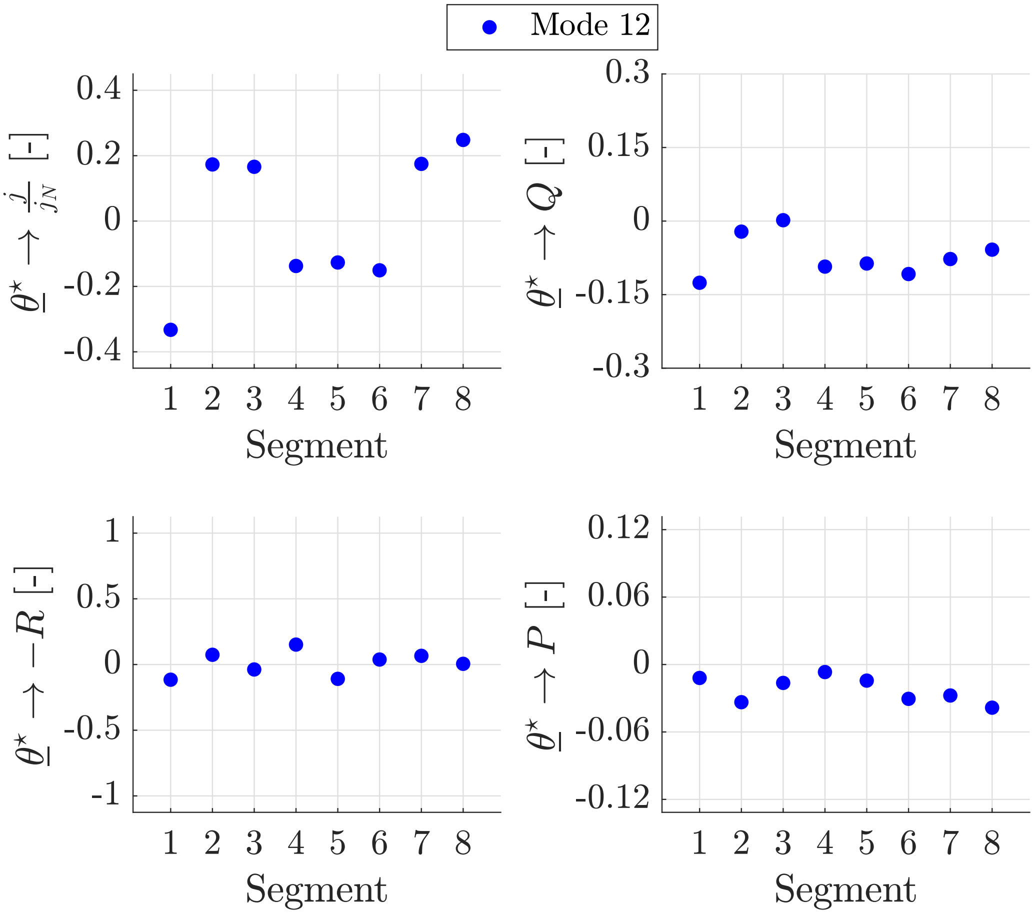

Figure A.50: Eigenmode associated with the observable vectors ($\underline{\theta}^\star_{12}$).

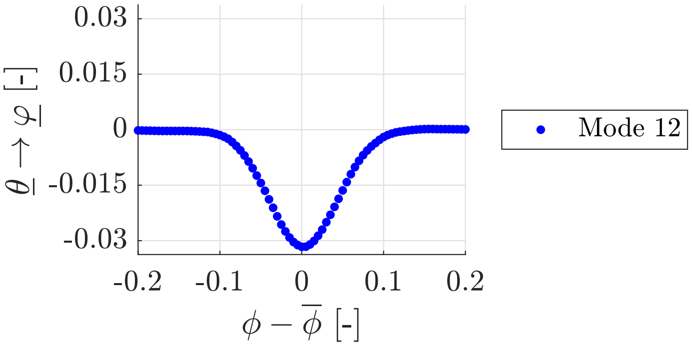

Figure A.51: Eigenmode associated with the mixing PMFs ($\underline{\theta}_{12}$).

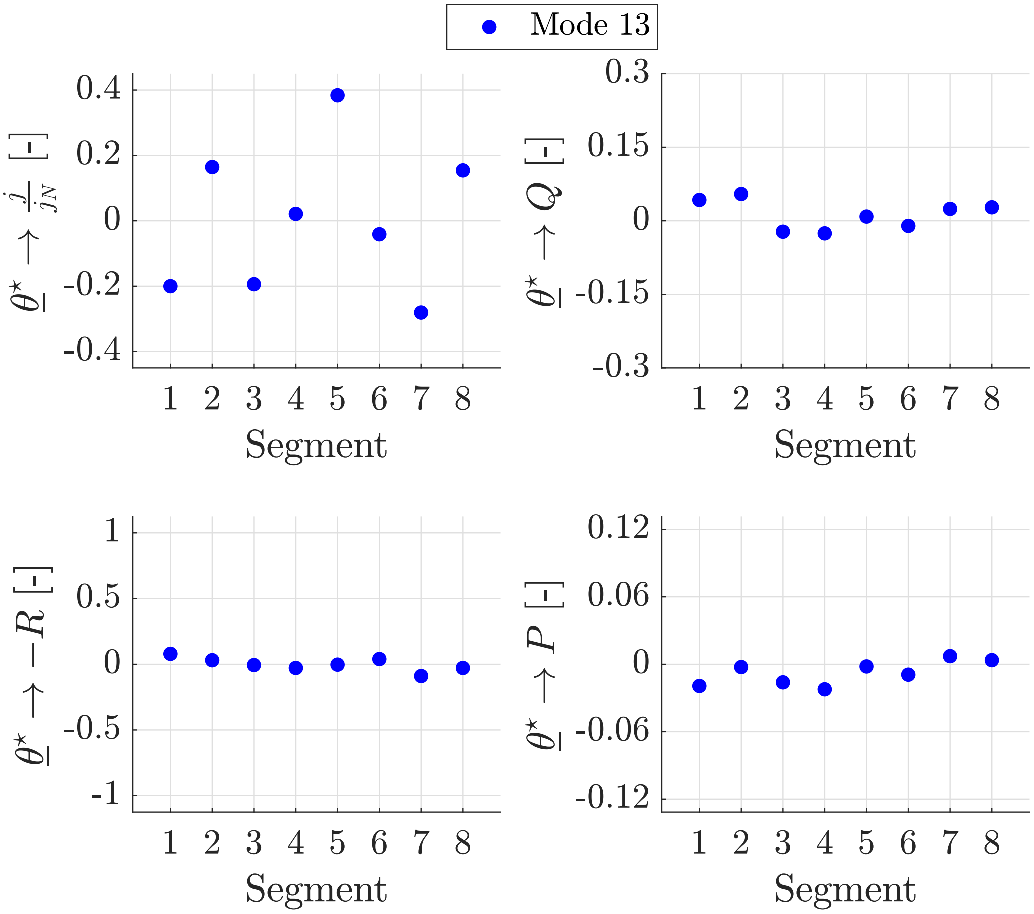

Figure A.52: Eigenmode associated with the observable vectors ($\underline{\theta_{13}^\star}$).

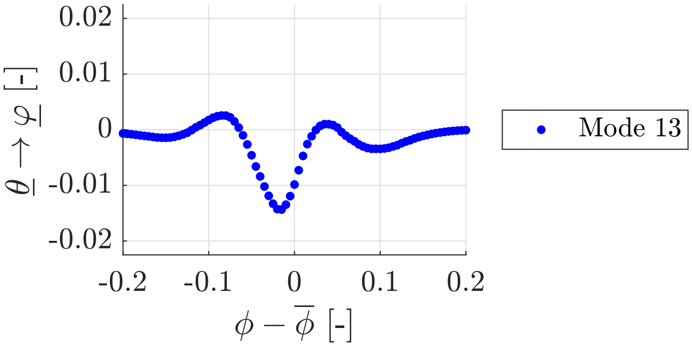

Figure A.53: Eigenmode associated with the mixing PMFs ($\underline{\theta_{13}}$).

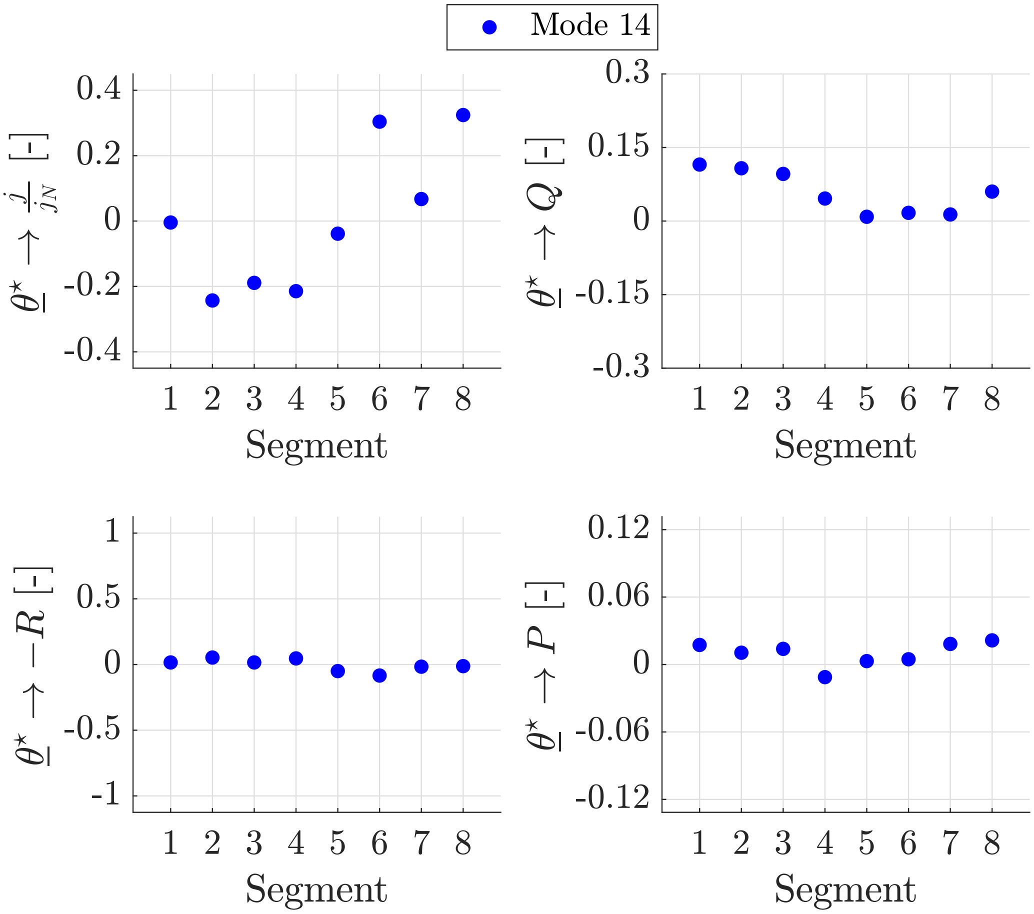

Figure A.54: Eigenmode associated with the observable vectors ($\underline{\theta_{14}^\star}$).

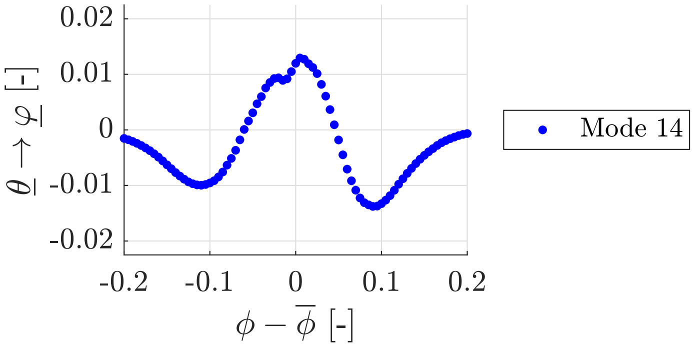

Figure A.55: Eigenmode associated with the mixing PMFs ($\underline{\theta_{14}}$).

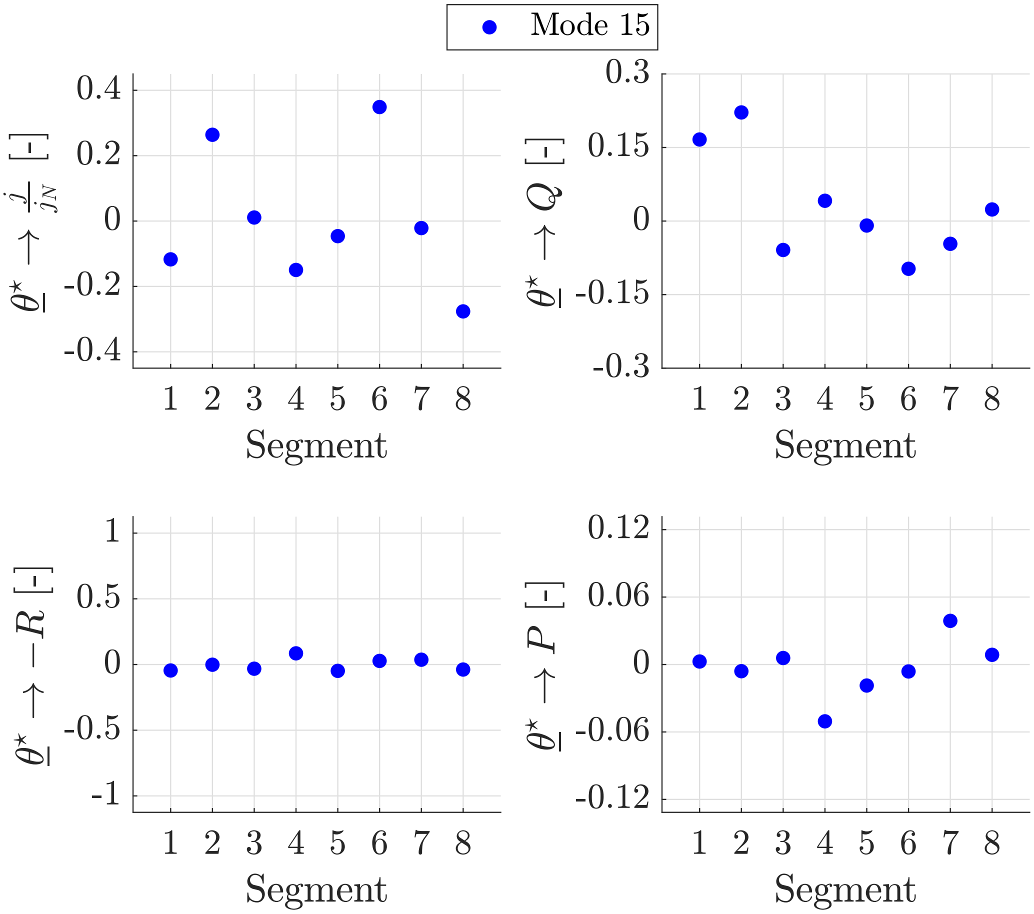

Figure A.56: Eigenmode associated with the observable vectors $(\underline{\theta}^{\star}_{15})$.

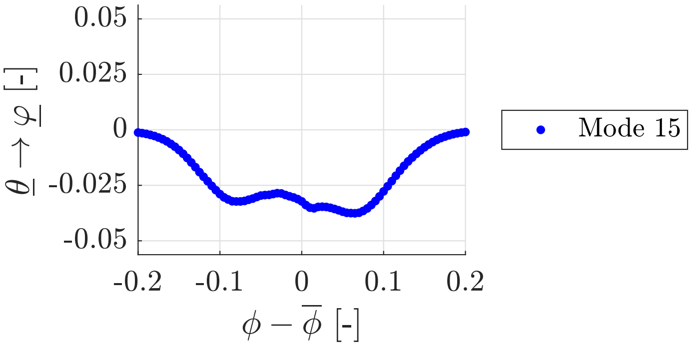

Figure A.57: Eigenmode associated with the mixing PMFs $(\underline{\theta}_{15})$.

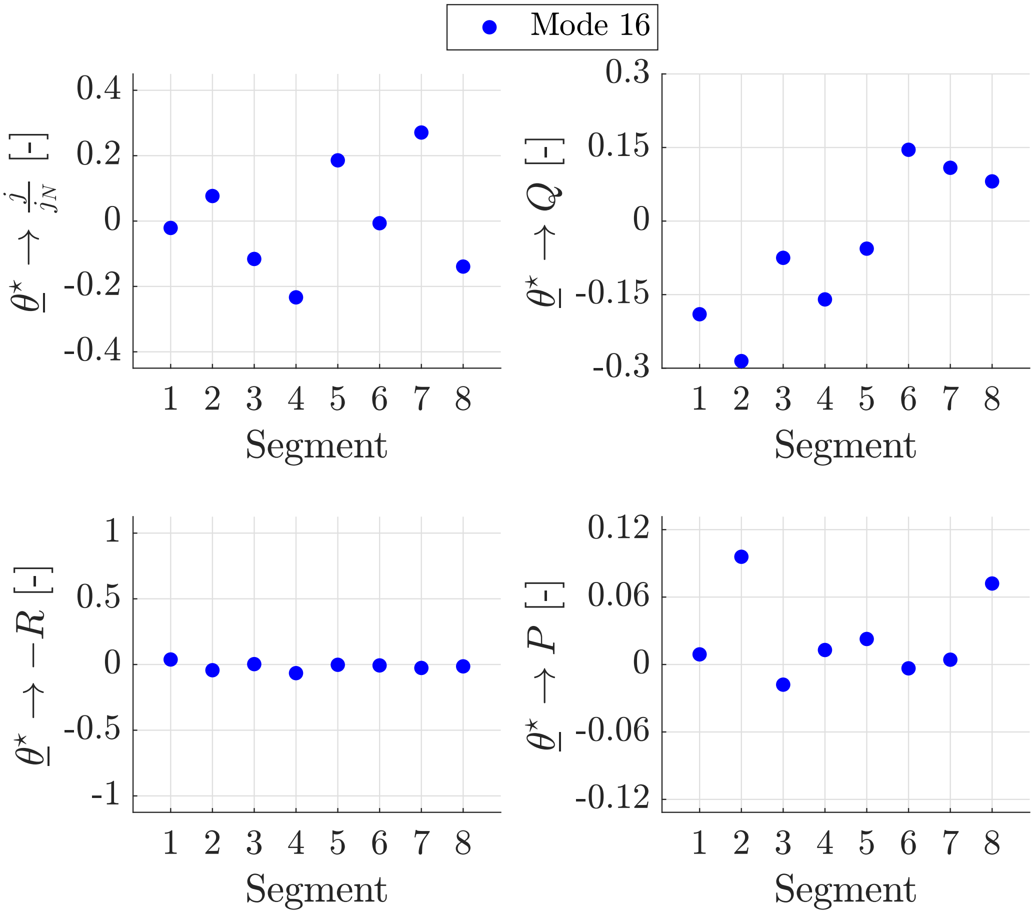

Figure A.58: Eigenmode associated with the observable vectors ($\underline{\theta_{16}^{\star}}$).

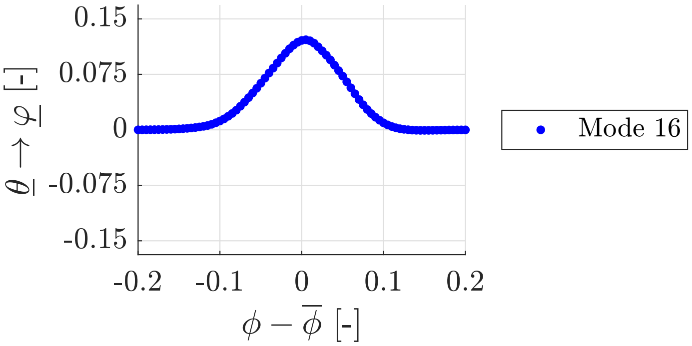

Figure A.59: Eigenmode associated with the mixing PMFs ($\underline{\theta_{16}}$).

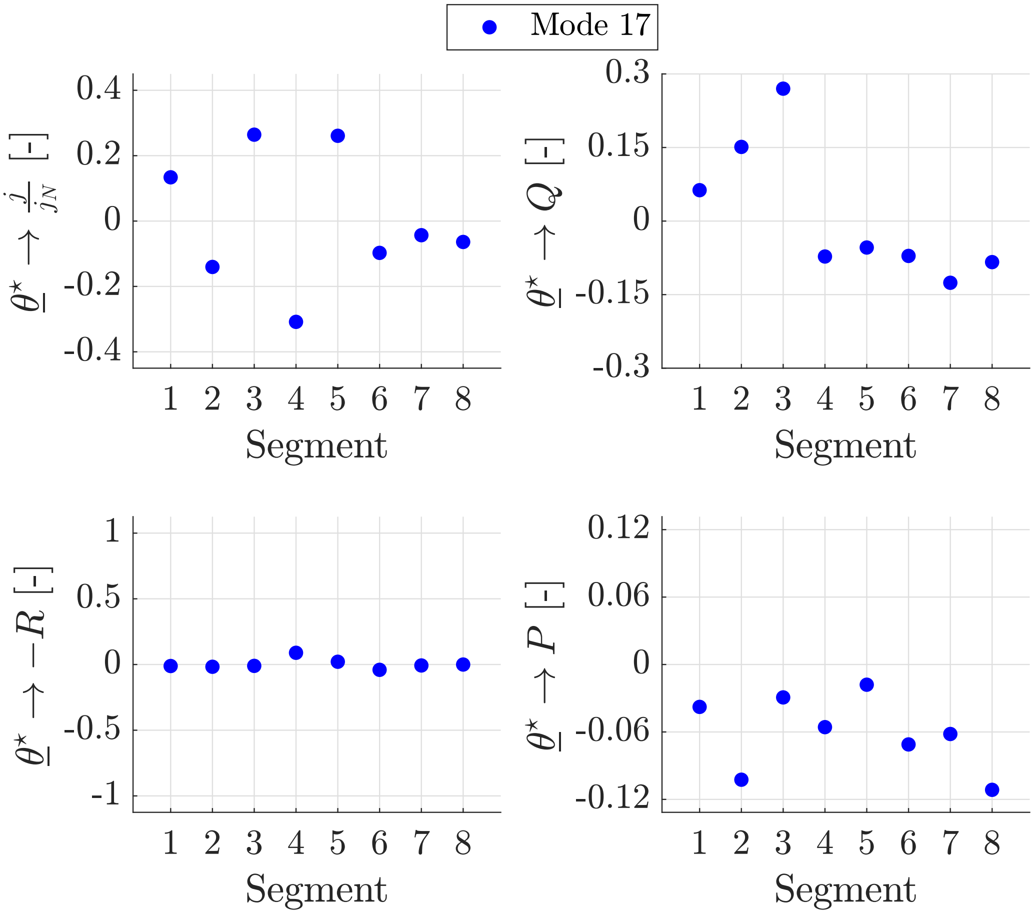

Figure A.60: Eigenmode associated with the observable vectors ($\underline{\theta}^\star_{17}$).

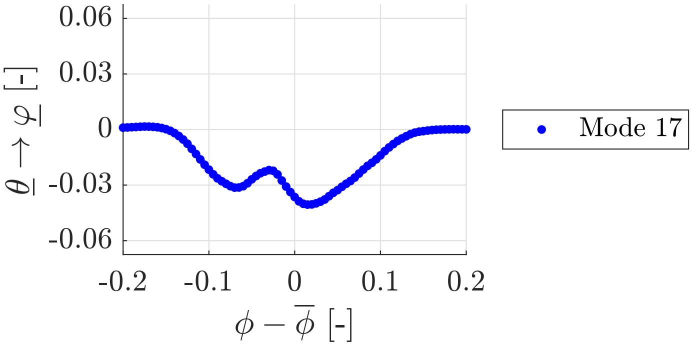

Figure A.61: Eigenmode associated with the mixing PMFs ($\underline{\theta}_{17}$).